From Close Binary White Dwarfs to White Dwarfs

A presentation of observational evidences
to link these evolutionary stages

A dissertation for the degree *doctor scientiarum*
by

José Miguel González Pérez

June, 2004

University of Tromsø
FACULTY OF SCIENCE
Department of Physics
Astrophysics Group

Preface

This thesis is the last piece of research done by the astrophysics group in the University of Tromsø. It has been built over the experience and work done in the group by many previous students during several years, with the common goal to understand better the AM CVn systems, and the possibilities to create peculiar white dwarfs as end result of the evolution of close binary systems. The activities developed in our small group have been numerous and focusing the problem from different perspectives: development of instrumentation for fast photometry, photometry, spectroscopy and modelling. My work has been built over the group large experience in fast photometry, and the development of an excellent instrument to achieve these observations: the Tromsø CCD Photometer, which was developed as part of Roy Østensen PhD program. I have had the privilege to use this instrument for its first research program: the search for pulsations in central stars of planetary nebulae.

This thesis presents observational evidences to link stages in the evolution of close binary systems, which may produce peculiar white dwarfs. This search of observational clues has been done using different approaches. Without a clear idea of the thesis main objectives, the different research lines presented may seem not to be connected. Therefore, I will present a detail explanation of the main goals, motivation and general background of the project in Chapter 1. Part of the thesis has been already published, as contributions to conference proceedings, and soon after the dissertation will be submitted to journals. Chapters 2 to 5 present works which will result in separate papers. Therefore, I have chosen to have references to each chapter at the end of the same chapter.

This thesis started as an adventure, and have finished as one of the most important steps done in my life, which have opened the possibility to dedicate my time to what I really wish and have wanted since I was child: look to the stars. I started this adventure sometime ago, in 1998. I had a stable job as computer administrator at home, Tenerife; the ideal job for many of us who had finished recently a university degree in physics, mathematics or computer sciences. This was a stable and good paid job. However, there was some personal lacks with this job: lack to do something that you really like, to solve problems that you feel interesting and make exiting the day. I was completing, at the same time, my master degree in Astrophysics, and knew that I wanted to give me a chance to dedicate my time to what I really

enjoyed, which at that time were the extra hours working with astronomy after finishing my daily duties as system administrator.

I contacted universities abroad looking for possibilities to do the doctoral degree. I contacted universities in Norway because I had visited the country before and was impressed with its beauty. I got positive response from Jan-Erik, a letter from Tromsø, the northernmost university; the place of fjords, mountains, aurora borealis and midnight sun. At the same time I was offered a permanent position as system administrator. The decision was so easy: I chose the adventure, the possibility to build a future that could allow me to dedicate my time to my hobby. So I came to Tromsø: from 27 degrees latitude to 70 degrees. I got the best support and help from my family. The first common question I received in Tromsø several times was: 'What are you doing here? Everybody try to go Tenerife and you move up here?!'.

These years in Tromsø have had its positive and negative aspects; but the positive have won by far, and I have learned about myself and have grown as person from the negative ones. My wishes were to do a lot of observational work, to do field work in astronomy, that is, to be close to telescopes. In this direction, the decision to work with the small group in Tromsø was surprisingly perfect! I was able to learn a lot of the observational part of the astronomy by 'playing' with the small (0.5 m) but interesting telescope in Skibotn. This telescope is perfect for educating new astronomers. I have had the possibility during these years to work actively in this telescope, and to participate in the improvements done to the system. I have learned a lot by participating in the development of instrumentation and software for fast photometry. By working in this group I have been able to participate in many observational programs. These participations have increased my knowledge and experience in the observational part of the astrophysics, and have given me the possibility to dedicate many nights to my favourite part of the research: the observations.

I got also the possibility to participate in multisite campaigns as member of the Whole Earth Telescope (WET). This group of astronomers is like a big family. The multisite campaigns and congress related with WET show the best positive spirit of science: collaboration, share of information, a lot of enthusiasm and a lot of fun. Be member of the WET community is one of the most amazing experiences I have experienced as astronomer. This collaboration has also helped me to see several times my personal favourite scene: the sunset beside 'Papa Teide' at Teide observatory.

There are many persons who have contributed to this work; who have made possible to complete this experience. I want to thanks all the member of the astrophysics group during my time in Tromsø for a lot of nice hours of good discussions, nice meetings and perfect

coffee sessions. I specially remember a lot of good moments shared with Dima, Ramin, Roy, Frank and my good friend Robert. I want also to express my gratitude to Professor Edmund Meistas who introduced me to the observational astrophysics and the telescope in Skibotn, He showed me how to be a good northern observer, including in the learning tasks like collecting snow and melting it to have water when the pipes are stacked and removing snow from the road to be able to reach the telescope! I want to thanks my colleague Travis for his motivating seminars when he was invited to Tromsø by Jan-Erik, and all his help and advise when working together with our project involving the supercomputer Darwin.

I also want to thanks many friends not related with astronomy but who has influenced so much in making so interesting and funny these years in Tromsø. From the first years, I remember a lot of nice moment with Truude, Ela, Marcela, Anders and Lena, Nacho, and specially my good friend Bea, who always attended my snowballs crashing her window asking for some hot chocolate! I have shared so wonderful moments and long conversations with Angel, talking a lot about the political situation and missing our lovely country, always around a couple of drinks at the Markens Grode, During the last years new friends appeared and, with them, more funny moments which I shared with Nerea, Gro, Jess, Maria, Torsten, Meseret, Malaku, Bob, Arnaut and specially Robert. Also my guapas roommates during my last months in Tromsø: Victoria and specially my jumping friend Jai, who has helped me so much during these last months. I want to express my gratitude to all of them for making so interesting these 5 years in Tromsø.

My last months in Tromsø were filled up with a lot of changes in my life; a lot of new shinning optimism, fresh support and big smiles which appeared when first my Añutka and, just few months later, a wonderful new project called Alexandra entered in my life. My pretty small family; they just appeared when the thesis was quite advance but motivated me so much to finish it to be able to build our future together. And not only that; do you know what difficult is to have 40 copies of my thesis of 190 pages that must be ordered because the printing left all pages 1 together, all pages 2 together and so on? Now Añutka knows! Thanks amorsik.

Finally, I want to mention and express my gratitude to the two major contributors, my main conductors in this adventure, always there, from the very beginning to the end; the two persons that by far have contributed more to make this project possible, and to finish it leaving a big smile in my face: my supervisor and mentor Jan-Erik, and my superamiga Montse.

José M. González Pérez (Tromsø, June 2004)

"¡Esta noche no se duerme!"

Los Suaves

Contents

List of Figures

List of Tables

Chapter 1

From Close Binary White Dwarfs to White Dwarfs: General introduction to the thesis background, motivations and objectives.

Abstract.

The main goal in this project is to test a hypothesis that some white dwarfs are the end product of mass transfer in a close binary system. We investigate the idea that close binary stars, which have undergone common envelope stages and have lost their outer hydrogen layers, can evolve into white dwarfs with certain characteristics, like having a thick external helium layer and a specific C/O internal profile. Such stars are observed and cannot be explained with the theories of evolution from a single star. Evolutionary models indicate the existence of evolutionary channels for close binary systems which may lead to the generation of white dwarfs with certain characteristic. However, there is a lack of observational evidences to support these ideas. This thesis focus on the search for and test of some of these observational clues. Photometric and asteroseismological analysis of selected candidates are our main tools. The aim of the project is to investigate if there are any possibilities to find differences between white dwarfs that have evolved from single stars, and white dwarfs which are descendants of close binary evolution.

'From Close Binary White Dwarfs to White Dwarfs': J. M. González Pérez, e-mail: jose@phys.uit.no

1.1. Introduction

An important characteristic of the scientific method is that it must be open and, therefore, it must include the possibility to share with the general public the exiting discoveries, to make understandable the research and conclusions. Several scientific works are full of technical vocabulary which make them understandable only to people who know this vocabulary (which does not means experts or more clever people). Unfortunately, several different disciplines in science are full of this specific vocabulary. This is also the case in astronomy. However, a large amount of scientific work and, in particular, part of this thesis, is payed for by the society, and it is my responsibility and honour to try to give something back. I wish to share what I am doing because I like it and have fun with it. However, the research presented in this thesis needs in several cases this collection of difficult terms and words which makes it extremely difficult to share all my work. However, I will try to write this chapter in a less complicated way, at least the firsts sections. The complexity in the following sections will increase, but I hope the impressions of the firsts can help to share the general aspects of my work, my motivation, and main goals. By complexity I mean the necessity to have some basic understanding and knowledge about some concepts and terms which are in several cases mentioned but not explained. On the other hand, I try to achieve my compromise with the tax-payers by trying to share my enthusiasm about the stars, stellar evolution and astronomy in general with kids and others who may want to know about these fascinating topics. I think my possibility to generate a positive 'WOAU' in kids, and awake even more their curiosity and criticism is the best way to give back to the society their support, which has allowed me to dedicate my time to my favorite hobby.

In addition, I want to apologize for the 'tricky things' that may appear in the language. The following example illustrates what I mean by 'tricky things': 'planetary nebulae' is a strange word but with some sense because 'planetary' seems to be related to planets and 'nebulae' with some gasses or something, maybe around the planet? This word was introduced in the nineteenth century to describe an important discovery: the observation of glowing objects around some stars. The first planetary nebula ever seen by a human was the Dumbbell Nebula M27 in Vulpecula, which was discovered by Charles Messier on July 12, 1764. The comparison to a "fading" planet was first pronounced by Antoine Darquier, the discoverer of the second of these objects, the Ring Nebula M57 in Lyra; he found it shortly before Messier when both were tracing the same comet in January, 1779. William Herschel eventually invented the name "Planetary Nebula" for these objects

in his classification of nebulae in 1784 or 1785, because he found them to resemble the planet newly discovered by him, Uranus. The astronomers thought at that time that these observations could indicate the formation of planetary systems. Therefore, they started to use the word 'planetary nebulae' to describe these type of objects. However, later on, better possibilities to observe and analyse these structures indicated that they must be related to the later stages during the evolution of stars like our Sun. Stars with low mass (less than about four times the mass of the Sun) die by gently ejecting their outer layers. These layers are illuminated by the remaining stellar core. Therefore, astronomers discovered that these nebulae have nothing to do with formation of planets around the star. However, the historical name was kept, so we still call them planetary nebulae! With the progress in astronomy, different groups study different topics related with planetary nebulae and new terms and words have appeared: PNN for planetary nebulae nuclei (the remnant star), PNe for planetary nuclei envelope... Therefore, now the texts can be full of terms like these (my chapters are good examples). In this case, the terms have only two things in common: a 'P' and a 'N', and one is wrong because this has nothing to do with 'P'lanets!

1.2. White dwarfs.

White dwarfs are among the dimmest stars in the universe. Even so, they have commanded the attention of astronomers ever since the first white dwarf was observed by optical telescopes in the middle of the 19th century. One reason for this interest is that most stars, including our Sun, will become white dwarfs when they reach their final, burnt-out collapsed state; another reason is that white dwarfs represent an intriguing state of matter. Over 90% of the stars in the universe will end their evolution as white dwarfs. Therefore, many of the stars we see with our eyes in the sky will one day become white dwarfs.

1.2.1. The evolution of the Sun.

Our Sun is one of the stars that will evolve into a white dwarf. The evolution of Sun like stars is well known if they are not part of binary systems. An isolated star will follow the single evolutionary channel predicted for the stars with masses near one solar mass which can be resumed as follow:

The Sun is now in a stable stage in its evolution where it will spend a big fraction of its life. The astronomers calls this stage the main sequence. The Sun has been already on

the main sequence around 5 billion years and it is expected to be there another 5 billions. When the Sun first became a star on the main sequence, its core was approximately 75% hydrogen and 25% helium. Hydrogen-to-Helium fusion is the predominant mechanism used for internal energy production. As it ages, the abundance of hydrogen within the Suns core will decrease and the helium abundance will increase.

In around 5 billion years, the Sun will form a core of helium "ash". The star will experience an energy crisis and its core collapses when the star's basic, non-renewable energy source - hydrogen - is used up. Eventually, the non-burning helium core begins to contract, releasing enough gravitational energy to heat the shell of hydrogen around the core. Hydrogen shell burning begins and becomes even more fervent as the helium core continues to contract. The nuclear fusion of the hydrogen in the shell will produce a new surge of power that will cause the outer layers of the star to expand. This is called the "red giant" phase of a star's existence. Red giants can swell up to 100 times the current radius of the Sun, and although they have a lower surface temperature than our sun currently does, their larger size makes these giant stars hundreds of time more luminous than our Sun. The orbit of Mercury and possible Venus, will be inside the Sun in this Red Giant stage and life will be not possible on the Earth. The astronomers call this stage the Red Giant Branch (RGB).

Continued contraction of the core increases the core temperature and density. When the core density reach the value $\sim 10^{11}$ kg/m^3, the central helium core ignite and begin fusing into carbon. The Sun will reach a new stable stage where steadily burning helium at the central core and fusing hydrogen within a shell around the core.

After a few tens of millions of years in this state, the helium in the core is all burned to carbon in a nuclear reaction called the triple alpha cycle. The core further contracts, igniting a shell of helium around the carbon ash. A new hydrogen shell is formed around the helium shell, heating the stars outer layers even more and resulting in a red super giant star. This stage is called Asymptotic Giant Branch (AGB). As the core continues to contract, it heats up again but doesn't get hot enough to fuse carbon into heavier elements. Electron degeneracy now supports the inner core while hydrogen and helium continue to burn in the outer shells of the stellar core.

Helium shell flashes liberate sufficient energy over time to blow off the stars outer layers into space forming a planetary nebula. Examples of such objects are M57 (Ring Nebula), M27 (Dumbbell Nebula), and M97 (Owl Nebula). Such nebulae are illuminated by the

Table 1. Typical parameters of white dwarfs

Luminosity		$2.5\text{x}10^{-2}$-$3\text{x}10^{-5} < L_{\odot}$
Radius	$\sim$7000 km	$< 0.01 R_{\odot}$
Mass	$\sim 10^{30}$ kg	$0.6 \pm 0.1 M_{\odot}$
Density	$\sim 10^{9}$ kg/m^3	$10^{6}\ \rho_{\odot}$
Surface Temperature	4000 - 150000 K	

remaining stellar core, which is no longer undergoing nuclear fusion reactions, but instead is shining due to its residual temperature. The planetary nebula shines because it absorbs high-energy ultraviolet radiation from the central star, which raises the energy level of electrons within the gas envelope. When the electrons return to their lower states, they emit photons at characteristic wavelengths, which cause the nebula to shine.

As the outer layers of the planetary nebula dissipate, the white dwarf, a sphere of ultra dense degenerate matter about the size of the Earth, is left to cool over billions of years, eventually becoming a burned-out cinder known as a black dwarf. White dwarf stars have enormous densities: an Earth-size white dwarf has a density of 10^9 kg/m^3. In comparison the earth average density is 5.4×10^3 kg/m^3. That means a white dwarf is 200.000 times as dense!

1.2.2. White dwarfs properties.

White dwarfs (WDs) are the final stage of stellar evolution for stars with a mass lower than about 8 $M_{\odot}$. They are stars that have wasted all their fuel and are significantly contracted, consisting mainly of fully ionized helium, carbon and oxygen. They have a white or blue colour and very low luminosities. Their surface temperatures, that can be deduced from their spectra, are in a between 3400 and 150 000 K. According to the Stefan-Boltzmann law and their low luminosity, WDs must have a very small radiating surface. In fact, the radius of a typical WD is about 0.01 times the radius of the Sun, or, in other words just the size of the Earth. Despite their small volume, WDs have still masses around 0.6 solar mass, resulting in very high densities. Table 1 presents the typical parameters of white dwarfs.

Due to their low luminosity, WDs are only visible in the solar neighborhood, up to a few hundred pc. So far, only about 1500 White Dwarfs are known, but 10% of all stars in

the solar neighborhood are assumed to be WDs. The first one, Sirius B, a faint companion of Sirius, was discovered in 1844 because of small perturbations in the trajectory of Sirius.

1.2.3. Why white dwarfs do not collapse?

When they were first discovered, white dwarfs presented a paradox to astronomers. If a white dwarf couldn't produce energy through nuclear fusion, how could it generate the pressure necessary to keep it from collapsing further? The paradox was not resolved until the quantum theory of matter was developed in the 1920s. This theory showed that matter in so-called "degenerate" states of extremely high density could produce a new type of pressure never observed in a terrestrial laboratory. This is because the quantum theory prohibits more than one electron from occupying the same energy state.

To see how this works, think about a parking lot. Only one car is allowed per space. When there are many empty spaces, there is very little motion in the parking lot. As an occasional car enters the lot it is quickly parked. When the parking lot is full, however, the picture changes. There is continual motion as cars move from one row to another while drivers search for a space. The pressure builds to get into position whenever a space is opened up.

Extremely dense matter is like a crowded parking lot. All of the low energy "parking spaces" are taken, so electrons are forced into higher energy states, not because they are hot, but because there is nowhere else to go. This creates a "degenerate" electron pressure (degenerate refers, not to the moral character of the electrons, but to the fact that all the low energy states are occupied). This pressure is what prevents white dwarf stars from collapsing under their own weight.

1.2.4. Chandrasekhar limit and close binary systems

While still in his twenties Subrahmanyan Chandrasekhar (1935) used relativity theory and quantum mechanics to show that degenerate electron pressure can do only so much. If the mass of the white dwarf becomes greater than about 1.4 times the mass of the Sun later called "the Chandrasekhar limit" it will collapse.

In a binary star system this could happen if a nearby companion star dumps enough material onto a white dwarf to push it over the Chandrasekhar limit. The resulting collapse and explosion of the white dwarf is believed to be responsible for the so-called Type Ia supernovae. These supernovae are very important because they are used as candles to

measure distances of remotes galaxies. These distances are used to study the structure and evolution of the universe.

1.3. Motivation for this thesis

One long standing problem in the theories for evolution of white dwarfs, is the so called "DB problem", which can be stated in the following way: white dwarfs are believed to be descendants of normal, not to massive stars, which have evolved through a giant stage, and when nuclear fuel is exhausted, have contracted to a stable configuration where the internal pressure is supplied by degenerate gas. During the contraction phase, the outer parts are lost and observed as a planetary nebulae, and the nucleus, or PNN star, is the pre-white dwarf, which is very hot and can be classified as a DO or a PG 1159 type. This evolves into a white dwarf which is simply the remains of a normal star, which slowly cools. The cooling at first is dominated by loss of neutrinos, later by radiation. The DO's have temperatures of the order of 100 000 K, and as they cool they can loosely be classified as DA's or non-DA's. A DA-star shows hydrogen lines indicating that hydrogen is present in the atmosphere. A non-DA does not show hydrogen lines in its spectrum, and if helium lines are present, it is called a DB.

The "DB problem", which has created a vigorous debate in the community of white dwarf scientists, the last 20 years, is the fact that only DA's are observed at temperatures between 45 000 K and 30 000 K. One explanation is that even in the non-DA's there exist some hydrogen, which floats up to the surface at T_{eff} = 45 000K. A DB, which shows helium lines when it is hotter than 45 000K, will then transform into a DA, and cool as a DA until $T_{eff} = 30\ 000K$, when the heavier element helium is dredged up and replace hydrogen as the dominant spectral element. The star then is "reborn" as a DB. The problem with this theory is that it requires a thin envelope, and a convective layer which can do this dredging up. This requires some fine tuning of models, which can hardly cover all the varieties of white dwarf composition and constitution that have been observed.

In this project we investigate another channel for creating non-DA's. We investigate the idea that close binary stars, which have undergone a common envelope stage, and lost their outer hydrogen layers, can evolve into DO or DB stars, without needing the dredge up process. This study can lead to a better understanding of the cooling track of the white dwarfs, which gives important cosmological information as the limiting age for the nearby stars in our galaxy.

1.4. Searching for observational evidences.

The aim of this project is to investigate if there are any possibilities to find differences between white dwarfs that have evolved from single stars, and white dwarfs which are the descendants of binary stars. This is done by analysing photometric properties of different objects that may be related to evolutionary channels which lead to the generation of white dwarfs deficient in hydrogen. The objects analysed are the nuclei of planetary nebulae (PNNs), which present characteristics that may indicate the presence of a close companion, and the family of interacting binary white dwarfs, the AM CVn objects. The AM CVn objects are some of the most exotic products of binary evolution and may produce abnormal white dwarfs deficient in hydrogen. This thesis looks for photometric features that may relate some PNNs to an evolutionary stage close to the AM CVn family or close binaries in general. Other idea developed in this thesis is that pulsations may reveal layered interior structures, which may be a result of the binary evolution. One parameter that can be determined from asteroseismology is the thickness of the outer helium layer. Pulsating DBs stars with abnormal thickness layers of helium are good candidates to be descendants of the AM CVns.

We proceed in the next sections with a short introduction to the AM CVn systems, an overview of the bipolar planetary nebulae as possible indicators of close binary evolution, and an introduction to the pulsating stars and, in particular, the pulsating PNNs and DBs which are the main candidates for our asteroseismological analysis.

1.5. AM CVn objects.

The AM CVn family (see Warner 1995 for a review) represents one of the most exotic products of the binary evolution. In the AM CVn stage what is left is a CO white dwarf accreting mass from the remaining semi-degenerate helium remnant of a star stripped of the bulk of its mass before helium could ignite.

The AM CVn objects form a small family with the following fundamental properties: they present ultra-short binary periods, between 5 and 65 minutes; they have helium rich spectra with no trace of hydrogen; they have extreme mass ratios ($q = M_2/M_1 < 0.1$); the secondary is strongly irradiated and is not seen in the spectrum; some objects present soft X-ray radiation which is associated with the boundary layers or accreting spots. Several of these systems have accretion discs. In these systems, the main contribution to the optical observations is due to the disc. Therefore, several of the modulation frequencies

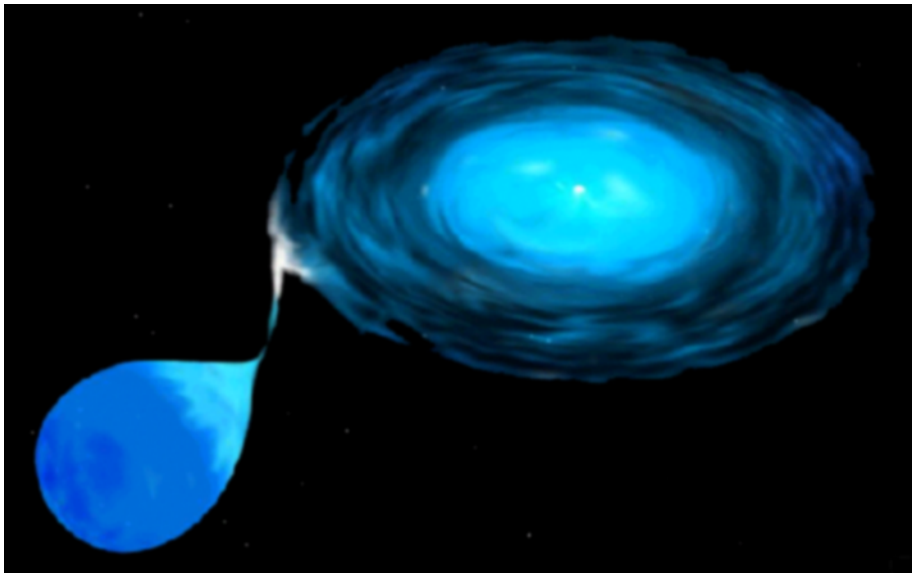

Fig. 1. Artistic impression of AM CVn.

observed are related to its geometrical characteristics. The discs can appear in high states showing absorption spectra, and in a low state 3–4 magnitudes fainter, showing emission spectra. The discs in high state are excentric discs having superhumps and spiral structure (Simpson & Wood 1998). Some systems are disc-less and the mass transfer is direct or driven by magnetic fields.

The interpretation of these observational evidences suggests that the AM CVn system itself is an extremely short period binary system with a CO degenerate dwarf of approximate one solar mass, which receive almost pure helium matter from a low mass ($0.08\ M_{\odot}$) semi-degenerate secondary helium dwarf. The mass transfer rate is estimated around $10^{-9}\ M_{\odot}/yr$. We can therefore interpret the AM CVn objects as Interacting Binary White Dwarfs (IBWD) with a low mass transfer rate of pure Helium, to a CO dwarf. Figure 1 presents an artistic impression of AM CVn.

1.5.1. Where do they come from?

The description and properties of the AM CVn systems, and in particular their ultra short orbital periods and the low mass transfer rate, establish them as one of the possible last steps in the evolution of the helium star cataclysmics, or He CVs (Iben & Tutukov 1991). These authors describe how there are many possible dramatic episodes in the evolution of such binary systems, with the likely outcome of total or partial disintegration of the primary star through supernova or dwarf nova explosions. However, some quieter scenar-

ios are also predicted for the terminal evolution, after helium flashes have ceased. The AM CVn family may follow one of these last scenarios. They may give us evidence about a possible evolution of helium star cataclysmics without dramatic episodes.

The evolution of the helium star cataclysmics before the AM CVn stage, basically depends of the mass transfer rate and the mass of the CO degenerate dwarf at the onset of mass transfer. For a very wide range of combinations of component masses, orbital shrinkage driven by gravitational wave radiation produce a transfer mass rate close to 3×10^{-8} $M_{\odot}$/year in the early AM CVn stage. Fixing this value for the accretion rate, the evolution will depend only of the mass of the accreting white dwarf. If this is more than 0.8 $M_{\odot}$, it probably has a supernova Ib outburst or dwarf supernova outburst and then evolve into a R CrB star. If the mass is under this limit, such dramatic episodes are not expected.

According to Iben and Tutukov (1991), the AM CVn systems may evolve within the second possibility ($M_{CO} \leq 0.8$ $M_{\odot}$) and then into R CrB stars. In addition, the mass transfer in these objects has decreased and no more helium shell flashes are expected. Therefore, they give us some evidences about evolution into degenerate binary stars on a semi stable scenario.

It should be mentioned that the evolution of a helium transferring binary was first outlined by Savonije et al. (1986). The starting point is a low-mass, non-degenerate helium burning star, with a white dwarf accretor. Loss of angular momentum via gravitational wave radiation (GWR) may result in Roche lobe overflow before helium exhaustion in the stellar core. When the mass of the helium star decrease below $\sim$0.2 $M_{\odot}$, core helium stops and the star becomes semi-degenerate. This causes the exponent in the mass-radius relation to become negative, and as the consequence the orbital period will increase (Nelemans et al. 2001). The minimum period is $\sim$10 min, and then the mass transfer rate decreases and the period increases up to 1 hr, while the luminosity of the secondary decreases below 10^{-4} $L_{\odot}$. Near the period minimum the mass transfer rate is, as mentioned before, 3×10^{-8} $M_{\odot} yr^{-1}$, and the helium layer may detonate when it reaches a certain thickness, and destroy the underlying CO white dwarf. This is called edge-lit detonation (ELD), and if this does not happen, we have an AM CVn system. Nelemans et al. (2001) have calculated the birth rate of AM CVn systems assuming extreme values of accreting 0.15 or 0.30 $M_{\odot}$ before ELD, and find Galactic birth rates or 1.1 or 6.8 10^{-3}, respectively.

Another explanation of the AM CVn objects was proposed by Faulkner et al. (1972, ApJ,175,L79) where the progenitor is a detached system of close double white dwarfs which are brought into contact by loss of GWR. The less massive white dwarf fills its Roche lobe first and then the AM CVn system is born.

The double degenerate and the semi-degenerate models give different relations between the mass transfer rate and orbital period (Nelemans et al. 2001), and it seems that the systems in high state have semi-degenerate secondaries and those with short periods and high mass transfer rate, probably are double degenerates without discs (Solheim 2003).

1.5.2. The evolution inside the AM CVn family.

This quiet evolutionary stage is expected to last as long as 10 Gyrs. During this phase we expect a slow evolution connected with a decreasing mass transfer rate: the secondary star looses mass at a decreasing rate while the orbit is expanding. The members of the family displays parameters which connect with this evolutionary sequence, from the objects with small orbital period, high transfer mass rate and high secondary mass, as AM CVn itself, to the systems where all these parameters have decreased, as for GP Com and CE 315 (Solheim 2003).

1.5.3. And after?

If we assume the physical interpretation presented for AM CVn objects, the mass losing object is degenerate or semi degenerate, and as the mass is transferred to the primary, the secondary will expand, and the mass transfer is sustained. In the process the accreting star may grow in mass beyond the narrow mass range near 0.6 $M_{\odot}$ of normal white dwarfs.

Two possible scenarios are expected in this phase: if some helium burning has taken place in the previous history of the secondary, it may have a small carbon core, or be mixed in carbon. When the mass transfer process starts to transfer the first carbon layer, the increased opacity due to carbon will quickly produce an expanding carbon rich envelope. The components may be forced to merge and the system will evolve into a R CrB star and later into a DB or DO white dwarf (Solheim 1996). Again the R CrB stars appear as a possible outcome of the evolution of the helium star cataclysmics. If the secondary is a pure helium semi degenerate object, the mass transfer will eventually stop when the secondary star has lost so much mass that degeneracy is lifted. Because of this helium rich mass transfer, the primary star has now a thick outer layer of helium, and its spectra

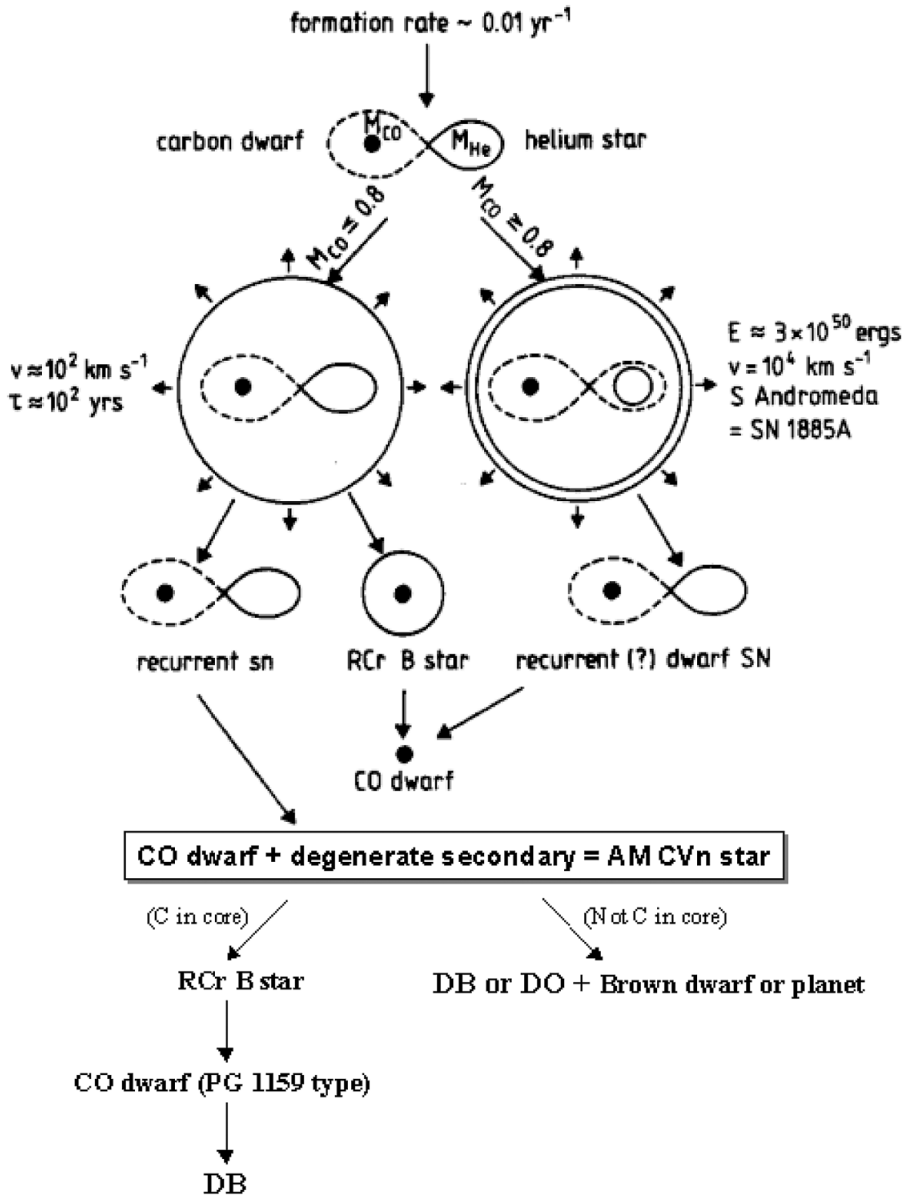

Fig. 2. Evolutionary channels from Interacting Binary White Dwarfs to White Dwarfs. Figure adapted from Iben & Tutukov 1991.

will be that of a helium white dwarf of abnormal mass. The star will have a small object, maybe a planet or brown dwarf in orbit (Solheim and Massacand, 1994).

Another interesting endpoint may happen if during the accretion process the white dwarf increases its mass over the Chandrasekhar limit. In this case the AM CVn object may explode as supernovae type Ia. An ELD will probably take place before this can happen (Nelemans et al. 2001).

The existing scenarios for evolution of helium cataclysmic variables (He CVs) suggest the possibility of some stages where the systems can evolve into single white dwarfs. In this way, some of the possible offsprings can be DB or DO white dwarf star with special characteristics, like abnormal mass and thickness of the outer layer of helium. The AM CVn family is situated in an advanced stage in the evolution of some helium star cataclysmics, which have survived all the previous helium flashes. It looks like a complex but semi stable structure, which is the best candidate to finally evolve into a peculiar DB or DO white dwarf star with abnormal properties.

An important goal in this thesis is to search for observational evidences to connect and understand better the precursors of the AM CVns and the possible offsprings. This analysis is necessary to investigate this path (proposed by R. E. Nather in 1985) of evolution from Interacting Binary White Dwarfs (IBWDs) to single white dwarfs. Figure 2 present the possible evolutionary channels for close binary systems which may produce AM CVn objects and end like abnormal hydrogen deficient white dwarfs. The graphs starts with a helium star and C/O white dwarf. Previous evolution through one or two common envelopes are necessary to create these starting point. These common envelopes may appear as peculiar planetary nebulae stages which will be the main objects investigated in this thesis.

1.6. Bipolar Planetary Nebulae.

From the evolutionary point of view, some planetary nebulae (PN) may be formed in evolutionary phases related with interacting binary stars. Historically, the main characteristics of hot and luminous PNNs have been interpreted in terms of post-asymptotic giant branch (post-AGB) stars at different phases in an alternating helium and hydrogen burning cycle. Departure from the AGB is attributed to a superwind, which strip off most of the hydrogen-rich envelope above the carbon-oxygen (CO) core. Some PNNs are known to be member of binary systems with orbital periods less than 1 day. In these cases, the PN systems are formed by close binaries when the primary fills its Roche lobe before it reaches the terminal AGB phase. Thus, the superwind, which was once accepted as the single mechanism for PN formation, is aborted in the case of close binaries and is replaced by a mass-loss mechanism which involve the formation of a common envelope (CE) containing matter which is supplied by the primary.

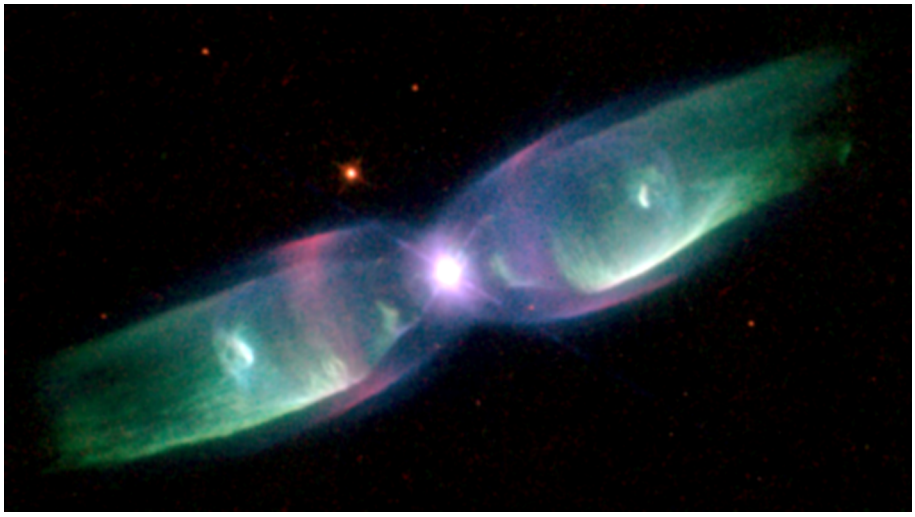

Fig. 3. Hubble Space Telescope image of M2-9, a striking example of a "butterfly" or a bipolar planetary nebula. Credit: Bruce Balick (University of Washington), Vincent Icke (Leiden University, The Netherlands), Garrelt Mellema (Stockholm University), and NASA.

CE may happen when one of the stars fills the system Roche-lobe during its giant phase (RGB or AGB). In this case the Roche-lobe filling star has a deep convective envelope and the mass transfer is dynamically unstable if the mass ratio exceeds a critical value (Hjellming & Webbing 1987). In this case the mass transfer is expected to generate a CE, which consist of the material from the envelope of the donor star. Embedded in this envelope are the core of the mass donor and the companion star which remains almost unaffected. This matter is driven outward by energy supplied by a frictional interaction between two orbiting stellar cores and the CE. The orbit of the binary system may decrease by an important factor due to the frictional interaction of the stars with the envelope (Livio & Sokker 1988). This spiral-in process releases orbital energy and a large fraction of it is deposited in the envelope. Therefore, the common envelope will be ejected and appear as a PN when the total deposited energy is larger than the envelope binding energy. A bipolar shaped nebulae may be formed due to the interaction of the PNe with the close companion. Photometric monitoring of these PNNs may also reveal modulation frequencies related to interaction of the PNN with its close companion. FIgure 3 presents an Hubble Space Telescope image of M2-9, which is an example of a "butterfly" or a bipolar planetary nebula.

Evolutionary channels for helium cataclysmic variables predict that these systems may have experienced several episodes of planetary nebulae ejections during their evolution. Two of them may happen as a result of the ejection of the two CE stages the systems

experience before the AM CVn stage (Iben & Tutukov 1991). The spiral in process of the stars during the CE episodes has to be effective in order to reduce dramatically the orbital period of these systems. Therefore, the deposition of orbital energy in the envelope must be high and the CE may be completely dissipated and appears as a planetary nebula for certain period of time. The first CE happens when the secondary star reaches the RGB stage. In this case the planetary nebula formed is hydrogen rich. The second CE happens when the primary reaches the AGB stage and the planetary nebula formed when the CE dissipates would be helium rich.

In addition to these 2 planetary nebulae episodes due to dissipation of CEs, others may happen when the system is close to the AM CVn evolutionary stage. The accretion of helium may ignite helium burning on the surface of the primary. The existence of the AM CVn family indicates that some systems survive this ignition without being disrupted. Several of these episodes may happen and each time a planetary nebula deficient in hydrogen may temporally appear.

It should also be mentioned that Soker (1998) presents criteria for binary progenitor models for bipolar planetaries, and he has classified 458 PNs with respect to such criteria (Soker 1997), and finds that 56% of the PNs can be classified as the result of having a common envelope with a substellar compainion, like a planet or a brown dwarf.

The search for photometric features which may indicate the presence of a hidden close companion in the PNNs with bipolar planetary nebulae envelope, is one of the main research lines described in this thesis. Chapters 2 and 3 are dedicated to this photometric search.

1.7. Pulsating stars.

The vast majority of what we can learn about stars is derived from observations of the thin outermost skins of their surface layers. For the most part, we are left to infer the properties of the interiors based upon our current best understanding of the constitutive physics. Pulsating stars represent the best opportunity for probing stellar interiors. Some stars, including the Sun, show very regular variations in brightness, and the pattern of this variation suggests that these stars are pulsating. By studying the patterns of light variation, we can learn about their interior structure in much the same way as seismologist can learn about the inside of the Earth by studying earthquakes. For this reason, the study of pulsating stars is called asteroseismology, and helioseismology in the case of the Sun.

Observations of light and velocity variations across the visible surface of the Sun, have lead to the identification of thousands of pulsation modes and precise constrains of the standard solar model (e.g. see Christensen-Dalsgaard 2002).

The observations of pulsation modes in stars are more difficult compared with the Sun. If we were to move the Sun to the distance of even the nearest star, most of the pulsations modes that we now know to be present would be undetectable since we would lose nearly all of the spatial resolution across the disc of the star, and only modes of the lowest spherical degree ($l \lesssim 3$) would produce significant variations in the total integrated light. The number of detectable modes would be reduced from thousands to merely dozens, leading to a corresponding reduction in the ability to constrain the internal structure from observations (e.g. see Kjeldsen et al. 1999). Even so, such data will still allow us to determine the global properties of the star and to probe the gross internal composition and structure, providing valuable independent tests of stellar evolution theory.

In general the variable stars in the pre-white dwarf evolution stage and in the white dwarf cooling sequence are non-radial gravity mode pulsators. If a high quality light curve, preferably covering a week or more, from multiple sites and without interruption, can be obtained for a pulsating PNN, variable PG 1159 type star, DBV or DAV white dwarf, a wealth of information may be derived: (1) The period spacing of the individual pulsation modes for normal modes with successive values of k at a given l is (nearly) constant, and its value is a simple function of the stellar mass. Hence the mass can be determined to very high accuracy. (2) Departures from strictly constant period spacing depend on the interior composition stratification. (3) Secular changes in the pulsation periods give the stellar evolutionary time scale. (4) Splitting in the power spectra gives the stellar rotation rate.

1.8. The instability strips.

Both the pulsating PNNs and the PG 1159 instability strips, are not "pure" instability strips. An instability strip is the region in the HR diagram (or equivalently in the log g-log T_{eff} diagram) where a family of pulsators is found. No "pure" instability strip indicates that both non-variables and variables stars are present in the same temperature and luminosity range. Theoretical models can not explain why some stars with certain effective temperature and surface gravity pulsate while others with the same effective temperature and surface gravity do not. In the case of PG 1159 the only known distinction comes from

spectroscopy: pulsating PG 1159 stars show nitrogen in their spectra while non-pulsating PG 1159 do not (Dreizler 1998; Dreizler & Heber 1998). Iben and Tutukov (1985) calculated evolutionary models for close binary systems and indicated that one possibility to recognize if a white dwarfs is coming from single or binary evolution is to investigate the amount of nitrogen present in the spectra. They obtained that hydrogen deficient white dwarfs which show high abundance of nitrogen are related to close binary evolution. This indicates that some of the pulsating PG 1159 stars may be possible remnant of binary evolution. Other white dwarfs instability strips are formed by the pulsating helium atmospheres white dwarfs (DBVs) and the pulsating hydrogen atmospheres white dwarfs (DAVs). Eight DBVs are currently known and inside a none "pure" instability strip. 31 DAVs are currently known. In contrast to pulsating PNNs, the PG 1159 and DBV instability strips, the DAVs form a "pure" instability strip, i.e., no stable stars are found within the domain of the HR diagram where the DAVs are located. Bradley (2000) summarizes the properties of the pulsating PNNs, variable PG 1159 type stars, DBVs and DAVs.

The main goal in this thesis is to look for observational clues to support the generation of white dwarfs deficient in hydrogen due to close binary evolution. By photometric analysis of PNNs with bipolar envelope we may discover some modulations frequencies which are signatures of interaction with a close companion. Others modulation frequencies may be due to pulsations in the PNNs. Asteroseismological analysis of these pulsations may reveal layered interior structures, which may be a result of the binary evolution. One parameter that can be determined from asteroseismology is the thickness of the outer helium layer.

This attempt to link photometric features of pulsating (pre)-white dwarfs and pulsations frequencies due to interaction with a close companion is a new field of study which has revealed the first results. Up to date four pulsating white dwarfs in cataclysmic variables have been discovered. Three of them are discovered in the Sloan Digital Sky Survey (SDSS). The CV pulsators are dwarf novae with white dwarf primaries that show large amplitude non-radial oscillations of the kind seen in ZZ Cet stars (DAVs). The objects discovered are GW Lib (Warner & van Zyl 1998, Woudt & Warner 2002), SDSS J161033.64-010223.3 (Woudt & Warner 2003), SDSS J013132.39-090122.3 and SDSS J220553.98+115553.7 (Woudt & Warner 2004). Warner and Woudt have started a systematic search so this number may increase soon. It is estimated that the final total number of CVs in the SDSS will be ∼400 (Szkody et al. 2002). Some of them may be pulsating. However, among all the 318 CVs known before the SDSS (Ritter & Kolb 1998) only GW Lib is pulsating.

The accretors have temperature as ZZ Ceti stars. The best candidates for this search are CVs of low rate of accretion ($\dot{M}$). The effective temperatures (T_{eff}) of the white dwarfs are determined by $\dot{M}$, largely through compressional heating in the interior (Sion 2003). A $\dot{M}$ that keeps T_{eff} in the instability strip for the DAVs is sufficient to produce Balmer emission lines, typical of CV disc emissions, which may be observable if the flux from discs is not too high.

The helium-atmosphere DB white dwarf stars are very interesting from the standpoint of stellar structure and evolution. The chemical evolution of their atmospheres cannot be satisfactorily explained to date (see Shipman 1997 for a review). In particular, the presence of the so-called DB gap, which is the absence of DB white dwarfs between temperatures of ∼30 000 - 45 000 K (Liebert 1986), is poorly understood. It is also not clear whether DBs are mostly produced by single-star evolution or whether a significant fraction of them originates from binary progenitors. The examination of these problems can be aided by asteroseismology. Compared with other classes of pulsating stars, the DBVs are promising candidates for asteroseismology: their mode spectra are shown or believed to be rich, and a pulsation theory for these stars is quite advanced and well tested.

The interior structure of the white dwarfs contains a record of the physical processes that operate during the later stages in the lives of most stars. The distribution of C/O from the core to the surface in the star contains information about the physical processes that took place at different internal radii of the star, and is a record of the evolutionary stages it has gone through during its previous evolution. Chapter 5 will present a method which analyses the possible evolutionary history of the DB white dwarfs GD 358 using asteroseismology. This is done by computing different C/O distribution profiles, some of them related to evolutionary models of close binary stars, and comparing those with the observed pulsation periods. Pulsating DBs stars with thick external helium layer are good candidates to be descendants of the AM CVns.

1.9. Chapters Overview.

1.9.1. Chapter 2.

Chapters 2 and 3 are related to the photometric analysis of a group of selected PNNs with characteristics that may indicate the presence of a close companion and an evolutionary stage affected by episodes of interaction between them. Chapter 2 presents the photometric

results of the survey. Three new pulsators are found and one is confirmed, and rapid changes in the temporal spectra of these PNNs are observed.

1.9.2. Chapter 3.

Chapter 3 presents 71.73 hours of photometric data over 4 years, destined to investigate the photometric behaviour of the PNN NGC 246. We present for the first time evidence of photometric changes on time scales of hours and less and the presence of a stable modulation at a frequency of 230 μHz, which shows an amplitude variable harmonic structure and has a phase which is kept with high precision over years. The stability found for the 230 μHz modulation frequency indicates that it may be related to an orbital period of 72 minutes. In this case, this PNN would have an orbital period where several CVs are predicted but not found. In addition we have observed pulsations related to g-modes presenting short lifetimes. We use wavelet analysis to study these rapid variations.

1.9.3. Chapter 4.

Chapter 4 presents a photometric analysis in light curves of the AM CVn objects in permanent high state: AM CVn and HP Lib. We report night to night changes in the amplitudes of the fundamental frequency and its harmonics, and use different methods to analyse the information that can be extracted from these changes. Methods such as wavelets and intrinsic noise are tested and discussed and a model for the disk structure to explain these features is suggested. We compare the light curves and temporal spectra properties found for these objects with previous results obtained for NGC 246.

1.9.4. Chapter 5.

The last chapter presents a method which analyse the possible evolutionary history of the DB white dwarf GD 358 using asteroseismology. This is done by computing different C/O profiles obtained from different evolutionary channels, and the use of a genetic algorithm to optimize the search in the parameters space. The first results indicates that binary evolution describes better the pulsation periods for GD 358.

References

Bradley, P. A. 2000, in Proc. of The Fifth WET Workshop, ed. E. G. Meistas, & G. Vauclair (Baltic Astronomy), 9, 485

Christensen-Dalsgaard, J., 2002, Rev. Mod. Phys., 74, 1073

Dreizler, S. 1998, in Proc. of the Fourth WET Workshop, ed. E. G. Meistas, & P. Moskalik (Baltic Astronomy), 7, 71

Dreizler, S., & Heber, U. 1998, A&A, 334, 618

Faulkner, J., Flannery, B. P., & Warner, B. 1972, ApJ, 175, L79

Hjellming, M. S., & Webbnik, R. F. 1987, ApJ, 318, 794

Iben, I. Jr., & Tutukov, A. V. 1985, ApJS, 58, 661

Iben, I., Jr., & Tutukov, A. 1991, ApJ, 370, 615

Kjeldsen, H., Bedding, T. R., Frandsen, S., & Dall, T. H. 1999, MNRAS, 303, 579

Livio, M., & Soker, N. 1988, ApJ, 329, 764

Liebert J., 1986, Proc. IAU Coll. 87. D. Reidel Publishing Co., Dordrecht, p. 367

Nather, R. E. 1985, in Interacting Binaries, Eggleton P. P., Pringle J. (eds.) NATO ANSI, series C, Vol. 150, Reidel, p. 349

Nelemans, G., Portegies Zwart, S. F., Verbunt, F., & Yungelson, L. R. 2001, A&A, 368, 939

Savonije, G. J., de Kool, M., van den Heuvel, E. P. J. 1986, A&A, 155, 51

Shipman H., 1997, in Isern J. et al., eds, White dwarfs: Proc. 10th European Workshop on White Dwarfs. Kluwer, Dordrecht, p.165

Simpson, J. C., & Wood, M. A. 1998, ApJ, 506, 360

Sion, E. M. 2003, in the proc. 13th European Workshop on White Dwarfs, eds, de Martino, D., Silvotti, R., Solheim, J.-E., Kalytis, R., Kluwer Academic Publishers, NATO Science Series II, Mathematics, Physics and Chemistry, 105, 303

Soker, N. 1997, ApJS, 112, 487

Soker, N. 1998, ApJ, 496, 883

Solheim, J.-E. 1996, in Hidrogen-Deficient Stars, Jeffrey S., Heber U. (eds.), ASP Conference Series, Vol. 96, p. 309

Solheim, J.-E. 2003, in in "White Dwarfs" ed D. Martino, et al., Nato Science series vol 105, Kluwer, p. 299

Solheim, J. E., & Massacand, C. M. 1994, in White Dwarfs, Koester D., Werner K. (eds), Springer, Lecture Notes in Physics, 443, 270

Szkody, P., et al. 2003, AJ, 126, 1499

Ritter, H., & Kolb, U. 1998, A&AS, 129, 83

Warner, B. 1995, Ap&SS, 225, 249

Warner, B., & van Zyl, L. 1998, IAU Symp. No. 185, 321

Woudt, P. A., & Warner, B. 2003, Ap&SS, 282, 433

Woudt, P. A., & Warner, B. 2003, in press

Warner, B., & Woudt, P. A. 2004, in Variable Stars in the Local Group, ASP Conf. Ser., Kurtz, D.W., & Pollanrd, K., eds., Vol. 2nn

Chapter 2

Photometric changes in the temporal spectra of planetary nebula nuclei (PNNs) with bipolar envelope

Abstract.

We present results of a survey for photometric variability in a sample of hot, hydrogen deficient planetary-nebula nuclei (PNNs) with 'PG 1159' or 'O VI' spectral type and presenting a bipolar or elliptical planetary nebula envelope (PNe). These characteristics may indicate the presence of a hidden close companion and an evolutionary stage affected by episodes of interaction between them. We report for the first time the detection of low-amplitude pulsations in the PNNs VV 47, NGC 6852 and Jn 1 from time-series photometry made at the Nordic Optical Telescope (NOT) from a sample of 11 candidates. In addition, we have followed the photometric variability of the PNN NGC 246. Time-series analyses show that the power spectra of VV 47, NGC 6852 and NGC 246 are highly variable on time scales of hours. Power spectra from consecutive nights of VV 47 and NGC 6852 show power in different frequency regions. The same type of variability is present in NGC 246 in 2 observing runs separated by 3 days. In addition, changes are found in the power spectra of VV 47 and NGC 246 during the same night. VV 47 temporal spectra are peculiar since they present modulation frequencies in a wide range covering from 200 μHz to 8500 μHz. This behaviour is in contrast with the previous known pulsating PNNs where no modulations frequencies are found above $\sim$3000 μHz. VV 47 temporal spectra present power related with periods shorter than 200 s, which may indicate for the first time the observation of g-modes triggered by the ϵ-mechanism. The rapid changes in the temporal spectra of these PNNs may be explained by a more complicated unresolved combination of modulation frequencies, but is more likely due to a combination of unstable pulsations of the PNNs plus modulations related to interaction with a close companion.

'From Close Binary White Dwarfs to White Dwarfs': J. M. González Pérez, e-mail: `jose@phys.uit.no`

2.1. The pulsating planetary-nebula nuclei.

The pulsating planetary-nebula nuclei (PNNVs) constitute a class of non-radial pulsating degenerates stars. Nine PNNs are known to be non-radial pulsators (Grauer & Bond 1984; Bond & Meakes 1990; Ciardullo & Bond 1996). Their photometric variations are due to the presence of many individual modulation frequencies with typical periods around 30 min and amplitudes $\lesssim$0.1 mag. The length and multiplicity of the periods indicate an origin in non-radial g-mode pulsations. The lowest modulation frequency registered for a PNN has been 191 μHz which corresponds to a period of 87.23 min, and was observed in NGC 1501 (Bond et al. 1996); while the highest modulation frequency observed has been $\sim$ 2175 μHz (period 7.66 min) in RX J2117+3412 (Vauclair et al. 2002). Peaks in RX J2117+3412 temporal spectra are found up to $\sim$4339 μHz but all peaks over $\sim$2175 μHz are found to be quadratic or cubic linear combinations of peaks at lower frequencies. Ciardullo & Bond (1996) (hereafter CB96) have completed the most extensive search up to date for pulsational variability among hydrogen-deficients PNNs with 'O VI' and 'PG 1159' spectral type. They identified 6 low-amplitude pulsators including NGC 246 which is included in our sample. They found that the PNNs pulsational properties are similar to the pulsating GW Virginis (PG 1159-035) stars but tend to have longer pulsational periods (11.5 to 31 min), and that most of them have power spectra that vary on time scales of months or less. Furthermore, extensive observations such as the detailed photometric study of NGC 1501 (Bond et al. 1996) show that a given pulsation apparently changes significantly and irregularly its amplitude from night to night. Such instabilities could result from intrinsic variations in the star, but it could also result from a beat between modes that are closely spaced in frequency. This seems to be a property of the entire class. Most, if not all, of the pulsating PNNs show complex and variable behaviour. This characteristic is different from which is found for GW Vir white dwarf pulsators, whose power spectra are more stable (Koupelis & Winget 1987; Winget et al. 1991; Kawaler et al. 1995) and in general vary only on time scales of years. So far no correlation has been found between PNN pulsators and no-pulsators and their spectral type. Pulsators have been found among all types of O VI central stars, from the WC 4 spectral type through the O(C)/PG 1159 spectral type.

To explain the PNNs pulsations, Starrfield et al. (1984, 1985) proposed a mechanism involving cyclical ionization and recombination of C and/or O in the outer layers of hot, hydrogen-deficient white dwarfs. This mechanism implies the existence of a C-O pulsa-

tional instability strip where the non-radial g-modes are triggered by the κ and γ mechanisms induced by this cyclical ionization-recombination process. This idea has been confirmed by the subsequent analysis of Stanghellini et al. (1991). More recently, instability studies using models computed with the He/C/O OPAL opacities (Iglesias & Rogers 1993) show a better agreement with the observed blue edge of the instability strip and put some constraints on the composition of the driving region (Bradley & Dziembowski 1996; Saio 1996; Gaitschy 1997). However, it is not clear why the excited modes in PNNs change on time scales of months or less. Although these PNNs are in a phase of rapid evolutionary contraction, this time scale is much too long to account for the observed power spectrum variations. One proposed explanation relates these changes with episodes of enhanced mass loss from the PNNs. Such changes in the stellar surface may alter the mode amplitude since the driving zone for pulsations becomes closer to the surface. The excitation mechanism (κ mechanism due to carbon and oxygen partial ionization) operates at the depth of $T \sim 10^6$ K, which lies in the outer $\sim 10^{-8}$ $M_\star$ mass fraction of the star (Bradley & Dziembowski 1996). A high mass loss rate from the surface of the star implies that the material in the driving region is renewed on a time scale considerably shorter than the evolutionary time scale ($\sim$50 days). Therefore, the chemical composition of the driving region could change on this time scale if there is compositional stratification of the outer layers. This change in the driving region may affect the efficiency of the excitation mechanism, especially if the mass loss is time dependent. This mechanism could explain irregular change in amplitudes on time scale of weeks. Shorter time scales for amplitude changes, i.e, days, can not be explained attending to this mechanism.

An additional driving mechanism that could drive g-modes during the planetary nebula (PN) and pre-white dwarf evolutionary phases is the ϵ-mechanism (Kawaler et al. 1986). In this case the g-modes are triggered because of a remnant He-burning shell. As the burning necessarily occurs at the bottom of the He-rich outer layers, the periods of these unstable g-modes are in the range of 70 s-200 s, corresponding to low k orders for $l = 1$ modes. Saio (1996) and Gautschy (1997) also find g-modes triggered by the ϵ-mechanism in some of their models with typical periods between $\sim$110 s and $\sim$150 s. He-burning in the outer layers of a star is predicted to happen during the post-AGB stage (Asymptotic Giant Brach) in the evolution of single stars, but may also be the consequence of accretion of helium from a helium rich atmosphere of a close companion, like in the helium CVs (He CVs) (Iben & Tutukov 1991). In several of these cases the accretion produces an explosive

ignition of the helium, but some remnant He may burn in a more static way. Short period g-modes excited by the ϵ-mechanism have not yet been observed.

The same theory that explain the non-radial modes also predict instability strips for high-overtone radial modes. As in the case of the cooler DB and DA pulsators, it is expected that the blue edge for radially pulsating PNNs will lie at a somewhat higher effective temperatures than the blue edge for the non-radial modes. The radial modes in pulsating PNNs with O VI or PG 1159 spectral types have periods of the order 2 to 10 s. The search for such short periods have been done for very few objects (e.g. the PNN K 1-16 and PG 1159-035 from HST data) and no radial pulsations have been found.

Several amplitude changes of peaks in PNNs have been reported. Most of these are from short runs and a possible explanation is that these variations are due to beats between close frequencies in a not completely resolved temporal spectrum. However, amplitude variations have also been observed in completely resolved temporal spectra from long campaigns so they must be real. One good example is reported by Vauclair et al (2002): the RXJ 2117+3412 temporal spectra from 1994 WET data (Whole Earth Telescope, Nather et al. 1990) showed a peak at 717.7 μHz which changed in amplitude on a time scale shorter than the WET campaign (15 days). The amplitude found for this peak during the second half of the campaign exceeded by 44% its value during the first half. The authors proposed as possible explanation the mass loss effects on the driving region. These changes in the temporal spectra on time scale of months or less are not a characteristic exclusively for PNNs. Some pulsating DB white dwarfs (DBVs) seem also to have rapid variations. Handler et al (2002) acquired 62 h of time-resolved CCD photometry of the pulsating DBV PG 1456+103 and concluded that its pulsational spectrum is variable on time-scales of approximately 1 week.

2.1.1. Asteroseismology on PNNs.

Despite the important information that asteroseismological studies may provide on the PNN family members, such investigations have been completed only for few of them (NGC 1501: Bond, Kawaler et al. 1996; and RXJ 2117: Vauclair, Moskalik and the WET collaboration 2002). One reason is the mentioned variability of the PNNs pulsational spectra which makes the mode identification difficult. Despite this variability, for a particular pulsating PNN the same period spacing is observed in different seasons even if the temporal spectra present different pulsation frequencies. Another reason which complicates aster-

oseismological studies on PNNs is that these objects are more difficult to observe than the pulsating PG 1159 stars. One problem is that, by definition, PNNs are surrounded by nebulosity. Therefore, the use of photoelectric aperture photometry is only possible for a few of them: those where the nebula is very faint. CCD cameras are required for the rest. Therefore, multisite campaigns for astereoseismology, such as those organized by the Whole Earth Telescope, are not appropriate since many of the observers still use photoelectric aperture photometry.

From the evolutionary point of view, and because of the pulsational and spectroscopic similarities between the PNNs and the PG 1159 stars, it is presumed that there is a direct evolutionary link, in the sense that PNNs are the precursors of the PG 1159 stars. Two observational properties suggest this link: GW Vir stars have shorter pulsation periods than the pulsating PNNs and the lack of surrounding planetary nebulae. A comparison of the temporal spectra of pulsating PNNs and GW Vir white dwarfs from CB96 (their figure 14) is presented in Fig 4. However, this connection presents important problems, like the lack of correlation inside the PNN family between pulsational properties and spectral type. It has been proposed that the different spectral types of PNNs form a spectroscopic sequence (e.g., Werner 1992, and references therein), which corresponds to an evolutionary sequence. Based on this scenario, one would expect that objects with spectral types less evolved would have longer pulsational periods than the PNN with spectral type closer to PG 1159. However, this evolutionary progression is not observed. Some later type PNNs have generally shorter periods than others with presumably less-evolved spectral type. In addition, one might expect that RX J2117+3412 is a transition object between PNNs and PG 1159 stars, since this object lies within a very large, low surface brightness planetary nebula (Appleton et al. 1993). This object do have high-frequency pulsations similar to those of the GW Vir pulsators, but has in addition several low frequency pulsations which have the lowest values typical of other PNNs (see Fig 4).

In the following we will present a CCD survey for photometry variability in a sample of 11 PNNs selected as hot, hydrogen-deficient PNNs with 'O VI' or 'PG 1159' spectral type with a bipolar or elliptical planetary nebula envelope (PNe). These characteristics may indicate the presence of a close companion and previous evolutionary phases with episodes of interaction between them. The spectroscopic class of PG 1159 stars consists of very hot hydrogen-deficient stars just entering the white dwarf cooling sequence. Their virtually hydrogen-free atmospheres cannot be explained by standard stellar evolutionary theory.

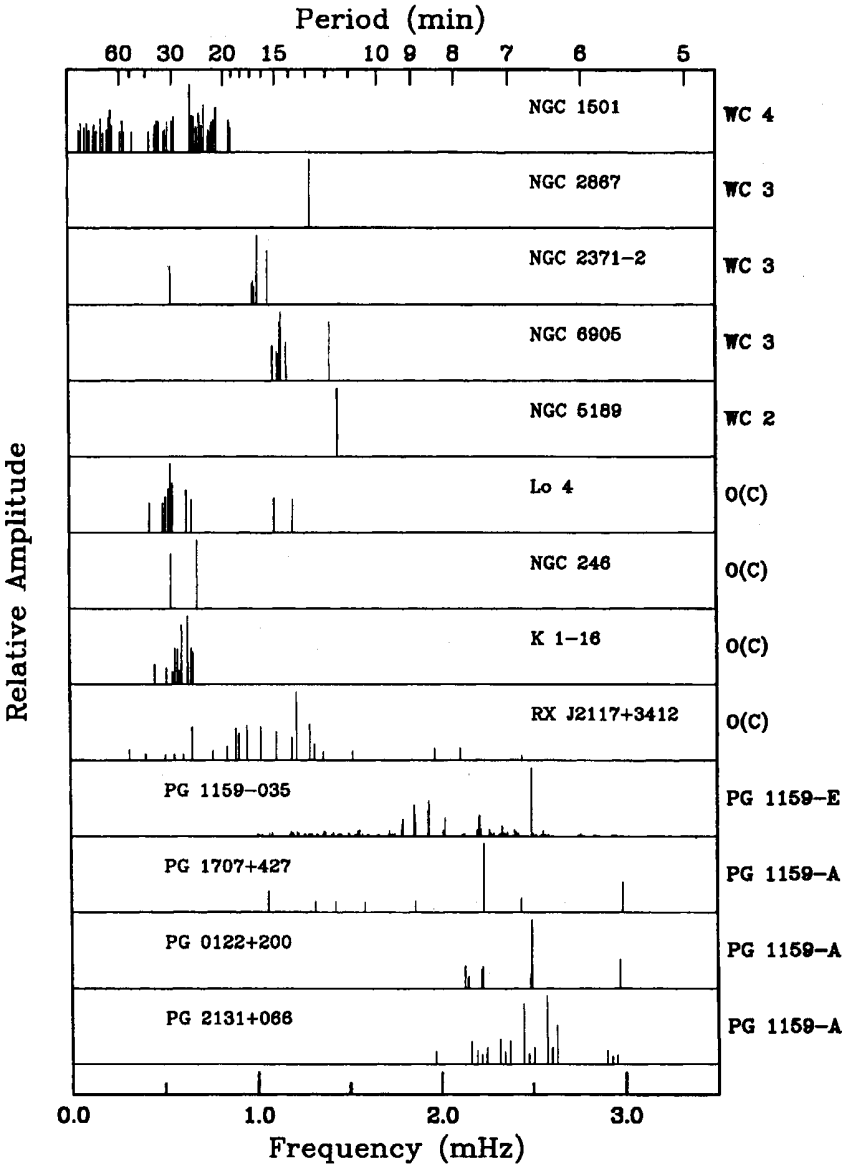

Fig. 4. Comparison of amplitude spectra for the nine known pulsating PNNs before our survey, and four GW Vir pulsating white dwarfs. Spectral classes are given on the right hand and will be explained in section 2.2. Although the ordering is presumed to be an evolutionary sequence, there is no clear correlation between the PNNs evolutionary stage and pulsational properties. However all GW Vir pulsators do have shorter periods (figure extracted from GB96).

In addition, the bipolar morphology of the nebulae may give strong indications of the presence of a binary system. Napiwotzki et al. (1996) found that the frequency of bipolar PNe in their sample of PG 1159 central stars is higher (75%) than is found in other samples of PNe ($\leq$25%). This implies that binarity is important for the production of a PG 1159

star. In Sec. 2.2 we describe the targets and briefly discuss their spectral type and shapes of the nebulas. In Sec. 2.3 we describe the observations and the reduction procedures. In Sec. 2.4 we present the results including the identification of 3 new pulsators: VV 47, NGC 6852 and Jn 1, and the rapid photometric variability observed for these objects and for NGC 246. We discuss and summarizes our results in Sec. 2.5.

2.2. Target selection.

Two main parameters were taken into account for the selection of our PNN sample: the existence of a 'PG 1159' or 'O VI' spectral type embedded in a preferably bipolar, or also elliptical, shaped nebula with relatively low surface emission. Table 2 presents the main properties of the PNNs selected in our sample including Galactic-coordinate designations, the PNNs apparent magnitudes, shape of the nebulae and their spectral types.

2.2.1. Spectral types.

The spectral type selected are hot hydrogen deficient PNNs. The spectral type 'PG 1159' for PNNs were designed by Schönberner & Napiwotzki (1990). They showed that several PNNs are spectroscopically indistinguishable from the PG 1159-035 white dwarfs, presenting broad He II and C IV absorption lines near 4686 Å. This spectral type do not show the strong O VI emission which is the main characteristic of other hot hydrogen-deficient PNNs which are assigned to the 'O VI' spectral type (Smith & Aller 1969, Heap 1982, Kaler & Shaw 1984). The 'O VI' class is defined by the presence of emission at O VI 3811-3834 Å. Heap (1982) proposed a more detailed classification scheme for the O VI type with a 'WC', 'C', or 'C-N' classification and a numerical subclass, with 'C' and 'N' denoting spectra that combine absorption lines with Wolf-Rayet WC or WN like emission features. A presumably evolutionary sequence as well as spectroscopic has been suggested (Méndez et al. 1986). This sequence proceeds from WC-type spectra with strong emission lines, through transitions objects like Abell 30 and Abell 78 which show absorption lines as well as strong emission lines, and then to 'O-type' objects with predominantly absorption lines plus weak emission spectra. In this scheme O(He) are objects which show only He II absorption and O(C) those which also show C IV absorption. This evolutionary sequence is completed with the PG 1159 spectral type. However, as was mentioned in the previous section, Ciardullo & Bond (1996) showed that the pulsational behaviour of the PNNs is not consistent with this evolutionary sequence.

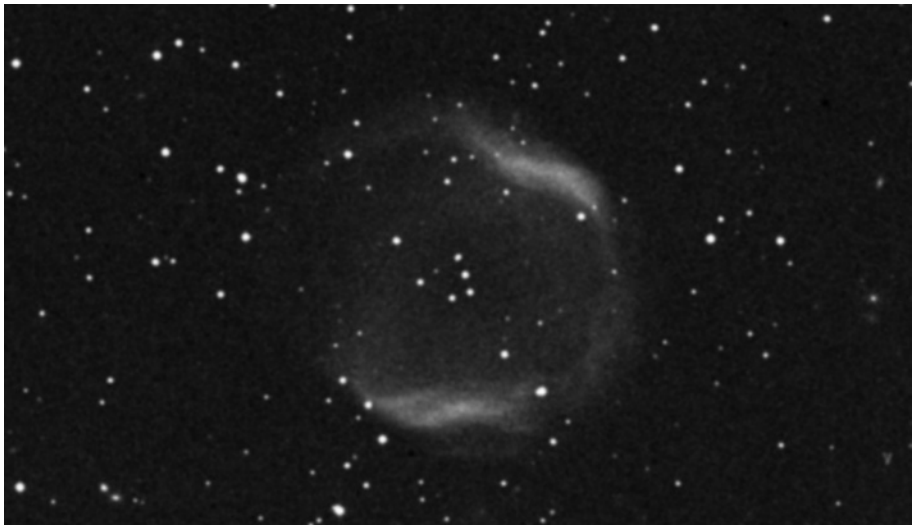

Fig. 5. Example of PNN with bipolar shape of the planetary nebulae. This case correspond to the PNN Jn 1. Picture obtained from STScI Digitized Sky Survey.

Werner (1992) subdivided the PNNs PG 1159 spectral type into three subgroups: 'lgE' (low gravity emission) denotes objects which have relatively sharp absorption components underlying their He II and C IV emission (these objects are the objects called O(C) above). 'E' (emission) denotes objects with higher gravity, with a mix of absorption and emission near 4686 Å. Finally the subgroup 'A' indicates object which have a 4686 Å absorption with no emission. Napiwotzki & Schönberner (1991) and Napitwotzki (1992, 1993) have identified several PNNs that appear to be 'hybrid' PG 1159 objects in the sense that they show Balmer absorption lines in addition to their PG 1159 features. These hybrids are denoted 'O(H,C)' by Napiwotzki (1993). The spectral types given in table 2 are based on the classification scheme proposed by Werner et al. (1991), Werner (1992) and Napitwotzki (1992, 1993).

2.2.2. Shapes of the nebulas.

The second main selection parameter for our sample is the existence of a bipolar or elliptical shape of the planetary nebulae (PNe). An example of a bipolar PNe, corresponding to the PNN Jn 1, is given in Fig 5. This selection parameter increases the possibilities for a selected PNN to be member of a close binary systems, and to be affected by possible episodes of interaction with the close companion during its evolution.

Most of the PNe present complex but highly axisymmetric shapes. Only a small fraction (around 20%) show spherical symmetry. The majority of PNe are either elliptical (around

30%) or bipolar (around 50%), including around 20% of PNe with butterfly shape morphology (see, for example, Zuckerman & Gatley 1988). A variety of scenarios has been proposed to explain the shapes of PNes. The most important of these are the interacting-winds model (Kwok, Purton & Fitzgerald 1978; Okorokov et al. 1985; Volk & Kwok 1985), binary interaction models (see, for example, Fabian & Hansen 1979; Bond & Livio 1990; Han et al. 1995) and magnetic models (Pascoli 1987a,b; Chevalier & Luo 1994). The interacting-wind model can account for the bipolarity of many PNe if there is a large density contrast in the slow wind (emitted during the asymptotic giant phase) between the equatorial plane and the polar directions. However, this model does not specify the origin of the density contrast. Magnetic models can also explain bipolar PNe, but seems to require a very strong dynamo. Binary interactions provide a more plausible mechanism for producing bipolarity. Han et al. (1995) conclude that binary interactions affect the shape of around 40% of all PNe. Since this fraction is comparable to the fraction of non-spherical PNe, binary interaction is likely to be an factor in explaining the asymmetric PNes. The formation of 3 to 15% of the PNes was found by these authors to be affected by mild and strong interaction processes in detached binary systems. Common-envelope (CE) evolution was found to be the most important channel of formation of bipolar PNes, accounting for the formation of 27 to 32% of the PNes and, therefore, the main channel for the production of bipolar nebulae. CE ejection and coalescence during the CE phase are found to be of similar importance: CE ejection is expected to produce up to 17% of the PNes, while the merger scenario can account for more than 10% of the asymmetric PNes. These results are in agreement with previous studies formation of PNe and Type Ia supernovae via various binary channels (e.g. Iben & Tutukov 1984a, b, 1993; Tutukov et al. 1992; Yungelson et al. 1993, 1994).

Table 2 shows the type of nebulae related with the different PNNs in our sample. A bipolar shape of the nebula is designed by 'bs' and elliptical shape by 'es'. Some nebulae are so faint that it is difficult to determine its shape. These are labeled with 'us' (unknown shape).

2.2.3. Previous observations.

Many of the selected PNNs (8 of 11) were also included in the CB96 survey. New observations on these candidates were decided because they present characteristics that fit one or both of our selection criteria and because the telescopes used in CB96 survey were smaller

(0.9 m and 1.5 m), which, in principle, give us better chance to detect smaller amplitude pulsations than in the CB96 data. CB96 used conservative restrictions to claim pulsational variability demanding a high confidence level for a peak to be real: the amplitude of the peak had to exceed 99% of the highest peaks found in the power spectra of randomized data possessing the same noise characteristics and time distribution as the real data. To label a PNN as pulsator they demanded that it either exhibited a higher power-spectrum peak than seen in any of the 500 randomizations, or that it displayed power at the 99% confidence level at the same (or similar) frequency on at least two different nights. The last demand may be too strong for many PNNs which have highly variable power spectra.

The selected PNNs already observed by CB96 are: NGC 246, NGC 650-1, NGC 7094, A 21, A 43, IsWe 1, Jn 1 and VV 47. Among these, the authors found evidence for coherent pulsations only for NGC 246. Their data showed it to be an extremely low amplitude (around 2 mmag) pulsator with periods of 24-31 min. The authors did not find evidence for coherent pulsations in the other PNNs selected. However, they suspected irregular variability for NGC 7094, since it varied quasi-sinusoidally with a time scale of about 2 hours and an amplitude of 0.02 mag during a run of 4.5 hours. For A 43 they also found a peak at 0.4043 mHz (P=41.2 min) with amplitude 3.5 mmag, but did not want to claim pulsational variability until more data was obtained since the peak came from only 2 cycles of the 41min period which occurred at the beginning of the 3.4 hours run, but later disappeared. They found two possible peaks for Jn 1 at 0.5405 and 0.5385 μHz (P=30.83 min and 30.95 min) but did not claim pulsational variability since these peaks were only significant at the 83 and 97% levels of the authors criterium. Finally, they did not find variability in the 4 nights of data for VV 47. This PNN was reported by Liebert et al. (1988) as a possible short period pulsator on the basis of photoelectric aperture photometry.

The others PNNs selected for monitoring in our survey were PG 1520+525, NGC 6765 and NGC 6852.

2.3. Observations and reductions.

The observations were done at the Nordic Optical Telescope (NOT) with the Andalucia Faint Object Spectrograph and Camera (ALFOSC), equipped with a Loral, Lesser thinned, 2048 x 2048 CCD chip, and modified with our own control software to be able to observe

Table 2. PNN spectral classification and nebula shape. Gal C indicates galactic-coordinates. The following coding is used for the nebula shape: bs (bipolar shape); es (elliptical shape); us (unknown shape). The following coding is used for references: N92, N93 (Napiwotzki 1992, 1993); NS95 (Napiwotzki & Schönberner 1995); W91 (Werner et al 1991) and W92 (Werner 1992)

Object	**Gal C**	$\mathbf{m_v}$	**Nebula**	**Spectrum**	**Reference**
PG 1520+525	85.4+52.2	16.6	us	PG 1159	W91
NGC 7094	066.7-09.5	13.68	es	"hybrid"	N92
				O(H,C)	N93
NGC 246	118.8-74.7	11.96	es	PG 1159/lgE	W92
NGC 6765	62.5+9.6	17.8	bs	O(C)	NS95
NGC 650-1	130.9-10.5	15.9	bs	PG 1159/E	N93
NGC 6852	42.59-14.53	18.2	bs	O(C)	NS95
Jn 1	104.2-29.6	16.13	bs	PG 1159/A:	W92
				PG 1159/E	N93
A 43	036.0+17.6	14.75	es	"hybrid"	N92
				O(H,C)	N93
IsWe 1	149.7-03.3	16.56	us	PG 1159/A:	W92
				PG 1159/A	N93
VV 47	164.8-31.1	16.83	bs	PG 1159/E:	W92
A 21	205.1-14.2	15.99	us	PG 1159/A:	W92
				PG 1159/E	N93

in high-speed multi-windowing mode (Østensen & Solheim 2000). The sky area available for locating a reference star is limited to the sky area on the chip: 3.7 x 3.7 arcmin^2.

Table 2 contains information related to the time-series observations. We observed the PNNs in windowed mode using two or more reference stars for constructing the relative light curve. Almost all the observations were made with a standard Bessell B-band filter (NOT #74, Bessell 1990). This filter minimized the contribution from the nebular emission since many of the objects selected in our sample are embedded in low-surface-brightness nebulae. The filter also helps in decreasing the atmospheric extinction colour terms. The cycle time varied from 30 s to 180 s depending on the magnitude of the object. The system in windowed mode needs ∼0.5 s per window to read out the chip. The read out time depends on the number of reference stars selected and the sizes of the readout windows. A typical run included one window for the target star, 2 or 3 for reference stars and 1 or 2 sky windows to compute sky levels. Two sky levels were selected in some observations: one contaminated and one uncontaminated by the nebula. Information about the sampling

Table 3. Time-series photometry. The observers are Robert Kamben (RK) and Jose M. González Pérez (JMGP). N_i denotes the number of independent samples, that is, the number of points in the light curve.

Object	**Date**	**Observers**	**Start (UT)**	**Length (s)**	**Sampling (s)**	N_i	**Resolution (μmp)**
PG 1520+525	2000 Jul 20	JMGP, RK	20:39:59	6150	30	205	163
NGC 7094	2000 Jul 20	JMGP, RK	23:55:25	5220	30	174	192
NGC 246	2000 Jul 21	JMGP, RK	02:55:52	7448	33	255	134
	2000 Jul 24	JMGP, RK	02:39:12	11868	12	489	84
NGC 6765	2000 Jul 21	JMGP, RK	21:24:55	6486	94,5	65	157
NGC 650-1	2000 Jul 22	JMGP, RK	02:28:54	10800	120	90	93
NGC 6852	2000 Jul 22	JMGP, RK	23:50:42	10800	180	60	93
	2000 Jul 23	JMGP, RK	21:13:28	11880	180	66	84
Jn 1	2000 Jul 23	JMGP, RK	03:09:53	5695	85	67	176
A 43	2000 Jul 24	JMGP, RK	01:13:52	4140	90	46	241
IsWe 1	2001 Jan 15	JMGP	20:30:59	13547	50	270	74
VV 47	2001 Jan 16	JMGP	00:36:53	20820	60	347	48
	2001 Jan 16	JMGP	21:04:03	22560	60	376	44
	2001 Jan 17	JMGP	05:04:47	6360	60	106	157
	2001 Jan 17	JMGP	20:17:01	30280	40	757	33
A 21	2001 Jan 17	JMGP	02:37:23	8000	40	200	125

time (integration time plus readout time) used in each observation is also presented in table 3.

The data were reduced on-line using the Real Time Photometry (RTP) computer program (Østensen 2000). This program allows us to detect periodic variable stars with small amplitudes from CCD data in real time. The RTP program automatically converts all data to the correct bias level, performs appropriate flat-fielding and computes the sum of ADU counts for the target and reference stars within a circular aperture. The sky level is computed from the pixels in the sky field using a three sigma median clipping algorithm to reject cosmic rays and bad pixels. This sky value is then subtracted from the counts of each star, and the differential photometry between target and reference stars is computed. RTP presents the raw data, sky subtracted and differential photometry light curves propagating in real time as the windowed frames are acquired from the CCD camera. At any point a Fourier Transform (FT) can be computed from the data acquired so far. Another important important feature of the RTP is the moving aperture photometry

(MAP) algorithm. MAP computes the center of the target and reference stars in each frame and recenters the aperture correspondingly. In this way it is possible to correct for small tracking errors on the order of 0.05 arcseconds. This is especially important when observing PNNs, since it gives us the possibility to fix the level of the nebula contamination in the aperture. An option in RTP allows us to compute sky levels not from the selected sky windows but for a ring around the objects. The number of pixels defining the ring width is a parameter that the user can change. This technique is also quite important for our PNNs observations since the nebula contamination may affect in different ways the different windows and therefore, the selection of a nearby sky region for the target is better than a common sky value. The data reduction procedure is completed with a procedure to correct for extinction, to compensate for long time-scale trends and improve the flat-fielding. Because our comparison stars were usually redder than the hot PNNs, we have, even after this procedure, a few long light curves which display low-amplitude changes over a time scale of several hours. Therefore, we do not consider as real modulation frequencies with periods half of the run length or 1/3 of it, since they most likely are due to changes in the atmospheric transparency which affect differently the PNNs and the reference stars due to their difference in colours.

The CCD multi-windowed photometry method also gives us the opportunity to later reprocess the data, applying different aperture sizes and correction schemes. The optimal combination of parameters including the size of the aperture, type of sky subtraction and width of the ring if annular sky subtraction is chosen, are selected after processing all data sets with apertures of a wide range of diameters and sky annulus of a wide range of sizes, and choosing the one that give the best signal-to-noise ratio in the FT, using the amplitude of the highest peak for signal and the mean of the amplitude spectrum outside the pulsation ranges for the noise. The apertures tested ranged between 10 and 40 pixels in radius, which correspond to between 1.9 and 7.6 arcsecs on the sky. The best results obtained were for relative small apertures ($\sim$10 to 15 pixels) using annular sky fields with relative large width values ($\sim$10 pixels).

In many of our observations, a length of the run of $\sim$1 hour was enough to decrease the noise in the FT to less than 1 mma (milli-modulation amplitude). We could then decide if we wanted to observe the PNN longer or move to a new one. In cases where the suspected real modulation frequencies had a low amplitude, we observed longer to improve the signal to noise ratio and thereby the chances to detect if peaks were real or not. Observations

were repeated for objects suspected to have low amplitude pulsations. This allowed us to confirm if the candidate had real periodic modulations and/or to study the daily changes in the temporal spectra.

The possible real modulation frequencies observed in some of our PNNs sample had quite low amplitudes and were highly variable on time scales of days. These facts add problems to our analysis trying to identify if those peaks in the FT were real or not. The noise in the FT decreases by increasing the length of the observation. For a stable pulsation it is easy to identify a real peak by observing until the FT signal to noise relation satisfies our criterium. This may not be possible if the periodic modulations change in amplitude on time scale of hours: a short run may produce a clear peak that may satisfy our criterium but, as the run continues, this real modulation frequency may reduce dramatically its amplitude. The static FT considers that the pulsations are stable in time. Therefore, the FT over the whole run may show a small peak over the noise which could not satisfy our criterium for a real peak. The on-line analysis done with RTP helps in this direction since we can monitor constantly the FT of the data acquired so far. Therefore, we can follow how high peaks which appeared during the first part of the observation evolve with time. We have analysed candidates for real peaks in runs longer than $\sim$ 4 hours calculating if they satisfy the confidence criterium for the whole run and for sections of it (first and second half). We will consider that the peak is real but unstable if the criterium is satisfied in one section even if it is not in the whole run.

The method used to estimate if a peak in the FT is real follows the procedure described by S.O. Kepler (1993), which is the method normally used for analysis of data obtained in WET campaigns. If the noise is randomly distributed, the probability of having a peak of power $P \leq P_{obs}$ (observed peak) in one trial (one frequency FT) is:

$$Prob(P < P_{obs}) = 1 - e^{\frac{-P_{obs}}{<P>}}, \tag{1}$$

where $< P >$ is the average power for the region of frequencies studied. By denoting A_i the amplitude of the peak i, and N the number of points in the region, $< P >$ can be written:

$$< P >= \sum_{i=1}^{N} \frac{A_i^2}{N}, \tag{2}$$

If FALSE is the false alarm probability (FAP), $[1-Prob(P_{obs})]$, the probability that one peak of noise in N_i independent samples (points in the light curve) is above $P_{obs}/ < P >$ is (Scargle 1982):

$$FALSE = 1 - (1 - e^{\frac{-P_{obs}}{<P>}})^{N_i} \approx N_i e^{\frac{-P_{obs}}{<P>}} \quad (3)$$

or

$$P_{obs} = ln(\frac{N_i}{FALSE}) < P > . \quad (4)$$

Therefore, if we have 10 000 independent samples N_i, and consider only as real peak if it has less than 1 possibility in 100 to be due to noise ($FALSE = 1/100$), then: $P_{obs} = 13.8 < P >$, that is, the peak must be 13.8 times greater than the average power to have one chance in 100 of it being due to noise only.

We have selected a more relaxed criterium using $FALSE = 1/20$. With this criterium, if a peak is over the estimated limit of confidence, it has less than 1 possibility in 20 to be due to noise. This is good enough for our search because of different reasons: the pulses which have been observed for PNNs have quite low amplitudes (few mmags) and, in addition, we expect possible variability in the amplitudes on time scale of hours. If this variability happens, the amplitude displayed by Fourier analysis for a certain peak will be averaged over the whole data set. If the amplitude decreases in time scale of hours, the FT will show a less significant peak. Our criteria considers a peak as real if the amplitude is above the amplitude needed for a false alarm probability $FALSE = 1/20$. The equation used is then:

$$P_{obs} = ln(N_i \times 20) < P > . \quad (5)$$

In this case, and considering $N_i = 200$, which is close to the number obtained in many of our runs, we get $P_{obs} = 8.3 < P >$. If the FT displays amplitudes, the peak must be $\sqrt{8.3} = 2.88$ times over the noise to be considered as real. Some previous studies consider a stronger confidence criteria where $FALSE = 10^{-3}$. However, these are mostly related with long sets of data and pulsating stars which present stable temporal spectra. Additional peaks with $FALSE < 1/20$ may be included as significant but only if: i) they have frequencies equal to, or close enough to, the frequency of significant peak observed in other runs, or ii) they have a frequency which is related to the frequency of significant peaks in the way that the ratio between these frequencies is close to 0.87. Ratios between

pulsation frequencies close to this number have been observed in others PNNs, and is predicted in the models to be related to non-radial g-modes. This ratio is described in the next section.

2.3.1. Analysis of FTs.

The candidates selected display features that are a result of modulation of wind by interaction with a close companion (Soker 1997). One of our objectives is to look for signatures in the FT that may reveal the presence of this hidden companion. But we also want to investigate pulsations that may be related to non-radial g-modes. Therefore, one important goal is to identify what is the origin of a specific peak in the FT. This is a difficult task but some photometric properties may help in this identification.

The FTs of some CVs present some properties related to interaction with close companions. An important case is the FT properties of some He CVs. Due to the main characteristics for our selected PNNs sample, some of them may be in an evolutionary stage close to these He CV and may display signatures of interaction with a hidden companion in the same way as these CVs do. The main peaks in the FT of some of these He CVs are harmonics of a main frequency with can be present or not. In the case of AM CVn, this main period does not appear in most temporal spectra, but up to 5 harmonics related to it are found (Solheim et al. 1998). During some runs, the amplitudes of the main peak and harmonics display daily changes. We have analysed, as part of this thesis, photometric data of the He CV HP Lib where we investigate the variability in amplitude for the main frequency and harmonics. The results, and a more detailed introduction to these systems, are presented in chapter 4. These pulsations, and the daily changes in amplitudes associated with them, are believed to happen because of structural changes in the accretion disc. Therefore, the presence of a peak in the FT with period between $\sim$ 15 and $\sim$ 45 min, which are the period displayed by the majority of the members of the He CV family, and a harmonic structure showing daily variations in the amplitudes between main peak and harmonics is a good indicator of the presence of an accretion disc because of interaction with the close companion.

Other photometric features help to identify pulsations related to PNNs non-radial g-modes. The most important are the search for constant period spacings and frequencies ratios close to $\mathcal{R}$=0.87.

Period Spacing: In the limit of high overtones, that is, when the number of radial nodes is much greater than l, g-modes are approximately equally spaced in period for a given value of l and consecutive values of k, i.e.,

$$\Pi_{nl} = \frac{\Pi_0}{\sqrt{l(l+1)}}(k+\epsilon), \tag{6}$$

where ϵ is a small number. The period spacing (Π_0) is determined largely by the mass of the star, and is only weakly dependent on the stellar luminosity and surface compositional stratification. Kawaler & Bradley (1994), and references therein, discuss how the value of this period spacing can be used to constrain the mass of GW Vir stars[1], and how departures from uniform spacing allow determination of the subsurface structure. Since the pattern of equally spaced (in period) multiplets has been seen in several of the GW Vir stars with period spacing of ∼20-23 s, we may expect a similar spacing in some of our candidates if the resolution of the run is good enough. This is not the case in the majority of our runs, but we can search in addition for multiples of the period spacing.

Frequency ratio $\sim \mathcal{R}$=0.87: The period spacing observed in GW Vir itself is not precisely equally spaced (Winget et al. 1991, Kawaler & Bradley 1994). These authors noted that this could result from mode trapping: a subsurface composition transition region can cause a density discontinuity which acts as a reflecting boundary between the surface and the deep stellar interior. Kawaler & Bradley (1994) identify this layer as the transition zone between the helium-rich surface layer and the carbon/oxygen core. The authors present in their equation 4 the period of trapped modes:

$$\Pi_i^2 = 4\pi\lambda_i^2 \ [(1 \ - \ \frac{r_c}{R}) \ l \ (l+1) \ \frac{GM}{R^3}]^{-1}, \tag{7}$$

where λ_i are called trapping coefficients, and are constants related to zeros in Bessel functions, and r_c/R are fractional radius of the composition transition region. Therefore, the trapping coefficients are related to the frequency ratio of trapped modes:

$$\frac{\Pi_i}{\Pi_{i+1}} = \frac{\nu_{i+1}}{\nu_i} = \frac{\lambda_i}{\lambda_{i+1}} \tag{8}$$

Kawaler & Bradley (1992) present in their table 2 the trapping coefficients λ_i for PG 1159 stars. These are presented in table 4.

[1] GW Vir=PG 1159+035

Table 4. Trapping modes for PG 1159 stars, from table 2 in Kawaler & Bradley (1992).

i	λ_i	λ_i/λ_{i+1}
0	3.33	0.68
1	4.92	0.80
2	6.15	0.82
3	7.45	0.85
4	8.76	0.86
5	10.17	0.88
6	11.46	0.89
7	12.77	0.92
8	13.82	0.91
9		

If trapped modes are identified in a star, then the period (or frequency) ratios between the modes can be compared with these coefficient ratios. Many of these ratios are close to the value $\mathcal{R}$=0.87. In fact, the dominant peaks in the temporal spectrum of the PNN RX J2117.1+3412 show period ratios nearly exactly equal to 0.90 (Vauclair et al. 2002), which is compatible with the coefficients computed. This suggest that the dominant peaks in RX J2117.1+3412 are indeed trapped modes. A similar ratio was found for the dominant peaks in the temporal spectrum of NGC 1501 (Bond et al. 1996) which show period ratio close to 0.87. These observed ratios are much closer to $\mathcal{R}$ than seen in the theoretical models of Kawaler & Bradley (1994). Apparently the PNNs NGC 1501 and RX J2117.1+3412 are better calculators of $\mathcal{R}$ than the theoretical models. Observations done in different seasons on NGC 1501 have showed the presence of some peaks in the temporal spectrum of a campaign but not in other. In many cases, the ratio between a pulsation frequency found in the FT of one season but absent in another, and another frequency of the temporal spectrum of the other season also fits $\mathcal{R}$.

The search for period (Π_i/Π_{i+1}) or frequency ratios (ν_{i+1}/ν_i) close to $\mathcal{R}$ is the best tool we have to identify pulsations related to trapped g-modes in our sample of PNNs.

2.4. Results.

2.4.1. The non detections.

We did not find evidence of pulsations in 7 of the 11 PNNs. No significant peaks were detected over the FT noise level. Table 3 present the results obtained for these objects.

Table 5. Results: non detections. The second column shows the amplitude of the highest peak in the FT in milli-modulation amplitude (mma). The third column presents the average amplitude (square root of average power) in mma and average power in μmp. The fourth column displays amplitude (in mma) and power (in μmp.) necessary for a FALSE alarm 1/ 20.

Object	**Max. amplitude** (mma)	**Average (amplitude, power)**	**FALSE=1/20 (amplitude, power)**
PG 1520+525	$\lesssim$1	0.50, 0.25	1.44, 2.08
NGC 7094	$\lesssim$0.7	0.32, 0.10	0.91, 0.83
NGC 6765	1.5	0.66, 0.44	1.77, 3.13
NGC 650-1	$\lesssim$3	1.32, 1.74	3.61, 13.03
A 43	$\lesssim$3	2.30, 5.29	6, 36
IsWe 1	$\lesssim$1	0.41, 0.17	1.20, 1.44
A 21	0.8	0.36, 0.13	1.04, 1.08

The second column gives the maximum amplitude found (i. e. the square root of the maximum power) in the temporal spectrum for each candidate. The third column gives the average amplitude which is the square root of the average power (see equation 2) and the average power. The fourth column shows the minimum value necessary for a peak to have a FAP=1/20 both in amplitude and power (eq. 5). The values for amplitudes are expressed in milli-modulation amplitude (mma). The power is expressed in μmp ($mma = \sqrt{\mu mp}$). Column 3 express the quality of the analysis, which depend on various parameters such as the magnitude of the object, length of the run, sampling and exposure times used, and conditions during the observation. Limited signal to noise ratios were obtained for fainter objects and those where the nebulae emission were stronger. In these cases the use of smaller apertures in RTP helped to increase this ratio since it minimizes the sky contribution.

In general, we cannot claim that these objects are not pulsators. We can only conclude that they do not show coherent pulsations satisfying our criteria for detection probability during the time the objects were observed. The PNNs may have showed variability during the observations, but with amplitudes below this threshold. In addition, previous observations of some pulsating PNNs have revealed variable power spectra that change on different time scales. In some cases the light curves occasionally exhibit intervals where their variations nearly disappear. Observations done during these intervals may not show any detectable coherent pulsations.

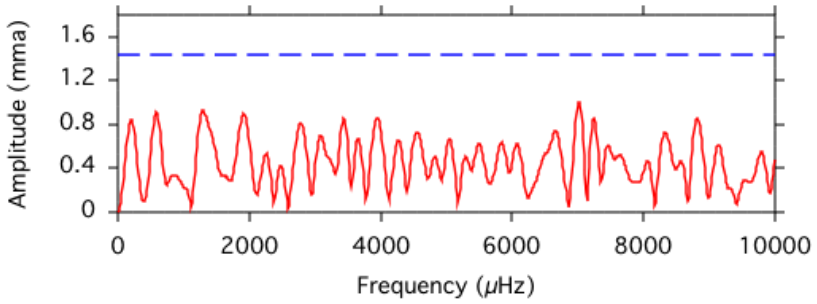

Fig. 6. PG 1520+525 temporal spectrum from NOT data. The dashed line shows the limit in amplitude necessary to reach a false alarm probability $FALSE = 1/20$.

Many of the runs for the nonpulsators were approximately 2 hours long, to search for periods close to 30 minutes as previously observed in many PNNs. However, from such short runs, we cannot detect possible variability happening on time scales over ∼1 hour. The results for the non-pulsators can be described in the following way:

PG 1520+525. No time series photometry has previously been reported for this object. We observed it for ∼2 hours. The average amplitude reached was 0.50 mma and the highest peak has an amplitude below 1 mma. Therefore, for this noise threshold, we found no evidence of pulsational variability. The temporal spectrum is presented is Fig 6.

NGC 7094. This star was included in CB96 survey. The length of our short run was ∼1.5 hours. This was enough to reach an average amplitude of 0.32 mma in the FT. No peaks are found over 0.7 mma (see Fig 7). CB96 reported 2 hours sinusoidally variability. The light curve obtained does not show any trend that might suggest variability on time scale ∼ 2 hours. This differs from CB96 result.

NGC 6765. We attempted for the first time time series photometry on this faint PNN. We did not find evidence of pulsational variability (see Fig 8). However, the average noise amplitude in this case is higher than in the previous cases, 0.95 mma.

NGC 650-1. CB96 observed this faint PNN for 5.06 hours (over two nights) and found no evidence of pulsational variability. Our 3 hours run on this object confirms this null result (see Fig 9). However, the noise in the FT is the highest obtained for our negative cases: the average amplitude is ∼1.32 mma, and smaller amplitude pulsations than 3 mma cannot be excluded.

A 43. We cannot conclude too much about possible pulsational variability in Abell 43 from our observations since we got only ∼1.15 hrs of useful data on this object. This fact,

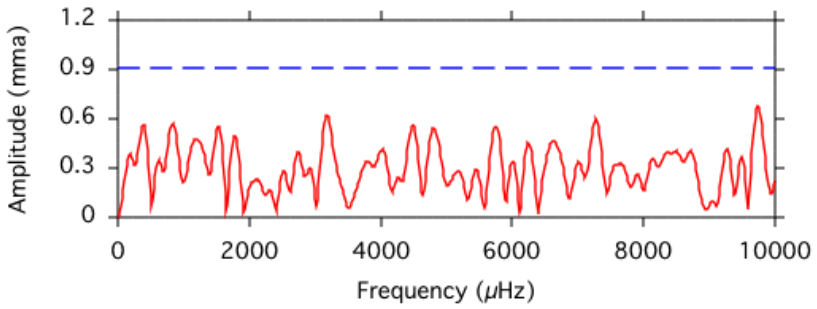

Fig. 7. NGC 7094 temporal spectrum from NOT data. The dashed line shows the limit in amplitude necessary to reach a false alarm probability $FALSE = 1/20$.

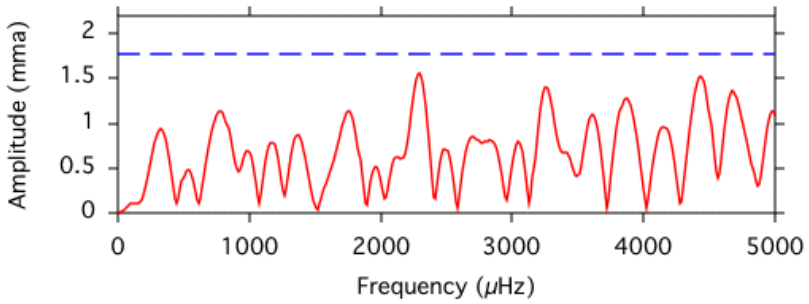

Fig. 8. NGC 6765 temporal spectrum from NOT data. The dashed line shows the limit in amplitude necessary to reach a false alarm probability $FALSE = 1/20$.

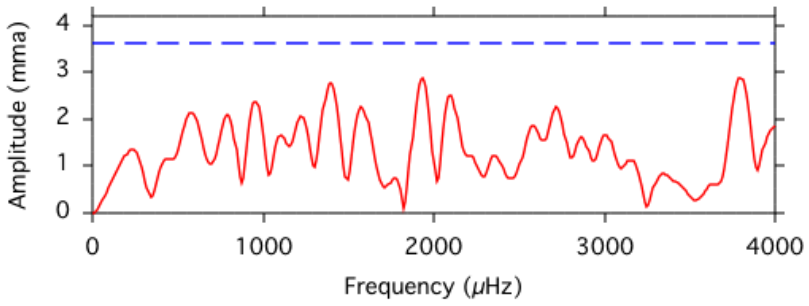

Fig. 9. NGC 650 temporal spectrum from NOT data. The dashed line shows the limit in amplitude necessary to reach a false alarm probability $FALSE = 1/20$.

together with the long sampling rate used, limited very much the analysis of the FT (see Fig 10). The average amplitude is high, 1.5 mma. Further data is necessary to investigate possible modulation frequencies with lower amplitudes.

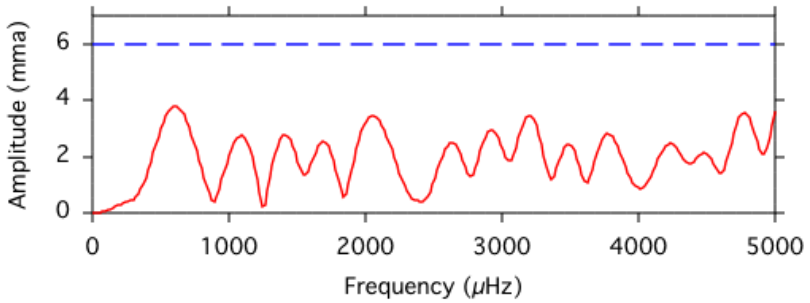

Fig. 10. A 43 temporal spectrum from NOT data. The dashed line shows the limit in amplitude necessary to reach a false alarm probability $FALSE = 1/20$.

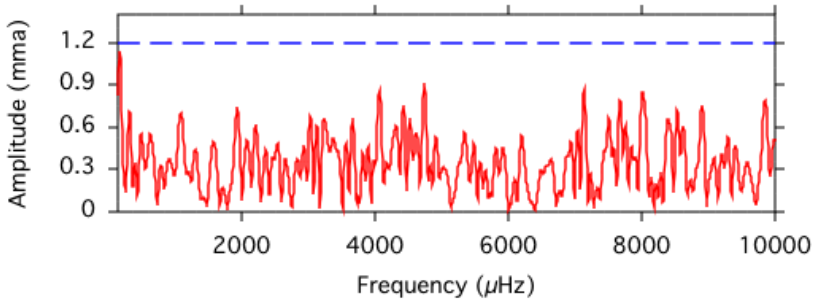

Fig. 11. IsWe 1 temporal spectrum from NOT data. The dashed line shows the limit in amplitude necessary to reach a false alarm probability $FALSE = 1/20$.

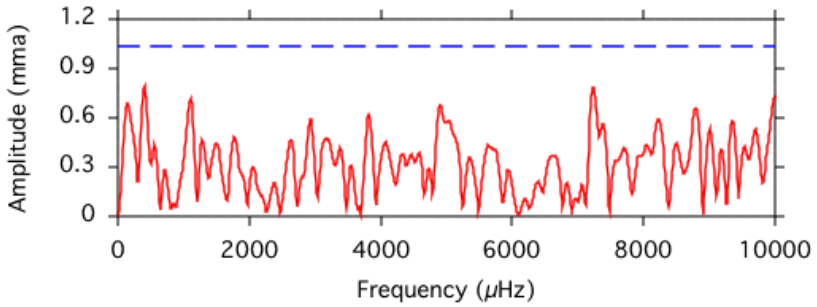

Fig. 12. A 21 temporal spectrum from NOT data. The dashed line shows the limit in amplitude necessary to reach a false alarm probability $FALSE = 1/20$.

IsWe 1. CB96 observed this object 13.33 hours (over three nights) and found no evidence of pulsational variability. Our run confirms this null result with better statistic: the highest peak observed in our FT is ∼1 mma and the average amplitude is 0.41 mma,

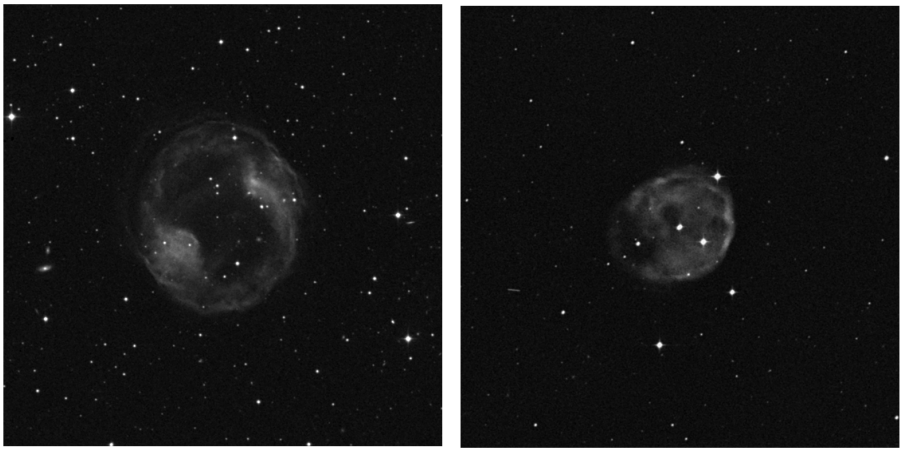

Fig. 13. Shapes of the nebulae of the pulsating PNNs VV 47, which shows a bipolar PNe, and NGC 246, which present an elliptical PNe. Both images are 15x15 arcmin. Pictures obtained from STScI Digitized Sky Survey.

while the amplitude of the higher peak found in the 'noise' in CB96 best run was 3.4 mmag. The temporal spectrum is presented in Fig 11.

A 21. As in the previous case, our results on this object agree on the lack of coherent modulations as found by CB96 but improving the threshold: the highest peak observed is 0.8 mma and the average amplitude 0.36 mma (CB96 best run higher peak was 5.3 mmag). The temporal spectrum is presented in Fig 12.

2.4.2. The pulsators

2.4.2.1. Jn 1

CB96 included Jn 1 in their survey. Their data show possible peaks at 540.5 and 538.5 μHz; however the level of confidence were not high so they did not claim variability. Our analysis suggests variability of this faint PNN with bipolar envelope. However, the results are at the limit of our criterium for variability, and the analysis is done over a short run. The light curve and FT obtained for this object are presented in Fig 14. We observed it 1.58 hours. This short length of the run was enough to reach an average noise amplitude of 0.36 mma. For this average amplitude, the amplitude necessary for a false alarm probability $FALSE = 1/20$ is 0.97 mma. We detected a peak at 2200 μHz just at this level (1.01 mma). Power is also present in the area related to the first harmonic of this frequency: 4400 μHz (0.706 mma). Our data do not show power around suspected peaks at 540.5 and 538.5 μHz reported by CB96.

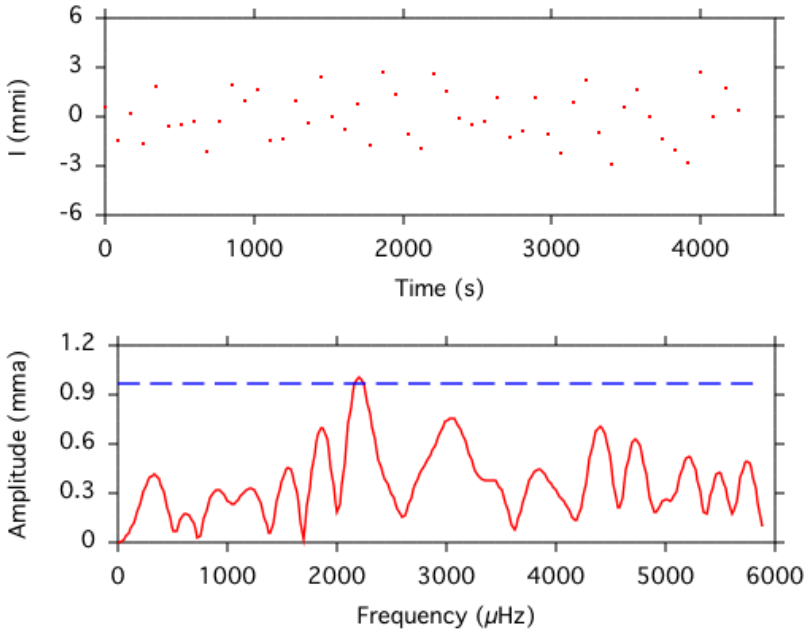

Fig. 14. Jn 1 from NOT data: the upper panel shows the light curve and the lower panel the temporal spectrum. The dashed line shows the limit in amplitude necessary to reach a false alarm probability $FALSE = 1/20$.

2.4.2.2. **NGC 246**

The bright (V=11.775) central star of NGC 246 is listed as a photometric standard star by Landolt (1983), and as a non-variable by Grauer et al. (1987). Later on, CB96 data showed it to be a low amplitude pulsator with periods of 24-31 min and amplitude ∼2 mmag. They observed this object in 3 different nights. Power was detected at 683 and 648 μHz in the temporal spectra of the first two runs, which were consecutive nights. A third run was obtained 9 months later and showed a different peak at a lower frequency (540 μHz). It should be noted that the central star of NGC 246 has a K-dwarf companion star which is located around 4" away (Minkowski 1965). Both stars were included in the aperture photometry measurements.

We included this PNN in our sample to monitor possible changes in the temporal spectra. We observed this object 5.36 hours, divided in two short runs: the first run was done on July 21st (2000), and lasted only 2.07 hours. The second run was done 2 nights later, on July 23rd, and was longer, 3.30 hours. The sampling rate was reduced from time 33 s in the first run to 12 s in the second. In the first run the sampling time was longer because we selected more reference stars and sky windows. For the second run we

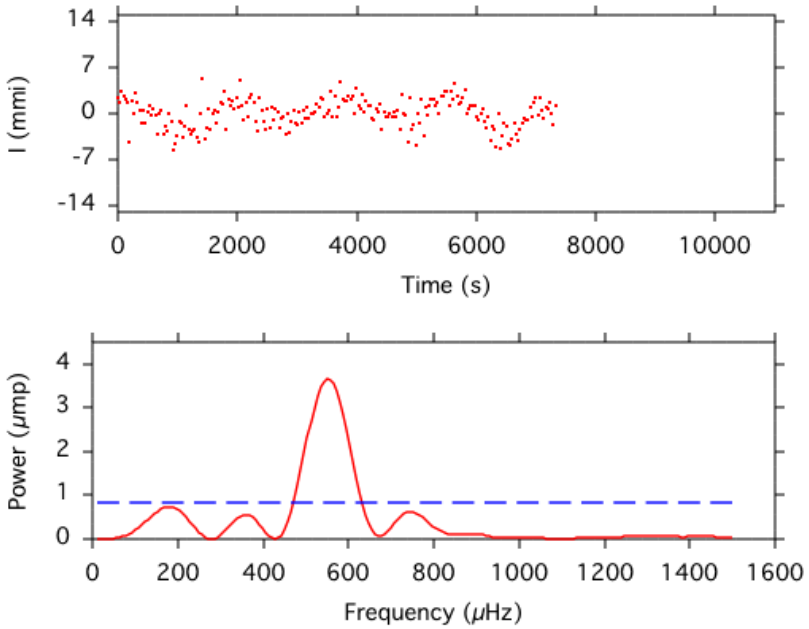

Fig. 15. NGC 246 from July 21st (2000) NOT data: the upper panel shows the light curve and the lower panel the temporal spectrum. The dashed line shows the limit in power necessary to reach a false alarm probability $FALSE = 1/20$.

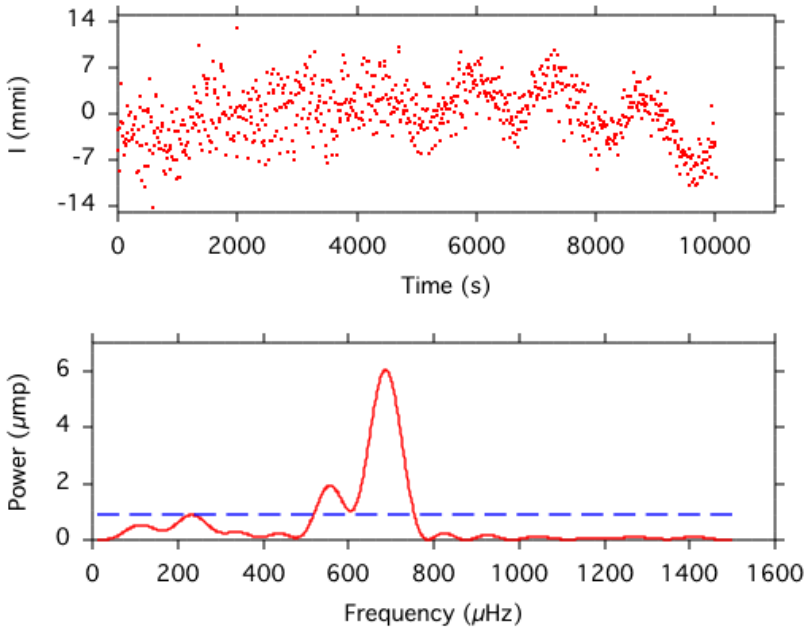

Fig. 16. NGC 246 from July 24th NOT data: the upper panel shows the light curve and the lower panel the temporal spectrum. The dashed line shows the limit in power necessary to reach a false alarm probability $FALSE = 1/20$.

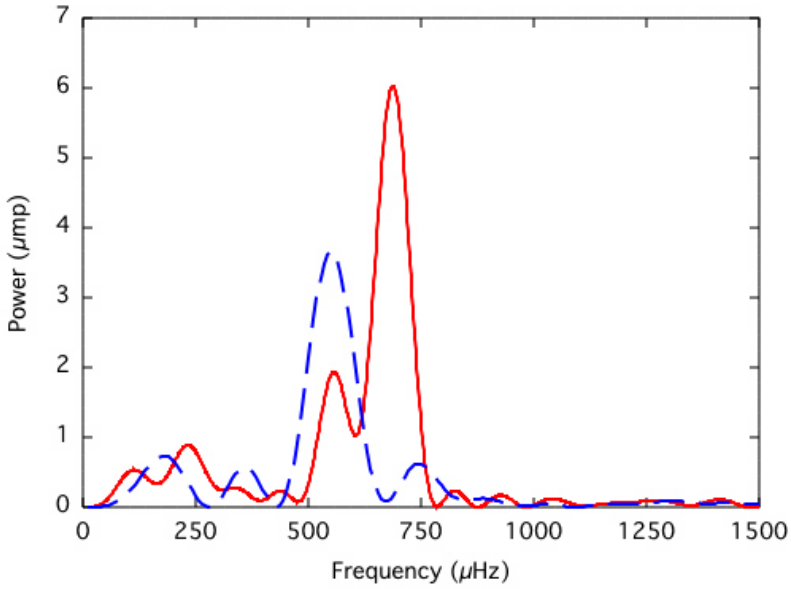

Fig. 17. Comparison of NGC 246 temporal spectra from NOT data. The dashed line is the temporal spectrum of the July 21st run and the continuous line the temporal spectra of the July 24th run.

shortened the readout time selecting only one reference star. As comparison star we used the one giving the least noise, that is, least average power, in the temporal spectrum of the first run. In addition, we selected less sky windows since the results were better by using the sky annulus option in RTP. In order to reach a short sampling time, we decreased the exposure time some. Therefore, the light curve for the second run is slightly noisier. The light curve and temporal spectrum for the first run are presented in Fig 15 and for the second run in Fig 16. These graphs present the temporal spectra in units of power (μmp) and, therefore, the false alarm probability is also in μmp. We use power for the temporal spectra where significant peaks are found to facilitate the visualization of the possible changes in the different FTs obtained.

The average power has been calculated excluding the frequency regions where significant peaks are found. The average power obtained is low in these runs: $\sim$0.1 μmp in both temporal spectra. The false alarm probability is 0.85 μmp for the first run and 0.92 μmp for the second. The temporal spectra show two regions of power with quite low amplitude and variability from night to night (see comparison in Fig 17). The amplitudes of these 2 peaks satisfied our confidence criterium. The first run shows power only in one region around 550 μHz (1.91 mma -3.66 μmp-) while the second run shows power in the same region but with smaller amplitude (1.36 mma -1.84 μmp-), and a new main peak at

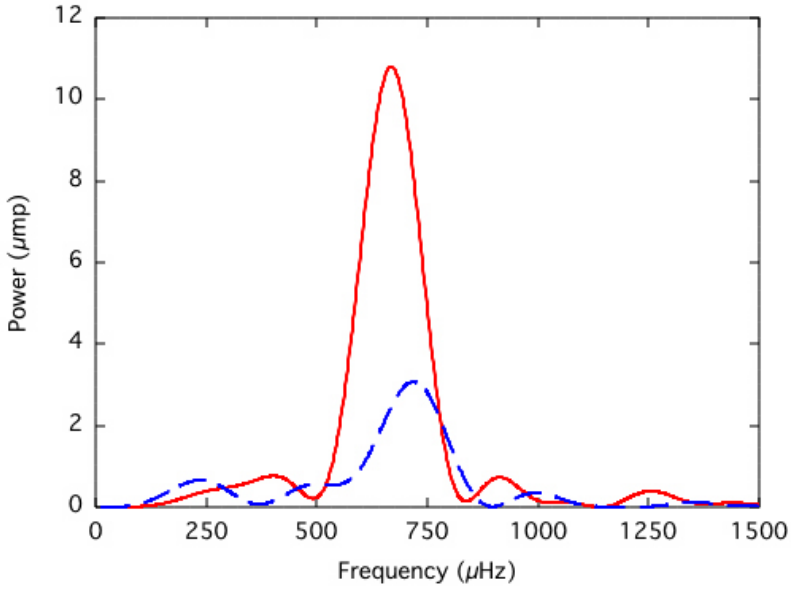

Fig. 18. Comparison of NGC 246 temporal spectra from July 21st NOT data. The dashed line is the temporal spectrum of the first half part of July 21st run and the continuous line the temporal spectra of the second half.

685 μHz (2.36 mma -5.56 μmp-) which is absent in the first set. Power at the level of the confidence criterium is also found at 233 μHz (0.93 mma -0.88 μmp-). Taking into account the short length of the observations, these changes in the FT may be the consequence of a more complex unresolved light curve. Daily changes in the temporal spectra has been observed before in other PNNs but then as amplitude variations. This time we observed the appearance of a modulation frequency complete absent in the previous data set. CB96 also found power in the same frequencies regions changing from run to run. However, the variations in the temporal spectra reported were from runs spaced many months, while now it was only 2 days.

2.4.2.3. **NGC 6852**

We observed this faint PNN with bipolar PNe and PG 1159 spectral type 6.3 hours divided in two runs over consecutive nights: the first was July 22nd (2000) and lasted 3 hours. The second was obtained ∼18 hours later and lasted 3.3 hours. We found no evidence of pulsational variability in the first run. However, the average amplitude is high, 0.98 mma. In this case the amplitude necessary for a false alarm probability $FALSE = 1/20$ is 2.61 mma. The temporal spectrum of this run is presented in Fig 19. It shows an important

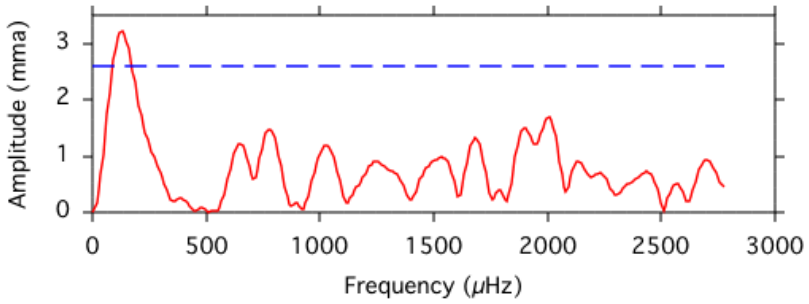

Fig. 19. NGC 6852 amplitude temporal spectrum from July 22nd (2000) NOT data. The dashed line shows the limit in amplitude necessary to reach a false alarm probability $FALSE = 1/20$.

peak but in the region of low frequencies (127.81 μHz). We do not claim this peak as a possible real modulation frequency since the length of the run was only slightly longer than the period associated to it (10 800 sec and 7824 sec respectively). Therefore, the run includes less than 2 cycles of this modulation period. In addition, the observing conditions during this run were not too good and during part of the run the object was observed through thin clouds. The differential photometry seems to have corrected for these clouds but some extra noise may be present in the low frequencies region due to the different colours of the target and reference stars.

The temporal spectrum of the second run shows two regions with power (see Fig 20). A peak with amplitude 2.7 mma (7.59 μmp) is seen near 912 μHz. To calculate the false alarm probability we use a local average amplitude covering 1000 μHz around 912 μHz. The average amplitude obtained is 0.95 mma (average power 0.9 μmp). This value gives a false alarm criterium of 2.55 mma (6.50 μmp). Therefore, the peak satisfied the confidence criterium. The period related to this modulation frequency is 1088 s, which can be seen in some intervals of the light curve (Fig 20). A close look at the modulations in the light curve suggest that they are not completely sinusoidal. This is especially noticeable towards the end of the run (after 8000 s), where a regular pattern seems to appear. We carefully investigated the raw data and reduced data before differential photometry, looking for possible instrumentation problems or bad weather conditions, but did not find anything. We also compared with the comparison star data which light curve does not present any variability in this time interval. Therefore, this variability must be intrinsic to the star. The lack of sinusoidal shape of the modulation may be a consequence of our long sampling rate (180 s) but may also reveal a more complex spectrum not completely resolved. On the

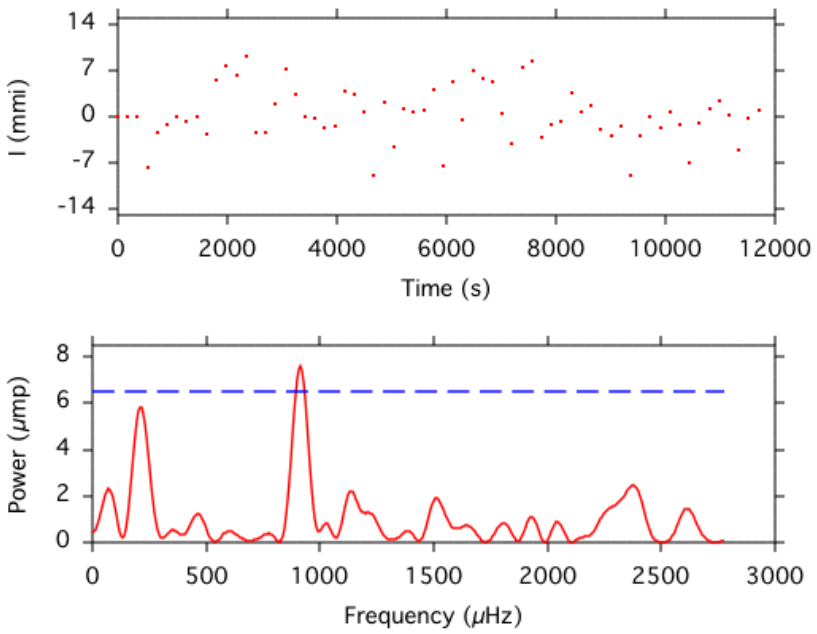

Fig. 20. NGC 6852 from July 23rd NOT data: the upper panel shows the light curve and the lower panel the power temporal spectrum.

other hand the pulse shapes of modulations in light curves in some CVs are not sinusoidal and this gives harmonics in the FT. However, no power is present in our data related to possible harmonics of the 912 μHz modulation.

Additional power is present at 209 μHz (2.4 mma -5.85 μmp-). This corresponds to a period of 5128 s. The length of this run was 11 880 s which is close to two cycles of this modulation period. Longer light curves must be obtained to check if this modulation is real.

Fig 21 presents a comparison of the temporal spectra from both runs near the peak at 912 μHz. It shows that this peak is not present in the temporal spectrum of the first run. Like for the NGC 246 case, we find a modulation frequency absent in a previous observation. In this case the time between the to runs is even shorter: 18 hours.

2.4.2.4. **VV 47**

Liebert et al. (1988) reported possible short-period variability for this object on the basis of photoelectric aperture photometry. GB96 included it in their survey. They observed this PNN 12.7 hours over 4 nights but could not confirm the suggested variability. We included it in our sample since it satisfies all our criteria (bipolar shape of the PNe and

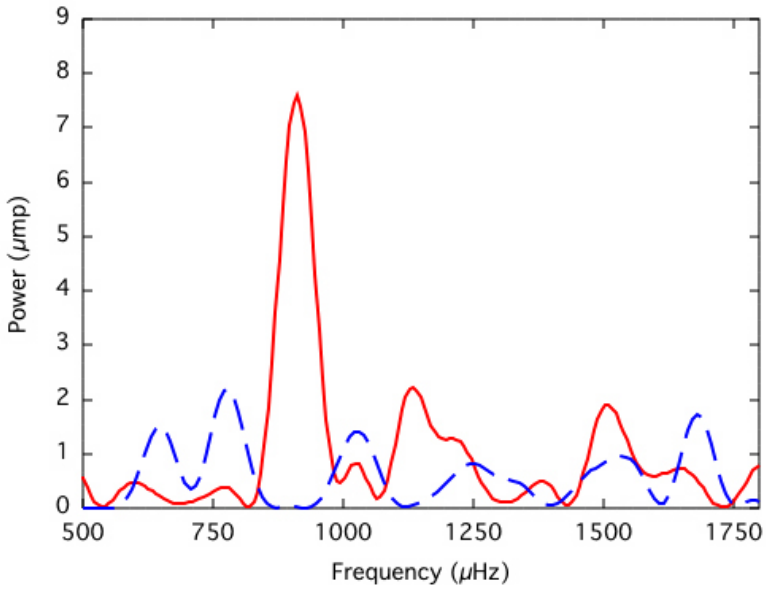

Fig. 21. Comparison of NGC 6852 temporal spectra from NOT data. The dashed line is the temporal spectrum of the July 22nd run and the continuous line the temporal spectrum of the July 23rd run, 18 hours after the first run.

PG 1159 spectral type), and because our system allowed us to reduce the average noise in the FT and, therefore, investigate possible variability below the noise threshold of previous observations.

We got 22.2 hours of data divided in 4 runs over three consecutive nights. The first run was January 16th 2001. The length of the run was 5.8 hours. The average power obtained in the FT is 0.153 μmp (average amplitude 0.39 mma). For this average power, the power necessary for a false alarm probability $FALSE = 1/20$ is 1.35 μmp (1.16 mma). Fig 22 shows the temporal spectrum obtained. Three peaks are found above 1.35 μmp but in regions below 500 μHz where the noise may be slightly higher. Some significant power is found associated with the frequencies 120 μHz (2.64 μmp -1.62 mma-), 176 μHz (1.61 μmp -1.27 mma-) and 284 μHz (2.14 μmp -1.46 mma-). The first modulation frequency is not considered since the run includes only 2 cycles of it. The peak at 284 μHz is a good candidate for a real modulation frequency since the power associated satisfies by far the confidence criterium. A small peak appears in the region of the first harmonic: 565 μHz (0.60 μmp -0.77 mma-). In addition, and taking into account the resolution of the run, power is also found in the region related with the 176 μHz first harmonic: 348 μHz (1.21 μmp -1.1 mma-). Another small peak is related to the frequency 232 μHz (0.90 μmp

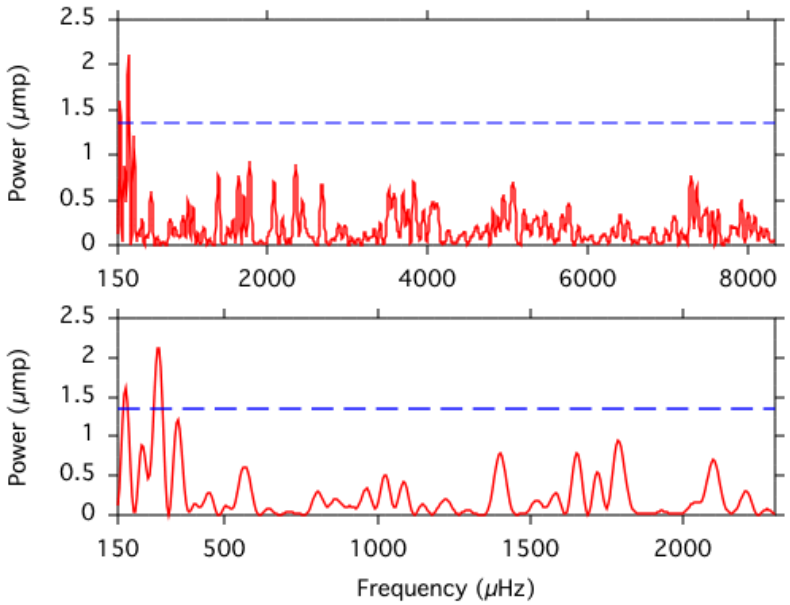

Fig. 22. VV 47 temporal spectrum from the first run. The upper panel shows the temporal spectrum over the complete range of frequencies. The lower panelshows in more detail the region where the higher peaks are found. The dashed line shows the limit in power necessary to reach a false alarm probability $FALSE = 1/20$

-0.95 mma-). The level of significance is not high but we mention it since power is found again in this region in the other long runs.

The second run on VV 47 was obtained ∼14 hours later. The length of the run was slightly longer: 6.27 hours. The average power for this run is 0.17 μmp (average amplitude 0.41 mma). This gives a false alarm probability 1.49 μmp (1.22 mma). Fig 23 shows the temporal spectrum obtained. Three peaks are found which satisfied this criterium: 150 μHz (1.90 μmp -1.38 mma-), 232 μHz (2.03 μmp -1.42 mma-) and 373 μHz (2.01 μmp -1.48 mma-). We do not want to claim as real the peak at 150 μHz because the amplitude of this peak depends of the reference star selected for the differential photometry. The peak at 232 μHz is a strong candidate to a real modulation frequency since it satisfies the confidence criterium in this run and it is present in others. On the other hand, the second highest peak 373 μHz is only found in this run. Additional power is found in the region related with its first harmonic: 742 μHz (1.13 μmp -1.06 mma-)

The third run was obtained the same night 1.5 hours after the second. This is a short run of 1.77 hours. Therefore, the average power is higher than in the previous cases: 1.03 μmp (average amplitude 1.01 mma), which gives a false alarm probability 7.78 μmp

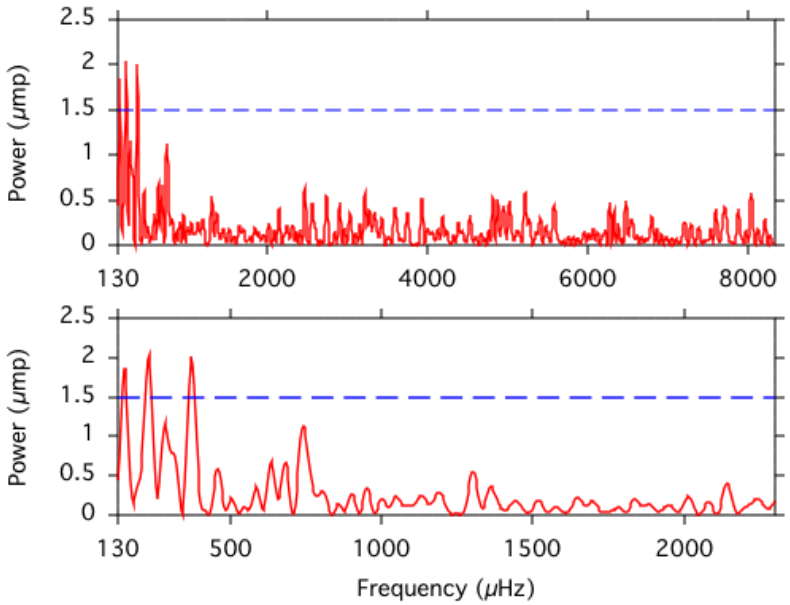

Fig. 23. VV 47 temporal spectrum from the second run. The upper panel shows the temporal spectrum over the complete range of frequencies. The lower panel shows in more detail the region where the higher peaks are found. The dashed line shows the limit in power necessary to reach a false alarm probability $FALSE = 1/20$

(2.79 mma). The length of the run sets a low frequency limit of 315 μHz. However, a peak satisfying the confidence criterium is present at 3826 μHz (9.37 μmp -3.06 mma-). The light curve and FT of this run is presented in Fig 24.

The last run on VV 47 was obtained the next night, around 13 hours after the previous one. We have mentioned that the RTP program allows us to follow the variability in the FT during the observation. In this case a high peak, which appeared during the first part of the run, started to decrease in amplitude after ∼2.5 hours observing. Therefore, we have included two analysis for this run: we have calculated the FT for the first section (2.32 hours) and for the whole run. The light curve and FT after 2.32 hours is presented in Fig 25. The average power is in this case 0.33 μmp (average amplitude 0.57 mma), which gives a false alarm probability 2.56 μmp (1.60 mma). A peak present at 7597 μHz satisfies the criterium: 2.92 μmp (1.71 mma). Taking into account the resolution of this part of the run, an important property of this peak is that it is in the region of the first harmonic of the peak discussed in the previous run. No power is found near the possible fundamental frequency.

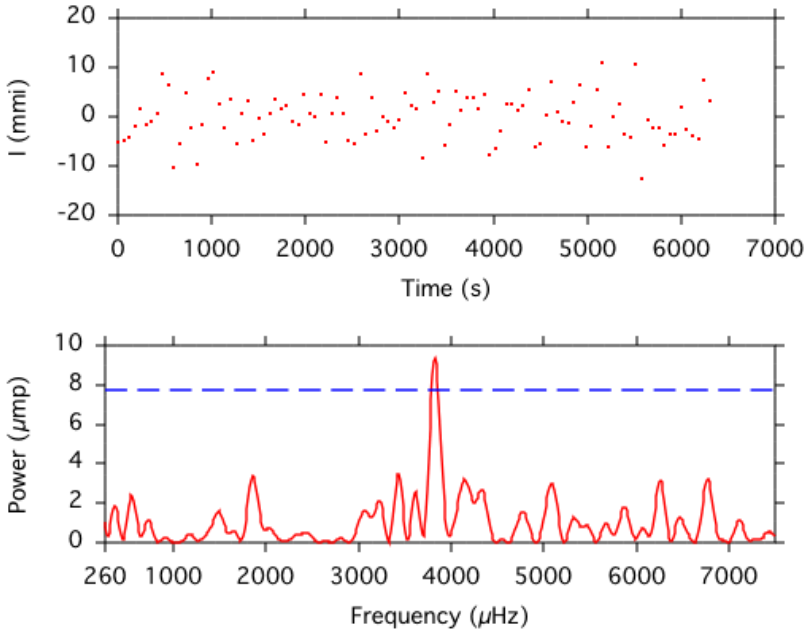

Fig. 24. VV 47 results from the third run. The upper and middle panels show the light curve and the lower panel the temporal spectrum. The dashed line shows the limit in power necessary to reach a false alarm probability $FALSE = 1/20$. A significant peak is identified at 3824 μHz

Fig 26 shows the light curve and FT over the complete data set obtained this night and Fig 27 shows in more detail the temporal spectrum. The length of the complete run is ∼4 hours. The average power is 0.42 μmp (average amplitude 0.65 mma), which gives a false alarm probability 3.57 μmp (1.89 mma). This average power is worse than what we obtained for the first section of the run. This may be due to the observing conditions since they deteriorated towards the end of the run. Only one peak satisfies the confidence criterium: 240 μHz (5.23 μmp -2.29 mma-). Power in the same region is found in the others two long runs. Power at the confidence level is present in the area close to the first harmonic: 460 μHz (3.57 μmp -1.89 mma-). Some power is also found at 847 μHz (1.73 μmp -1.31 mma-). The level of significance is not high but it may be related to the second harmonic of the peak at 284 μHz found in the previous two long data sets.

No significant peaks are found in this run at higher frequencies. The amplitude of the peak at 7597 μHz present in the FT of the first section of the run is significantly reduced in the complete set, but some power still is present above the local noise. However, some of the higher peaks present over 3000 μHz may be real since the relation between them fit $\mathcal{R}$=0.87. Other parameter mentioned as a detection criterium is the spacing in periods of the most

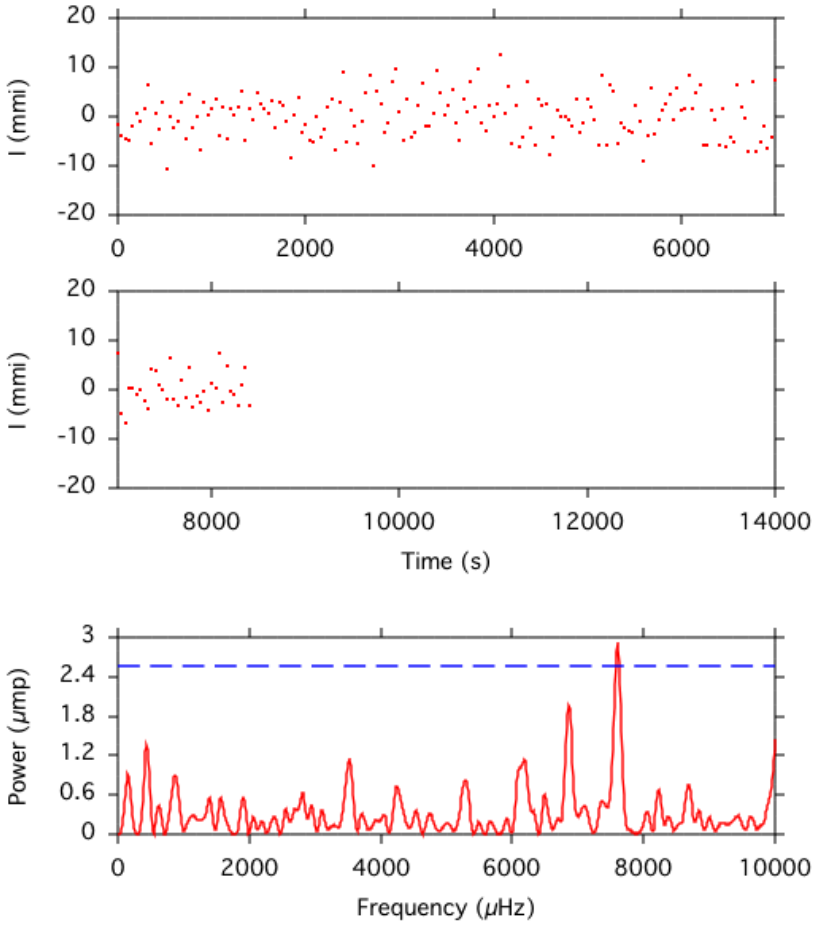

Fig. 25. VV 47 results from the first section of the last run (run 4) on this object. The upper panel shows the light curve and the lower panel the temporal spectrum. The dashed line shows the limit in power necessary to reach a false alarm probability $FALSE = 1/20$. The maximum power is identified at 7604 μHz, which is in the region of the first harmonic of the peak identified in run 3.

relevant peaks we find at higher frequencies. The period spacings found in other pulsating PNNs and GW Vir stars are remarkably similar: $\Delta P = 22.3$ s in NGC 1501 (Bond et al. 1996), 21.5 s in PG 1159-035 (Winget et al. 1991), 21.6 s in PG 2131+066 (Kawaler et al. 1995), 21.1 s in PG 0122+200 (Vauclair et al. 2001) and 21.5 s in RXJ 2117+3412 (Vauclair et al. 2002). We do not understand what mechanism forces these pulsators that have different masses and luminosities to display the same period spacing. However, this give us an extra chance to investigate possible real pulsations frequencies looking for spacing in period ∼21 s or multiple of this value in the highest peaks found above 3000 μHz.

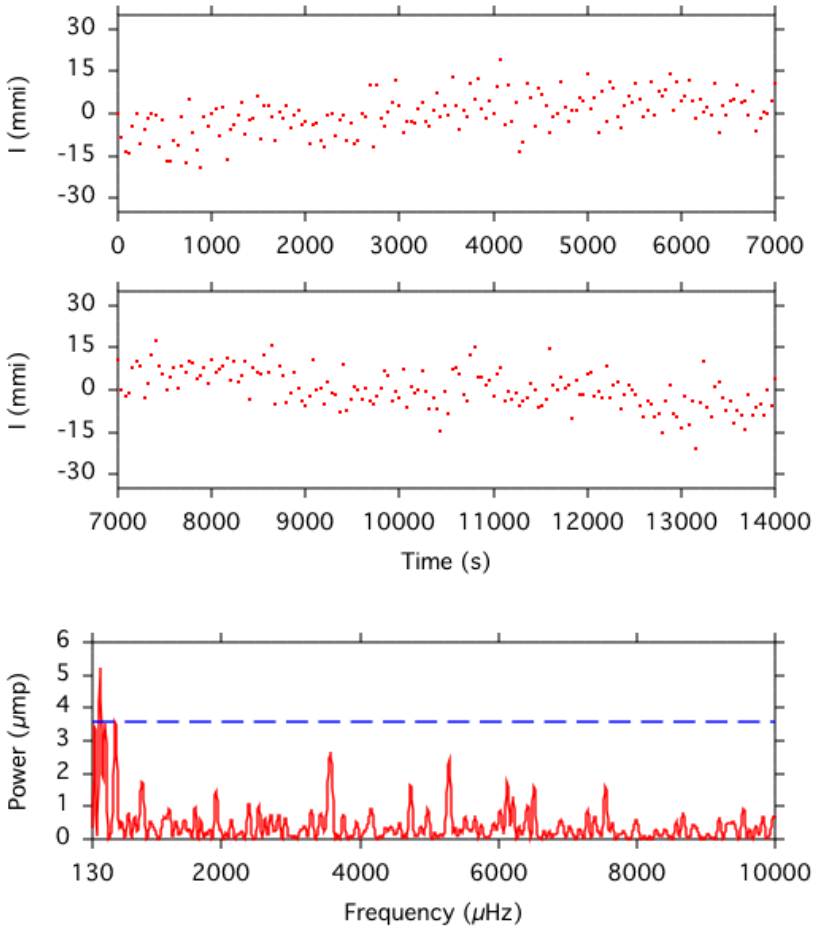

Fig. 26. VV 47 results from the last run (run 4) on this object. The upper and middle panels show the light curve and the lower panel the temporal spectrum. The dashed line shows the limit in power necessary to reach a false alarm probability $FALSE = 1/20$

The peaks with most power in this area are 3570 μHz (2.65 μmp), 4731 μHz (1.62 μmp), 5286 μHz (2.40 μmp), 6127 μHz (1.75 μmp), 6516 μHz (1.62 μmp) and 7550 μHz (1.58 μmp). Taking into account the resolution of the run (69 μHz), the ratios 5286/6127 and 6516/7550 fit $\mathcal{R}$. Additional power is found in 4159 μHz (0.92 μmp) which is also present in the previous short run but with low significance level (3.2 μmp and average power 1.03 μmp). The ratios 3570/4159, 4159/4731 and 4731/5286 are also close to $\mathcal{R}$. On the other hand, the period spacing between the peaks at 3570 μHz (P=280.1 s) and 4159 μHz (P=240.4 s) is 39.7 s or $\sim$2 times a possible period spacing of 21 s. The spacing for the peaks at 4731 μHz (P=211.4 s) and 5286 μHz (P=189.2 s) is 22.2 s; and we find 21 s between the peaks at 6516 μHz (P=153.5 s) and 7550 μHz (P=132.5 s). However,

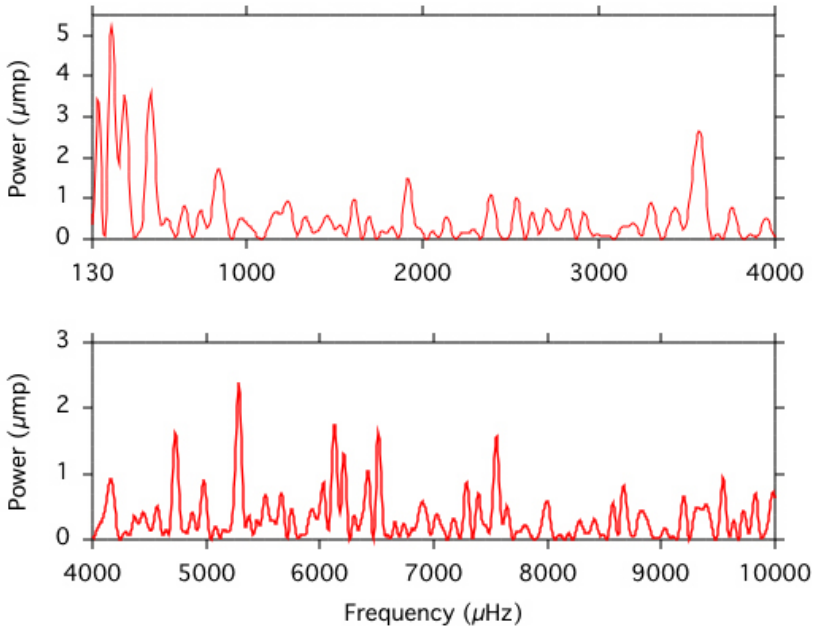

Fig. 27. VV 47 temporal spectrum from the last run (run 4).

there is not a clear general spacing of ∼21 s for all the relevant peaks found in the section but only these pairs. The period spacing between 4159 μHz ($P = 240.4$ s) and 4731 μHz ($P = 211.4$ s) is 29 s ; 26 s between 5286 μHz ($P = 189.2$ s) and 6127 μHz ($P = 163.2$ s); and 9.7 s between 6127 μHz ($P = 163.2$ s) and 6516 μHz ($P = 153.5$ s). Rotational splitting or linear combinations may create these extra peaks.

The ratio between frequencies over 3000 μHz with significant power close to $\mathcal{R}$, and the connection of others with a period spacing close to 21 s or multiple of this number suggest that, even if the FAP confidence criteria are not reached, some of these pulsations may be real and related to VV 47 g-modes. However, this characteristic in the FT were not present in the previous long runs. Some of the peaks may exist but confused with noise and, therefore, with lower amplitudes.

A comparison of the low frequency region between different runs is presented in Fig 28, and a comparison of the FTs over 2000 μHz in Fig 29. A resumé of the significant peaks found in the different runs is presented in table 6. Our analysis suggest that VV 47 is a low amplitude pulsator presenting an extremely complicated temporal spectrum. In general the most significant peaks have highly variable amplitudes from run to run or are only found in one of them. Power is found covering a wide area of frequencies: possible real peaks may exist from 176 μHz to 7597 μHz. Many of these peaks are

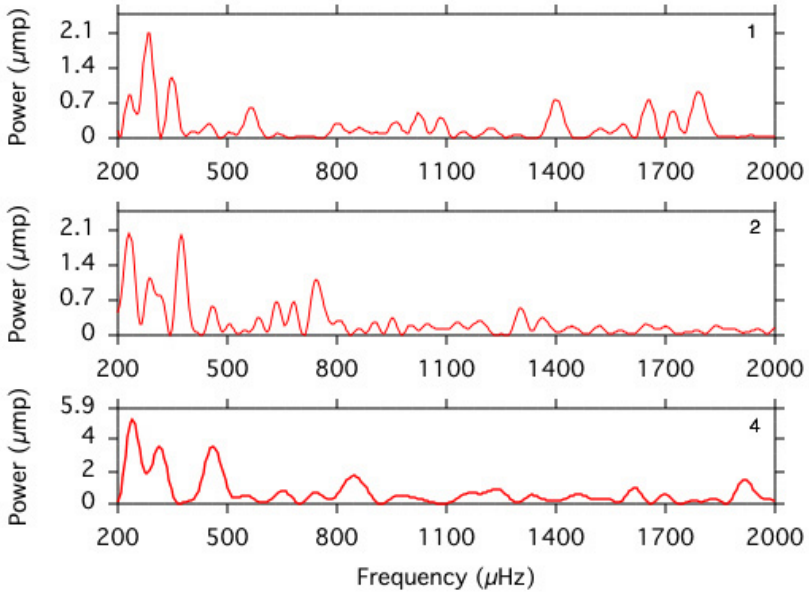

Fig. 28. VV 47 comparison of the low frequencies region of the temporal spectra from 3 different runs (1, 2, 4). Notice that the vertical axis (power) of the third FT is different for the rest.

below the confidence criterium and therefore may not be real modulations frequencies. However, other considerations suggest that they may represent real pulsations. Some peaks satisfying the confidence criteria have low frequencies where the local average power may be slightly higher. However, some of them repeat in different long runs. In this frequency range the best candidates for real modulation frequencies are 232 and 284 μHz. Other peaks at higher frequencies satisfying the confidence criteria are found only in one short run, like the peak at 3826 μHz. The same happens with the peak at 7597 μHz, which is the first harmonic of the previous one, but appearing in the next run. This peak satisfies the confidence criterium if considering only the first part of the run but is far below the limit if considering the whole run. This may indicate a short life time for these modulation frequencies, maybe only a couple of hours.

Evidence for ϵ-mechanism in VV47?

Starrfield et al. (1984, 1985) suggested that the non-radial g-mode instability in pre-white dwarfs is triggered by the κ and γ mechanism induced by partial ionization of carbon and oxygen at temperatures around 10^6 K. However, Kawaler et al. (1986) proposed that during the PN and pre-white dwarf evolutionary phases, the possibility of a remnant

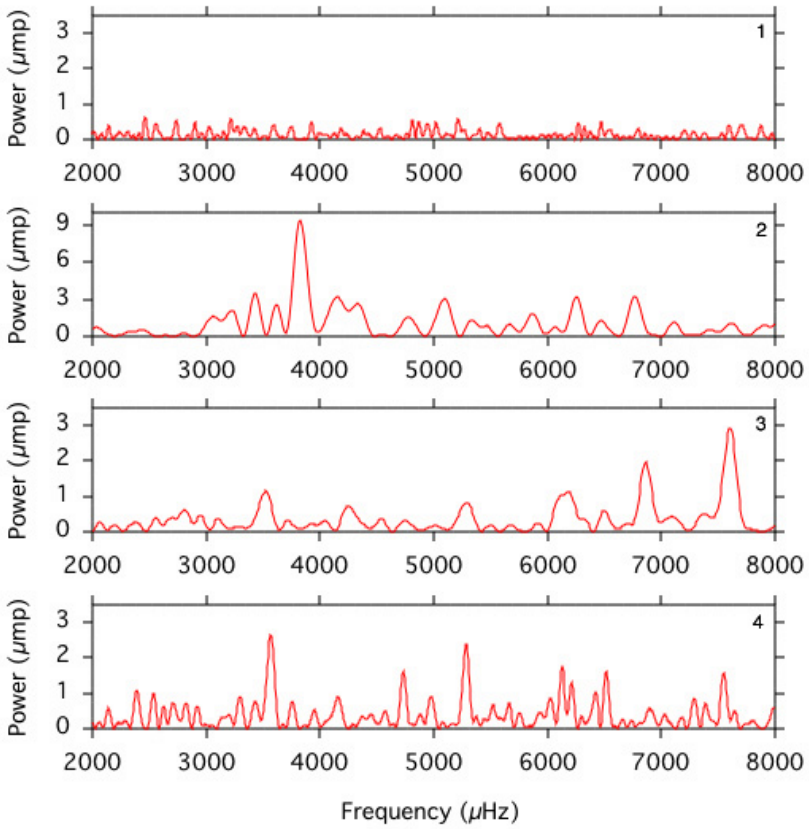

Fig. 29. VV 47 comparison of the high frequencies region of the temporal spectra from 4 different runs (1, 2, 3, 4). Notice that the vertical axis (power) of the second FT is different from the rest.

He-burning shell that could drive g-modes by the ϵ-mechanism. These g-modes are predicted to be unstable and in the period range of 70 s-200 s, corresponding to low k orders for $l = 1$ modes. Models by Saio (1996) and Gautschy (1997) also find g-modes due to the ϵ-mechanism with typical periods between $\sim$110 s and 150 s. However, such short period g-modes excited by ϵ-mechanism have not been found in previous PNN surveys. G. Vauclair et al. (2002) did not find evidences for ϵ-mechanism in their detailed asteroseismological study of RXJ 2117+3412, the hottest pulsating PG 1159 star. They found some peaks in the high frequency range which could be candidates for ϵ-mechanism driven modes. However, all of them could be interpreted as the result of linear combinations of lower frequency modes and, therefore, they are not independent modes.

Our analysis over VV 47 indicates the presence of some possible real peaks in the high frequency range which may be candidates for low-k order g-modes driven by the

Table 6. Peaks in VV 47 temporal spectra. The frequency and the false alarm probability are expressed in μmp. The second column lists the period associated. A 'X' in the fifth column indicates that the modulation frequency satisfied the confidence criteria. The last column shows other criteria used: 1- indicates that the peak has an harmonic related or is harmonic of a significant peak present in the same run; 2 - indicates that the peak has an harmonic related or is harmonic of a significant peak present in another run; 3 - indicates that the peak satisfied the ratio $\mathcal{R}$ with another peak and/or period spacing around 21 s or multiple of this value. Bold indicates the peaks with best chances to be real.

Freq (μHz)	**P** (s)	**Run**	**FAP**	**Power** (μmp)	**Over FAP?**	**More**
∼176	5682	1	1.48	1.6	X	1
∼**232**	4310	1	1.48	0.9		
		2	1.68	2.0	X	
		5	4.01	5.2	X	
∼**284**	3521	1	1.48	2.1	X	2
		2	1.68	1.2		
∼348	2874	1	1.48	1.2		1
∼**373**	2681	2	1.68	2.0	X	1
∼460	2174	5	4.01	3.6		2
∼742	1348	2	1.68	1.1		1
∼847	1181	5	4.01	1.73		2
∼3570	280.1	5	4.01	2.65		3
∼**3826**	261.4	3	8.90	9.4	X	
∼4159	240.4	3	8.90	3.19		
		5	4.01	0.92		3
∼4731	211.4	5	4.01	1.62		3
∼5286	189.2	5	4.01	2.40		3
∼6127	163.2	5	4.01	1.75		3
∼6516	153.5	5	4.01	1.62		3
∼7550	132.5	5	4.01	1.58		3
∼7597	131.6	4	3.01	2.92		2

ϵ-mechanism. The highest peak found during the third run at 3826 μHz may be a good candidate. In addition, we have mentioned the presence of power over local noise at higher frequencies which do not satisfy the FAP confidence criterium but other criteria such as the ratio between them fitting $\mathcal{R}$ or a period spacing ∼21 s. Such criteria indicate that these peaks may be candidates to be g-modes and, due to their localization in the high frequencies area, triggered by the ϵ-mechanism. However, these peaks are found only in one

of our long runs. They may be present in others, but with lower amplitude and confused with noise. If those peaks are real, the ϵ-mechanism which is supposed to trigger them is quite unstable and generate g-modes that may vary in amplitude in time scale of hours.

Interaction with close companion?

We have found possible peaks related with harmonics of significant peaks, both in the same FT or in FT of another runs. This may also indicate complex processes happening in the star on short time scales. Such processes may create different symmetries that modulate the light curve and produce harmonics of a modulation frequency. This characteristic is observed in systems with accretion discs or accretion driven by magnetic fields. In some cases, like in temporal spectra of AM CVn, harmonics may be present in the FT but not the main modulation frequency (Solheim et al. 1999). This is explained by considering symmetries in the structure of the accretion discs. Harmonics are also observed related to normal modes in other pulsating PNNs, but never harmonics of a main modulation frequency which is not present in the FT.

The complex temporal spectra of this PNN may indicate a combination of processes going on around the star plus normal oscillation modes of the star. However, they are unstable, changing quickly with time. This add difficulties in defining confidence criteria to use in order to be completely sure about which of the modulation frequencies are real and which are not. This variability may hide modulation frequencies which could only be found by considering sections of a run, like is the case for the peak at 3826 μHz. The short time scale involved suggests other processes besides normal oscillation modes and that those may affect the oscillation modes themselves.

2.5. Discussion

We have completed a survey for pulsational variability in a sample of 11 PNNs selected by the following criteria: 'PG 1159' or 'O VI' spectral type and a bipolar or elliptical shaped planetary nebula envelope (PNe). These characteristics suggest presence of a close companion. We report the discovery of three new pulsators: Jn 1, VV 47, and NGC 6852. Our results increases to 12 the known pulsating PNNs: RX J2117.1+3412, NGC 1501, NGC 2867, NGC 2371-2, NGC 6905, NGC 5189, Lo 4, K 1-16, NGC 246, NGC 6852, VV 47 and Jn 1. Some of the objects selected in our sample were already included in the survey by CB96. We checked again these PNNs since our system allowed us to reduce the noise level

in the FT and, therefore, observe possible pulsations with lower amplitudes. In general, all our pulsators present low amplitude modulation frequencies and a complex photometric behaviour which change on very short time scales: NGC 246 temporal spectra present significant changes between two runs 3 days apart, with the appearance of a significant peak at 685 μHz completely absent in the first run. The analysis of NGC 246 second run indicates that all the pulsation power is concentrated in the second part of the run. It seems that the modulation frequencies were switched on in this part. This behaviour is peculiar since the daily changes observed in other PNNs show variations in the amplitudes of certain peaks, but never the appearance of a new peak. Our runs are not long ($\sim$4 hours), so one possible explanation could be the beating of close modes in a not completely resolved temporal spectrum. However, changes in amplitude have also been reported in completely resolved temporal spectra for others PNN as RX J2117.1+3412. This result indicates that the observed changes in NGC 246 may be real. On the other hand, taking into account the big difference between the temporal spectrum of two sections of the last run, the beating between close modes may not be a good alternative since they are observed to produce a gradual change of the light curve and, therefore, a slower increase or decrease in the amplitudes. We have compared this light curve with published light curves of others PNNs, looking for changes like the one observed during the second run for NGC 246. The longest light curves up to date has been obtained for RX J2117+3412 (Vauclair et al. 2002) which has been observed in 3 different multisite campaigns. This PNN do present variations in the amplitude of the modulations which are easily visible in light curves (see for example Fig 3 and Fig 4 in Vauclair et al. 2002). However, these differences are seen in light curves obtained many months apart. The light curves seems to be more stable during the same campaign.

The Fourier analysis seems not to be appropriated for these objects, since it considers that all the modulation frequencies are static. If we want to investigate the possible changes of the pulsations with time, the only option is to use Fourier analysis on sections of the run and look for possible variations in the temporal spectra. Other tools such as the wavelet analysis would help in the study of these cases. The evolutionary time scales in the PNNs phase is very short, and process like mass loss may alter the amplitude of the PNNs g-modes in time scales of weeks. However, this mechanism seems to be insufficient to explain the observed variations in NGC 246, which are produced in time scales of days or less. The same behaviour was observed for the PNN NGC 6852. We observed this PNN two

consecutive nights. The FT from the first run does not show any evidence of pulsations, but a second run obtained only 18 hours later shows a peak ∼912 μHz. These rapid variations imply time scales which are difficult to explain by processes happening inside the star. Our currents models can not explain those changes. Another option is to try to explain them with processes related with interaction with close companions that appear in dynamical time scale, like the presence of an accretion disc and mass transfer which may modulate the light curve. The presence of a disc can be supported by signatures typical of CVs with accretion discs. Those are the presence of several harmonics to a main period, which is associated to the shape and dynamics of the accretion disc. The main periods may be the orbital period, superhump period or period of rotation. We have search for such features but have not found harmonics to the changing modulation frequencies for NGC 246 and NGC 6852. However, for NGC 246 we have discovered such features in longer observing runs obtained 2001-2003 and reported in chapter 3.

VV 47 present even more complicated and variable temporal spectra. We followed this objects for 3 consecutive nights and obtained pulsations covering a wide range of frequencies: from 176 μHz to 7597 μHz. This is the first time that possible modulation frequencies for a PNN above ∼2175 μHz are found. The temporal spectra are again quite variable from night to night but some modulation frequencies at lower frequencies are present in at least 2 long runs (232 μHz and 284 μHz). Power is also found near the first harmonic of 232 μHz and second harmonics of 284 μHz. The high frequency region for this object is quite interesting. The first long run did not show evidence of pulsations in this region. However, in the third short run a peak appeared at 3826 μHz. Something seems to had happened to the star because in the next run several low amplitude pulsations candidates to g-modes appeared in the region above 3500 μHz. This may be the first time that we have observed candidates for low-k order g-modes driven by the ϵ-mechanism. An additional interesting feature is the presence of power in the region of the first harmonic of 3826 μHz in the last run, but lack of power at this fundamental frequency. This interesting object may in addition presents photometric features indicating interaction with a close companion, because of the changing presence of harmonics between the different runs.

In general, the new pulsators discovered and the rapid changes in their temporal spectra obtained for them and for NGC 246 suggest the necessity to investigate the use of additional tools for analysis, such as wavelets. The rapid changes indicates also that the search for new PNN pulsators is complicated since one must monitor a candidate several

times to be sure if it pulsates. Confidence criteria based on presence of power at the same frequency in all runs seems not to be appropriated in these cases. In addition, the search for peaks filling the confidence criteria must be done analysing carefully not only the complete run but sections of it. An example is the peak at 7597 μHz obtained in the fourth run on VV 47, which is the first harmonic of the peak found on the third run. This peak satisfied the confidence criterium during the first half of the run, but decreased quite a lot in amplitude and did not satisfied the confidence criterium when considering the whole run. This change suggest that process on time scale of ~ 2 hours may be happening in the star, which certainly points to processes on dynamical time scale.

The rapid photometric changes seems to be a property common for many of the pulsating PNNs. However, we have reported for the first time evidences that suggest that these photometric changes may happen on time scale of hours. Due to this property, and because the low amplitude pulsations displayed by the pulsators, we can not claim that the PNNs analysed where not relevant peaks were found in the FT, do not pulsate. We can only conclude that they did not show pulsations satisfying the confidence criteria during the time the objects were observed by us. The variable power spectra and low pulsation amplitudes suggest that the true fraction of hot, hydrogen-deficient PNNs may be higher than found in our survey. In the next chapter we follow up the photometric behaviour of NGC 246 with more observations and use wavelet analysis to investigate in more detail the time scales associated to these variations.

Acknowledgment: The results presented in this chapter are based on observations obtained at the Nordic Optical Telescope, operated on the island of La Palma jointly by Denmark, Finland, Iceland, Norway, and Sweden, in the Spanish Observatorio del Roque de los Muchachos of the Instituto de Astrofísica de Canarias. The data presented here have been taken using ALFOSC, which is owned by the Instituto de Astrofisica de Andalucia (IAA) and operated at the Nordic Optical Telescope under agreement between IAA and the NBIfAFG of the Astronomical Observatory of Copenhagen. I would like to thanks the staff at NOT for their kind support and to my colleagues Roy Østensen, for his patient help with the software for windowing photometry, and Robert Kamben who helped me during the observations. I wish to thanks Jan-Erik, for his important contributions to this work, fruitful discussions and patient revision of the earlier manuscripts.

References

Appleton, P. N., Kawaler, S. D., & Eitter, J. J. 1993, AJ, 106, 1973

Bessell, M. S. 1990, PASP, 102, 1181

Bradley, P. A., & Dziembowski, W. 1996, ApJ, 468, 350

Bond, H. E., & Livio, M., 1990, ApJ, 355, 568

Bond, H. E., Kawaler, S. D., Ciardullo, R., et al. 1996, AJ, 112, 2699

Bond, H. E., & Meakes, M. G. 1990, AJ, 100, 788

Ciardullo, R., & Bond, H. E. 1996, AJ, 111, 2332 (CB96)

Chevalier, R. A., & Luo, D., 1994, ApJ, 421, 225

Fabian, A. C., & Hansen, C. J., 1979, MNRAS, 187, 283

Gautschy, A. 1997, A&A, 320, 811

Grauger, A. D., & Bond, H. E. 1984, ApJ, 277, 211

Grauer A. D., Bond H. E., Liebert J. et al. 1987, ApJ, 323, 271

Han, Z., Podsiadlowski, P., & Eggleton, P. P. 1995, MNRAS, 272, 800

Handler, G., Metcalfe, T. S. & Wood, M. A. 2002, MNRAS, 335, 698

Heap, S. R. 1982, in Wolf-Rayet Stars: Observations, Physics, Evolution, IAU Symposium No. 99, edited by C. W. H. de Loore and A. J. Willis (Reidel, Dordrecht), p. 423

Iben, I. Jr, Tutukov, A. V. 1984a,ApJS, 54, 335

Iben, I. Jr, Tutukov, A. V. 1984b, in Chioso C., Renzino A., eds, Stellar Nucleosynthesis. Reidel, Dordrecht, p. 181

Iben, I. Jr., Tutukov, A. V. 1991, ApJ, 370, 615

Iben, I. Jr, Tutukov, A. V. 1993,ApJ, 418, 343

Iglesias, C. A., & Rogers, F. J. 1993, ApJ, 412, 752

Kaler, J. B., Shaw, R. A. & Kwitter, K. 1990, ApJ, 359, 392

Kawaler, S. D., Winget, D. E., Hansen, C. J., & Iben, I. Jr. 1986, ApJ, 306, L41

Kawaler, S. D., & Bradley, P. A. 1994, ApJ, 427, 415

Kawaler, S. D., et al. 1995, ApJ, 450, 350

Kepler, S.O. 1993, Baltic Atronomy, 2, 515

Koupelis, T., & Winget, D. E. 1987, The Second Conference on Faint Blue Stars, IAU Colloquium No. 95, edited by A. G. D. Philip, D. S. Hayes, and J. W. Liebert (Davis, Schenectady), p. 623

Kwok, S., Purton, C. R., & Fitzgerald, P. M., 1978, ApJ, 219, L125

Landolt, A. U. 1983, AJ, 88, 439

Liebert, J., Fleming, T. A., Green, R. F., & Grauer, A. D., 1988, PASP, 100, 187

Mendez, R. H., Miguel, C. H., Heber, U., & Kudritzki, R. P. 1986, in Hydrogen-Deficient Stars and Related Objects, edited by K. Hunger, et al. (Reidel, Dordrecht), p. 323

Minkowski, R. 1965, in Galactic Structure, edited by A. Blaauw and M. Schmidt (university of Chicago Press, Chicago), p. 321

Nather, R. E., Winget, D. E., Clemens, J. C., Hansen, C. J., Hine, B. P., 1990, ApJ, 361, 309

Napiwotzki, R., 1992, in The Atmospheres of Early-Type Stars, edited by U. Heber and C. S. Jeffery (Springer, Berlin), p. 310

Napiwotzki, R., 1993, Acta Astron., 43, 343

Napiwotzki, R., & Schönberner, D. 1995, A&A, 301, 545

Napiwotzki, R., & Schönberner, D. 1991, A&A, 249, L16

Napiwotzki, R., et al 1996, in "Hydrogen-Deficient Stars", ASP Conference series, C.S. Jeffery and U. Heber eds., 96, 213

Okorokov, V. A., Shustov, B. M., Tutukov, A. V., Yorke, H. W., 1985, A&A, 142, 441

Pascoli, G., 1987a, A&A, 180, 191

Pascoli, G., 1987b, Ap&SS, 134, 73

Saio, H. 1996, in Hydrogen-Deficient Stars, ed. C. S. Jeffery, & U. Heber, ASP Conf. Ser., 96, 361

Schönberner, D., & Napiwotzki, R. 1990, A&A, 231, L33

Smith, L. F., & Aller, L. H. 1969, ApJ, 157, 1245

Soker, N. 1997, ApJS, 112, 487

Solheim, J.-E., et al. 1998, A&A, 332, 939

Stanghellini, L., Cox, A. N., & Starrfield, S. G. 1991, ApJ, 383, 766

Starrfield, S., Cox, A. N., Kidman, R. B., & Pesnell, W. D. 1984, ApJ, 281, 800

Starrfield, S., Cox, A. N., Kidman, R. B., & Pesnell, W. D. 1985, ApJ, 293, L23

Tutukov, A. V., Yungelson, L. R., & Iben, I. Jr. 1992, ApJ334, 357

Vauclair, G., Moskalik, P., Pfeiffer, B., et al. 2002, A&A, 381, 122

van Zyl, L., & Warner, B. 1998, International Astronomical Union. Symposium no. 185. New Eyes to See Inside the Sun and Stars, edited by Franz-Ludwig Deubner, Joergen Christensen-Dalsgaard, and Don Kurtz. Kyoto, Japan, p. 321.

Volk, K. M., & Kwok, S. 1985, A&A, 153, 79

Warner, B. 1995, Ap&SS, 225, 249

Werner, K., Heber, U. & Hunger, K. 1991, A&A, 244, 437

Werner, K. 1992, in The Atmospheres of Early-Type Stars, ed. U. Heber and C. S. Jeffery (Springer, Berlin), p. 273

Winget, D. E., et al. 1991, ApJ, 378, 326

Yungelson, L. R., Tutukov, A. V. & Livio, M. 1993, ApJ, 418, 794

Yungelson, L. R., Livio, M., Tutukov, A. V. & Saffer, R. A., 1994, ApJ, 420, 336

Zuckerman, B., & Gatley, I., 1988, ApJ, 324, 501

Østensen, R., & Solheim, J.-E. 2000, Baltic Astronomy 9, 411

Østensen, R. 2000, Time Resolved CCD Photometry, Ph.D. Thesis, University of Trømso

Chapter 3

Rapid photometric changes in the PNN NGC 246.

Abstract.

We present a study based on single site campaigns destined to investigate the photometric behaviour of the central star of the planetary nebulae (PNN) NGC 246. We have observed this object 71.75 hours in different campaigns from 2000 to 2003. The analysis of the light curves indicates complex and variable temporal spectra. We present for the first time evidences of photometric changes in time scales of hours and less. The study of these rapid variations have been done using wavelet analysis on the 2000 and 2003 datasets. The temporal spectra obtained during 2001 are quite different from the results in the other years. The modulations in the light curve are more noticeable. One characteristic is the presence of amplitude variable harmonic structures related to 230 μHz and 280 μHz. We have analyzed O-C diagrams related with modulation at frequency 230 μHz and found that the phase is kept with high precision over years. The photometric behaviour may be explained by an unresolved combination of modulation frequencies, but more likely due to a combination of stellar pulsations and modulations related to interaction with a close companion. The stability found for the 230 μHz pulsation frequency indicates that may be related to the orbital period. Wavelet analysis on 2003 data shows short life time of many pulsations that may be non-radial g-modes. Many of these pulsations are activated and deactivated 2 or 3 times during the length of the run. Some of them are present at periods below 200 s and may be triggered by the ϵ-mechanism. Wavelet analysis indicates a short lifetime, $\sim$500 s, of these pulsations.

'From Close Binary White Dwarfs to White Dwarfs': J. M. González Pérez, e-mail: jose@phys.uit.no

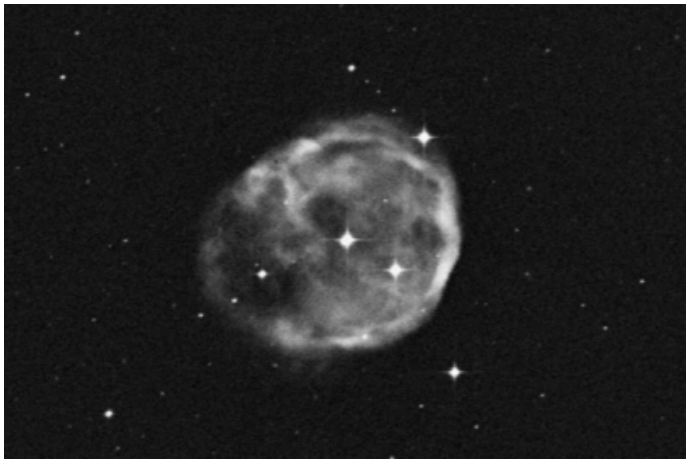

Fig. 30. NGC 246 field. This image covers an area of ∼11.5 x 8 arcmin around the PNN.

3.1. Introduction.

We have conducted a program of photometry on the PNN NGC 246. The bright central star of NGC 246 (V=11.78) is listed as a photometric standard star by Landolt (1983), and as a non-variable by Grauer et al. (1987). However, Ciardullo and Bond (1996) reported it to be a low amplitude pulsator with periods of 24 and 31 min and amplitudes ∼2 mmag. We included this object in our survey for pulsations of PNNs with PG 1159 and bipolar or elliptical shape of the nebula (see previous chapter), and found power in the same frequency regions as observed by Ciardullo and Bond with rapid variations in amplitudes. It should be noted that the central star of NGC 246 has a K-dwarf companion ∼4" away (Minkowski 1965).

NGC 246 is an interesting PNN to monitor due to these previous photometric results. The object is quite bright and surrounded by a faint elliptical nebula. Therefore, photometry can be done with small telescopes and photoelectric tubes. The spectral type of NGC 246 central star is O(C) (Mendez et al 1986) which is closely related to the spectral type of PG 1159 (Schönberner & Napiwotzki 1990). Spectroscopy has revealed changes in NGC 246 optical spectrum over years (Mendez & Niemela 1979). In particular, spectra taken in 1971, 1973 and 1977 show how the He II λ4685 Å line changed from absorption to emission (see Figure 31). A progressive development of an envelope around the central star was suggested to explain this feature. Moreover, strange abundances are observed, as the lack of nitrogen and overabundance of neon (Werner and Rauch 1994). Neon is enhanced through the reactions: $^{14}N(\alpha,\gamma)^{18}F(\beta,\nu)^{18}O(\alpha,\gamma)^{22}Ne$ that takes place in the post-AGB stellar interiors or due to He burning in the upper layers of a star that accretes matter as

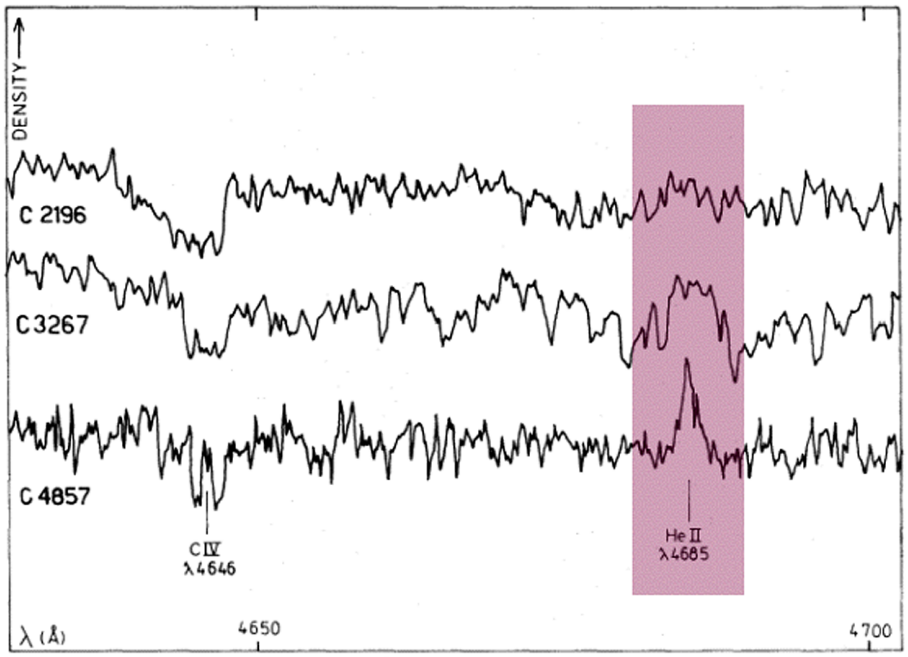

Fig. 31. NGC 246 spectra showing changes in the He II λ4685 Åline (from Mendez & Niemela 1979)

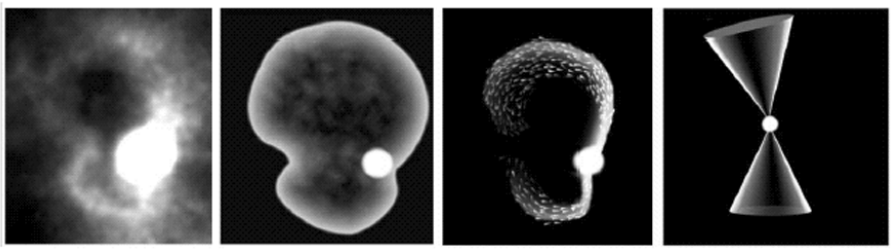

Fig. 32. NGC 246, Ne V image of the inner core compared with various models for this region, i.e., the peanut, the sprinkler, and the biconical model; figure extracted from Szentgyorgyi et al. (2003).

in the helium cataclysmic variables (He CV). Another peculiarity is that NGC 246 is one of the few PNNs that shows X-ray emission (Tarafdar & Apparao 1988). In fact, it has the strongest X-ray emission of known PNNs. NGC 246 has also been detected with ROSAT (Hoare et al. 1995). The X-ray flux is observed as supersoft X-rays, which is also the case for some He CVs. Therefore, this pulsating PNN may be a good candidate for evolution through interacting binary stages.

Koester & Werner (1998) derived a surface temperature T∼150 000 K and log g=5.7 (cgs) for the central star, with abundances He: 64, C: 30, O: 6, N: none per cent and, using evolutionary tracks of Blöcker (1995), a luminosity of $\log(L/L_{\odot})$=4.2 and a mass of 0.84 $M_{\odot}$. This effective temperature is consistent with the production of Ne V ion by photoionization (Werner & Rauch 1994). Observations with IUE high-dispersion spec-

tra indicates the presence of a fast wind ($v_{terminal} = 4120 \pm 200$ km s^{-1}) in the nebula (Feibelman 1995). Koesterke & Werner (1998) determined a mass-loss rate of the central star of $10^{-6.9}$ $M_{\odot}$ yr^{-1}. Szentgyorgyi et al. (2003) have imaged the planetary nebula envelope (PNe) in the near-ultraviolet and observed a clumpy structure, with a number of bright knots. Most of these features are interpreted as due to instabilities and interactions of the expanding nebula. They also observed the emission from a small, two lobed, figure-eight region in the inner parts of the nebula (see FIgure 32). Muthu (2001) presented a morphological study of three asymmetrical PNes including NGC 246. The author attributes the distorted morphology to the PNe interaction with Interstellar Medium. However, Soker (1997) made a classification of PNNs based in a study of the morphological properties of their nebulae, and classified NGC 246 as result of a common envelope with a substellar companion, like a planet or a brown dwarf. The author finds that 56% of the planetary nebulae classified by him are in this class.

We present in this chapter a photometric analysis of data for NGC 246 from 4 different single site campaigns: IAC80 in September 2001, Mt Dushak-Erekdag (Turkmenistan) in November 2001, and IAC80 in November 2002 and August 2003 , and a reanalysis of the data obtained at NOT (Nordic Optical Telescope) in July 2000. This reanalysis includes a study of the stability of the temporal spectra during the run using wavelet techniques. We present a study over the NGC 246 temporal spectral changes during these years covering 71.75 hours of photometric data. The chapter is organized as follows: section 2 describes the observations and reduction techniques, including a description of the wavelet analysis; section 3 presents the results of the different campaigns; finally we discuss the results and present the conclusions in sections 4 and 5.

3.2. Observations and reductions.

The observations describe in this paper result from single-site rapid photometry campaigns done on four consecutive seasons in 2000, 2001, 2002, 2003. Different telescopes and instruments were used for the observations. The first campaign, which data is reanalysed here, was done at the 2.56 Nordic Optical Telescope (NOT) in July 2000. Further data were obtained using the 0.8 m Ritchen-Chretien telescope of Odessa Astronomical Observatory at the Mt Dushak-Erekdag (Turkmenistan, Central Asia) in October-November 2001, and the 0.84 m IAC80 telescope (Teide Observatory, Tenerife, Spain) during 3 campaigns: September 2001, November 2002 and August 2003. CCD photometers were used as de-

Table 7. Telescopes and instruments. The instruments are: TCP (Tromsø CCD Photometer) and ALFOSC, which are CCD photometers; TTP (3 channels PMT Tromø Texas Photometer) and Two-Star (2 channels PMT photometer.

Telescope	Size (m)	Longitude	Latitude	Altitude (m)	Instrument
NOT	2.5	17 53.1 W	28 45.3	2382	ALFOSC
Mt Dushak	0.8	37 55.5	57 53.1	2020	Two-Star
IAC80	0.84	16 30.5 W	28 18.0	2400	TTP, TCP

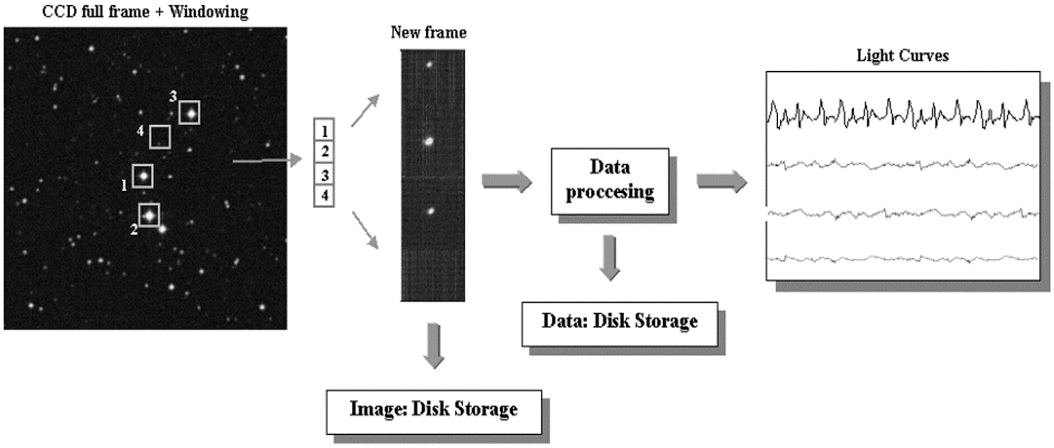

Fig. 33. TCP multi-windowing technnique.

tectors at NOT and during the 2002 and 2003 campaigns at IAC80; a 2-channel photomultiplier photometer was used at Mt Dushad-Erekdag and a 3-channel photomultiplier photometer during the 2001 campaign at IAC80. Table 7 describes the main characteristics of the telescopes used in the campaigns.

The observations at NOT were done with the Andalucia Faint Object Spectrograph and Camera (ALFOSC), equipped with a Loral, Lesser thinned, 2048 x 2048 CCD chip, and modified with our own control software to be able to observe in high-speed multi-windowing mode. The sky area available for locating a reference star is limited to the area of the chip: 3.7 x 3.7 arcmin^2. This small field is not a problem in NGC 246 because of the proximity of bright reference stars in the field. All observations were made with a standard Bessell B-band filter (NOT #74, Bessell 1990).

A similar technique were used at IAC80 during the 2002 and 2003 campaigns. which used the Tromsø CCD photometer (TCP). This portable CCD photometer was built as part of the R. Østensen Ph.D. project (Østensen 2000) as a collaboration between the Department of Physics at the University of Tromsø and the Astronomical Observatory at

Table 8. Specifications for the thinned TK1024 CCD chip.

Property	**value**	**unit**
Format	1024x1024	pixels
Pixel size	24x24	μm
Imaging area	24.6x24.6	mm
Area IAC80	14x14	arcmin
Dark current (MPP)	0.1	nA/cm^2 (20^oC)
Dark current (non-MPP)	0.5	nA/cm^2 (20^oC)
Readout noise	7	e^-
Full well (MPP)	100.000	e^-
Full well (non-MPP)	300.000	e^-

Copenhagen University. It also uses the multi-windowing technique to reduce the overhead introduced when sampling the pixel array on the CCD chip and improves considerably the time resolution and efficiency relative to traditional systems (Østensen & Solheim 2000). Figure 33 presents the multi-windowing technique. The TCP is equipped with the thinned SiTe TK1024 CCD chip. The main characteristics of this chip are specified in table 8. The TCP contains its own filter unit where 5 filters are installed, including a standard Bessell B-band filter which was the one used in the observations.

A two channels PMT based photometer called Two-Star was used during the campaign at Mt Dushak-Erekdag. The Two-Star channels are equipped with FEU-136 (s-20 (Cs)Na2K Sb) photomultipliers and standard B-band Bessell filters. The data from the 2001 campaign at IAC80 were obtained with the Tromsø Texas Photometer (TTP). TTP is a 3-channel photometer equipped with blue sensitive photomultipliers (Hamamatsu R647-04), and also using a standard B-band Bessell filters. The TTP fulfill the specifications and requirements as prescribed by Kleinman et al. (1996) as a WET (Whole Earth Telescope) photometer. Table 9 contains the information related to the time-series observations.

3.2.1. CCDs photometers observations and data reduction.

We describe in this section the observations with the CCD photometers. Both systems (ALFOSC at NOT and TCP at IAC80) use the same control software to be able to observe in high-speed multi-windowing mode. We observed the stars in windowed mode using two or three reference stars for constructing the relative light curves. Figure 35 shows the target and main reference stars selected. The cycle time was set to 20 s, except for

Table 9. NGC 246 time-series photometry. The observers are: Robert Kamben(RK), Nicolai I. Dorokov (NID), Tatyana N. Dorokova (TND), Jan-Erik Solheim (JES) and José M. González Pérez.

Label	Date	Telesc.	Instrum.	Observers	Start (UT)	Length (s)	Resolution (μHz)
A1	2000 Jul 21	NOT	ALFOSC	JMGP, RK	02:55:52	7448	130
A2	2000 Jul 24	NOT	ALFOSC	JMGP, RK	02:39:12	11868	84
B1	2001 Sep 18	IAC80	TTP	JMGP	00:12:30	15360	65
B2	2001 Sep 18	IAC80	TTP	JMGP	22:43:30	22960	44
C1	2001 Oct 21	Mt D-E	2-Star	NID, TND	19:49:23	6845	146
C2	2001 Oct 23	Mt D-E	2-Star	NID, TND	18:57:59	5856	170
C3	2001 Oct 25	Mt D-E	2-Star	NID, TND	19:42:59	4950	200
C4	2001 Nov 16	Mt D-E	2-Star	NID, TND	15:16:39	13400	75
D1	2002 Nov 8	IAC80	TCP	JES	19:55:02	22280	45
D2	2002 Nov 9	IAC80	TCP	JES	19:13:34	25460	39
E1	2003 Ag 24	IAC80	TCP	JMGP	00:25:30	19880	50
E2	2003 Ag 25	IAC80	TCP	JMGP	00:12:40	21160	47
E3	2003 Ag 26	IAC80	TCP	JMGP	00:28:40	20060	50
E4	2003 Ag 27	IAC80	TCP	JMGP	00:03:40	21740	46
E5	2003 Ag 28	IAC80	TCP	JMGP	00:17:40	17440	57
E6	2003 Ag 29	IAC80	TCP	JMGP	00:01:40	21580	46

the two runs from NOT where it was set to 30 s during the first run and 12 s during the second. For the 20 s cycles with the TCP, the actual exposure time was between 17.7 and 18.1 s, depending on the number of reference stars selected (2 or 3).

The data were reduced on-line using the Real Time Photometry (RTP) program (Østensen 2000). Some details about this software procedure are given in the section 2.3. The data processing includes bias level removal, flat fielding, sky subtraction, extinction correction and aperture photometry using optimal apertures that track each stars geometrical center. This procedure is called moving aperture photometry (MAP) and computes the center of the target and reference stars in each frame and recenters the aperture correspondingly. The light curves are constructed using differential photometry between the target and the best combination of the available reference stars.

The optimal aperture for each run was selected after processing all data sets with apertures of a wide range of radii and choosing the one that gave the best signal-to-noise ratio in the FT, using the amplitude of the primary peak for the signal and the mean

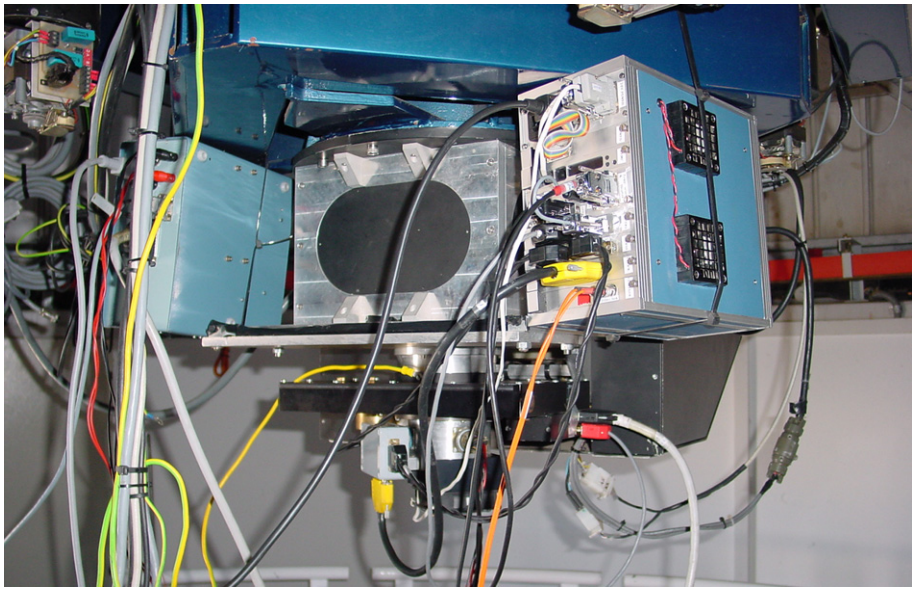

Fig. 34. The Tromsø CCD Photometer (TCP) mounted at the IAC80 telescope in Tenerife.

of amplitude spectrum outside the pulsation range for the noise. The apertures tested at NOT had radii between 10 and 40 pixels, which corresponds to 1.9 and 7.6 arcsec on the sky. The best results were obtained with 15 pixels (2.8 arcsec) for the first run and 35 pixels (6.6 arcsec) for the second. This big difference may be the result of the different atmospheric conditions. Figure 36 present an example of images obtained with an aperture radius of 35 pixels, which was the best for the second run. The composite image consist of 5 columns of individual images. Each column displays the 4 windows selected. NGC 246 is in the lowest window. The reference stars are in the middle windows and sky region in the upper one. The combination of 5 columns shows 5 images taken at times during the run and also shows how the MAP procedure is working, keeping permanently all the stars in the middle of their apertures. In the lowest aperture containing NGC 246 it is possible to see its K-dwarf companion which is located ∼4 arcsec away and, therefore, is included in the photometry since the aperture radius on sky is ∼7 arcsec. The best results obtained with the TCP on the IAC80 was in the range 7 to 10 pixels, which corresponds to 5 and 7 arcsec radii on the sky. Therefore, the NGC 246 companion was included in all the aperture photometry measurements.

3.2.2. PMTs data reduction.

Photomultiplier based photometers were used for the campaign at Mt Dushak (2-channel) and for the 2001 campaign at IAC80 (3-channel). The data have been reduced in the

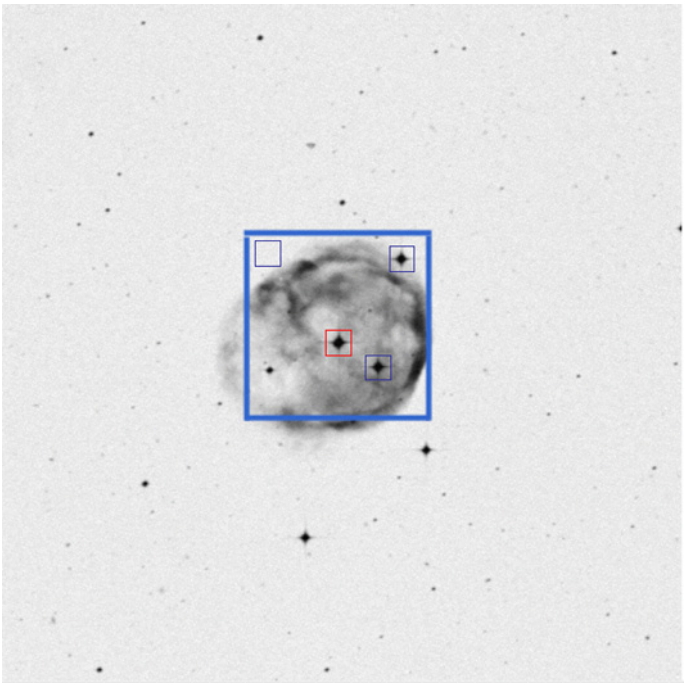

Fig. 35. NGC 246 field with readout windows selection. This image covers an area of ∼14 x 14 arcmin recorded on the TCP chip using IAC80. The large blue box indicates the area displayed by ALFOSC at NOT. The small red box indicates the window selected for NGC 246 , and the small blue boxes define the windows for the reference stars and sky region used.

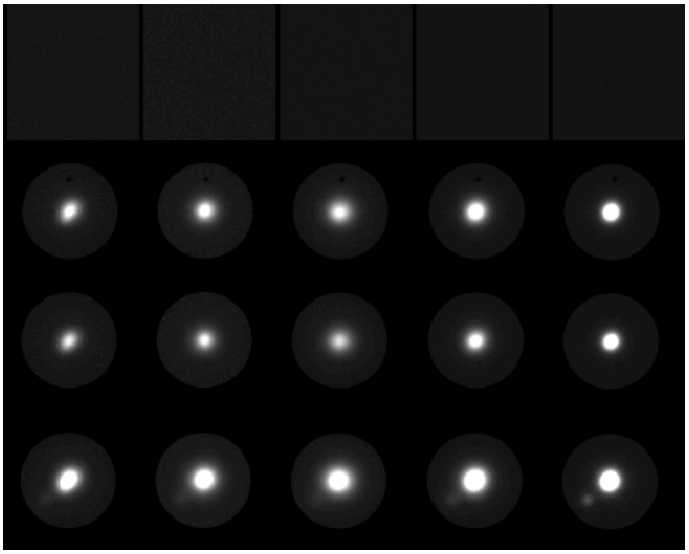

Fig. 36. NGC 246 field: windows selected. In this case it was selected 4 windows and aperture 35 pixels on the NOT: NGC 246 is the star which appear in the lowest window. The reference stars are in the second and the second and third windows in each column, and the sky in the upper window. The different columns show images taken at different times during the July 24th run and show how the MAP procedure keeps the stars in the middle of the apertures.

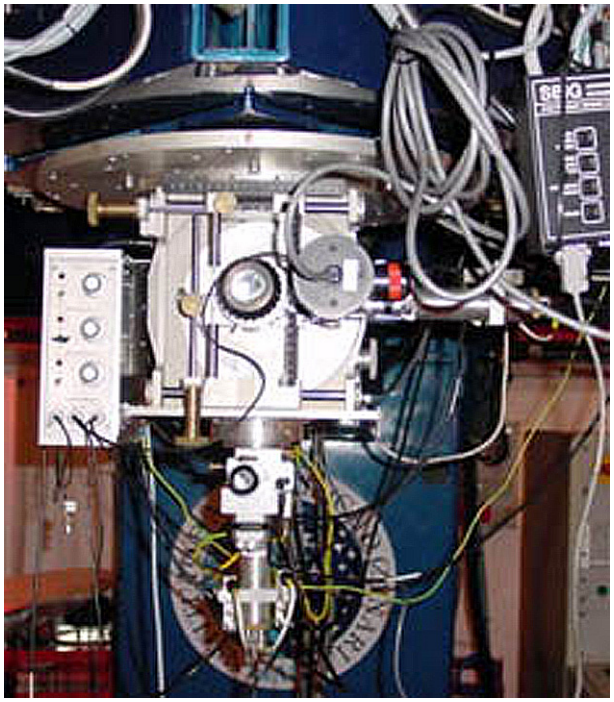

Fig. 37. The Tromsø Texas Photometer (TTP) mounted at IAC80 telescope in Tenerife.

standard way described by Nather et al. (1990) and Kepler (1993). Some small IDL extra routines were written to convert the original format obtained from the Two-Star photometer to a more standard format to proceed with these procedures. The diaphragm diameter were in both cases ∼30 arcsec. In both the 2- and 3-channel photometers, the sky background is measured at the beginning and at the end of each run in all channels. This is used to determine the sensitivity ratios of the channels. In 3-channel photometry (TTP), the sky background is monitored continuously in one channel, allowing for point by point subtraction of the sky background from the target and comparison star channels after application of the proper sensitivity ratios. For 2-channel data, the sky background is normally measured at irregular intervals in both channels. The sky background is then constructed by polynomial interpolation and subtracted. Each star channel is then corrected for extinction and normalized. When conditions show evidence for transparency variations, the normalised target star channel counts are divided by the smoothed comparison star channel counts. In the case of the 2-channel data from Mt Dushak, this division was extended to all the points in all the runs due to the persistent bad weather conditions. A few runs have been rejected where the noise level was too high, which was usually due to clouds or to instrumental problems. In the case of the TTP data, where the sampling time was set to 20 s and constant, the power spectrum of each time series is obtained by

a Fast Fourier Transform. Fo the Two-Star data, where the average sampling is 20 s but not constant (deviations of ∼1 s), a Deeming Fourier Transform was used.

3.2.3. Wavelet analysis.

In the previous chapter photometric results in a sample of 11 PNNs including NGC 246 has been reported. In general, the pulsators showed low amplitude modulations and a complex photometric behaviour which changed on short time scales. In particular, NGC 246 presented significant changes between two runs done 3 days apart, with the appearance of a clear peak at 685 μHz completely absent in the first run. The analysis of the NGC 246 second run indicated that all the power was concentrated in the second part of the run. It seems that the modulation was switched on in this second part. This behaviour is peculiar since the daily changes observed in previous observation of PNNs show variations in the amplitudes of certain peaks, but never the appearance of a peak completely absent the previous run. Other, even more extreme, rapid variations were reported for VV 47 and NGC 6852, where new peaks appeared in runs separated by less than 20 hours.

To go further in our analysis, we have searched for the possible lifetime of the modulation frequencies using the wavelet transform. Wavelet analysis is becoming a common tool for analyzing localized variations of power within a time series. By decomposing a time series into time-frequency space, one is able to determine both the dominant modes of variability and how those modes vary in time. An introduction to wavelet analysis is provided by Lau and Weng (1995), and an excellent practical guide to wavelet analysis including statistical significance testing is written by Torrence and Compo (1998).

The wavelet transform can be explained as an instantaneous Fourier transform and can be used to analyse time series that contain non-stationary power at many different frequencies. Assume that one has a time series, x_n, with equal time spacing. Also assume that one has a wavelet function $\Psi_0(\tau)$, that depend on a non-dimensional 'time' parameter τ. The wavelet function must have zero as mean and be localized in both time and frequency space. An example is the Morlet wavelet, consisting of a plane wave modulated by a Gaussian:

$$\Psi_0(\tau) = \Pi^{1/4} e^{i\omega_0\tau} e^{\tau^2/2}, \tag{9}$$

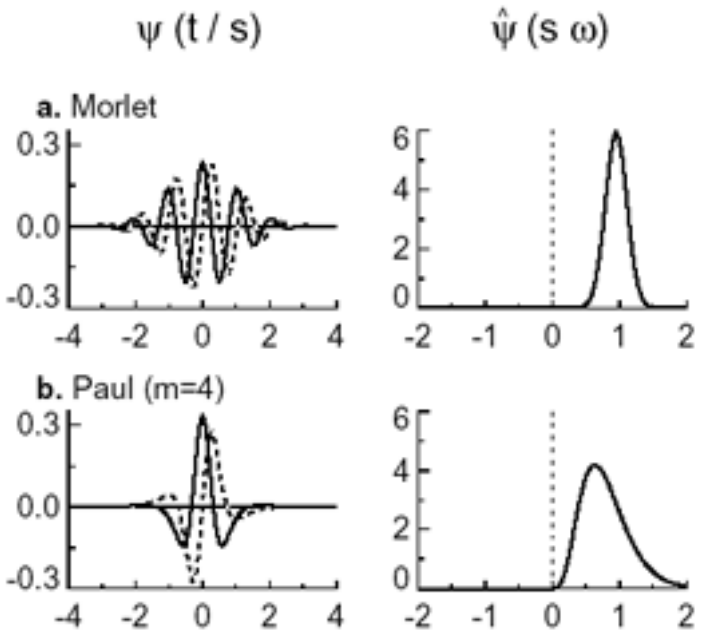

Fig. 38. Two different wavelet functions: (a) Morlet order 6 (ω_0=6) and (b) Paul. The plots on the left give the real part (solid) and imaginary part (dashed) for the wavelet in the time domain. The plot on the right give the corresponding wavelets in the frequency domain.

where ω_0 is the nondimensional frequency. Figure 38 shows the Morlet wavelet function, with ω_0 taken to be 6 to satisfy the admissibility condition, and the Paul function. These wavelets are the ones selected for the analysis of NGC 246 time series.

The wavelet analysis produces a 3 dimensional grid of data: the frequency and amplitude fields (as in the FT) and a time axis. The use of Morlet wavelet function gives better resolution in the frequencies but not as good in the time while the Paul wavelet function gives the opposite. This qualitative comparison between different wavelets is important since it is not possible to get good resolution both in time and frequency units with only one type wavelet. In any case, the frequency resolution obtained with wavelet analysis is not as good as with the FT. The regions of power are not as well confined. Figure 39 presents an example of wavelet analysis that will be used in this chapter. This example is from an NGC 246 time series analysis using Morlet wavelet and will be studied in detail in the results section (3.3). The upper part of the graph presents the light curve, the middle section the two dimensional wavelet analysis with time scale in seconds and the main modulations presented in periods (s). The lower part present the colour legend related with the size of the power. Despite the poor frequency resolution compared to the same analysis but done with the FT, this analysis introduces the possibility to obtain

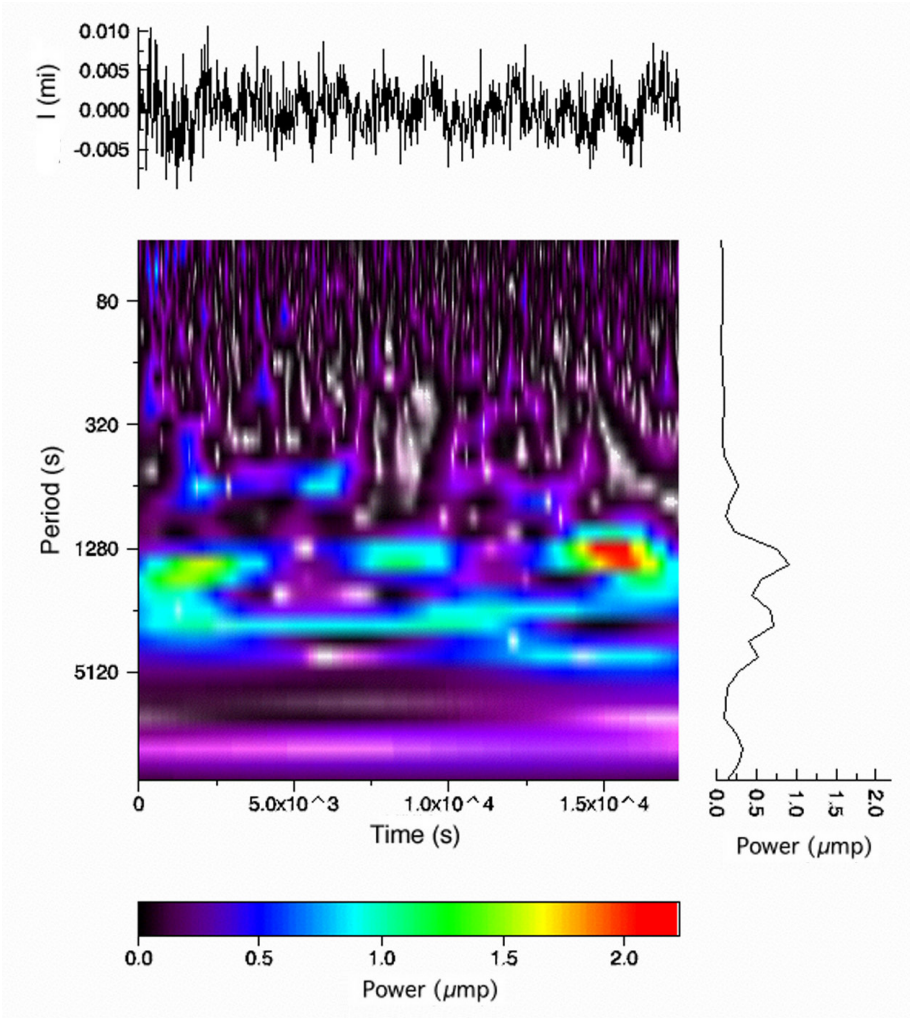

Fig. 39. Wavelet analysis example using Morlet.

extra information, like the possible changes in frequency of a certain modulation: in this case, the frequency band would move diagonally in a 2D representation like the one presented in figure 39; or if this frequency is confined to a specific time interval during the observations: the frequency band would not appear for the entire set. The FT does not give valid information in these cases since it is constructed assuming that no changes will occur in time. The routines used in this wavelet analysis also produce a graph showing the sum of all the contribution in the time domain, which is an approximation to the FT output (see the right section in figure 39). The selection of the parameters that define the wavelet analysis (type of wavelet and order), was chosen in order to obtain this last graph as close as possible to the FT output from the data set.

3.3. Results

3.3.1. Previous observations

Ciardullo and Bond (1996) reported NGC 246 to be a low amplitude pulsator with periods of 24 and 31 min and amplitudes ∼2 mmag. Power in the same regions has been reported from data taken with the Nordic Optical Telescope at La Palma in July 2001 showing rapid changes in amplitude: the FT of the first run showed power only in one region around 550 μHz (amplitude=1.9 mma; power=3.7 μmp) while the second run observed 2 days later showed power in the same region but with smaller amplitude (1.4 mma;1.8 μmp), and a new main peak at 685 μHz (2.4 mma; 5.6 μmp). The latest was completely absent in the first set. In addition, the analysis of NGC 246 second run indicated that all the power was concentrated in the second part of the run like if some modulation frequencies were switched on during this second part. Figure 21 presents the comparison of the temporal spectra of the two runs.

3.3.2. IAC80 2001 campaign.

Our first attempt to monitor NGC 246 was in September 2001, using IAC80 telescope with the TTP. We had scheduled 5 days to observe NGC 246 but, due to bad weather, we only could observe it two nights. Therefore, only two light curves were obtained during this campaign. The light curves and temporal spectra of the two runs are presented in figures 41 and 42.

Compared to the NOT results, the modulations during this campaign were stronger and less sinusoidal. At certain times it is possible to identify a double humped feature. This may indicate a complex FT with presence of harmonics. A double humped feature is a known characteristic of the light curves of certain CVs like the AM CVns (Warner 1995). Figure 43 shows a comparison between the light curve A2 from the 2000 campaign, and B1 from this campaign.

The temporal spectra are again highly variable from night to night showing in general more modulation frequencies. The temporal spectra from runs B1 and B2 show power at ∼550 μHz which was also found in the runs A (2000). B2 temporal spectrum shows power at ∼690 μHz which was the main peak in the A2 FT. Figure 44 presents a FTs comparison between the IAC80 runs and run A2 (NOT) in the range of frequencies where power is found in NOT data. Additional important peaks are now located at lower frequencies. The

Fig. 40. Teide observatory and IAC80.

highest peaks are located at ∼230 μHz (34 μmp) , 340 μHz (18 μmp) and 442 (30 μmp) μHz which correspond to periods ∼4300, 2940 and 2260 s. No power was found in this range in 2000 data. In general, the amplitudes of these peaks are huge comparing to amplitudes reported before. The average noise power in this run is ∼0.8 μmp. The following peaks have power ≥4 times over the noise (≥2 times over the noise in amplitude): 920 μHz (3.9 μmp), 1520 μHz (3.2 μmp), 1630 μHz (4.7 μmp), 1807 μHz (4.5 μmp). Power is also found at 550 μHz (1.5 μmp) which appears in previous observations.

The next run (B2) was started only 18 hours after the first one and variations are found in the temporal spectrum. Peaks are found again at the low frequencies zone but the power has decreased significantly. On the other hand, more peaks are identified in this range. One reason may be because the length of the run which increases the FT resolution. However, other differences between the temporal spectra may be associated to real changes in the source. The highest peak is found at 135 μHz (11μmp). However this peak is not considered because the period (7407 s) is very close to 1/3 the length of the run. The photometric variation related to this frequency may be due to transparency variations. The average power noise for this run is is ∼0.8 μmp. The power necessary for a false alarm probability FALSE=1/20 is 5.8 μmp (see equation 4 in chapter 2). Only two peaks satisfy the criteria: 235 μHz (5.9 μmp), same as in the previous run but with significantly lower amplitude, and 549 μHz (6.75 μmp). Some peaks have power ≥4 times over the noise: 270 μHz (4.9 μmp), 331 μHz (2.4 μmp), 450 μHz (3.2 μmp), 500 μHz (4

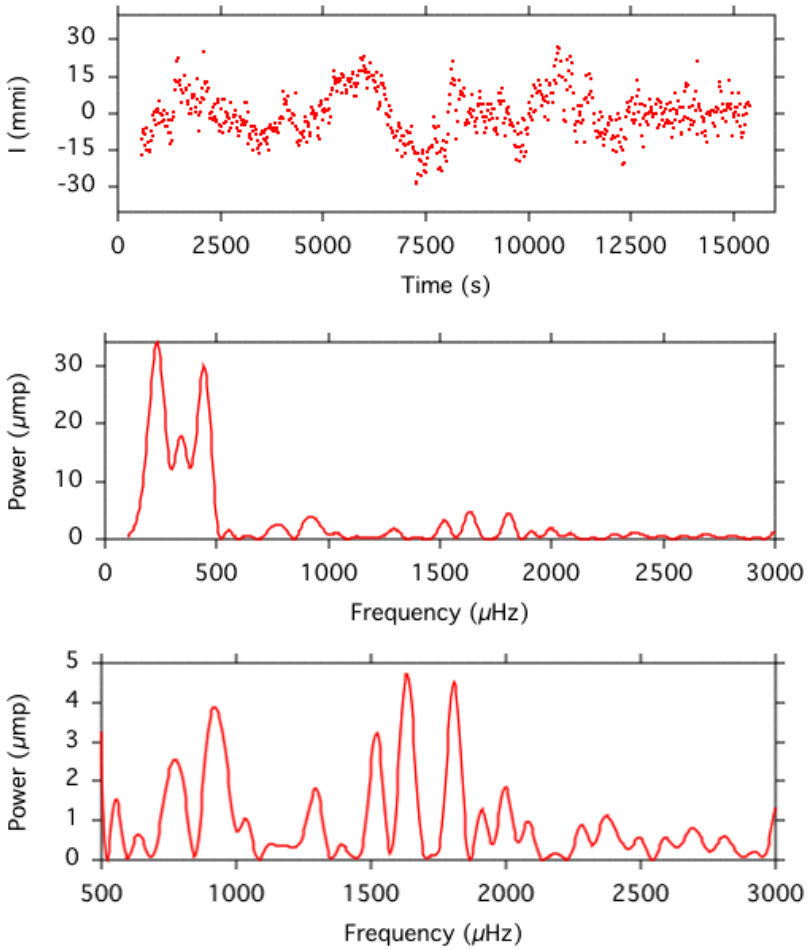

Fig. 41. NGC 246 light curve and temporal spectrum from run B1 (IAC80). The lower panel shows a more detailed FT above 500 μHz.

μmp), 691 μHz (3.6 μmp), Taking into account the resolution of the runs, power is found in both temporal spectra at 235, 331, 450, 500, 549 μHz. Some power is present in additional frequencies which also have power in the previous run: 901 μHz (2.2 μmp) and 1804 μHz (1.6 μmp). The values for the frequencies are selected from the second run because it has better resolution. In general, the peaks at lower frequencies (235, 331 and 450 μHz) have decreased dramatically in amplitude. The highest peak for this run is at 549 μHz (6.75 μmp) which has been observed before but with less power. Power in this region also appear in the previous run but with significantly less power (1.5 μmp). A peak found in the NOT data which is found here (B2) but not in the previous run (B1) is 691 μHz (3.6 μmp). In addition, an interesting harmonic structure is displayed in this temporal spectrum: the peaks at 450, 691and 903 μHz are related to the first, second, and third harmonics of the

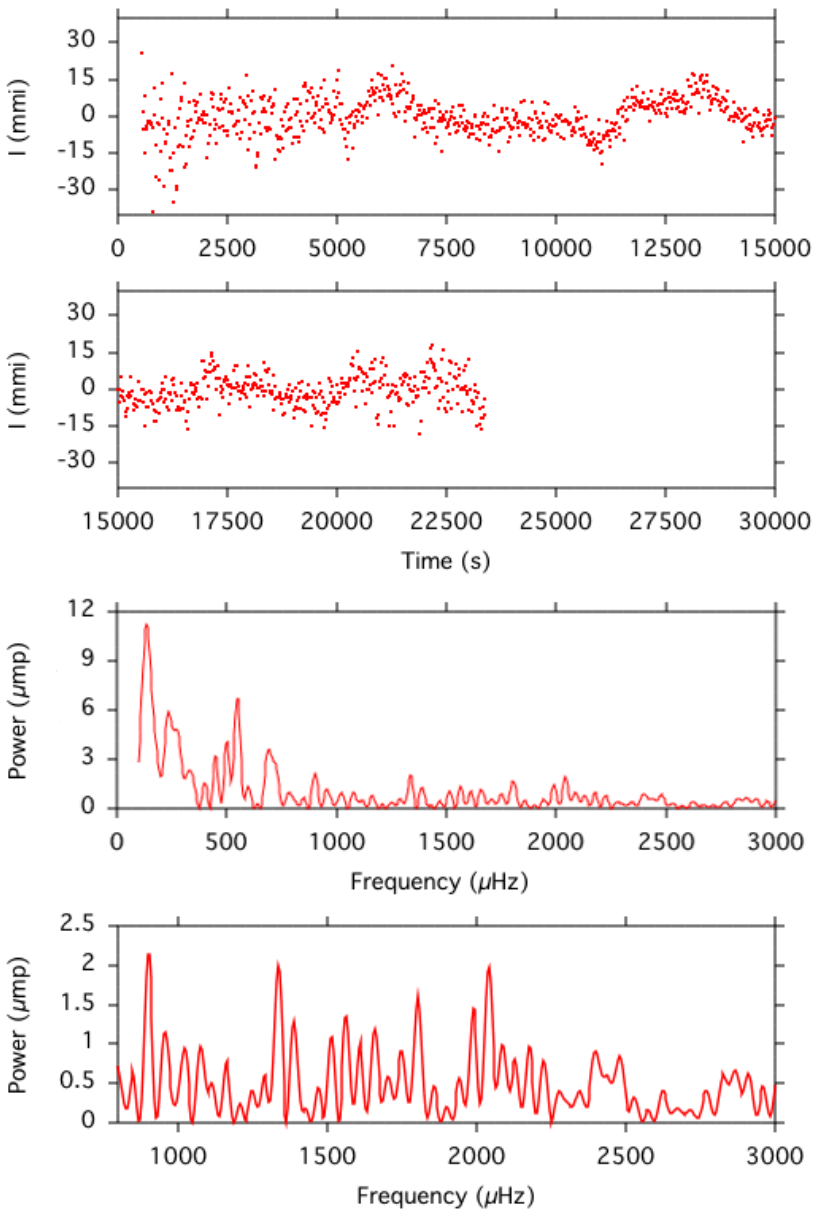

Fig. 42. NGC 246 light curve and temporal spectrum from run B2 (IAC80), 18 hours after the end of the previous run. The light curve is presented using two figures to keep the same scale used in the previous run and facilitate the comparison. In the first section of the light curve it is possible to notice a big scattering. This was due to transparency problems during the first part of the run because of bad weather conditions. For the FT, this first section was not considered. The FT is presented using two panels to show more clearly the power associated to frequencies over 800 μHz.

peak at 230 μHz. Figure 45 shows a comparison of the FT from these consecutive nights showing the dramatic change the power spectra.

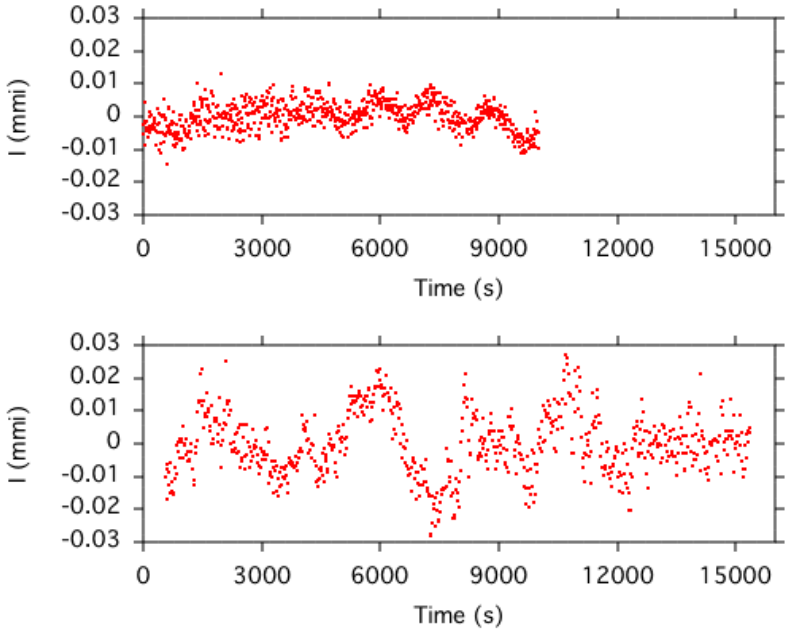

Fig. 43. NGC 246 light curves comparison. The upper part shows a light curve (A2) taken at NOT during 2000 campaign and the lower part a light curve (B1) from IAC80 2001 campaign.

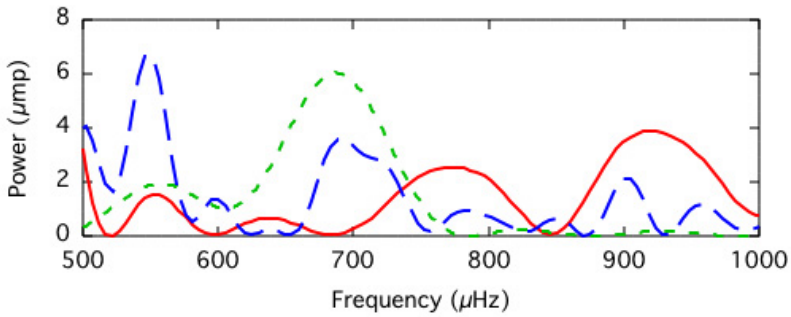

Fig. 44. NGC 246 temporal spectra comparison. The dashed blue line corresponds to the run B1 (IAC80), the dashed green line to the run B2 (IAC80) and the solid line to the run A2 (NOT).

We proceed to merge the two data sets to create a more detailed temporal spectrum and locate more precisely the pulsations frequencies. The resolution 1/T is increased to $\sim$10 μmHz. The idea was also to analyse if some of the changes in the temporal spectra of the single runs could be due to beating of close frequencies that may be resolved in the merged data. We merged the data using the standard procedure and software for WET (Whole Earth Telescope) which takes into account the barycentric correction. Figure 46 shows the temporal spectrum of the data merged. In this temporal spectrum a complex structure is found in the region between $\sim$ 200 and 270 μHz with several peaks over

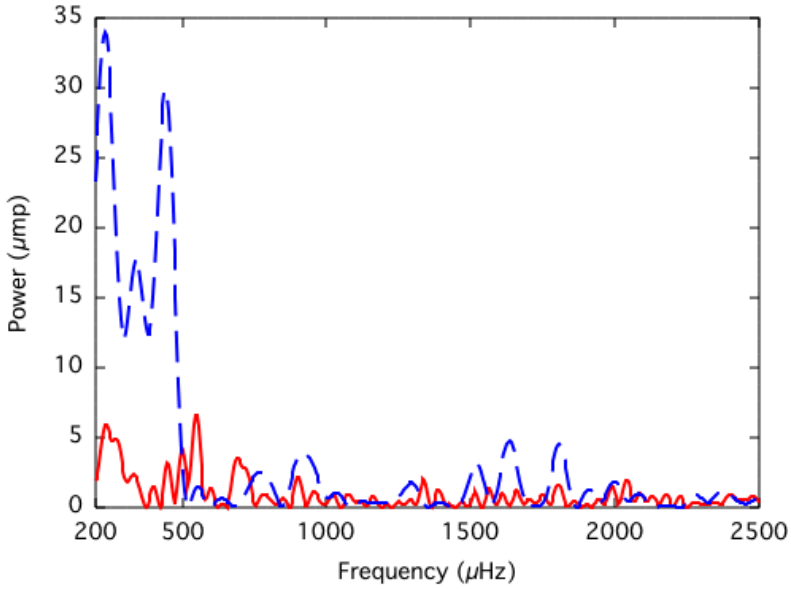

Fig. 45. NGC 246 temporal spectra comparison. The dashed line corresponds to the temporal spectrum obtained from run B1(IAC80), and the solid line to the temporal spectra taken 18 hours later (B2).

10 μmp. A expanded view of this range including the windows function is presented in figure 47. This indicates the presence of various modulation frequencies in this region. The highest peaks are located at 227 μHz (12.2 μmp) and 260 μHz (12.9 μmp). The FT of the merge data shows the highest power related to the peak at 260 μHz. However, peaks at $\sim$227 μHz have higher power in both single runs B1 and B2. This may be due to the aliasing which we see in the window function. Other important peak are located at: 331μHz (5.7 μmp). The power found for this peak is between the power found for the first (17.8 μmp) and second (2.5 μmp) runs. The same happens for the peaks that may be harmonics of 227 μHz: the first harmonic at 442 μHz (9.8 μmp), second at 688 μHz (1 μmp) and fourth harmonic at 903 μHz (1.6 μmp). We have assigned the following identification to this structure:

$f_1 = 227 \pm 10$ μHz ; $f_2 = 2 \times f_1 = 452 \pm 20$ μHz

$f_3 = 3 \times f_1 = 681 \pm 30$ μHz ; $f_4 = 4 \times f_1 = 908 \pm 40$ μHz

Some intrinsic changes may have happened to the object which have decreased the power in the peaks between $\sim$200 and 500μHz, including the peak at $\sim$442 μHz, the possible first harmonic

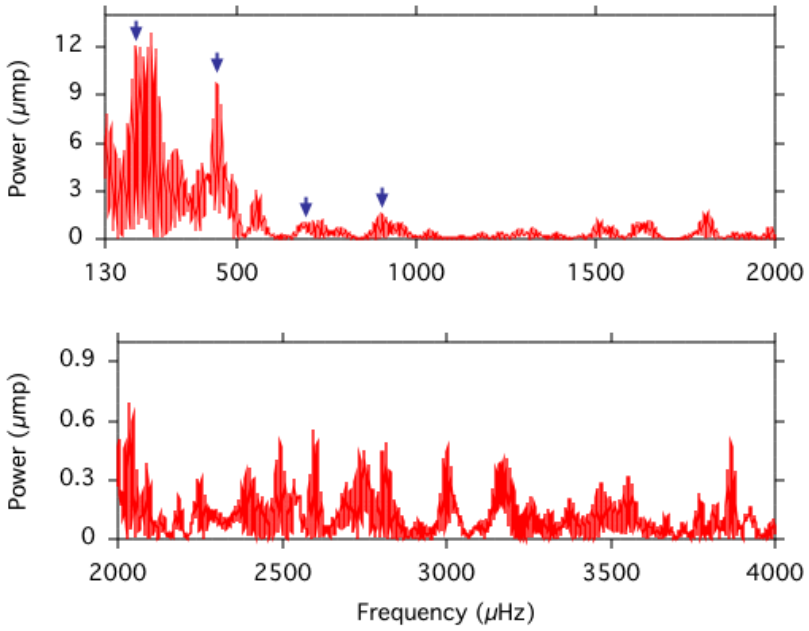

Fig. 46. NGC 246 temporal spectrum from merge data from the runs B1 and B2. The blue arrows indicate peaks at 227 μHz and possible harmonics.

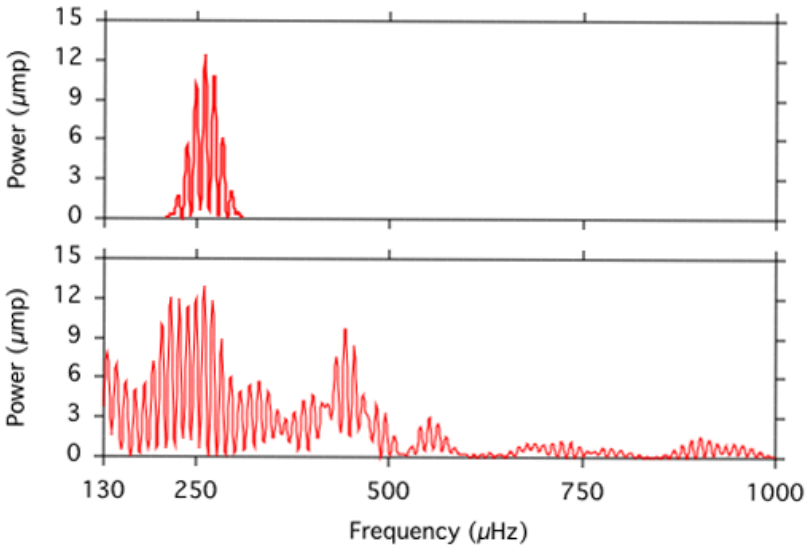

Fig. 47. NGC 246 temporal spectra of merge data from the runs B1 and B2. The upper panel present the window function, and the lower panel a expanded view of the FT around 230 μmHz.

of the peak at ∼227 μHz. The power related with the third harmonics in this structure has also decreased. However, the power related with the second has increased. The presence of a harmonic structure showing daily changes in their amplitudes has been observed before and

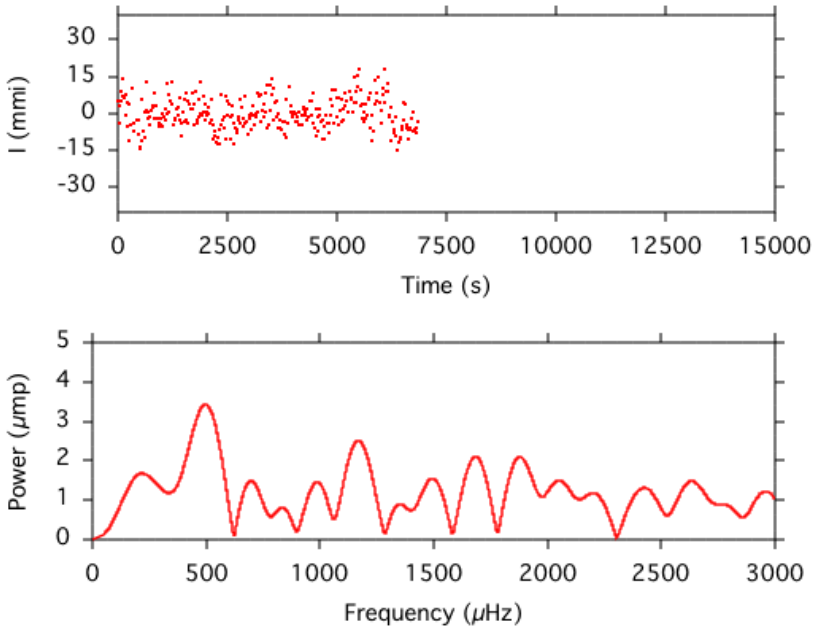

Fig. 48. NGC 246 light curve and temporal spectrum from run C1 (Mt Dushak).

is a characteristic property of He CVs with discs (see chapter 4). We have explained such behaviour for objects like AM CVn and HP Lib. This is attributed to changes in the structure of their accretion discs. Therefore, this structure may indicate a similar process going on around NGC 246.

3.3.3. Mt Dushak 2001 campaign

NGC 246 was observed in November 2001 from Mt Dushak-Erekdag in Turkmenistan using a 80 cm telescope and 2 channel photometer. The first idea was to observe together with IAC80 in September to obtain better coverage. However, different sort of problems made it impossible to start the campaign until later October. This was the first time this telescope was used after some time. Therefore, it was necessary to solve some technical problems in order to provide good data. This fact, together with bad luck with the weather, limited the amount of data that was obtained. The data are in general noisier than in Tenerife, and the length of the runs shorter. These circumstances limit the analysis that could be achieved with data from these runs (C1, C2, C3 and C4 in table 9). However, the light curves shapes are close to those obtained in Tenerife. Figures 48 to 51 present the light curves and temporal spectra obtained at Mt Dushak.

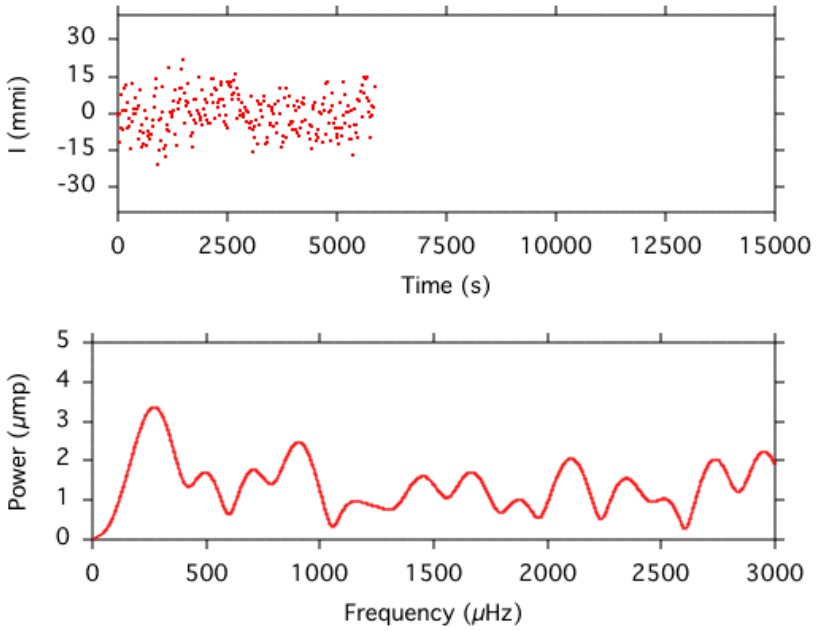

Fig. 49. NGC 246 light curve and temporal spectrum from run C2 (Mt Dushak).

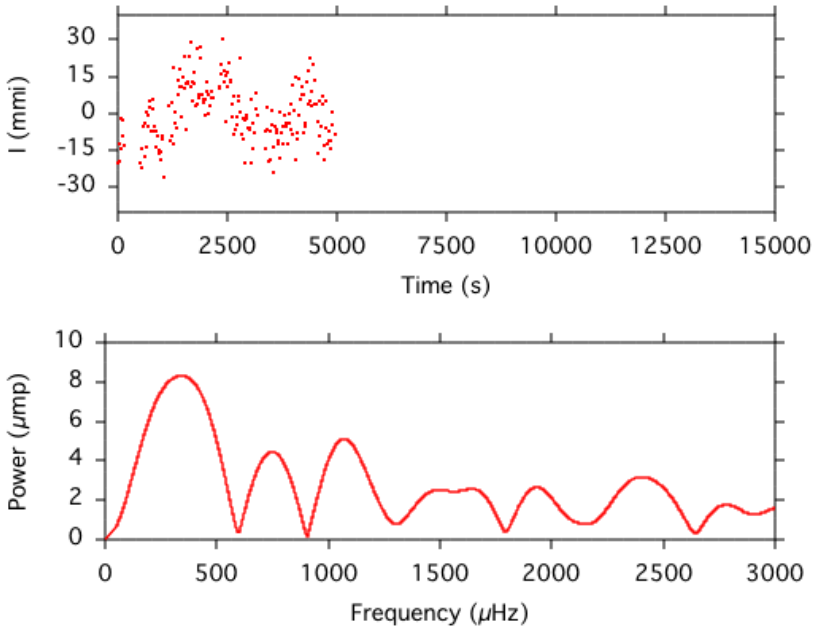

Fig. 50. NGC 246 light curve and temporal spectrum from run C3 (Mt Dushak).

Despite the poor resolution of some of the temporal spectra due to the short length of the runs, it is possible to identify again changes in the photometric variability from run to run. The first run (C1) presents lack of power in the regions ∼200 - 350 μHz, where the

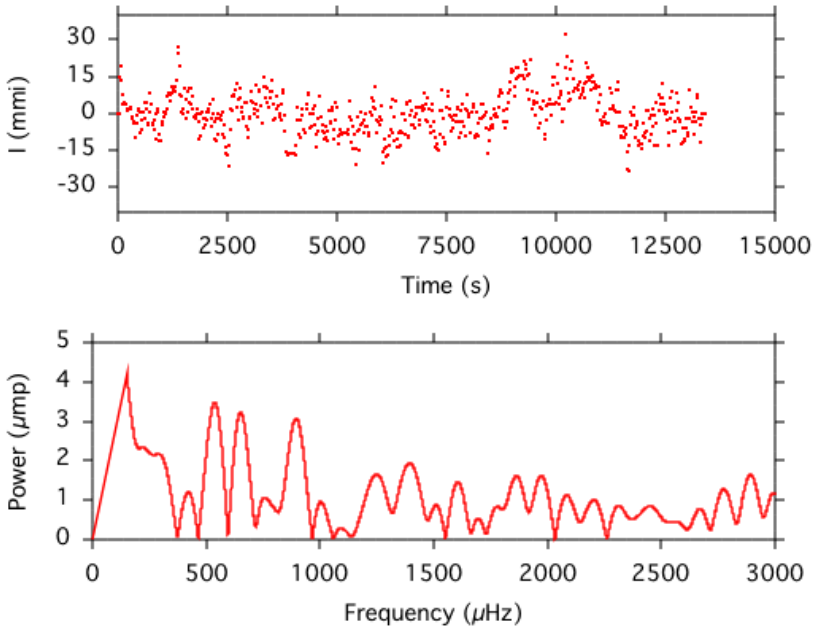

Fig. 51. NGC 246 light curve and temporal spectrum from run C4 (Mt Dushak).

most power was found in the runs B. However, a peak is identified at ∼500 μHz, which is a modulation frequency observed in several of the previous data set. This FT resemble more the temporal spectra obtained at NOT in 2000 (runs A). However, the modulations in the light curve grows in the second run (C2), obtained 2 nights later, and even more during the third run (C3). The light curve of this run starts to resemble runs B. A double humped feature is again present. It seems that NGC 246 was changing towards a configuration closer to the one observed in Tenerife and, therefore, quite different to its state in the 2000 and previous observations. The best run from this campaign (C4) was obtained around 3 weeks later, November 16th. It is again possible to recognize the double humped feature. The temporal spectrum is quite similar to the one obtained from run B2. The average noise power is high (∼1 μmp). The higher peaks are in the same regions where important peaks are present in the C runs: ∼222μHz (2.2 μmp), ∼288μHz (2 μmp), ∼540μHz (3.5 μmp) and ∼900μHz (3 μmp). Therefore, power is found related to frequencies f_1, and f_4 but not with f_2 and f_3. Taking into account the resolution of the run (75 μHz), a peak is found close to f_3, at 650 μHz (3 μmp). Figure 52 compares the temporal spectra obtained from runs B2 and C4, and figure 53 compares the temporal spectra obtained from C runs (Mt Dushak).

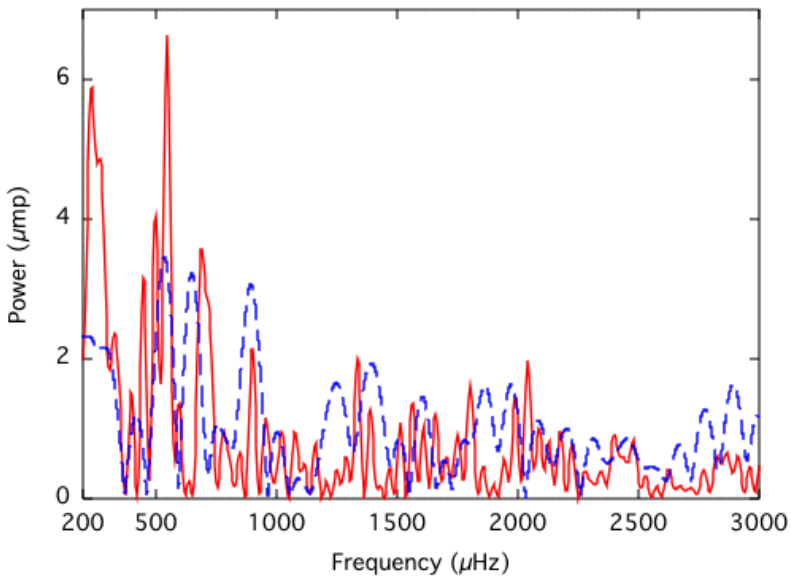

Fig. 52. NGC 246 comparison of temporal spectra. The dashed line corresponds to the temporal spectrum from run C4, and the solid line from the run B2.

The most interesting characteristic observed from the comparison of IAC80 and Mt Dushak temporal spectra is the variability of power in the intervals corresponding to the ∼230 μHz harmonic structure. In this case the power related with the possible fourth harmonic (∼900μHz) is higher (∼3μmp) than the power associated the main modulation frequency (∼2μmp). This variability between power of the main peak and its harmonics was indicated from the analysis of IAC80 September data and now seems to be confirmed. The presence of significant power in harmonics higher than in the main modulation frequency is a characteristic of the temporal spectra of AM CVn objects, and related to the structure of the accretion disk. The inclusion of such phenomena is a natural way to explain the complex temporal spectra observed for NGC 246.

3.3.4. IAC80 2002 campaign.

The next campaign in our program for monitoring NGC 246 photometric behaviour was done again using IAC80 telescope in November 2002. This time the instrument used was the TCP. This allow us to obtain better quality data. Two long light curves were obtained: we observed NGC 246 for 22280 s (6.2 hours) the 8th November and for 25460 s (7.07 hours) the next night. The light curves and temporal spectra of the two runs are presented in figures 54 and 55.

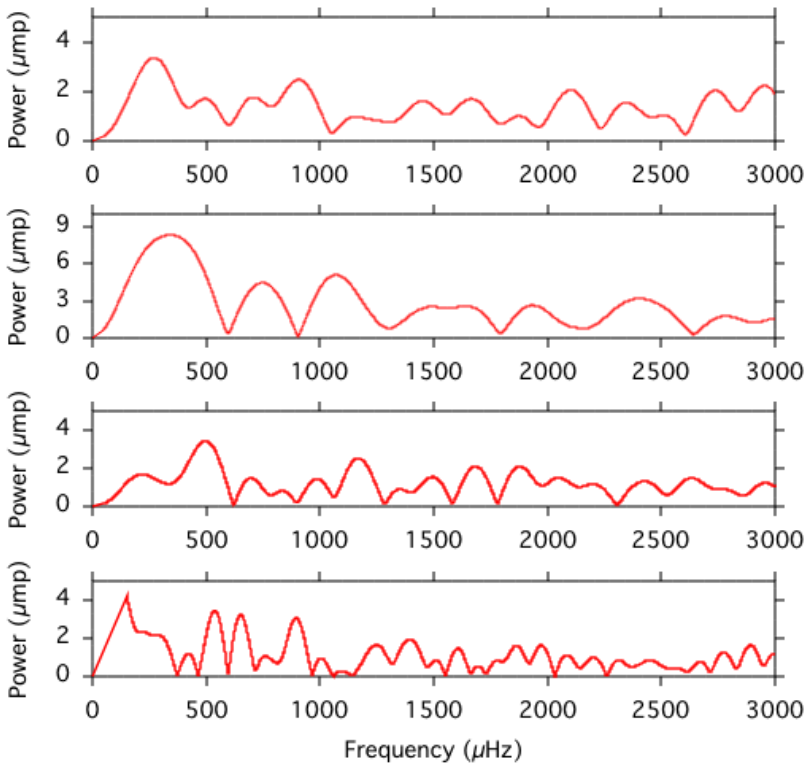

Fig. 53. NGC 246 comparison of temporal spectra from data acquired at Mt Dushak. The graphs correspond (from up to down) to the temporal spectrum obtained from C1, C2, C3 and C4 runs. Notice that the scale for the second graph is different than for the rest.

The quality of the data obtained during this camping using the CCD photometer (TCP) improves the quality taken at the same telescope the year before using the photomultiplier photometer TTP. In addition, the length of the runs are longer. Both circumstances have improved the quality of the temporal spectra. The average noise for these runs is lower ($\sim$0.05 μmp in run C1 and $\sim$0.07 μmp in run C2), which in principle allow us to search for pulsations with lower amplitudes. The power necessary to satisfy a false alarm probability $FALSE = 1/20$ is 0.50 μmp for run C1 and 0.51 μmp for run C2 (see equation 4 in chapter 2). However, during this campaign, the photometric variability in the light curves is quite small. It seems like the object were found in a state similar to the NOT (2000) campaign. Only one high peak is found for the first run and, comparing with previous campaigns, with low power: 574 μHz (1.6 μmp). Power in this region has not been reported before. A close peak at 550μHz appear in some previous runs including A1, A2, B1 and B2. In addition, small peaks is located at 503 μHz (0.3 μmp) and in the range related with f_1

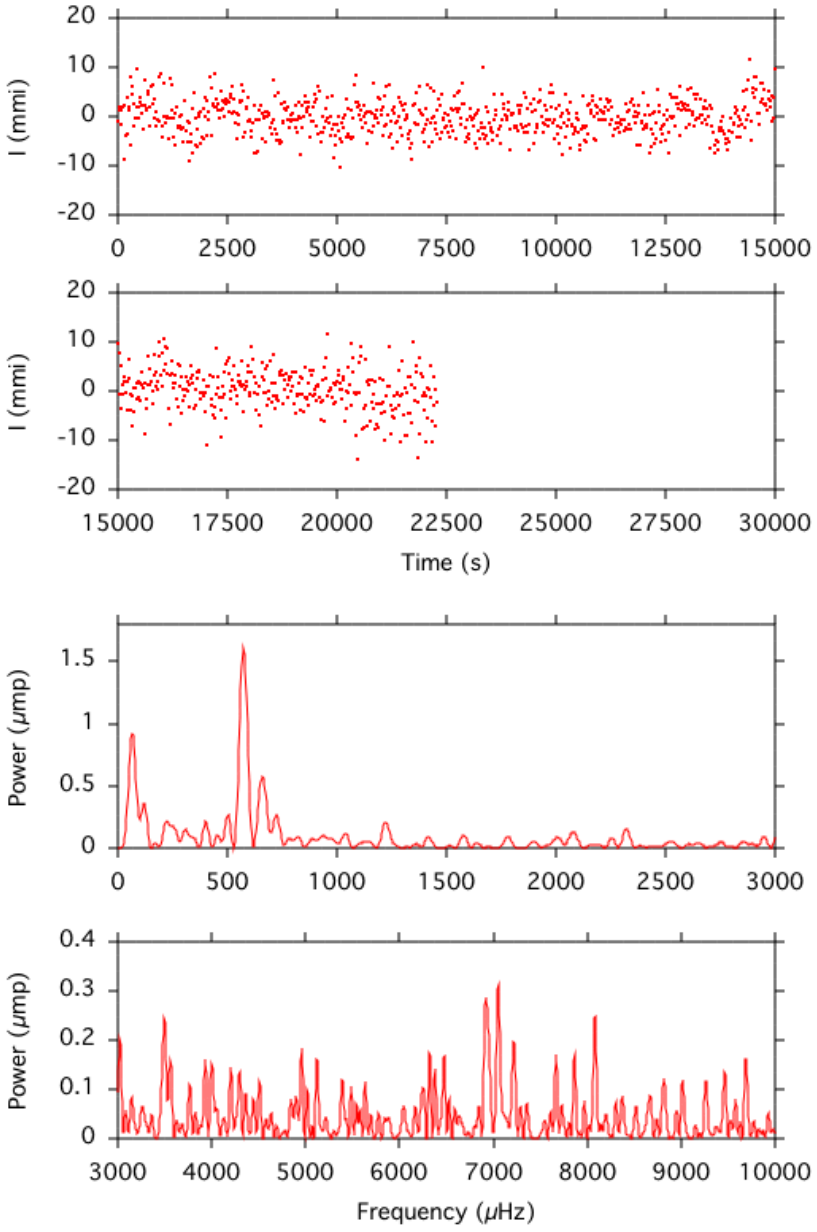

Fig. 54. NGC 246 light curve and temporal spectrum from run C1 (IAC80).

(223 μHz 0.2 μmp). The power is quite low but power in these intervals were found in previous runs. Power is also located at 660 μHz (0.57 μmp) and 724 μHz (0.26 μmp).

The good quality of the data make possible the search for pairs of low amplitude peaks with ratio close to $\mathcal{R}$=0.87. The relation of some real pulsation frequencies with this number has been reported for others PNNs. These are related with g-modes pulsation frequencies. See section 2.3, for a more detailed description of this number. This relation was found for some frequencies in the temporal spectra of VV 47. The better quality

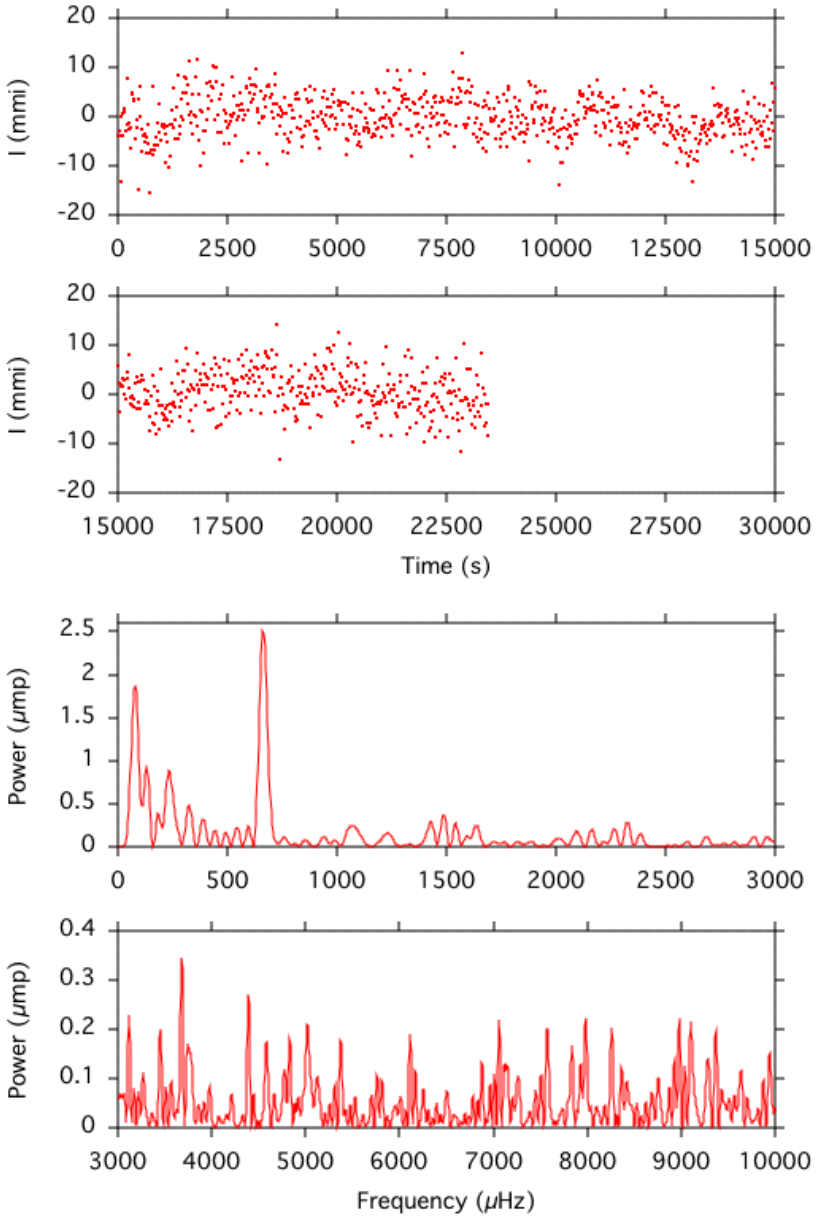

Fig. 55. NGC 246 light curve and temporal spectrum from run C2 (IAC80).

of the temporal spectra from runs C, compared with the previous cases, facilitate the search for pulsations at higher frequencies and, in general, with lower power.The ratio between the two highest peaks of this run is very close to $\mathcal{R}$: 574/660=0.87. Also the ratio 503/575=0.87. This indicates that these three pulsation frequencies may be due to g-modes.

The peaks found in the temporal spectrum of the run C1 above 1000 μHz, and with power at least four times the average noise (0.05 μmp) are the following: 1223 μHz

(0.2 μmp), 3020 μHz (0.2 μmp), 3495 μHz (0.2 μmp), 6920 μHz (0.3 μmp), 7050 μHz (0.3 μmp), 8080 μHz (0.3 μmp). From these, the ratios 3020/3495 and 7050/8080 are very close to $\mathcal{R}$. The last pair is related with periods shorter than 200 s and, therefore, these pulsations frequencies may be $g-modes$ triggered by the ϵ-mechanism.

The second run was obtained the next night. Like in the previous campaigns, important changes were found in the temporal spectrum from consecutive nights. In general, the photometric behaviour remains in the same 'state' with few peaks and these with low power. However, the main peak is now located at 664 μHz (2.5 μmp). This peak was observed in the previous run but with lower power (0.6 μmp). Power is not found in the range related with the highest peak of the previous dataset (574 μHz). Peaks with power over a false alarm probability (FAP) 1/20 are: 234 μHz (0.9 μmp), and 325 μHz (0.5 μmp). Therefore, power related to the frequency of the main peak in B and C4 runs, $f_1 \sim 230$ is also present in this run. Additional peaks with power at least four times over the average noise (0.07 μmp) are the following: 1429 μHz (0.3 μmp), 1487 μHz (0.4 μmp), 1636 μHz (0.3 μmp), 2326 μHz (0.3 μmp) and 3679 μHz (0.3 μmp). The ratio 1429/1487 is close to $\mathcal{R}$.

The difference between the temporal spectra of the two runs is very noticeable (see figure 56). The highest peak of the first run is completely absent in the second dataset and the highest peak of this last run is also present in the previous one but with considerably less power. Power in the region between $\sim$200 and 350 μHz has increased in the second run.

3.3.5. IAC80 2003 campaign.

The last campaign in our program of monitoring NGC 246 was done again at IAC80 using TCP the following year, in August 2003. The discovery of possible modulation frequencies at higher frequencies related with $g-modes$ motivated us to a more detailed exploration of the high frequency area of the temporal spectra. This campaign was the most successful. The weather conditions were good during the 6 nights of the campaign. Therefore, we obtained 6 individual light curves; the shortest one lasts 17440 s (4.84 hours) and the longest 21740 s (6 hours). Our strategy was to look for daily changes in the temporal spectra but also to try to analyse possible changes during the run for the longest ones. Figures from 57 to 62 present the light curves and temporal spectra of the different runs.

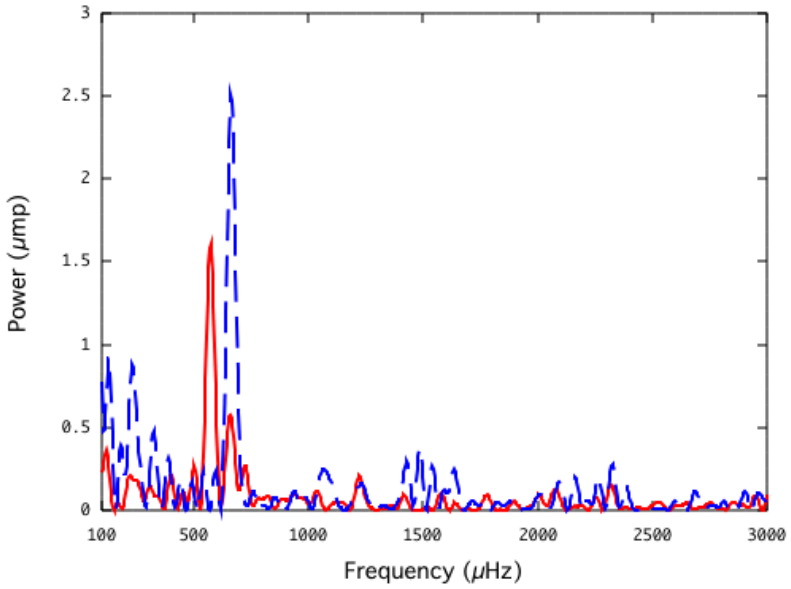

Fig. 56. NGC 246 temporal spectra comparison. The solid line corresponds to the temporal spectrum obtained from run C1 (IAC80), and the dashed line to the temporal spectrum taken the following night.

The quality of the runs is again good, so the noise in the FT is low in all the runs (below ∼0.1 μmp), allowing us to investigate pulsations with low power. The average noise and power necessary to satisfy a confidence criteria FAP=1/20 are the following: run E1, average power 0.07 μmp and FAP 0.7 μmp; E2: 0.03 μmp and 0.3 μmp; E3: 0.1 μmp and 0.8 μmp; E4: 0.05 μmp and 0.5 μmp; E5: 0.05 μmp and 0.5 μmp; E6: 0.04 μmp and 0.4 μmp.

We have searched for possible pulsations up to 10 000 μHz. In general, the modulation frequencies found are related with quite low power, and only few of them are over 1 μmp. It seems that we found the star again in a quiet state. This is more specially noticeable during the first run (E1). The highest peak in this run is located at 89 μHz (0.9 μmp), however, we do not consider it since its period (11169 s) is close to half the length of the run, so it may be related to small changes in the atmospheric transparency conditions. Besides this peak, the highest peak is below 0.4 μmp! All the modulations of the star seems to have been switched off during this night, or presenting extremely low power. From all the individual runs analyzed, E1 is the one where the highest peak has the lowest power. The pulsation frequencies having highest power are at 1602 μHz (0.3 μmp), 4189 μHz (0.3 μmp), 5770 μHz (0.3 μmp), 6670 μHz (0.4 μmp) and 7761μHz (0.3 μmp). These peaks do not satisfied the confidence criterium, but are above 4 times the average noise.

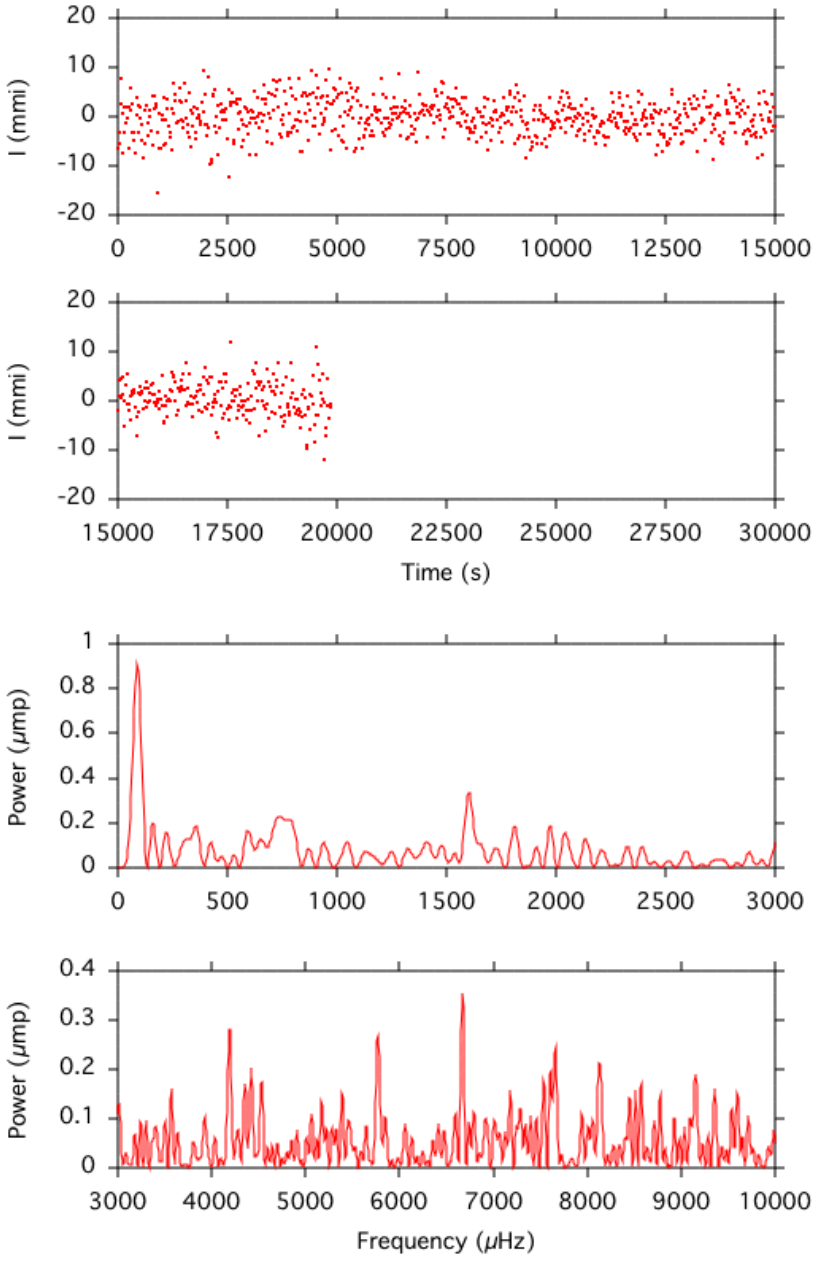

Fig. 57. NGC 246 light curve and temporal spectrum from run E1 (IAC80).

It is interesting to notice that the highest peak is found in the high frequency range, > 6000 μHz.

This quiet photometric behaviour is also extended to the next run (see fig 58). However, some power has appeared in regions below 1000 μHz. Like for the previous case, we will not consider the peak at 77 μHz (0.9 μmp) since its period is close to half the length of the run. The highest peak is now located at 356 μHz (0.77 μmp). Further peaks are found

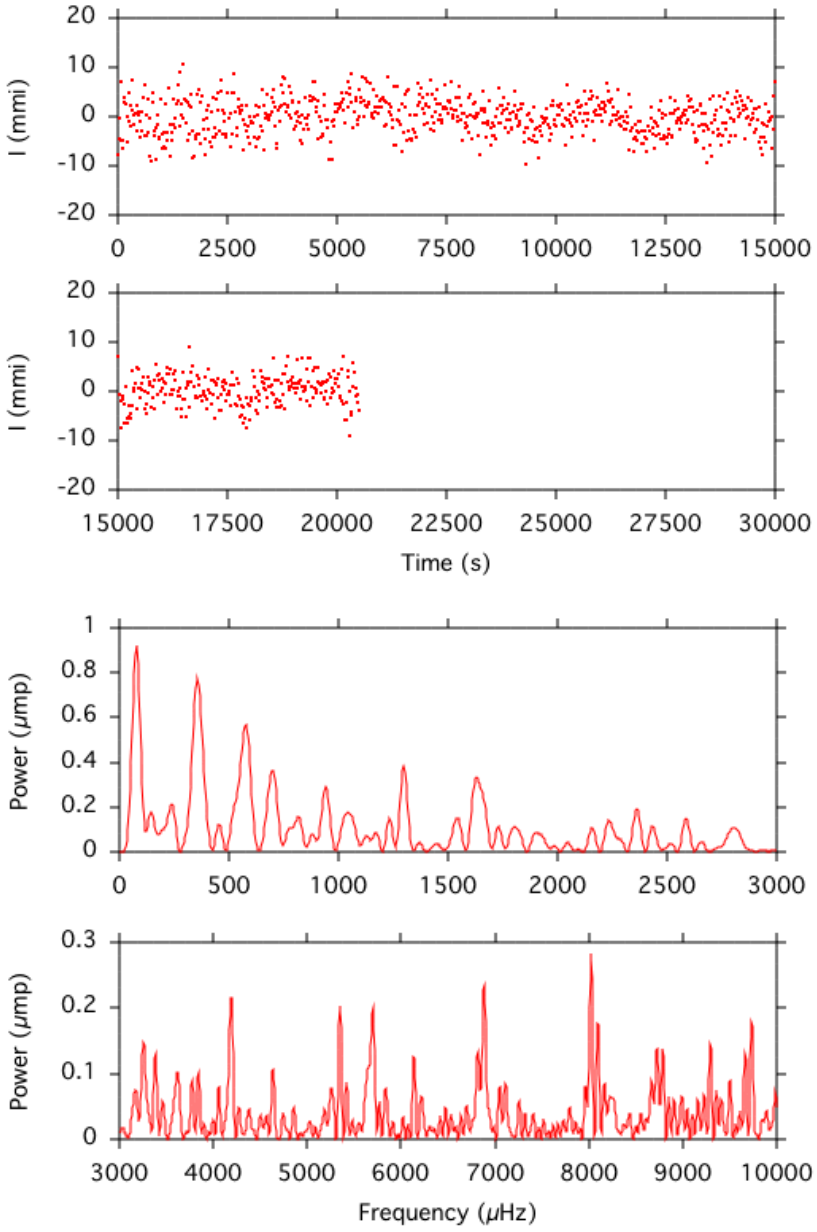

Fig. 58. NGC 246 light curve and temporal spectrum from run E2 (IAC80).

at: 576 μHz (0.6 μmp), 699 μHz (0.4 μmp), 941 μHz (0.3 μmp), 1298 μHz (0.4 μmp) and 1629 μHz (0.3 μmp). All these peaks satisfy the confidence criteria (FAP=1/20). Power was also observed close to the 576 μHz peak in run D1; close to 699 μHz peak in the runs A2 and B2, and close to 1629 μHz peak in the run D2. The highest peaks in the high frequency domain are located at 4190 μHz (0.2 μmp), 5350 μHz (0.2 μmp), 5700 μHz (0.2 μmp), 6884 μHz (0.25 μmp), 8023 μHz (0.3 μmp -highest peak in this domain) and

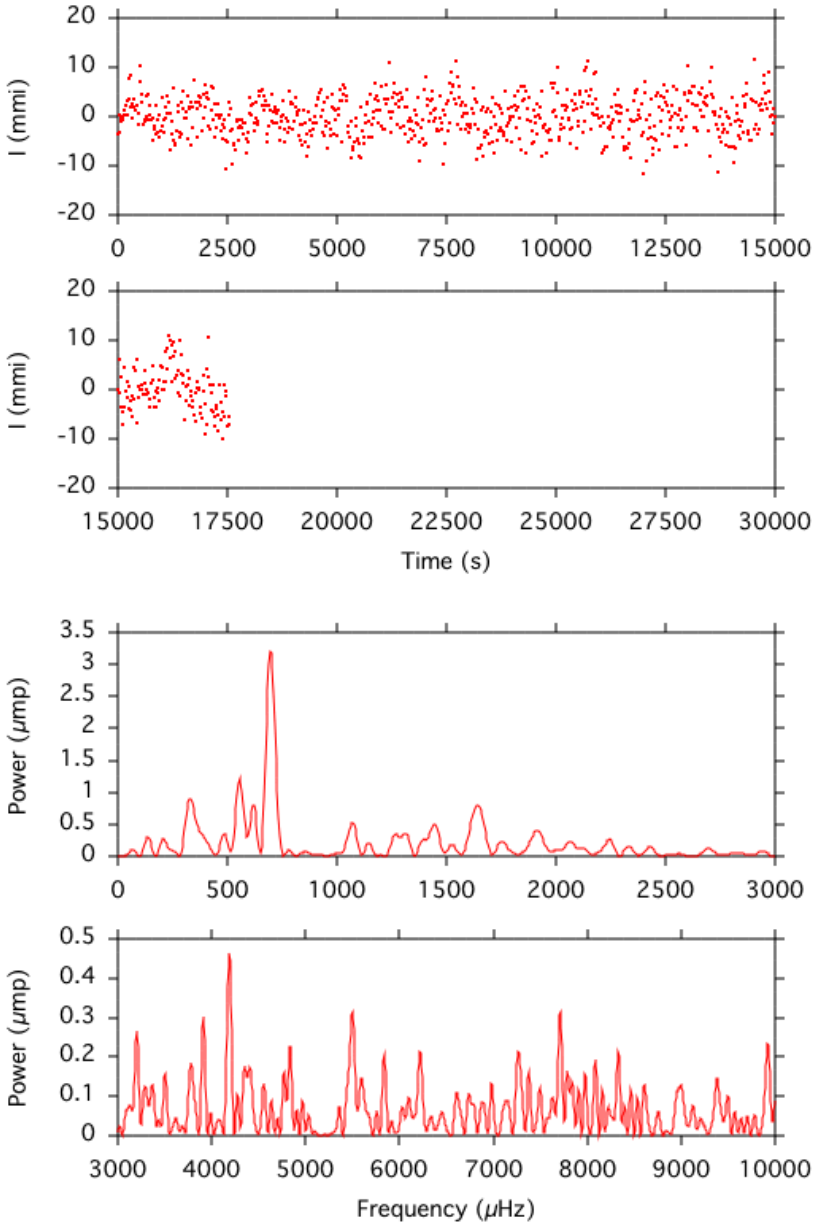

Fig. 59. NGC 246 light curve and temporal spectrum from run E3 (IAC80).

9732 μHz (0.2 μmp). All these peaks haver power above six times the average noise. The peak at 8023 μHz is in the limit of the confidence criteria.

The modulations in the E3 light curve has become more noticeable (see fig 59). From this run we find the peak with highest power in all datasets from the IAC80 2003 campaign. This is located at 697 μHz (3.2 μmp). Power close to this frequency (f_3) has been reported in some previous runs: A2, B2 and E1. Other peaks detected in the temporal spectrum of this dataset are: 330 μHz (0.9 μmp), 556 μHz (1.2 μmp) and 1642 μHz (0.8 μmp). All

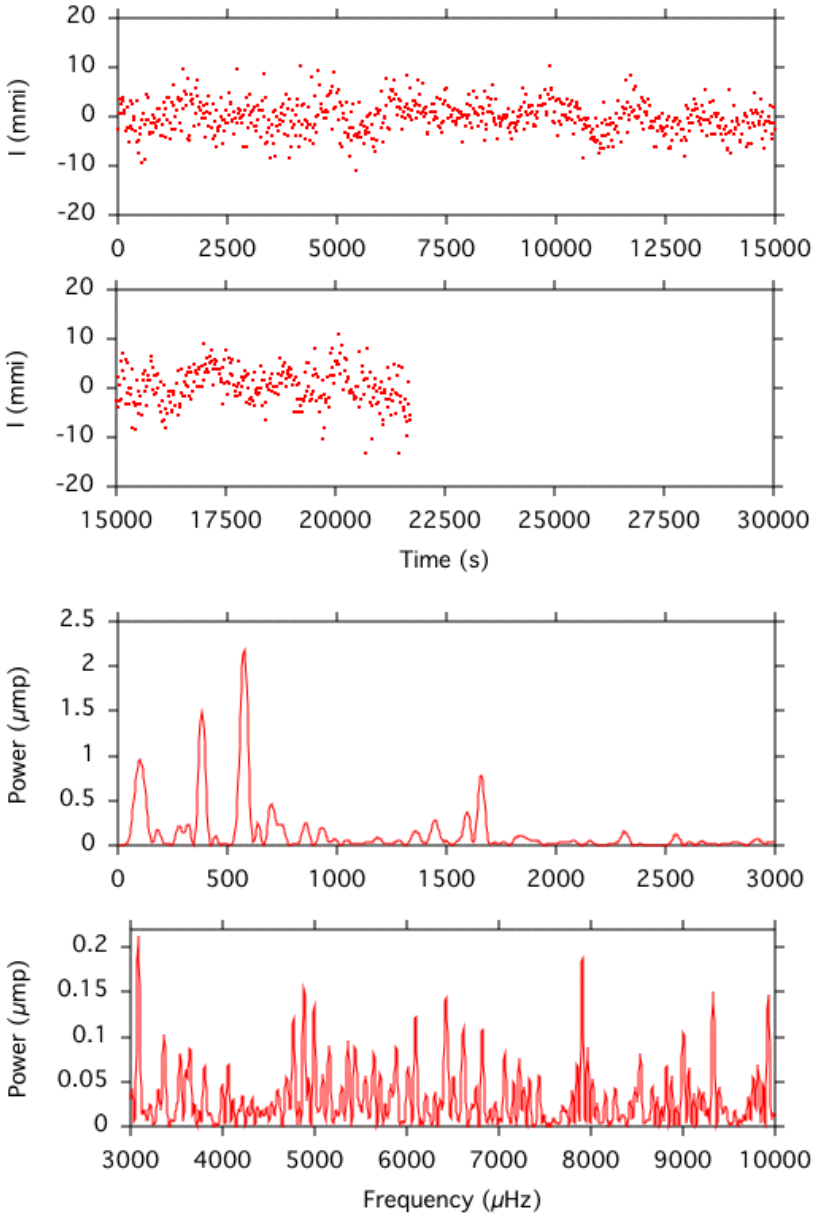

Fig. 60. NGC 246 light curve and temporal spectrum from run E4 (IAC80).

these peaks satisfy the confidence criterium (FAP=1/20). The high frequencies domain is noisier compared to previous runs. Only one peak has power above 4 times the average noise: 4190 μHz (0.5 μmp). This peak is also found in the run E2.

Significant changes are observed again in the temporal spectra of the next night, run E4, (see fig 60). The main peak is now located at 576 μHz (2.2 μmp). This peak was also observed during the runs D1 and E2 but not in the previous (E3). Some power is located again related with the highest peak the night before (697 μHz -3.2 μmp-), but with

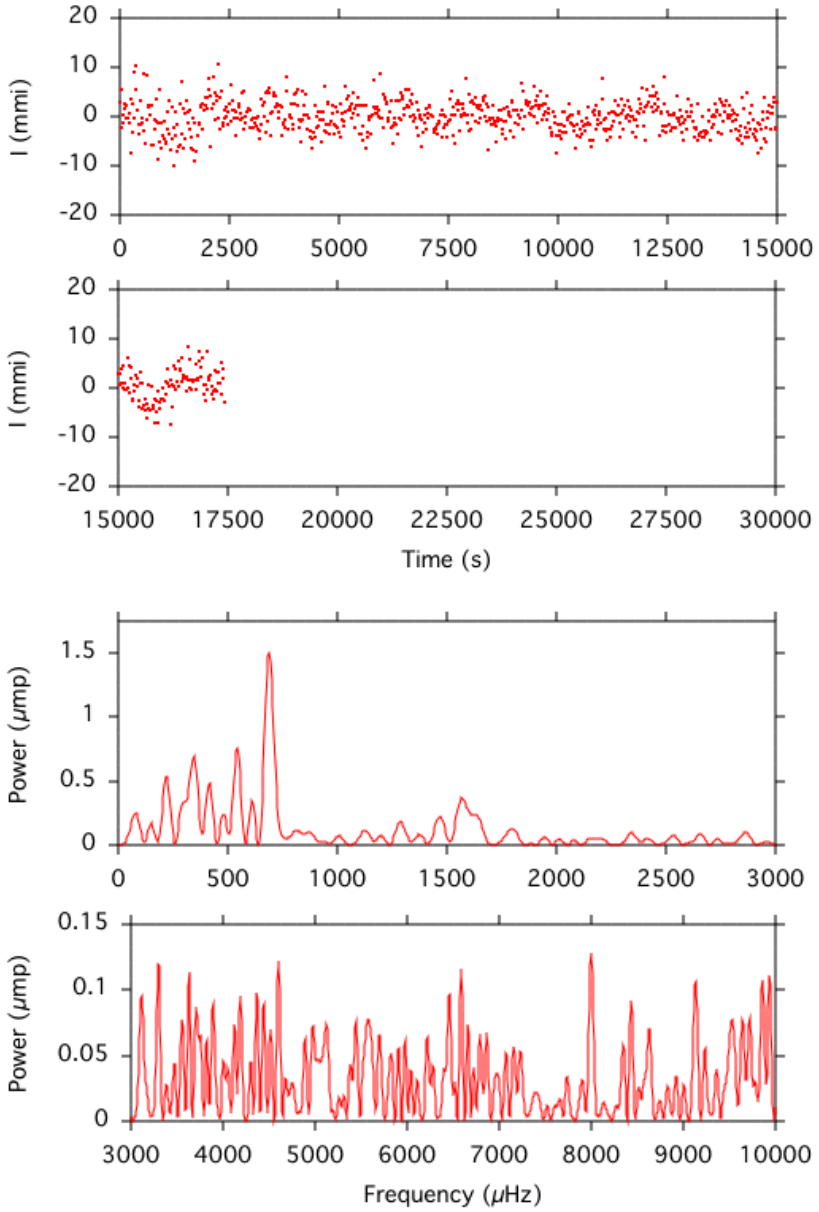

Fig. 61. NGC 246 light curve and temporal spectrum from run E5 (IAC80).

significantly less power (0.45 μmp). Other peaks are: 384 μHz (1.5 μmp) and 1658 μHz (0.8 μmp). These three peaks satisfy the confidence criterium. In addition some power is also found at 1595 μHz (0.4 μmp). This peak is also present in run E1. Only two peaks in the high frequencies domain has power $\sim$4 times the average noise: 3083 μHz (0.2 μmp) and 7907 μHz (0.2 μmp).

During the fifth run (E5), the modulations frequencies seems to have again decreased (see fig 61). The main peak is now located at 688 μHz (1.5 μmp) close to the region where

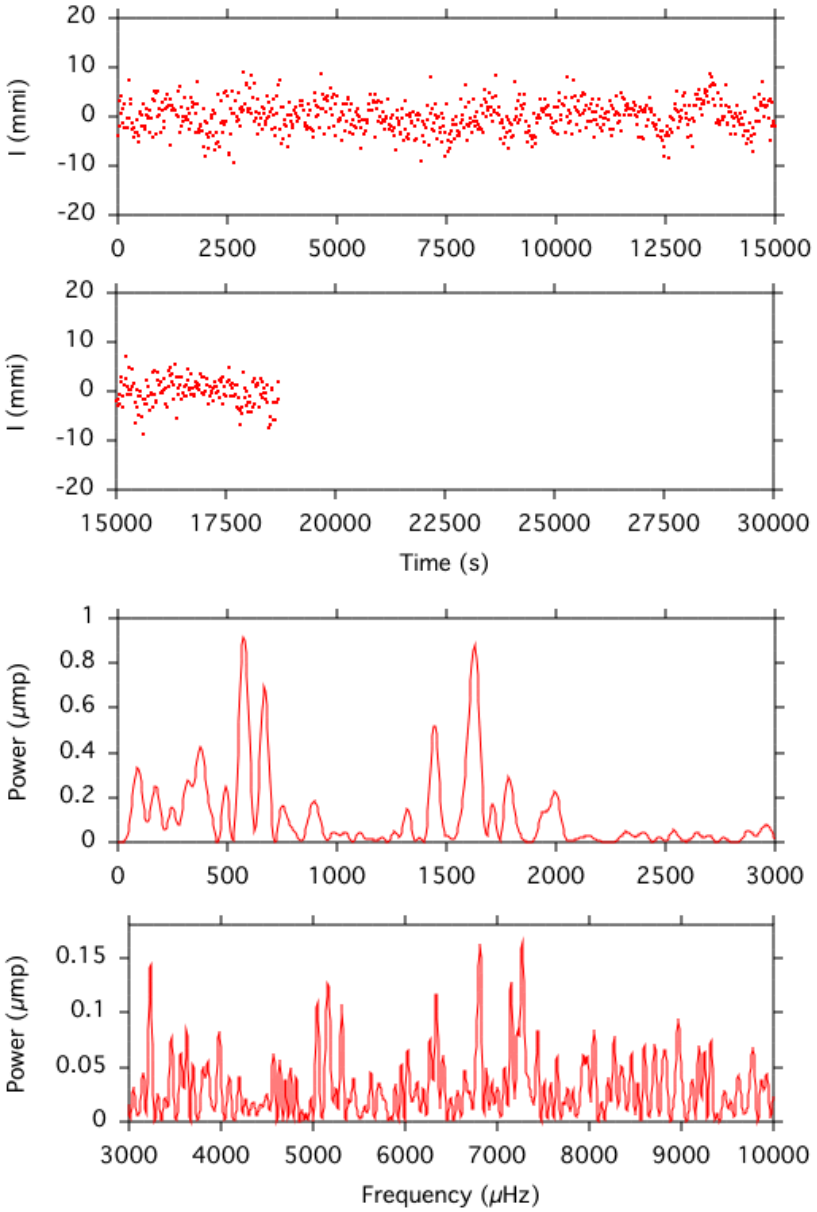

Fig. 62. NGC 246 light curve and temporal spectrum from run E6 (IAC80).

the main peak was detected in the second run (697 μHz -3.2 μmp-). This peak, which has been labeled f_3, is also present in runs A2, B2. A complex structure appear at low frequencies but with low power. The higher peaks there are: 220 μHz (0.5 μmp), which is in the region of f_1 (runs B1, B2, C4, C1 and C2), 345 μHz (0.7 μmp) and 543 μHz (0.8 μmp). All these peaks satisfy the confidence criterium (FAP=1/20) which is 0.5 μmp in this case. Some power 4 times above the average noise is detected at 1570 μHz (0.8 μmp). No peaks above this level are identified at frequencies above 2000 μHz.

Some important changes are also reported for the last run.The highest peak is found again at 575 μHz (0.9 μmp). This was the pulsation frequency with highest power in the runs E2 and E4. The complex structure at frequencies below ∼400 μHz remains but with lower power. The second highest peak is located at 1628 μHz (0.9 μmp). A close peak is observed also at 1446 μHz (0.5 μmp). These three peaks satisfy the confidence criteria (FAP=1/20) which is 0.4 μmp in this case. This peak ∼1630 μHz is also present in runs B1, D2, E2, E3 and E4. A peak is located also at 669 μHz (0.7 μmp). Two peaks are identified in the high frequency region (>5000μHz) with power above 4 times over the average noise: 7151 μHz (0.15 μmp) and 6811 μHz (0.15 μmp).

3.3.5.1. The low frequency domain

In this section we will investigate in more detail the photometric characteristics displayed in NGC 246 temporal spectra during the runs E in the low frequency domain. By low frequencies we will refer to the frequencies below ∼3000 μHz. Figure 63 presents a comparison of the temporal spectra up to 5000 μHz of the six runs obtained during the campaign.

The temporal spectra show in this region daily photometric changes. Pulsations frequencies are not present or have extremely low amplitude in the first two runs; suddenly some frequencies seem to have been activated and the third run shows the peak with the highest power of all runs (697 μHz -3.2 μmp-). The modulations observed are far smaller than those obtained during 2001 campaigns (runs B and C). After the third run, the pulsations start to decrease in power and during the last run all the pulsations are again below 1 μmp. The pulsation with highest power of the different runs is always changing from run to run: the highest peak of the second run (576 μHz -0.6 μmp-) is not present in the third one, is again the highest peak in the 4th and with higher power (2.2 μmp), is not present in the 5th run and is again the highest peak in the last, but with less power (0.92 μmp). On the other hand, the highest peak of the third run (697 μHz -3.2 μmp-) is also present in the second run but with substantially less power (0.4 μmp), and is not present in the next runs. The highest pulsation frequency of the 5th run is located at nearby peaks of the 697 μHz: 688 μHz (1.5 μmp), which is 9 μHz away from the previous.

Another stable peak is located at ∼1629 μHz. Power in this region is found over the confidence criteria in the second and last runs (E2 and E6), and in run B1, where it was found with high power: 1630 μHz (4.7 μmp). Power is also found at nearby frequencies in the run E3, at 1642 μHz, and in the run D2, at 1636 μHz. The difference between

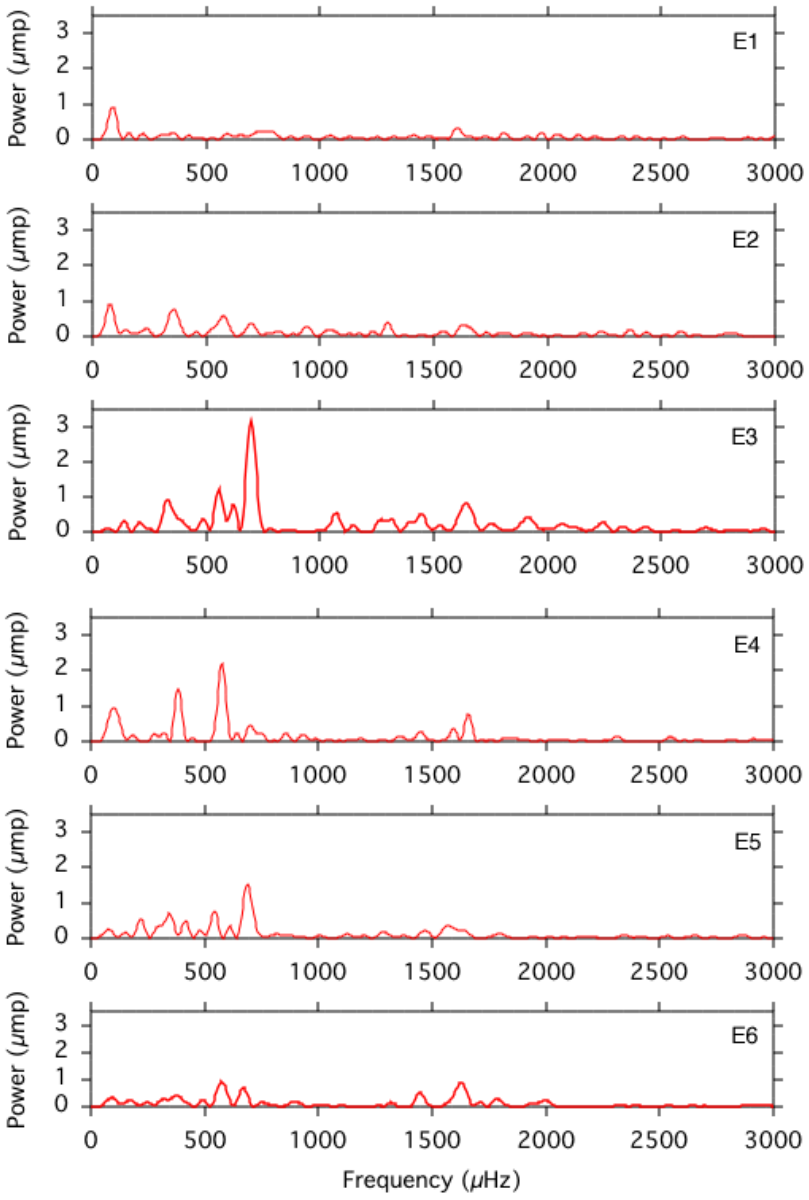

Fig. 63. NGC 246 comparison of temporal spectra up to 3000 μHz. The graphs correspond (from up to down) to the temporal spectra obtained from the runs E1 to E6.

these frequencies are 8 μHz 7 μHz respectively. It seems that this difference of $\sim$8 μHz is a characteristic of some peaks appearing in certain runs, compared with others which may appear in others. This may indicate that these pulsations are related with rotational splitting of g-modes. In this case we may observe triplets, that is, 3 pulsations frequencies related to oscillation modes with same k and l values but different m. For pulsating white dwarfs one or two members of a triplet are not detected in many cases. To explain our

observations we may assume that one member is strongest one night and another another night. The difference in frequency of the members of all these multiplets is always the same and depends on the rotation of the star. For example, Vauclair et al (2002) found for RXJ 2117+3412 a rotational splitting of around 5 μHz. However the tentative idea of a rotational splitting of $\sim$8 μHz for NGC 246 is quite risky to conclude from our data because, taking into account that the average of the length of the runs is 20000 s, the resolution of the temporal spectra is only $\sim$50 μHz! Therefore, this kind of search is impossible to achieve from only one run and looking for all the members of a triplets or doublets present in the same run, because they would not be resolved. However, some extra information may be extracted in cases like ours, comparing different individuals runs and expecting that only one of the member of the group is present or dominating.

Our search for possible pulsations related with g-modes can also be achieved looking for ratios between frequencies of the higher peaks of different runs close to $\mathcal{R}$. The best candidate is the peak at $\sim$575 μHz which appears in different runs: E2, E4, E6 and D1. The ratio between this frequency and 662 μHz, which is the highest peak in the temporal spectrum of the run D1 and the second highest in D2 gives, 575/662=0.87, equal to $\mathcal{R}$. 500/576 ratio is also equal to 0.87. Power at $\sim$500 μHz is found in the runs B2, C1 and D1. Therefore, all these pulsations frequencies ($\sim$500, 576 and 662 μHz) may be related to g-modes.

Power at $\sim$697 μHz is present in runs: E2, E3 and E4, and at a nearby frequency ($\sim$688 μHz) in run E5. This pulsation frequency has the highest power in run E2 and is also present in runs A2 and B2. The analysis of B runs suggested the presence of an harmonic structure related to the pulsation frequency at $\sim$230 μHz (f_1). The pulsation frequency found at $\sim$697 μHz may be related with the second harmonic. However, power close to the main frequency at $\sim$230 μHz is only found in run E5. The power found in runs E2 and E5 at frequency $\sim$350 μHz may also be related to this structure since the ratio $f_1/350$ is almost 2/3.

3.3.5.2. The high frequency domain.

In this section we will investigate in more detail the photometric characteristics displayed in NGC 246 temporal spectra between 3000 and 10000 μHz. Figure 64 presents a comparison of the temporal spectra of this region of the six runs obtained during the campaign.

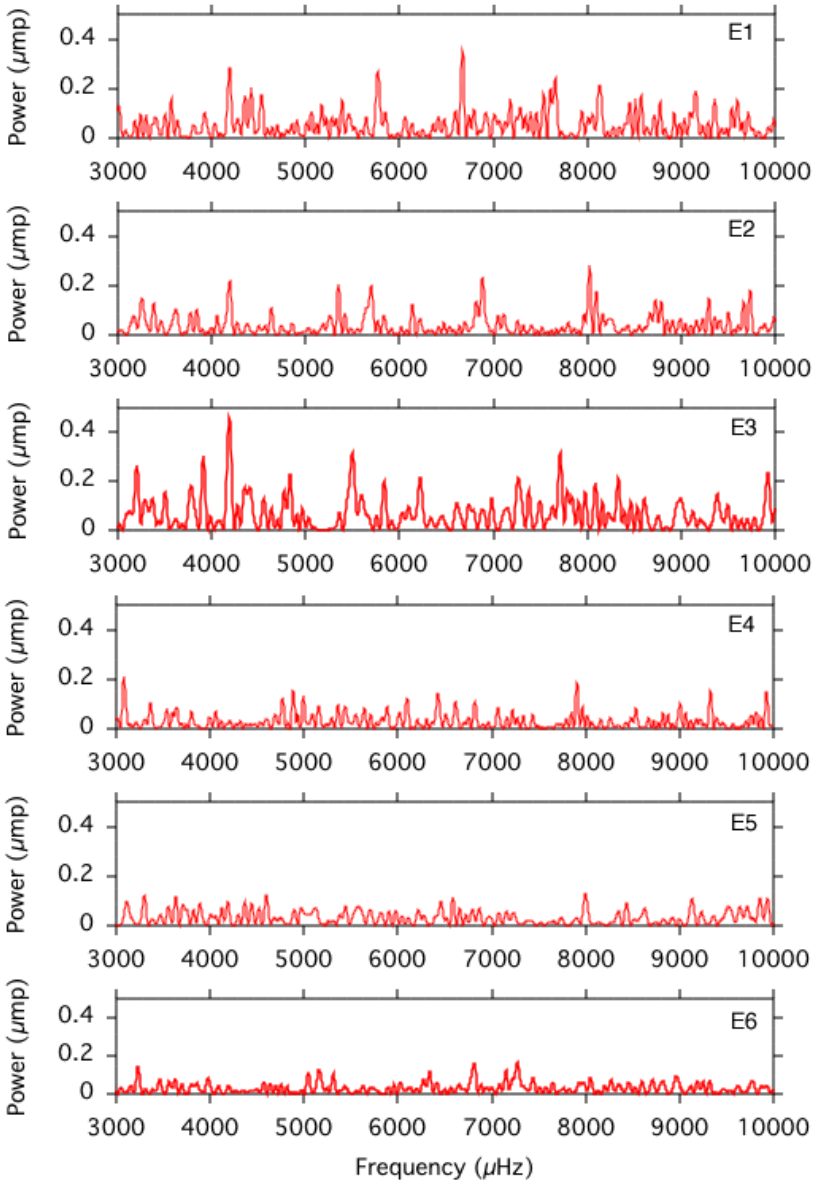

Fig. 64. NGC 246 comparison of temporal spectra covering from 3000 μHz to 10000 μHz. The graphs correspond (from up to down) to the temporal spectra obtained from the runs E1 to E6.

In general, all the peaks in this region have quite low power and many of them may be just noise. Only one peak has power over the confidence criteria (FAP=1/20) and is found at 8022 μHz in run E2. Another peak which is a good candidate to be a real pulsation is found at 4190 μHz. Power in this region above 4 times the average noise is present in runs E1, E2 and E3. The noise levels in runs E1 and E2 are low and it is possible to identify some peaks with power 4 times above the local noise. The noise for the third run is higher

so this identification is more difficult. During the three last runs (E4, E5 and E6), the noise level is again low but all the previous peaks have disappeared or decreased in amplitude. Therefore, we have concentrated the study of this high frequency domain to the runs E1, E2 and E3.

As for the low frequency domain, we have searched for pairs of frequencies with power 4 times over the local noise and ratios close to $\mathcal{R}$. For the first run, the ratio of the peaks at 5769 μHz and 6670 μHz, and 6670 μHz and 7661 μHz is equal to $\mathcal{R}$. We have found this ratio in other pairs like, for example, 3570 μHz (0.2 μmp) and 4189 μHz (0.3 μmp) but we do not want to consider these cases since the power of one of the members is below 4 times the average noise. Therefore, the pulsations frequencies at 5769, 6670 and 7661 μHz may be related to g-modes.

The second run also shows some peaks at least four times above the noise ($4 \times 0.03 = 0.12$ μmp in this case). We repeated the search and found the following pairs which ratios fit or are close to $\mathcal{R}$: 5350 μHz (0.2 μmp) and 6138 μHz (0.12 μmp); and 8023 μHz (0.3 μmp -highest peak in this domain) and 9295 μHz (0.14 μmp). Therefore, the pulsations frequencies at 5350, 6138, 8023 and 9295 μHz may also be related to $g - modes$.

All the pairs showing ratio $\mathcal{R}$ are found at frequencies > 5000 μHz, corresponding to periods shorter than 200 s. Therefore, these pulsations may be due the ϵ-mechanism. Kawaler et al. (1986) anticipated that during the PN and pre-white dwarf evolutionary phases, the possibility of a remnant He-burning shell that could drive g-modes by the ϵ-mechanism. These g-modes are predicted to be unstable and in the period range of 70-200 s, corresponding to low k orders for $l = 1$ modes. Evidence of possible g-modes driving by the ϵ-mechanism has been reported for the first time in the chapter 2 for the PNN VV 47. We have not found the same pair of frequencies with ratio close to $\mathcal{R}$ in more than one run. Therefore the candidates observed must have an associated life time of hours.

3.3.5.3. Photometric changes during the time observing.

We have presented important night to night changes in the temporal spectra of NGC 246. These are reported for all the consecutive nights we have data. It seems that for this object, the abnormal situation is to observe two similar temporal spectra! This may be due to the presence of a high number of modulations frequencies not completely solved, but it is more likely that many modulations change irregularly in amplitude and even appearing and disappearing from run to run. Complex physical process happening in the star and/or

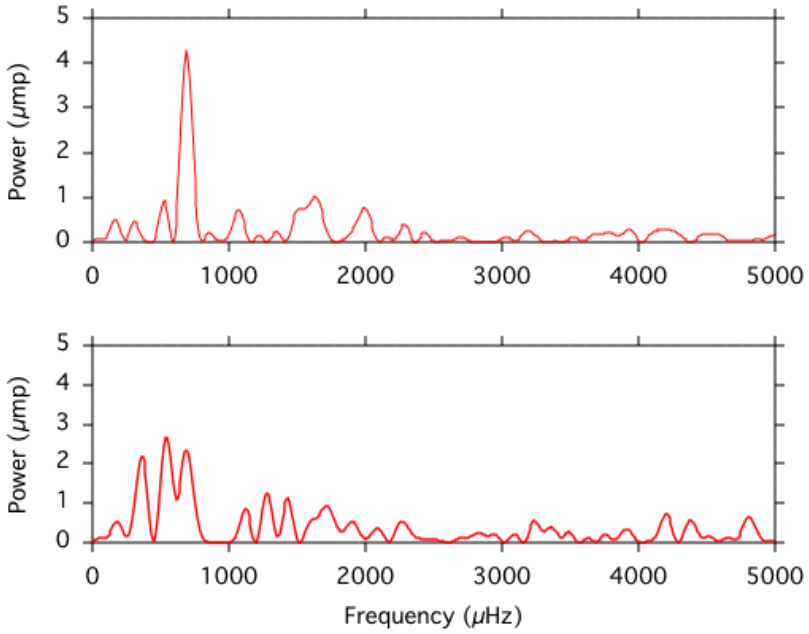

Fig. 65. NGC 246 comparison of the temporal spectra of the first (upper panel) and second (lower panel) sections of the run E3.

around it may be the responsible for these rapid changes. One of our main objectives is to study more in detail these changes and to investigate if they also happen on shorter time scales than from night to night. Our on-line analysis using RTP showed that changes on time scale of hours were evident during some of the runs. Therefore, and as first step in this analysis, we have selected some of the longest runs from this campaign and have divided them in two sections of nearly the same length, in order to compare the temporal spectra of these sections. Figures 65 to 68 present the results obtained. The length of the individual sections of the runs is about half the complete run, around 10000 s. Therefore, the resolution of of the temporal spectra is also 2 times worse, around 100 μHz so the localization of the peaks is less precise. However, this resolution is in many cases good enough to study variability in some of the important regions were power is present.

All the comparisons display important changes during the two sections of the night. Therefore, many of the photometric changes reported for NGC 246 must happen on time scale of hours or less. Some indications of such rapid changes were obtained before for other PNN: VV47 (see chapter 2). In general, the temporal spectra of the PNNs display irregular changes in the amplitude of the peaks. This seems to be a main property of the whole family of PNNs. However, many of the daily variations observed are small changes

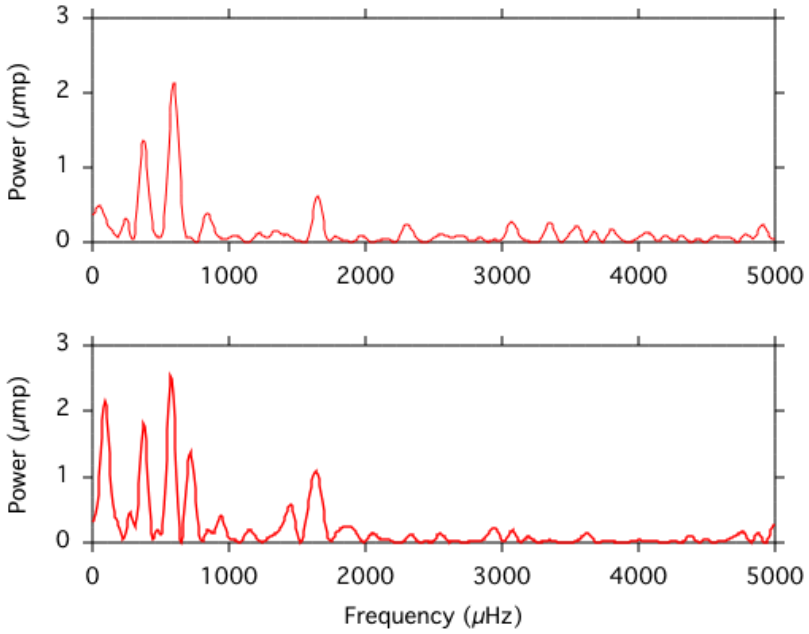

Fig. 66. NGC 246 comparison of the temporal spectra of the first (upper panel) and second (lower panel) sections of the run E4.

in the amplitude of the main peaks. Further important changes, including the appearance of new peaks, have been reported but from observations weeks apart. We have indicated in the previous chapter and for the first time more rapid changes for some of our candidates (NGC 6852 and VV 47). Detailed studies based on more complete light curves for objects like RXJ 2117+3412 (Vauclair et al 2002) confirm that some of these changes are not due to beating of close frequencies but to real variations in the photometric properties of the star. The changes observed in RXJ 2117+3412 include variations of the amplitudes of some peaks. One proposed explanation relates these changes with episodes of enhanced mass loss from the PNNs. Such changes in the stellar atmosphere may alter the mode amplitude since the driving zone for pulsations is close to the surface and the chemical composition of the driving region could change on time scale of order of weeks. This change in the driving region may affect the efficiency of the excitation mechanism, especially if the mass loss is time dependent and could explain irregular change in amplitudes on time scale of weeks. Shorter time scales for amplitude (power) changes, i.e, days, can not be explained by this mechanism.

However, changes on time scales of the order of hours are evident from the analysis presented for NGC 246. Figure 65 presents a comparison between the two half of the run

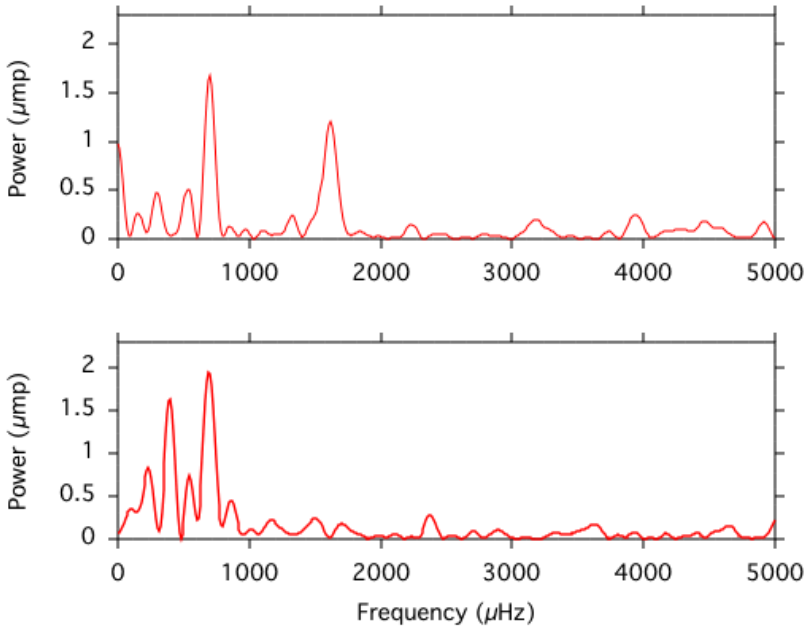

Fig. 67. NGC 246 comparison of the temporal spectra of the first (upper panel) and second (lower panel) sections of the run E5.

E3. The temporal spectrum of the first section of the night shows a high peak at ∼690 μHz which decreases dramatically in power, from 4.3 to 2.3 μmp, in the second section; and a peak at ∼530 μHz which increases from 0.9 to 2.7 μmp. In addition, a new peak at ∼360 μHz (2.2 μmp) is detected in the second section but is absent in the first. Changes are also present comparing the two section of the next night, E4 (see figure 66). Two main peaks, at ∼374 and 595 μHz, remains almost the same but a new peak at ∼716 μHz (1.3 μmp), which is not present in the first section, is detected in the second. Some increase in power is displayed in the region located at ∼1640 μHz.

Figure 67 presents the comparison for the next night (E5). The changes here are even more spectacular: power detected at ∼1620 μHz (1.2 μmp) in the first half is completely absent in the second section; and a peak at ∼396 μHz (1.64 μmp) is detected in the second part of the night but not present in the first. The last comparison of temporal spectra of two sections of the night is done the last run E6. The highest peak of the temporal spectrum for the first section (∼180 μHz) is not considered since its period is close to half the length of the run. However, a clear peak at ∼333 μHz (0.9 μmp), which is not present for the first section, appears in second. In addition, power in the region ∼1640 μHz increases substantially in the second section of the run.

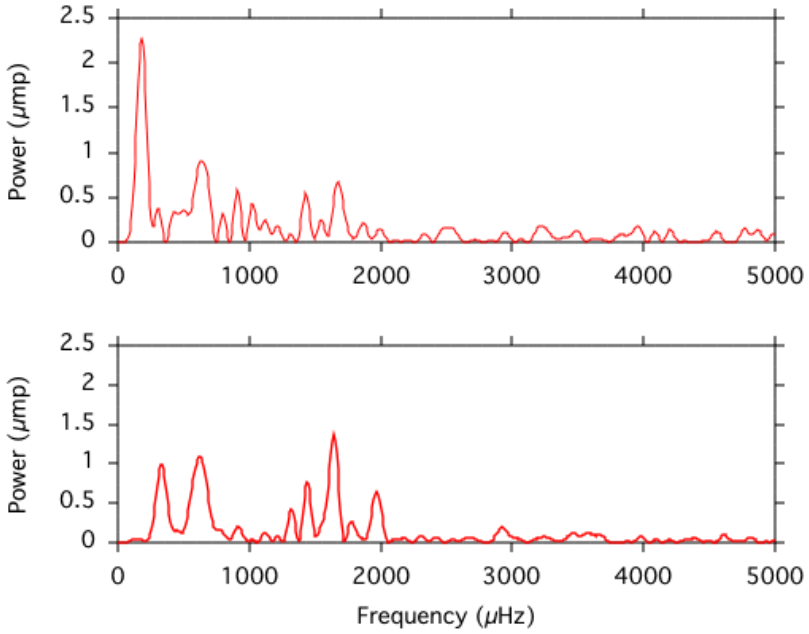

Fig. 68. NGC 246 comparison of the temporal spectra of the first (upper panel) and second (lower panel) sections of the run E6.

Many changes on time scales less than ∼2 hours seem to happen in the star. Some pulsations are turned on and off on this short time in the star itself or in its neighborhood. Taking into account the observed ratios between some frequencies fitting $\mathcal{R}$, many of these pairs of peaks may be related to g-modes. However, the actual status of the theoretical model involves time scale ∼ week for the fastest changes in amplitudes of the non-radial g-modes. This inconsistency between theoretical predictions and observations implies that our knowledge of what happens in these stars is not complete.

On the other hand, these rapid changes in the temporal spectra need a better tool for the photometric analysis in order to try to extract further information. In this case, the Fourier Transform is not a good tool since it assumes that the pulsations are constant with time. Therefore, the information extracted by the FT, if changes happen during the observations, is not correct. We can not, for example, trust the power associated (or amplitudes), since it calculates an average power. In addition, a possible change of a frequency of a pulsation can not be analysed with the FT.

Table 10. NGC 246 pulsation frequencies. This table present the peaks below 3000 μHz obtained in the FT of the different runs. The frequencies are presented in μHz, and also is presented, in brackets, their power in μmp. The main table shows the peaks which repeats in more than one run, and below the rest of peak identified.

Run	f_1	u_1	$\frac{3}{2}$ f_1	f_2	R_{1a}	u_2	R_{1b}	R_{1c}	f_3	f_4	R_{2a}
A1						550 (3,7)					
A2						550 (1.8)			685 (5.6)		
B1	230 (34)		340 (18)	442 (34)		550 (1.5)				920 (3.9)	1630 (4.7)
B2	235 (5.9)	270 (4.9)	331 (2.4)	450 (3.2)	500 (4)	549 (6.8)			691 (3.6)	901 (2.2)	
C4	222 (2.5)	290 (2.2)				540 (3.5)		650 (3.2)			
D1	223 (0.2)				503 (0.3)		574 (1.6)	660 (0.57)			
D2	234 (0.9)		325 (0.5)					664 (2.5)			1636 (0.3)
E1											
E2			356? (0.7)				575 (0.6)		699 (0.4)	941? (0.3)	1629 (0.3)
E3			330 (0.9)			556 (1.2)			697 (3.4)		1642 (0.8)
E4							576 (2.2)		700 (0.5)		1658? (0.8)
E5	220 (0.5)		345 (0.7)			543 (0.8)			688 (1.5)		
E6							575 (0.9)	670 (0.7)			1628 (0.9)

Aditional peaks below 3000 μHz:

B1: 770 (2.5), 1520 (3.2), 1807 (4.5); **B2**: 1337 (2), 1804 (1.6), 1990 (1.7), 2040 (2)

D1: 1223 (0.2); **D2**: R_{2b} 1429 (0.3), 1487 (0.4)

E1: 1602 (0.3); **E2**: 1298 (0.4); **E4**: 1595 (0.4); **E5**: 1570 (0.4); **E6**: 1446 (0.5)

3.3.6. The harmonic structure.

Table 10 presents the main peaks observed in the FT of the different runs below 3000 μHz. Two harmonic structures are identified and the frequencies associated labeled with

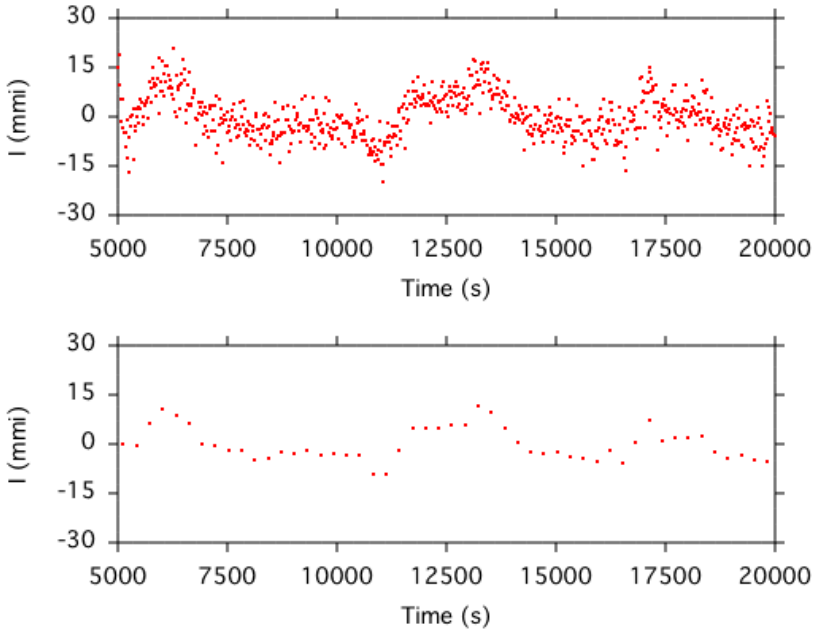

Fig. 69. NGC 246 light curve section of run B2 (upper panel) and light curve averaged over 15 points (lower panel).

f and u, where f_1 and u_1 are the fundamental frequencies. Some peaks are identified with R. Pair of frequencies labeled with R, e.g. R_{1a}/R_{1b}, have ratios close to $\mathcal{R}$ and may be related to g-modes pulsations.

In the temporal spectra of many of the runs (B1, B2, C3, D2) we find a peak near the frequency f_1=230 μHz (P_1=4350s), and in almost all runs we find one or more peak near harmonics of this frequency (f_2=460 , f_3=690 and f_4=920 μHz) and a few times we even find a peak near 330 μHz which is 3/2 that frequency which we may call $f_{3/2}$. The occurrence of the harmonics peaks and their power is summarised in table 10. In the following we will investigate the stability of this harmonic structure, and discuss its origin. As a first step we construct light curves averaged over 15 points to get rid of high frequency noise and improve the signal to noise in the low frequency region. An example of a long light curve before and after this averaging is shown in figure 69.

The next step was to use the linear least square algoritm to determine the amplitude and phase of P_1 for each run which was long enough. We got solutions from runs B1, B2, C4, D1, E1, E2, E5, E6. We also folded the long runs on the period P_1, in order to investigate the pulse form. Figure 70 displays the pulse forms of the runs B1, B2, C4, D1 and D2, and Figure 71 the pulse forms of the runs E. Each pulse period is displayed two

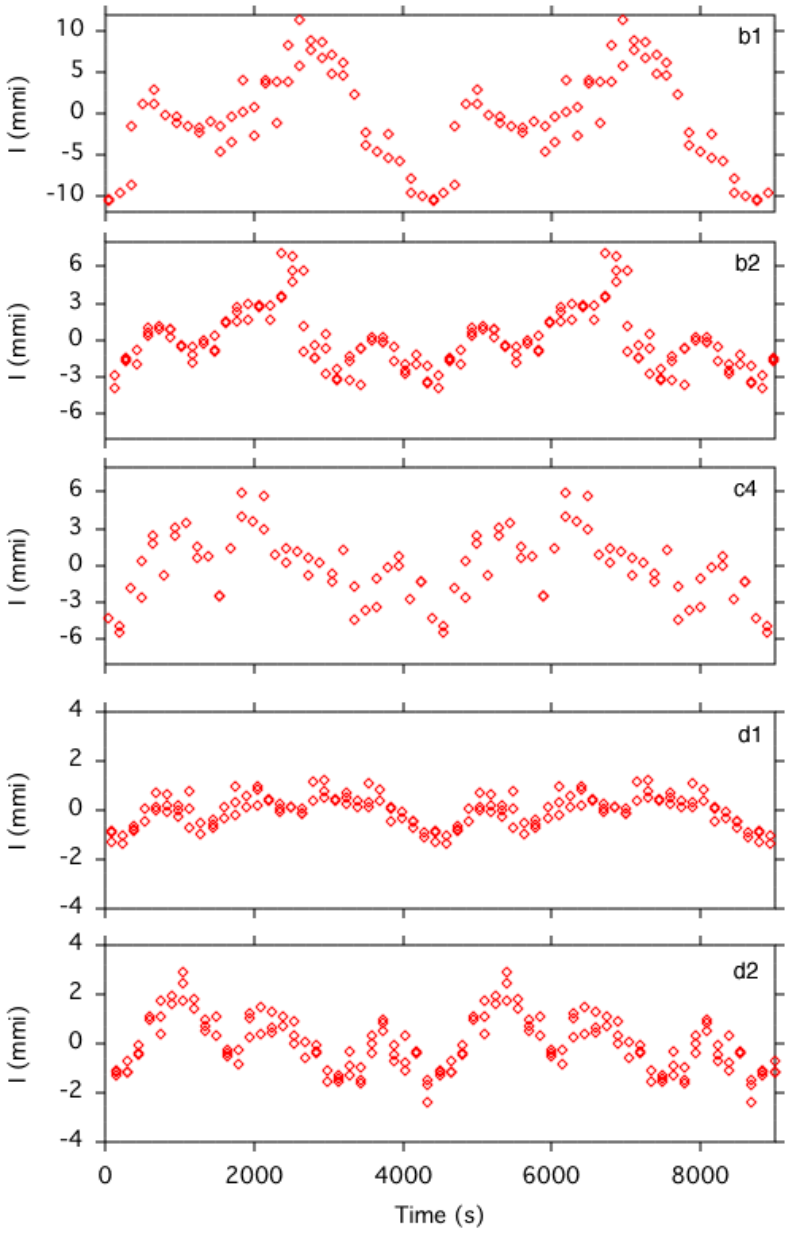

Fig. 70. NGC 246; pulse forms of period P_1 in runs B1, B2, C4, D1 and D2.

times. In the 3 long runs from 2001 (B1-2, and C4) we find in B1 a strong double humped form which in B2- one night later change to a triple humped form when f_3 increases. For the two runs in 2002, we recognise in D1 the pulse shape with a low amplitude f_1 and some signs of f_3, while in D2 (next night), both f_1 and f_3 are somewhat stronger. Finally the E sequence demonstrates how the pulse shape changes from night to night, from almost flat (E1) to a well defined one hump (E6), and three humps of variable amplitudes in E2-5.

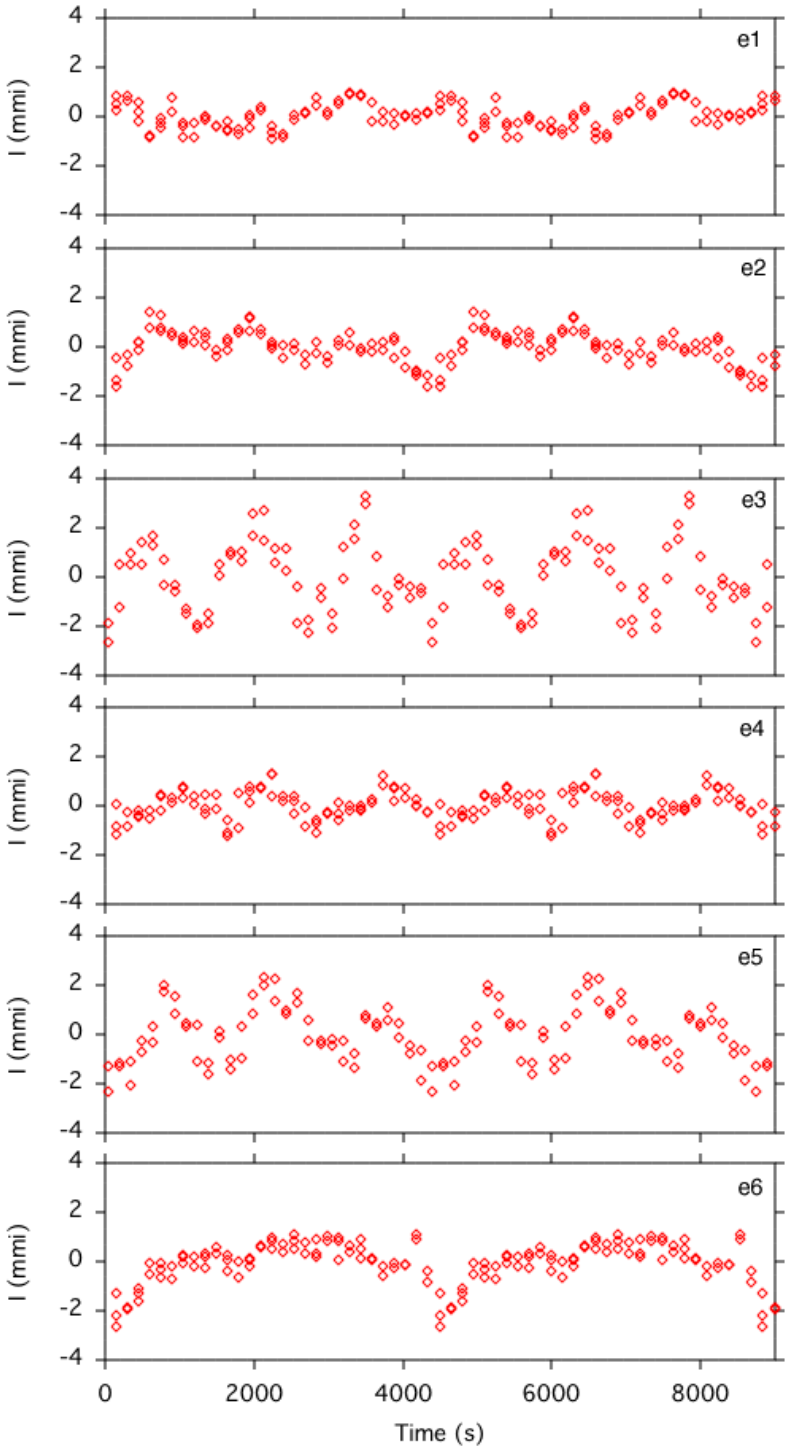

Fig. 71. NGC 246; pulse forms of period P_1 in runs E.

Then, we finally calculate the time in heliosentric julian days for the first minium for each run determined by the linear least square, and make our first observed minus calculated (O-C) diagram (figure 72) for the 2001 season. The result is a straight line

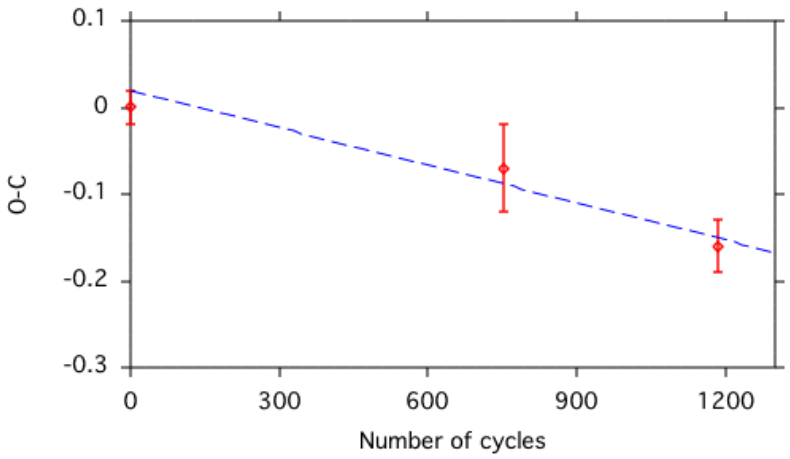

Fig. 72. NGC 246; $P_1 = 4350$ O-C diagram for the 2001 season.

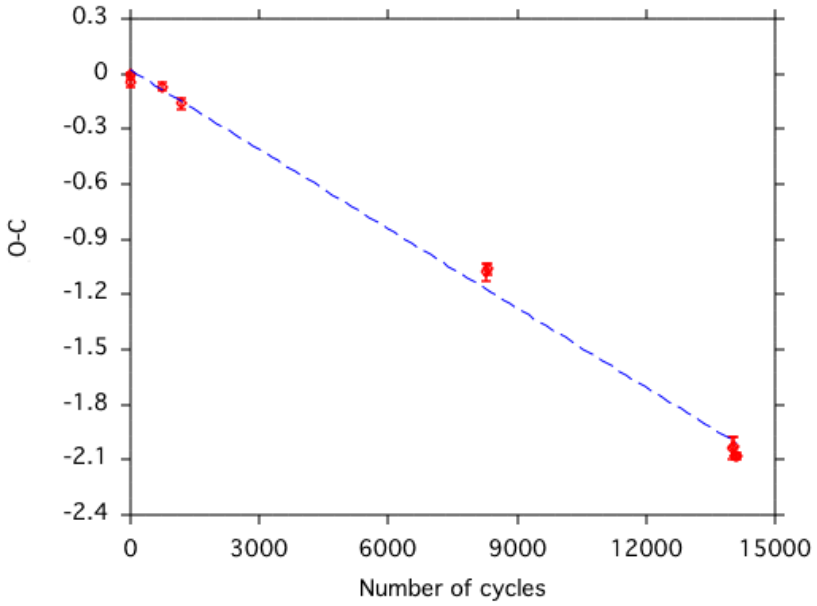

Fig. 73. NGC 246; $P_1 = 4350$ s O-C diagram for the whole data set.

with a negative slope, covering more than 1200 cycles. This means that we have a stable clock in the system, and can include the data for the following years in our O-C diagram (figure 73). In this we have also included a minium for the run C3, determined from the light curve directly, since only one minimum was observed. The best fit is with a period P= 4349.4±0.14 s (figure 74) and an Ephemeris for the pulse minimum related to f_1:

$$T = HJD2452170.563023(2) + E \times 0.050340(2), \quad (10)$$

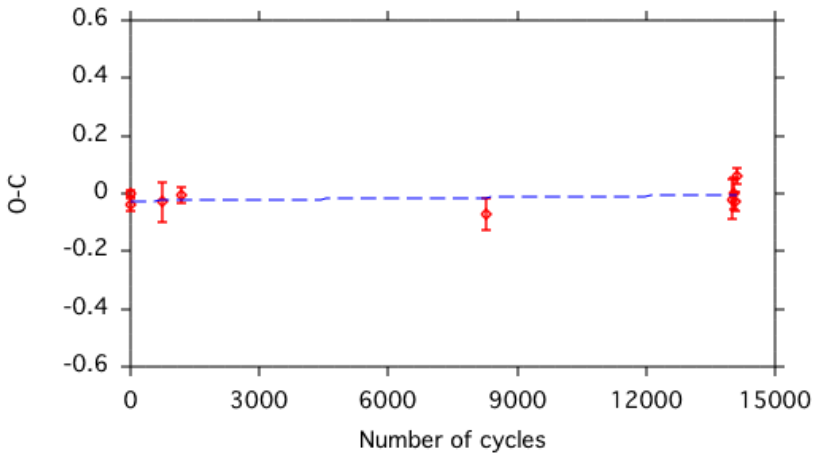

Fig. 74. NGC 246; $P_1 = 4349.4$ s O-C diagram for the whole data set.

where E is the number of cycles since the first minimum of run B1.

The high precision obtained in the Ephemeris determination means that we have a stable clock in the system, which always is there and keeps its phase even if its visibility becomes low. The stable period can either be the orbital period, the period of rotation, or a superhump period. We have many examples of very stable stellar pulsations but these are linear pulsations without any harmonics. Pulsations with harmonics do exist but only when they are very strong, in the non-linear regime. Also in the case of sdBs we may expect harmonics when we have radial pulsations which are so strong that the atmosphere is moved upwards with velocities $\geq$1000 km/s - definitely supersonic velocities where shocks can develop. In addition, pulsations may also be stable for some time but, if they disappear and come back again days or weeks later, like it happens in our data, it is unlikely that the phase is kept. Therefore, the low amplitudes and harmonic structure found for P_1 suggest that this stable period may be more likely an orbital period, superhump period or period of rotation.

3.3.7. Wavelet analysis on NGC 246 light curves.

Wavelet analysis gives information about possible changes in the temporal spectra with time. This tool can be explained as a instantaneous Fourier Transform. The wavelet analysis produces a 3 dimensional grid of data: frequency and amplitude (as in the FT) and a time axis. We use two ways of presenting the results: a 2 dimensional (2D) representation where the two axis represent the time and periods. The power is given as a colour scale.

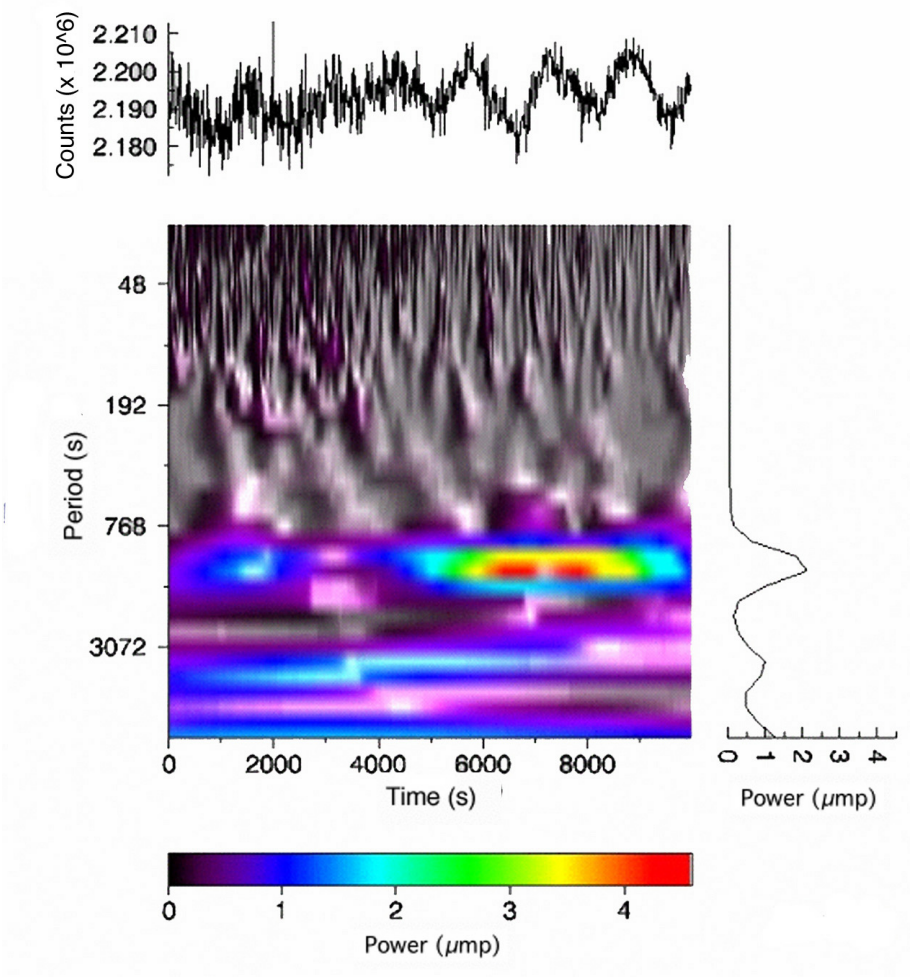

Fig. 75. NGC 246 wavelet analysis displayed in 2 dimensions of the run A2. The Morlet wavelet, order 6, is used in this case.

The data has been adapted to the same units as in the previous Fourier Transform analysis. Therefore, time is in seconds and power in μmp. The graphs also display the light curve (upper part in the 2D graphs), and an integration of all the contributions of periods during the time of the run (to the right in the 2D graphs), which is close to the FT output. Figure 75 is an example of this 2D representation of the results of the wavelet analysis.

We also present graphs in three dimension (3D), as an alternative way to display results. In this case the third dimension is used to represent the power. However, the colour scale is kept. Figure 76 present an example of this 3D representation.

Like for the FT, the resolution in the frequency space (periods in this case) increases for longer runs. This is even more noticeable in the wavelet analysis. However, the resolution of the parameters (time and periods) also depend of the wavelet function selected. Morlet wavelets gives better resolution in period space and Pauli in time space. Therefore, a

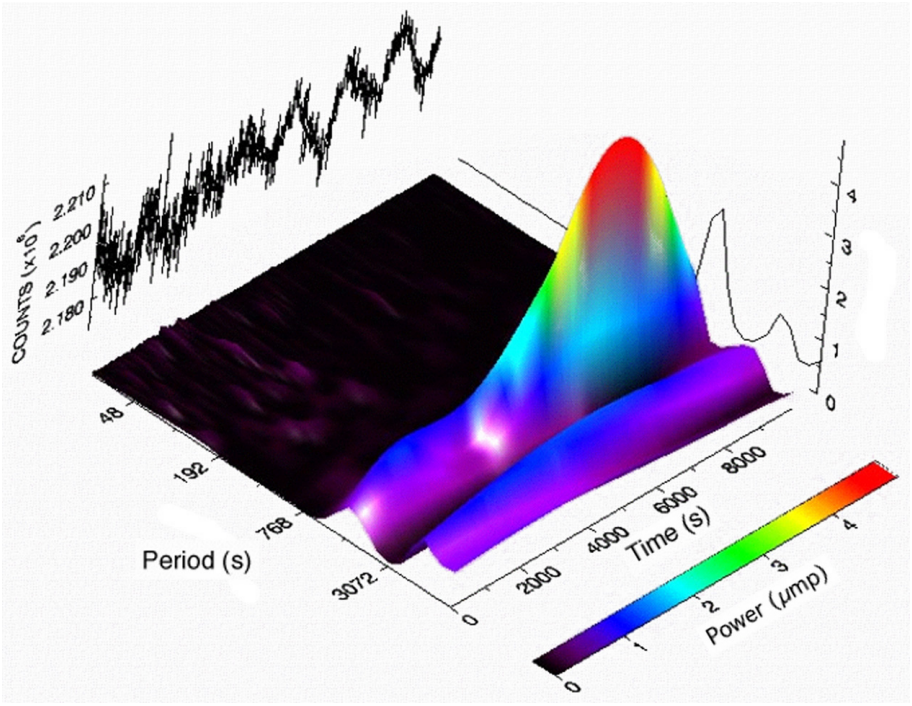

Fig. 76. NGC 246 wavelet analysis displayed in 3 dimensions of the of the run A2. The Morlet wavelet, order 6, is used in this case.

comparison between both give more precise information about the localization in time and period of possible changes in the distribution of power. One problem with the wavelet analysis is that by default the calculated periods depends on the order used for the wavelet function. Different orders (ω_0 in equation 9) make the complete set of power to move a little up or down the period axis. One of our main goals is to be able to use the information which we already have from the Fourier analysis, and to compare with it. We then found that the optimal order to use for Morlet wavelet function is ω_0=6, since then the output in periods is almost same as from the FT. This gives us chances to use the output of the wavelet analysis not only in a qualitative way but also quantitative. Therefore, this is the order we have chosen for the wavelet function.

Good data sets should have low noise and have constant sampling rate. We have analyzed the runs A2 (NOT), E3 and E5 (IAC80) which indicate possible rapid changes in the temporal spectra in time scale less than the length of the run.

3.3.7.1. NOT (2000) wavelet analysis.

The wavelet analysis for the run A2 shows how the amplitude of the 685 μHz peak increases very much in the second part of the run, around 4000 seconds after the beginning. This is

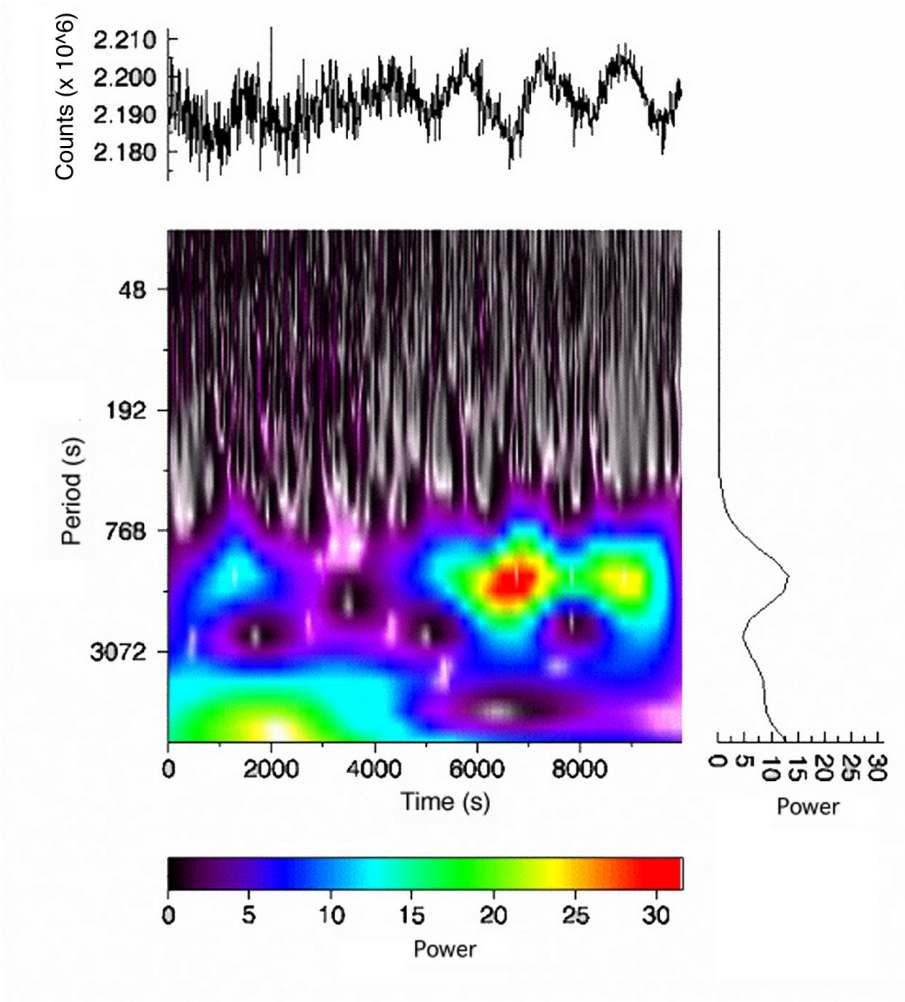

Fig. 77. NGC 246; wavelet analysis displayed in 2 dimensions of the of the run A2. Paul wavelet is used in this case.

clear for the two analysis presented: figure 75 presents the result using Morlet wavelet and figure 77 using Paul. This indicates that this change in amplitude is not a result of a beat between close frequencies. The 3D representation of the wavelet using Morlet type, which is presented in figure 76, also shows this increase. However, the length of this run is only 3.27 hours so longer data sets are needed to confirm this behaviour. The wavelet analysis suggests that the modulation frequency may have been activated around 4000 seconds after the beginning. No known mechanism related with the stellar atmosphere can do it. New mechanisms are needed to explain this feature.

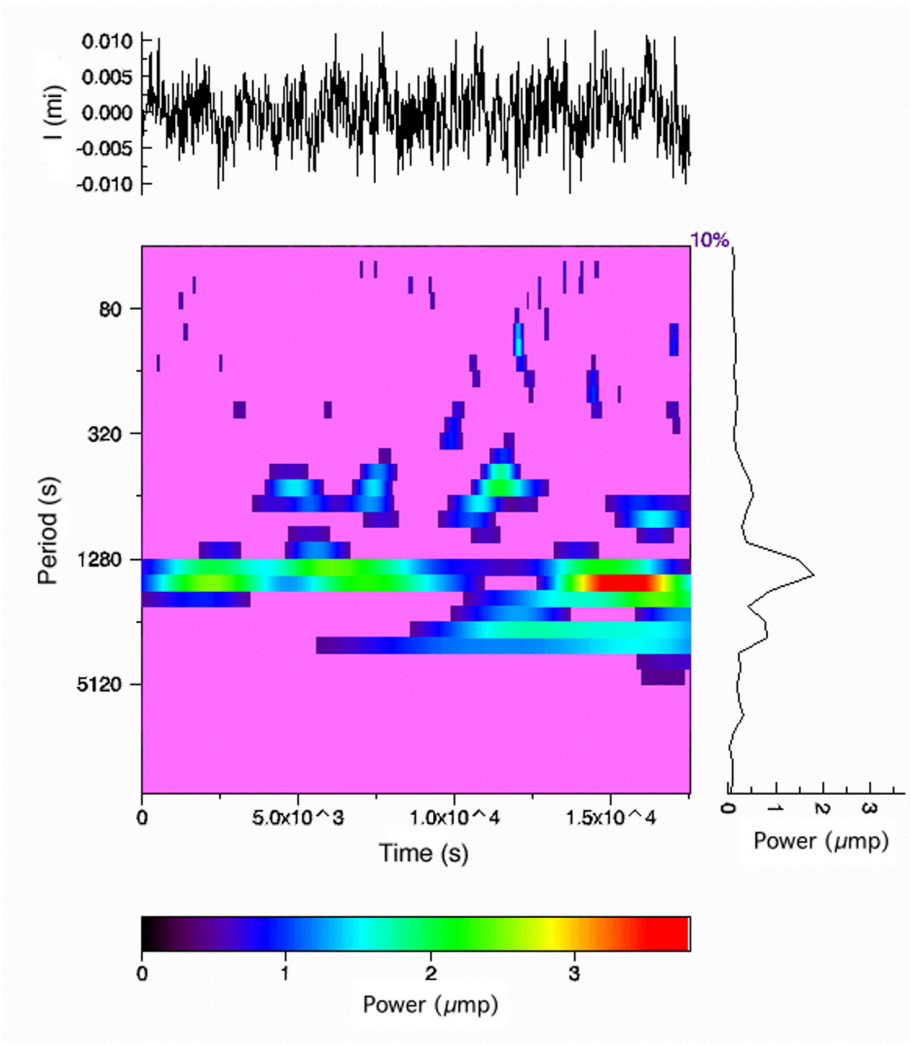

Fig. 78. NGC 246; wavelet analysis displayed in 2 dimensions of the run E3. Morlet wavelet, order 6, is used in this case. Lego function is used (see text for details).

3.3.7.2. IAC80 (2003) wavelet analysis.

Based in the results obtained from the wavelet analysis of run A2, we have selected the wavelet function Morlet order 6 to present the set of results for 2003 light curves. Pauli wavelet is not used in the following analysis since the previous results show that it looses too much information in the period space, so the comparison with the FT is quite complicated. Morlet 6 gives acceptable information in time space and is by far more precise in the period space. In addition, this is the only wavelet function where the frequency axis (periods in this case) is almost directly comparable with the FT. In addition we present the wavelet output with a lego type function, which produces a block structure, making partial averages over the period space in order to group the power during short

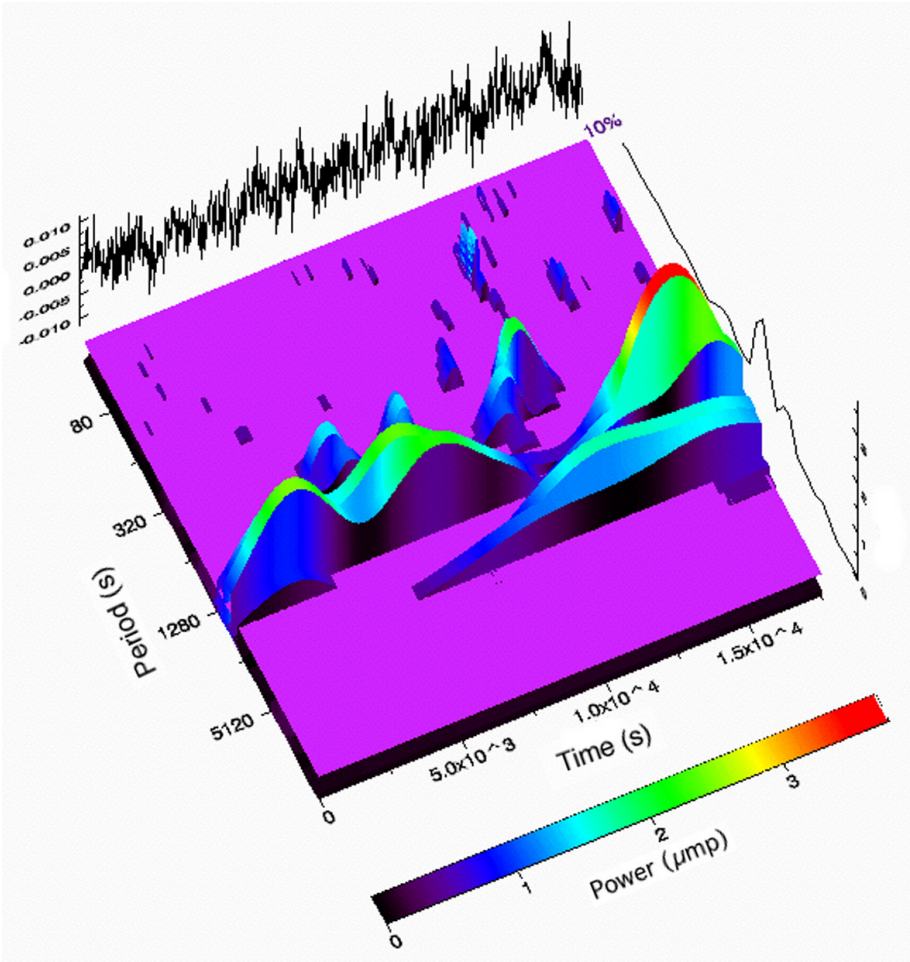

Fig. 79. NGC 246; wavelet analysis displayed in 3 dimensions of the run E3. Morlet wavelet, order 6, is used in this case. Lego function is used (see text for details).

time intervals in periods. This type of function also facilitates the comparison with the FT. It makes the change in power more clear for certain periods, and if they are activated and/or deactivated during the length of the run. In addition, a new 'floor' appears, which cut power with level less than 10% over the noise. This helps to identify the possible real power.

The first wavelet analysis was done for the run E3. The length of this run was ∼5.6 hours and presents substantial changes in the temporal spectra of the first and second parts of the run (see figure 65). FT of the complete run showed the following main periods: 3027 s (corresponding to the frequency 330 μHz and with power 0.9 μmp), 1797 s (556 μHz, 1.2 μmp), 1434 s (697 μHz, 3.2 μmp), and 609 s (1642 μHz, 0.8 μmp). The wavelet analysis confirms a short time scale associated with several regions of power, and periods which appear and disappear during the run. Figures 78 and 79 present the wavelet analysis

results in 2D and 3D. The main regions of power are displayed by two horizontal stripes which almost cross all the time axis (length of the run). This feature is more clear in the 2D representation. These are situated at around P=1400 and 1600 s. Therefore, these can be related with the peaks obtained in the FT at 697 μHz, and 556 μHz. These periods display an important variation in the power. Three fluctuations in power are registered, that is, the power associated to these periods seems to have increased and decreased three times during the run. This is specially noticeable for the period at 1600 s which is partially deactivated around 10 000 s after starting the run, and is not present for the next 2000 s. It appears again around the second 13 000 and increases rapidly in power until it reaches the maximum registered during the run (red colour). Clearly, power related to longer periods are only associated with the second section of the run. Power is also present in periods around 600 s. During this run, if power at this period appears, it never lasts more than $\sim$2000 s. The highest power related to the period at $\sim$600 s appears $\sim$11 000 s after starting the run. The power is then quite significant ($\sim$2 μmp) but only lasts $\sim$2000 s. It is important to notice that this power appears exactly when the main periods at $\sim$1400 and 1600 s are with quite low power or deactivated. Significant power also appear in regions related to the high frequency domain but for an extremely short time: a period at $\sim$140 s has power $\sim$1.5 μmp located around 12 000 s after starting the run and lasts only $\sim$500 s. This power is also only present when the main periods has quite low power and deactivated.

If we compare the results with the temporal spectra of the first and second sections of the run (figure 65), we can notice the limitations of the Fourier analysis. The FT of the first section of the run (first 9000 s) presents the highest peak of the two FTs. Its period is $\sim$1450 s (688 μHz, 4.3 μmp) . Since the resolution in the frequency domain is less, this is associated with the two stripes at around 1400 and 1600 s, which has relatively high power (green color) over almost the complete first section of the run. In the second section, the power associated with this peak decreases, and others appear at lower frequencies. These new pulsations at lower frequencies during the second part of the run are clearly seen in the wavelet transform.

The result from the Fourier analysis hides the fact that the peak with highest power appears towards the last part of the run and has period $\sim$1600 s. This peak may be the peak at $\sim$556 μHz. The Fourier Transform of the second section gives less power because it makes an average of the power associated to the periods $\sim$1400 and 1600 s over the whole

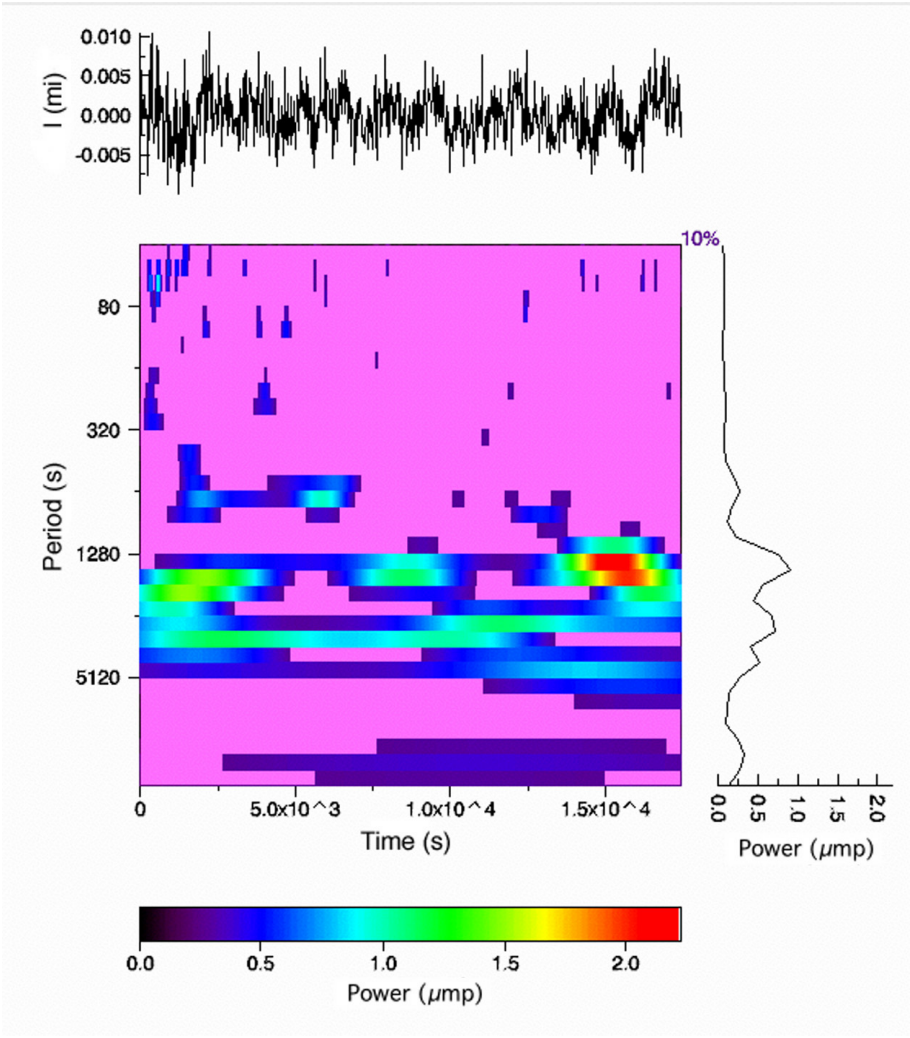

Fig. 80. Wavelet analysis displayed in 2 dimensions of of the run E5. Morlet wavelet, order 6, is used in this case. Lego function is used (see text for details).

time of the section. The peak at 1400 s has quite low power for around the first half of the second section, and the period at ∼1600 s is deactivated almost half of it. This period reaches the maximum amplitude (power) just towards the end of the run. The FT of the second part is an average and, therefore, has produced a low amplitude for the range. The wavelet analysis indicates that if the FT is done only over the last 5000 s of the run, the power displayed in this area would be quite high; however the resolution will be poor. Another limitation of the Fourier analysis is the impossibility to detect at all short lived pulses. This happens in this run with power at period ∼140 s, which has a life time of only ∼500 s.

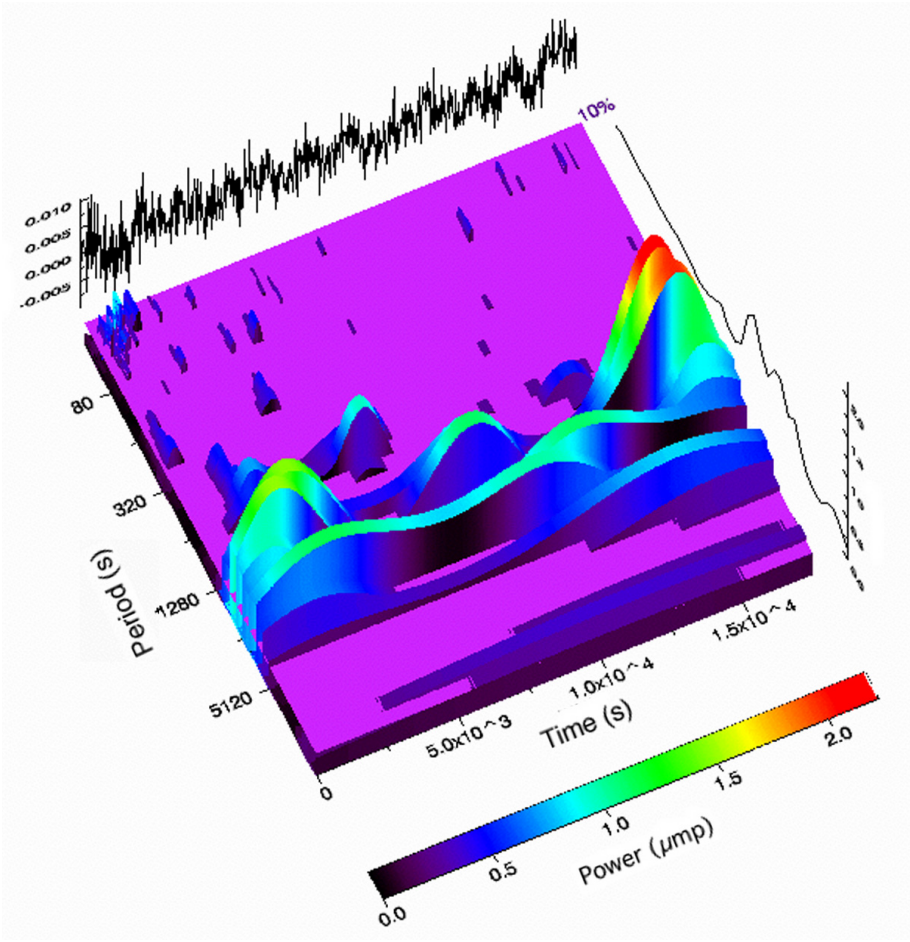

Fig. 81. Wavelet analysis displayed in 3 dimensions of the run E5. Morlet wavelet, order 6, is used in this case. Lego function is used (see text for details).

The other wavelet analysis is done for the run E5. The length of this run is ∼4.8 hours and it also presents substantial changes in the temporal spectra of the first and second sections of the run (see figure 67). In this case, the result obtained from the FT analysis over the whole run presents the main peaks at the following periods: 4500 s (220 μHz, 0.5 μmp), 2900 s (345 μHz, 0.7 μmp), 1850 s (543 μHz, 0.75 μmp), 1450 s (688 μHz, 1.05 μmp), and 637 s (1570 μHz, 0.36 μmp). The wavelet analysis shows a result with characteristics similar to the previous one. Figures 80 and 81 present the wavelet analysis results in 2D and 3D. The main power is located again at periods around 1400 and 1600 s. These periods show important variations in power and even more dramatic than in the previous run. The power at ∼1400 s is present in the first part of the run but with low power. It increases toward the middle of the run, decreases again and increases towards then end, reaching the maximum power in this region (red colour). The power related with the period ∼1800

s appear in a cyclical way 3 times during the length of the run, lasting around 5000 s each. It is not present or deactivated two times for around 1000 s. Comparing with the previous run, power is found in more ranges of the periods space: a period around 5000 s cover the whole run but increases slightly in power towards the end (last 3000 s). Another longer periods appear in the second part of the run. Other interesting feature obtained from the comparison of the temporal spectra of the two sections of the night, is the presence of a clear peak at around 1570 μHz during the first part and completely absent in the second. This result is clearly seen in the wavelet analysis, where, like in the previous case, a period $\sim$650 s has power a short time interval in the first part of the run. Power starts to be present $\sim$2000 s after starting the run and last for around 5000 s. The period reaches the maximum power at t$\sim$5000 s. This area is related, like in the previous run, with the temporally lack of power associated to the periods at $\sim$1400 and/or 1600 s.

The frequency 688 μHz (period 1450 s) is close to 2 times the frequency at 345 μHz (period 2900 s). Therefore, it may also be the first harmonic of 345 μHz. The wavelet transform presents an interesting opportunity to analyse how the power of the main frequency and its first harmonic are distributed in time. Power related with the period at 2900 s (main period) is present from the beginning of the run until the t$\sim$13000 s, but absent towards the end of the run. The power is almost constant in the interval where it is present decreasing slightly with time. On the other hand, power related with the period at $\sim$1450 s (possible first harmonic, the strip just below the 1280 s mark in the period scale), is found almost in the whole length of the run, but with relatively low values. However, the power increases dramatically towards the end of the run, exactly in the area where the main period, which this harmonic is related to, has been switch off. This may indicate that this harmonic is associated to a real symmetry of the star or surroundings that modulates the light curve in this particular way.

3.4. Discussion

We have followed the photometric behaviour of NGC 246 over 4 years and have observed rapid photometric changes in its temporal spectra. We have analyzed 71.75 hours of photometric data on this object from 5 single site campaigns held during 2000. 2001, 2002 and 2003. Our main conclusion is that this PNN present variability in its pulsation pattern which change on different time scales, including from season to season, from month to

month and from night to night. In addition, changes related with time scales of hours or less have been observed. This variability is reported for all the temporal spectra analyzed.

The large amount of pulsation frequencies observed in the different runs (see table 10) can be divided in three groups. The first group is formed by the two harmonics structures: one related to the frequency at $f_1 \sim 230$ and other to $u_1 \sim 280$ μHz. Peaks are present in many runs in regions associated with the harmonics of these frequencies. We have observed 3 harmonics of f_1 ($f_2 \sim 450$ μHz, $f_3 \sim 450$ μHz, $f_4 \sim 920$ μHz), and the first harmonic of u_1 ($u_2 \sim 550$ μHz). Another peak $f_{3/2} \sim 340$ μ, which appears in several runs, is also related to f_1: the ratio between these frequencies is 3/2. This may suggest that the f harmonic structure has main frequency at $f_0 = f_1/2$. The second group in this division is formed by peaks at frequencies which ratio is close to $\mathcal{R}$. This relation is found for the frequencies labeled R (see table 10). These pulsations may be associated to non-radial g-modes of the star. The ratio between g- trapped modes in PNNs is predicted in theoretical models to be close to this number $\mathcal{R}$.

These two groups include a large fraction of the peaks observed and all the pulsations that have been observed in more than in one run. The third group is formed by the rest of pulsations, which can not be associated neither with the harmonic structures nor the $\mathcal{R}$ ratio.

The light curves from the 2001 campaigns (runs B and C) presents more clear modulations and the temporal spectra peaks with more power. NGC 246 seems to have been found in a more exited state during some nights in 2001. The power during some nights is a factor of 5 to 10 higher than observed in the other campaigns. The harmonic structure related f_1 is quite clear in the run B1. The longer run B2 shows both harmonic structures. The presence of periods with harmonics is a characteristic present in some CVs like intermediate Polars, which may show as many as 3 periods with harmonics: the orbital period, period of rotation of accretor, and the beat period between these. We have also reported variations in the power found for the main frequencies and its harmonics in different nights, some of them consecutive. This behaviour is also observed in some CVs. In addition, the light curve obtained in some if these runs present a clear double humped structure, which is a characteristic of systems with accretion disks or accretion driven by magnetic fields. These properties may indicate that an accretion ring or disk is present at times. If this is related to a superhump period, then the mass ratio $q = M_2/M_1 < 0.25$.

We have analyzed the pulse shape and stability of f_1. Our results for the pulse shape show a strong double humped form for some of the runs and triple humped in others. We have analyzed the pulse shape of the runs E obtained during 6 consecutive nights and have shown how it changes from night to night, from almost flat the first night, to a well defined one hump in the last run, and three humps of variable amplitude in the runs E2 to E5. O-C diagrams were calculated for f_1 to study its stability. The results is a straight line covering 3 years of data. The high precision obtained in the Ephemeris determination means that we have a stable clock in the system, which always is there and keeps its phase even if its visibility becomes low. The stable period can either be the orbital period (P_{orb}), the period of rotation, or a superhump period. The most likely is that P represents the orbital period because of the high stability. The superhump period normally will give more harmonics (Simpson & Wood 1998), but is not so stable (Patterson et al. 2002). It may also be that $P_{orb} = 2P$, where P is the period related to $f_0 = f_1/2$ which will make $f_{3/2}$ its first harmonic. Otherwise $f_{3/2}$ will be difficult to explain.

This stable clock in the system associated with f_1 may indicate the presence of a close companion and interaction with it. Stellar pulsations may also be stable for some time, but if they disappear and come back again days or weeks later, like it is observed, it is unlikely that the phase is kept. The period related with f_1 (72 min) is interesting since it is in the interval where CVs should be numerous, but none are found with periods between 78 and 65 minutes. The existence in NGC 246 spectra of He II in emission and soft X-rays is also a sign of accretion. If the star has a magnetic field and accretes on one or two poles, a single or double humped light curved will be formed. This may explain nicely that the pulse amplitude diminish -and this can happen suddenly- if the accretion stream is turned off. However, the high mass loss reported by Koesterke et al (1998) makes difficult the presence of a disk. The authors analyzed NGC 246 HST spectra and modeled OVI line and the result is a mass loss of $\log(\dot{M}/M_{\odot})\ yr^{-1}$=−6.9 . This strong wind may blow away any accretion structure around the PNN. On the other hand, this strong wind may make the secondary accrete. Soker (1997) analyzed shape of the NGC 246 planetary nebulae and conclude that it has its form due to common envelope interaction with a substellar companion, like a planet or a brown dwarf. In general he finds that 56% of the planetary nebulae are in this class. In this case, a ring may be formed around the companion and/or a magnetic field may produce bright spots. These structures may modulate the light curve. The variable stellar wind explains the changes evident on short time scales.

Power is also found for many runs in the frequency range 5000-10000 μHz, and the ratio between some frequencies also fits or it is close to $\mathcal{R}$. Therefore, they may be related to g-modes. Examples are shown in the temporal spectra of the runs E1 and E2 observed at IAC80, the 23rd and 24th of August (2003) (see figures 57 and 58). If this is the case, these non-radial g-modes are triggered by the ϵ-mechanism (Kawaler et al. 1986). We have presented evidences of g-modes triggered by the ϵ-mechanism for the other PNN VV47 in the previous chapter. Power at some of these frequencies appear only one particular night and it is not found in other runs. This may indicate rapid changes in amplitude on time scale less than 1 day for these g-modes triggered by the ϵ-mechanism. Many of these peaks have very low amplitudes, so they are possible to find only in good quality data. They can be confused with noise in others.

We have presented wavelet analysis for some of our runs and have reported extra information not possible to extract from the Fourier Transform analysis. The most important conclusions based on the wavelet analysis are: (1) The time scale of many peaks presenting substantial power is hours or less, with many peaks appearing and disappearing during the length of the run. A clear example is the power found associated to the period $\sim$1850 s which appears and disappears 3 times during the run E5 (see figure 80). (2) Wavelet analysis on runs E3 and E5 confirms the presence of power associated with some periods only during a short interval of time. This result is also indicated by the comparison of the temporal spectra of the first and second sections of the run, but it is better located and described with wavelet analysis. An example is the power found associated to the period at $\sim$650 s which only appears in a section of the first part of the run E5. (3) We have also reported power associated with periods $P < 200$ s, related with short time scales: the most clear example is a period at $\sim$140 s with power $\sim$1.5 μmp turned on 12000 s (3.3 hours) after starting of the run E4 and which lasts only $\sim$500 s (see figure 78). (4) The wavelet analysis offers a possibility to follow the distribution of the changing power, that is, to analyse when power associated with some periods appears and disappears and investigate what happens with the power associated to other periods. An example is the power associated to the period at $\sim$600 s which is more significant significant in both E3 and E5 runs when the periods at $\sim$1400 and 1700 s have quite low power and/or deactivated.

The wavelet analysis presented also show the limitations of the Fourier analysis in cases where rapid photometric changes happens. This is clearly shown by comparing the results obtained from the analysis of the Fourier Transforms of partial sections of nights

and the wavelet analysis over the same night data sets. We have shown some examples which illustrates this: in the run E5, the FT has missed the period with shows maximum power. This is the period at ∼1400 s but its high power is only present during the last quarter of the night. The averages done by doing Fourier analysis of the complete and partial (half) sections of the night give maximum power for the period at ∼1600 s. This is because the power associated with the period ∼1400 s is low during the first part of the run and deactivated during half of the second part.

Another clear example of the FT analysis problems is the power found in the high frequency domain and associated with extremely short time scales. This power will never appear in the FT where it would be lost in noise because the time it is present is very short compared to the length of the run. Therefore, the average done by the FT will decrease significantly its amplitude (power) and, in many cases, make the peak be confused with the noise.

3.5. Conclusions

The analysis of the complex and rapid photometric changes shown in NGC 246 temporal spectra suggest that they may be due a combination of processes happening in the star neighborhood due to interaction with a close companion, like the rearrangement of structure in a disk or ring surrounding the PNN or the companion; and the presence of a complex and variable non-radial g-modes structure. Some of the frequencies observed and related to g-modes pulsations are above 5000 μHz so they must be triggered by the ϵ mechanism. The short time scales displayed by many of these non-radial g-modes are not well understood from our current knowledge about how and why the PNNs pulsate. Our analysis has revealed indications that a lot of physics is missing in our current models. We have also shown the importance of the comparative analysis between the temporal spectra of different runs. This may display extra information which will not appear in classical ways to analyse photometric data for asteroseismogical studies, like, for example, merging all data to present a temporal spectrum with better resolution. The wavelet analysis performed in our data sets has been an powerful tool to find many of these observational facts which, otherwise, would be complete hidden if using only Fourier analysis.

Our analysis has revealed interesting aspects related with NGC 246 and has opened many questions. Further studies are necessary to conclude about the nature of this object. A multisite campaign will be valuable to get longer uninterrupted light curves. These will

improve the period resolution and time coverage of the wavelet analysis and facilitate the search of the life times associated with periods and possible relations between the presence of power at different intervals in the period and time spaces. Time resolved spectroscopy will also be very valuable to solve the question about the possible nature of f_1 as orbital period. This can be achieved by finding a S-curve in the HeII emission line. We have submitted an application to the NOT to test this possibility.

Acknowledgment: The results presented in this chapter are based on observations obtained at the Nordic Optical Telescope, operated on the island of La Palma jointly by Denmark, Finland, Iceland, Norway, and Sweden, in the Spanish Observatorio del Roque de los Muchachos of the Instituto de Astrofísica de Canarias (IAC), and the telescope IAC80 operated in the island of Tenerife by Spain in the Observatorio del Teide of the IAC. Some data presented here have been taken using ALFOSC, which is owned by the Instituto de Astrofisica de Andalucia (IAA) and operated at the Nordic Optical Telescope under agreement between IAA and the NBIfAFG of the Astronomical Observatory of Copenhagen. I would like thanks to the observers who have helped providing NGC 246 observations: Jan-Erik Solheim, Tatyana N. Dorokova and Nicolai I. Dorokov, and to the University of Tromsø, Astrophysics group, for funding the Observing expedition to Mt. Dushak-Erekdak Observatory in Turkmenistan. I wish also to thanks Roy for his kind support with the TCP hardware and software problems, and Jan-Erik for his important contributions to this work, fruitful discussions and patient revision of the earlier versions of this chapter.

References

Bessell, M. S. 1990, PASP, 102, 1181

Blöcker, T. 1995, A&A, 299, 755

Ciardullo, R., & Bond, H. E. 1996, AJ, 111, 2332

Feibelman, W. A. 1995, PASP, 107, 531

Hoare, M. G., Barstow, M. A., Werner, K., & Fleming, T. A. 1995, MNRAS, 273, 812

Kawaler, S. D., Winget, D. E., Hansen, C. J., & Iben, I. Jr. 1986, ApJ, 306, L41

Kepler, S.O. 1993, Baltic Atronomy, 2, 515

Kleinman, S. J., Nather, R. E., & Phillips, T. 1996, PASP, 108, 356

Koesterke, L., & Werner, K. 1998, ApJ, 500, L55

Landolt, A. U. 1983, AJ, 88, 439

Lau, K. M., & Weng, H.Y. 1995, Bull Amer. Meteor. Soc., 76, 2391

Mendez, R. H., & Niemela, V. S. 1979, ApJ, 232, 496

Mendez, R. H., Miguel, C. H., Heber, U., & Kudritzki, R. P. 1986, in Hydrogen-Deficient Stars and Related Objects, edited by K. Hunger, et al. (Reidel, Dordrecht), p. 323

Minkowski, R. 1965, in Galactic Structure, edited by A. Blaauw and M. Schmidt (university of Chicago Press, Chicago), p. 321

Muthu, C. 2001, BASI, 29, 381

Nather, R. E., Winget, D. E., Clemens, J. C., Hansen, C. J., Hine, B. P., 1990, ApJ, 361, 309

Patterson, J., Fried, R. A., Rea, R. et al. 2002, PASP, 114, 65

Schönberner, D., & Napiwotzki, R. 1990, A&A, 231, L33

Simpson, J. C., & Wood, M. A. 1998, ApJ, 506, 360

Soker, N. 1997, ApJS, 112, 487

Szentgyorgy, A., Raymond, J., Franco, J., Villaver, E., López-Martín, L. 2003, AJ, 594, 874

Tarafdar, S. P., & Apparao, K. M. V. 1988, ApJ, 327, 342

Torrence, C., & Compo, G. P. 1998, Bull Amer. Meteor. Soc., 79, 61

Vauclair, G., Moskalik, P., Pfeiffer, B., et al. 2002, A&A, 381, 122

Warner, B. 1995, Ap&SS, 225, 249

Werner, K., & Rauch, T. 1994, A&A, 284, L5-L8.

Østensen, R., & Solheim 2000, Baltic Astronomy 9, 44

Østensen, R. 2000, Time Resolved CCD Photometry, Ph.D. Thesis, University of Tromsø

Chapter 4

Analysis of light curves of AM CVn and HP Lib, and possible connection with NGC 246.

Abstract.

We present in this chapter analysis using different methods of light curves of the AM CVn objects in high state: AM CVn and HP Lib. We have simulated 'intrinsic noise' in amplitude and phase and have compared it with external noise. Intrinsic noise is noise which belongs to the physical source and, therefore, may provide extra information about the nature of the modulation frequencies. We present the results of the Intrinsic Period Scatter method (Koen & Lombard 1995). This method determines when the period jitter is distinct from any measurement error in the determination of pulsation cycle lengths, being intrinsic to the source of the modulation. We also present an analysis over three light curves of HP Lib obtained in consecutive nights. These runs shows changes in temporal spectra in the amplitude of the main period and harmonics from run to run. This is especially noticeable in the first harmonic, which has the same amplitude as the main period during the first run, but decreases $\sim$7 mma in the temporal spectrum of the next run. We have used wavelet analysis to look for variations of the amplitude of the pulsations during the run. We have found that the presence of amplitude in the harmonics depends on the pulse form of the main period. In particular, we found the second harmonic only during short intervals of time, which are related to the presence of a triple humped pulse form of the main period in the light curve. We have revised the energy production time series in smoothed particle hydrodynamics (SPH) accretion discs (Simpson & Wood 1998) to explain the light curves in AM CVn and HP Lib, and have introduced the active density wave model to attempt to explain the presence of high amplitude in the first harmonic. We discuss similarities found for the light curves of HP Lib and the average pulse shapes presented in chapter 3 for NGC 246, which may indicate that an accretion disc may be the responsible of the 4350 s period harmonic structure.

'From Close Binary White Dwarfs to White Dwarfs': J. M. González Pérez, e-mail: `jose@phys.uit.no`

4.1. Introduction.

The AM CVn family (see Warner 1995) represents one of the more exotic products of binary evolution. The complete lack of hydrogen in their spectra points to a peculiar previous history, where two common envelope (CE) stages have happened (Iben & Tutukov 1991). In the AM CVn stage, what is left is a CO white dwarf accreting mass from the remaining semi degenerate helium remnant of a star stripped of the bulk of its mass before helium could ignite. It is also possible to create AM CVn systems where the secondary has started He-burning, but this stops when its mass (M_2) is stripped down to 0.2 $M_\odot$. During the CE phases the outer hydrogen atmosphere is lost, and the mass transfer is of almost pure helium.

Observations show that the AM CVn stars have orbital periods between 9 and 65 minutes. Patterson et al. 2001 describe how their orbits increase while the mass transfer rate decreases. For the objects with periods more than 15 minutes, the mass is transferred through an accretion disc. Photometry shows that they have nova or dwarf nova like variability. Two of the objects, AM CVn and HP Lib, are stuck in a high, superoutburst state. Warner (1995) argued that these two members are equivalent to H-rich nova-like variables with high mass transfer rate $\dot{M}$, which leads to a stable high state disc. V803 Cen, CR Boo and CP Eri are the helium analogues of the VY Scl stars, moving from high to low states as a result of the disc instability cycle. GP Com is probably a SU UMa analogue, spending long time in the low state with very infrequent outburst.

Some of the AM CVn stars: AM CVn, CR Boo and GP Com are weak, soft X-ray emitters (Ulla 1995). The X-rays come from the accretor or the inner part of the accretion disc (boundary layer), and is evidence for non-magnetic behaviour (Teeseling et al. 1996). A reanalysis of the ROSAT Position Sensitive Proportional Counter (PSPC) data for AM CVn gave as a best fit a blackbody source of temperature $\sim 3 \times 10^6$ K from a hot boundary layer between the disc and the white dwarf (Kellogg et al. 2000).

Table 11 gives some basic parameters for some of the objects of the AM CVn family. In this table P_{orb} is the orbital period, P_{sh} is the superhump period. Data for these periods are mostly for Patterson (2001) and Patterson et al. (2002). The mass ratio $q = M(2)/M(1)$ is determined by the formulae (1) in Warner (1995), except for GP Com and CE 315 where q is determined by spectroscopy. Figure 81 presents the modulation frequencies observed for the AM CVn systems.

Table 11. Basic parameters for some members of the AM CVn family.

Object	**V**	$\mathbf{P_{orb}}$	$\mathbf{P_{sh}}$	**q**
RX J1914+24	>19.7	569		
AM CVn	13-7-14.2	1029	1051	0.084
HP Lib	13.7	1103	1119	0.056
KL Dra	16.8	1502	1531	0.076
CR Boo	13.0-18.0	1471	1488	0.045
V803 Cen	13.2-17.4	1611	1643	0.078
CP Eri	16.5-19.7	1701	1716	0.052
CP Com	15.7-16.0	2790		0.02
CE 315	17.5	3906		0.022

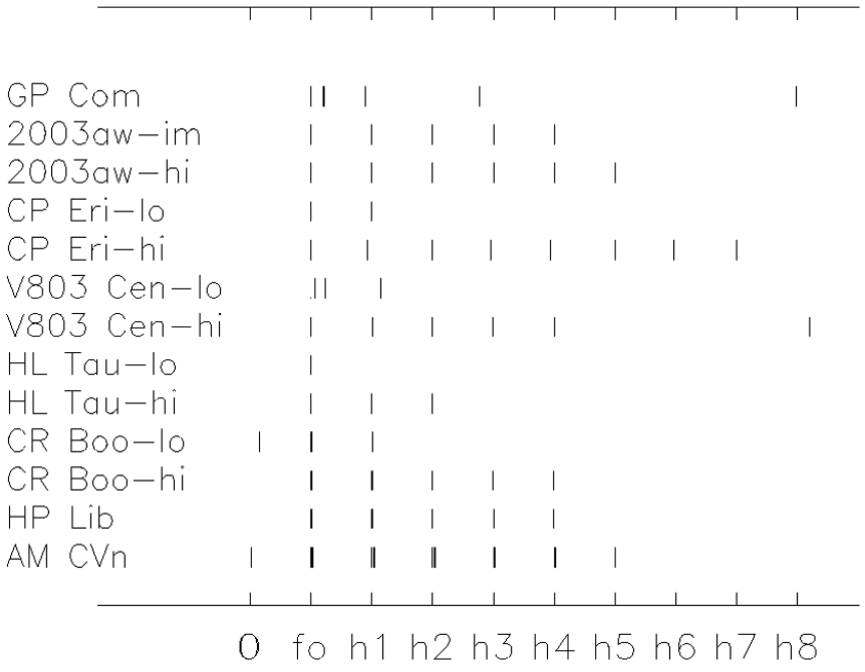

Fig. 82. Modulations frequencies observed for AM CVn objects. Frequencies detected are shown relative to a fundamental frequency f_0 which is the superhump frequency if that is detected, otherwise the orbital frequency. *hn* is the harmonics of number n. The lowest frequency (0) represent Ω: the apsidal advance frequencies.

The analysis presented in this chapter focus on the nova like member of the family: AM CVn and HP Lib. For the AM CVn there has long been controversy on what is the orbital period and what is the superhump period. Based on WET observations in 1990, Provencal et al. (1995) and Solheim et al. (1998), concluded that the period 1051 s was

stable over time and should therefore be the orbital period, even if the period itself was not detected in the FT of the light curve, while the low amplitude 1029 s peak was the superhump period, classifying AM CVn as a negative superhumper. Skillman et al. (1999) observed the star 670 hours over 227 nights in the period 1992-1999 and concluded that P=1029 s is the orbital period and P=1051 s is the superhump period, with 5 harmonics and sidebands representing periods of *apsidal advance* Ω and *nodal regression* N of 13.36 and 16.69 hours, respectively. The apsidal advance period is also observed as a sideband with difference 21 μHz from the harmonic frequencies (Solheim et al. 1998).

The controversy is settled with the detection of a S-wave in spectra folded on the 1029 s period, and at the same time Doppler tomography showing a prominent hot spot superimposed on a weak disc emission when folded on this period (Nelemans et al. 2001).

For the second nova like, HP Lib, Patterson et al. (2002) observed this object in a campaign covering 720 hr over 185 nights and show that the main photometric signal varies between 1118.89 and 1119.14 s on a time scale of a few years, and display a waveform characteristic of superhumps. After subtracting the main signal they found a weak residual signal at 1102.7 s, which they interpreted as the underlying orbital period of the binary. The full amplitude of this variation is just 5 mma. The star showed a remarkable constancy in magnitude and superhump behaviour, and displayed sidebands giving a precession period of Ω=21 hr. It has much more power in the fundamental period and much less power in the harmonics than AM CVn. This may be related to their different angles of inclination and different disc structures.

We report in section 4.2 the use of the statistical method called Intrinsic Period Scatter (Koen & Lombard 1995 -hereafter KL95) which is done to analyse the nature of some modulation frequencies present in the light curves of the AM CVn objects in permanent high state: AM CVn and HP Lib. We report in the next section substantial differences in the amplitudes of the fundamental frequency and its harmonics observed in the temporal spectra of HP Lib in 3 consecutive runs. We interpret this photometric variations as a sign of the presence in the accretion disc of an active density wave which may develop changes in the energy production of the two spiral arms structure over one superhump period. The active density wave model is explained in section 4.4.

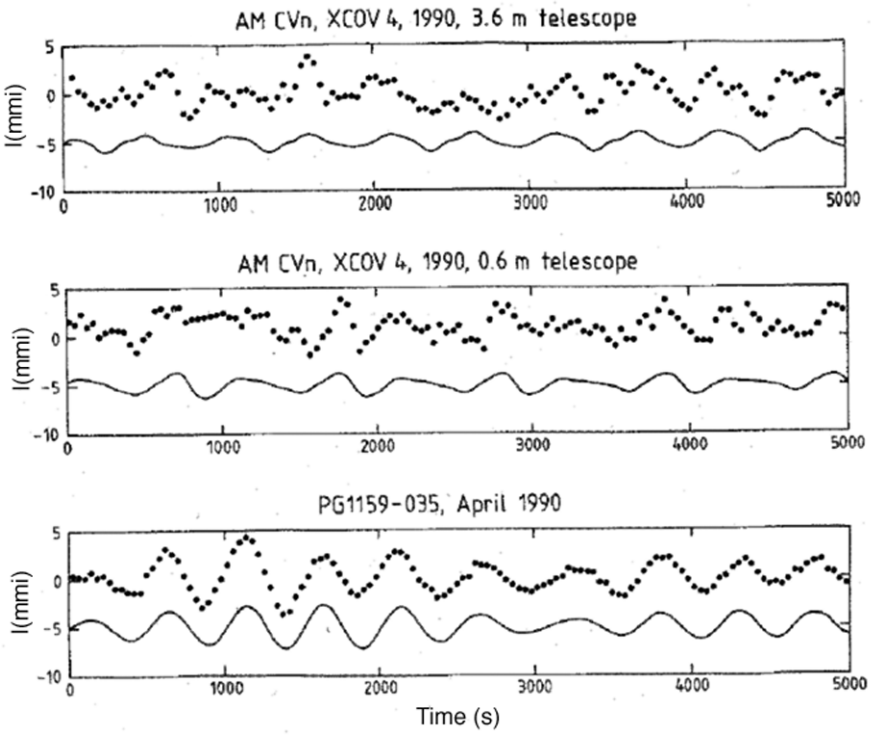

Fig. 83. Part of the light curve of AM CVn (up and middle) and PG1159 (down). The solid curve is a synthetic light curve calculated from the frequencies, amplitudes and phases determined. Figure from Solheim et al. (1998). Even with a large telescope of 3.6 m (upper panel) the light curve has additional 'noise' coming from the star.

4.2. Intrinsic noise

Usually, one of the conclusions after the analysis of a complex light-curve could be the following: something is missing. This is especially important in systems as the AM CVn family: even using data from good coverage campaigns, the comparison of the resulting synthetic light-curve doesn't completely fit with the observations (see figure 82). Moreover, the 'missing' part may provide evidences to better understand the physics related to this kind of systems.

Historically, some previous interpretations of just 'noise' have become extremely important for the understanding of the phenomena. Understanding of the flickering presented in the AM CVn light curves, was the first main clue to interprete it as a binary system with mass transfer (Warner & Robinson 1972). We think that we have still noise left which could provide crucial information of the systems. We can refer to it as 'intrinsic noise', because it belongs to the physical source, and, therefore, it is noise which should be 'listened to'. In the following we will present some simulations of 'intrinsic noise' due

to small deviations from a mean value in amplitudes and phases. This behaviour could be related to some physical sources and therefore, should be differentiated from the pure noise (external to the physical source).

The AM CVn family is a good candidate for this kind of test. The different modulation frequencies that appear in their complex temporal spectra, are related to different physical sources. The main contribution is due to dynamical processes which occur in the disc, as the superhump or the orbital periods. From hydrodynamic accretion disc simulations, the discs in close binary systems with mass ratio less than q=0.25 can be explained as circular disc modified due to tidal shocks (Savonije et al. 1994), which leads to a two-armed spiral structure, and modified by the mode coupling of Lubow (1991), which leads to a three-fold azimuthal symmetry in the outer parts of the disc and a prograde processing wave. This complex geometry of the discs could be the reason for the additional presence of several harmonics of the main modulation frequency. Moreover, some members of the family (CR Boo, CP Eri and V803 Cen) can be found in both high and low states, showing a complete different pattern in the modulation frequencies observed. These changes may be related to such structural changes in the disc. In addition, some new modulations can appear in low state. Their origin could be due to pulsations in the accreting white dwarf, which is now more accessible.

Therefore, we have quite different physical sources to explain the variability of the systems. The different modulation frequencies may present some small differences in behaviour just because of this, like small differences in stability. This could be present in the data, appearing as noise, but being intrinsic to the system and containing information about it. The measurement of the intrinsic noise could help in the understanding of the physical source of the pulsation. The objective is to identify statistical signatures which could relate one modulation frequency with their physical source.

4.2.1. Simulations of intrinsic noise.

We have simulated some possible simple behaviour of intrinsic noise to compare it with an external noise. Basically we produce a synthetic light-curve where each modulation frequency has a phase or amplitude that is not always a fixed value, but a mean value increased or decreased a small amount randomly. The random distribution used is a gaussian distribution (mean zero and small standard deviation), in order to keep a robust mean value and avoid large displacement.

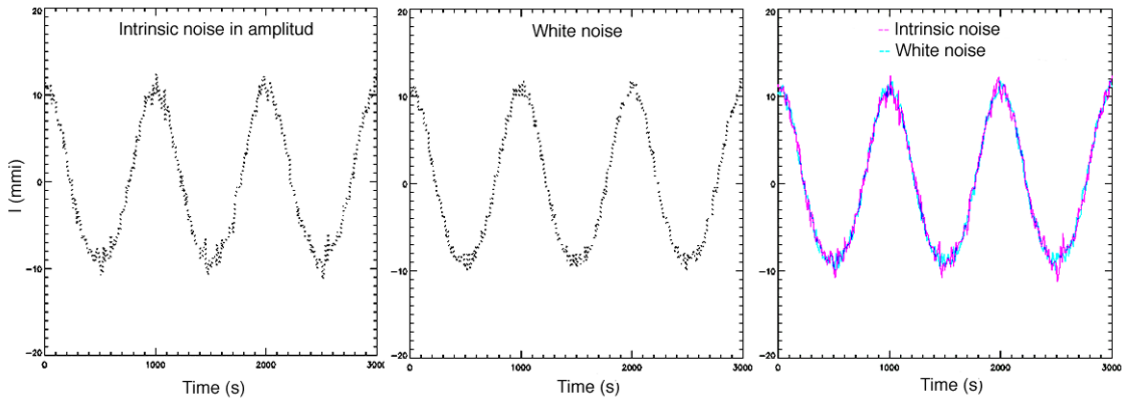

Fig. 84. Intrinsic noise in amplitude: the left panel presents the simulation of intrinsic noise in amplitude, the center panel white noise, and the right panel a comparison between both (see text for details).

The basic 'noise phase' equation can be written:

$$F = \sum_n A_n \cos(2\pi\omega_n t + (\phi_{mean,n} \pm R_n(t))) \tag{11}$$

The 'noise amplitude' equation:

$$F = \sum_n (A_{mean,n} \pm R_m(t)) \cos(2\pi\omega_n t + \phi_n) \tag{12}$$

where $\phi_{mean,n}$ and $A_{mean,n}$ are respectively the mean value of the phase and the mean value of the amplitude for the nth modulation frequency, and $R_n(t)$ and $R_m(t)$ are a normally-distributed (gaussian) random number.

Then, it is added an external white noise a. For this proposes, we used a uniformly distributed sequence of random numbers confine to an adequate interval. Therefore: $F_r = F + a$.

In this chapter we present some simple simulations of the intrinsic noise and the comparation with the white noise. The basic construction of the synthetic light-curve was done by simulation of a sampling time of 10 s and one main modulation period at 1051 s and its first harmonic 525 s; both in phase and with the amplitude of the first harmonic ∼10 times the amplitude of the main frequency. These parameters were taken just as a first approach to the simulation of the light curve of AM CVn.

4.2.2. Simulations of intrinsic noise, results.

1. The amplitude intrinsic noise is especially noticeable in the maxima and minima of the light-curve simulations. It appears as extra jumps in these regions (see figure 83). A

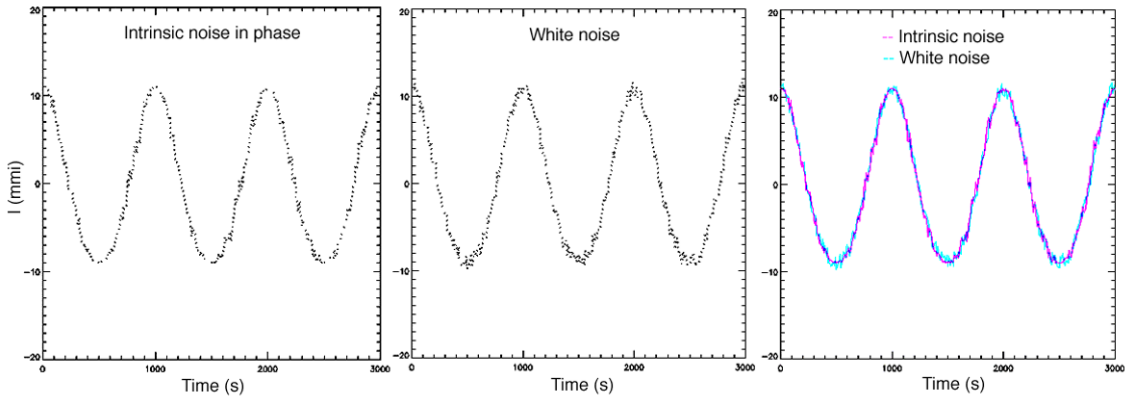

Fig. 85. Intrinsic noise in phase: the left panel presents the simulation of intrinsic noise in phase, the center panel white noise, and the right panel a comparison between both (see text for details).

candidate for such noise is the bright spot phenomena (related to small variations in the brightness of the spot), and may be due to variations in the mass transfer.

2. The phase intrinsic noise has the opposite behaviour: it is not noticeable in the maxima and minima of the light curve, but in the slopes (see figure 84). Variations in phase may be present in the modulations related with the structure of the accretion disc, especially if the spiral arms are modulating the light-curve. If it is true, then variations in the length of the spiral arms are always happening, and it may generate this kind of noise. It may also be due to movement of the accreting bright spot due to variations in the accretion stream.

However, this simulations shows how easy it is to confuse external noise with intrinsic fluctuations. In this direction , the use of statistical methods based in the MA(1) (moving average of order 1), could help in this search. This is the base of the statistical method 'Intrinsic Period Scatter' (KL95). This statistical tool provide information about the amount of intrinsic noise that belong to one light curve. We have tested it on some data from AM CVn and HP Lib and have found 'intrinsic noise' in both of them.

4.2.3. Intrinsic Period Scatter

We concentrate this section on the results obtained using the test Intrinsic Period Scatter (KL95). This method determines when the period jitter is distinct from any measurement error in the determination of pulsation cycle lengths, being intrinsic to the source of the modulation. It is formulated as a special case of the MA(1) model. We will present a

Table 12. Intrinsic Period Scatter results.

Object, run	**Period (s)**	θ_1	**A**	**B**
HP Lib, 1993	1119	0.92 ± 0.24	$2151 \Rightarrow \pm 46s$	$2151 \Rightarrow \pm 46s$
HP Lib, 1998	1119	-0.08 ± 0.19	$5500 \Rightarrow \pm 74s$	$1140 \Rightarrow \pm 34s$
AM CVn	525.6	0.97 ± 0.07	$5147 \Rightarrow \pm 72s$	$5147 \Rightarrow \pm 72s$

reanalysis of some results obtained for AM CVn and HP Lib (Aminzade 1998). The steps to determine the Intrinsic Period Scatter are the following:

1. Identification of maxima in the light curve related with one modulation frequency. This is the critical step because we can only access to the periods with the highest amplitudes in these complex light curves. We look for the maxima associated to the modulation at P=1119 s for HP Lib (main period), and at P=525.6 s for AM CVn (first harmonic). We repat the analysis for two runs for HP Lib, one from April 1993 (run 1), and the other (run 2) from the longest run obtained in the multisite campaign of 1998 (Aminzade 1998, table 13-run2).
2. With these sets of maxima, and using the package MINITAB, we look for the indexes of the model MA(1) for each set. The MA(1) model can be written as follow (see details in KL95):

   $$\eta_t = \theta_l \xi_{t-1} \xi_t \tag{13}$$

   The index θ_l gives a qualitative idea about if there is Intrinsic Period Scatter, $-0.05 < \theta_l < 1$, or not, $-1 < \theta_l < -0.5$. The value $\theta_l = -1$ means pure measurement error.
3. If we find the existence of Intrinsic Period Scatter, we can solve the equations (17) and (18) from KL95 to look for the magnitude of this scatter. It is not possible to obtain the exact value, but we get the range between the maximum and minimum limits possible for it. These maximum and minimum possibilities are represented in the graphs with the letter **A** (maximum) and **B** (minimum). In some cases, they are quite close, so it is possible to set a good unique value for the scatter.

4.2.3.1. Results and comments.

Figure 85 presents the identification of maxima in run 1 due to the modulation period at 1119 s (left panel), and the intrinsic period scatter result (right panel). Figure 86 presents

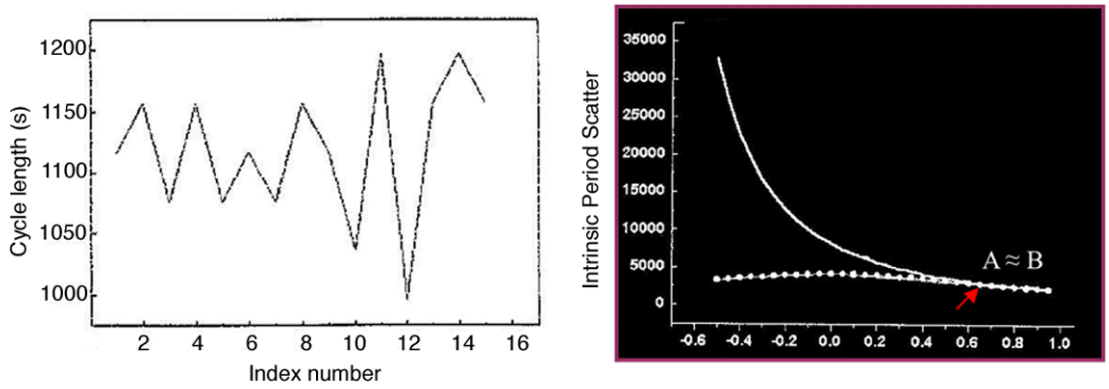

Fig. 86. HP Lib, Intrinsic Period Scatter for run 1: the left panel presents the identification of maxima and the right panel the intrinsic period scatter result. In this panel the horizontal axis gives the index θ_l (see text for details).

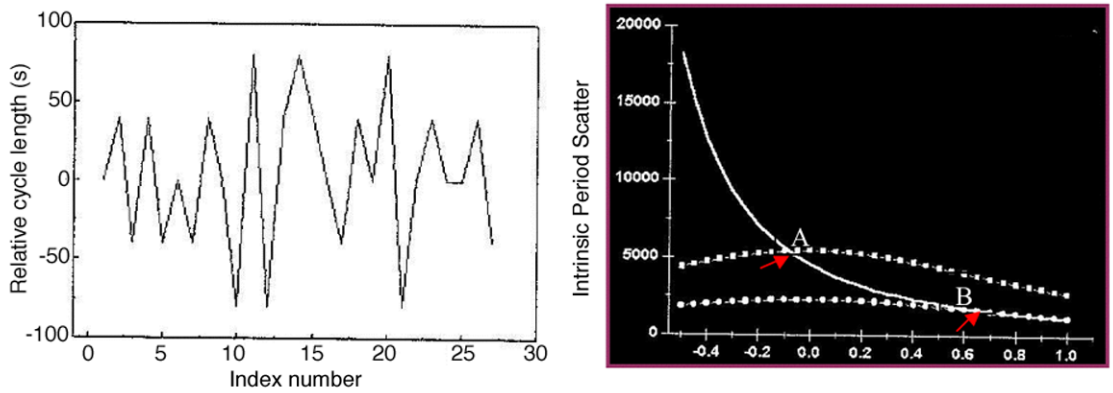

Fig. 87. HP Lib, Intrinsic Period Scatter for run 2: the left panel presents the identification of maxima and the right panel the intrinsic period scatter result. In this panel the horizontal axis gives the index θ_l (see text for details).

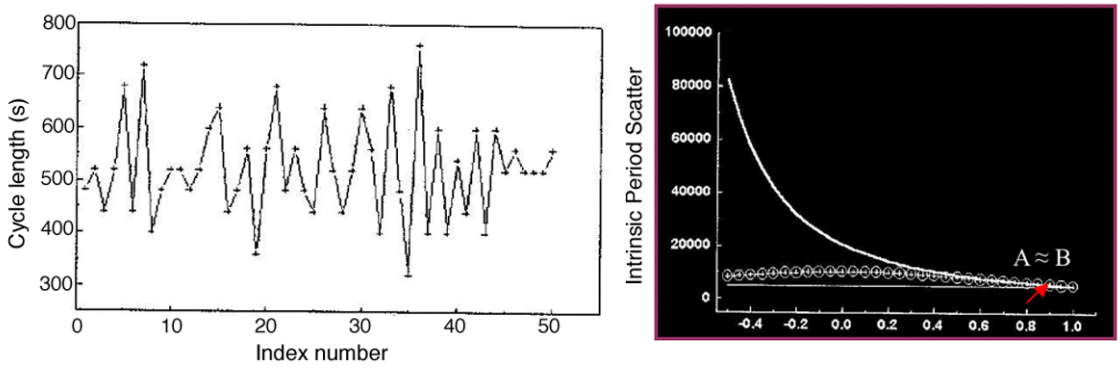

Fig. 88. AM CVn, Intrinsic Period Scatter: the left panel presents the identification of maxima and the right panel the intrinsic period scatter result. In this panel the horizontal axis gives the index θ_l (see text for details).

the same results for run 2 and figure 87 for the AM CVn run. Table 12 summarizes the results obtained.

We repeated the procedure for HP Lib in different single runs from 1993, and all of them were consistent with this intrinsic deviation of $\sim \pm 46$ s. This value is not so different with the interval found for the 1998 run. For this run, a rough average indicates an intrinsic scatter of around ± 54 s. The difference in the determination of θ_l in both runs is due to the differences in the quality of the datas: the run from 1998 contains more external noise. Therefore, the value found for the run 1 is more precise and will be used for the comparison with AM CVn result.

The value found for AM CVn is ± 72 s, which is $\sim$1.5 times higher than the one obtained for HP Lib. In this case the period analysed for HP Lib is its superhump period (Patterson et al. 2002), and the period analysed for AM CVn is the first harmonic of its superhump period. Therefore, both are related to the disc structure.

4.3. Photometric changes in the temporal spectra of HP Lib.

We report in this section changes in the amplitudes of harmonics in the temporal spectra of HP Lib obtained during 3 consecutive nights. Patterson et al. (2002) showed that HP Lib main photometric signal varies between 1118.89 and 1119.14 s on a time scale of a few years, and display a waveform characteristic of superhumps. The authors found a remarkable constancy in magnitude and superhump behaviour. However, we reanalysed some data from a 1998 campaign (Amizande 1998) and found changes in the temporal spectra of 3 consecutive runs.

The observations were done at the 1 meter telescope of Assy Turgen in Kazakhstan the 19th, 20th and 21st of May, using the 3 channels photomultiplier photometer Pancake with no filter (white light), and 10 s for integration time. Table 13 presents information of the runs.

The data have been reduced using the WET software in the standard way described by Nather et al. (1990) and Kepler (1993). Figure 88 presents the temporal spectra obtained for the different runs. The amplitude of the first harmonic changes from the first to the second night. Its peak has nearly the same amplitude as the main period in run 1 ($\sim$ 20 mma). This is the first time that such high amplitude for the first harmonic is observed in HP Lib. The amplitude of this peak decreases in the next runs. The amplitudes for the main period and first harmonic found in runs 2 and 3 are as usually observed (see, e.g.,

Table 13. HP Lib time-series photometry. N_i denotes the number of independent samples, that is, the number of points in the light curve.

Run	Date	Start (UT)	Length (s)	N_i	Resolution (μmp)
1	1998 May 19	19:02:10	10580	1058	94
2	1998 May 20	17:25:00	16010	1601	62
3	1998 May 21	18:38:00	10490	1049	95

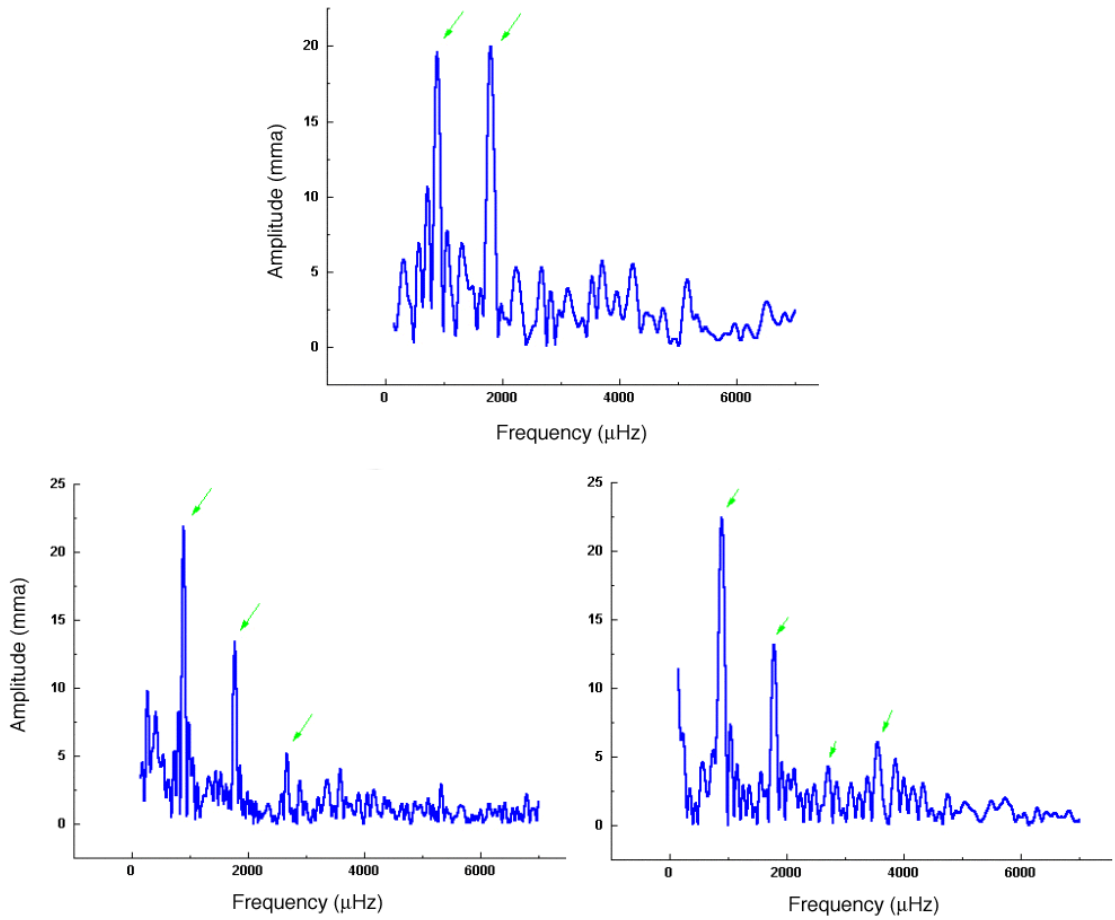

Fig. 89. HP Lib temporal spectra of the run 1 (upper panel), 2 (lower left panel) and 3 (lower right panel). The main peak and harmonics are indicated with arrows. The amplitude scale for the upper panel is different than for the others.

Patterson et al. 2002). The amplitude of the main period in runs 2 and 3 is the same ($\sim$ 22 mma) and slightly higher than the amplitude found in run 1 ($\sim$ 20 mma). The amplitudes found for the second and third harmonics are also different in runs 2 and 3: the amplitude of the second harmonic is nearly the same in both runs ($\sim$ 5 mma) but slightly higher in

Table 14. HP Lib pulsation fequencies. The frequencies are presented in μHz. Below each modulation frequency, is shown the amplitude in mma.

Run	f	h_1	h_2	h_3
1	890	1802		
	(19.5)	(20)		
2	894	1774	2668	3590
	(22)	(13)	(5)	(4)
3	897	1788	2707	3551
	(22)	(13)	(4)	(6)
P(s)	∼1117	∼558	∼372	∼279

run 2. The amplitude of the third harmonic has increased ∼ 2 mma from run 2 to run 3, and is higher than the amplitude for the second harmonic in the last run. Table 14 summarizes these results.

This changes in the amplitude of the harmonics in consecutive nights may be due to rapid changes in the structure of the accretion disc. We have analysed in more detail this phenomena, looking for possible changes in amplitude during each run. This has been done by using the wavelet analysis described in chapter 3. We have used Morlet wavelet function order 6 (see section 3.2.3 for details). This time the output of the wavelet is given in amplitude (mma), to compare easily with the temporal spectra presented. Wavelet analysis has been done on runs 1 and 3. Figure 89 presents the results obtained for run 1 and figure 90 for run 2.

The wavelet analysis of the runs 1 and 3 shows different photometric behaviour. During run 1 the amplitude of the main peak at 890 μHz (period ∼1123 s) changed during the night. The amplitude is constant during the first section of the night, ∼18 mma, but starts to decrease ∼4000 s after the beginning of the run, reaching a minimum value, ∼10 mma, around the second 5000. The amplitude increases again towards the last section of the night reaching the highest value registered during the run (∼22 mma), which is constant during the last 2000 s.

The first harmonic also changes amplitude during the night. The amplitude is ∼10 mma during the first section of the run (firsts ∼3800 s), but starts to increase around the time that the amplitude of the main peak decreases. The amplitude of this first harmonic is found to be relatively high (∼18 mma) during 2 parts of the run of around 1200 s each. This time is close to the superhump and orbital periods. The high amplitude for the first

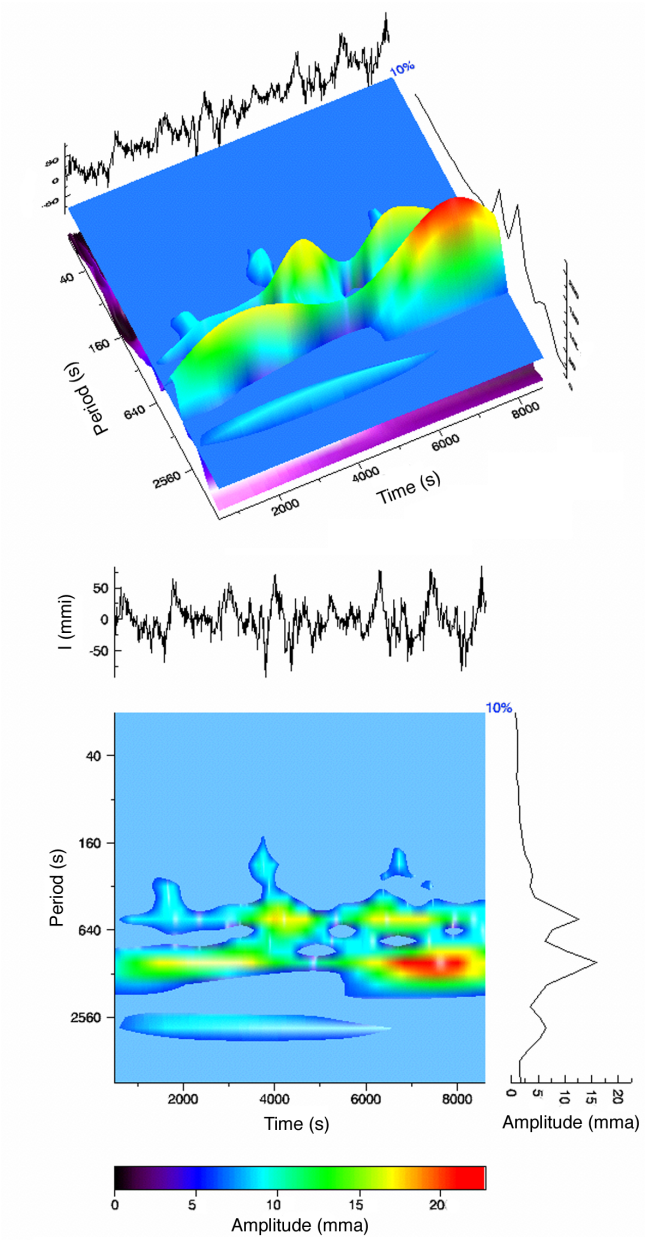

Fig. 90. HP Lib wavelet analysis of the run 1. The upper part of the figure shows the wavelet result in 3 dimensions (3D) and the lower panel in 2D. The light curve of the run is presented on the top of both panels.

harmonic is concentrated around two modulations of the superhump period which have pulse forms presenting a pronounced double humped structure. The first time this high amplitude is found when the main period goes into a minimum amplitude but, during the second time, ∼4000 s after the beginning of the run, both modulation periods increases at the same time in amplitude. The wavelet also presents two regions related to the third

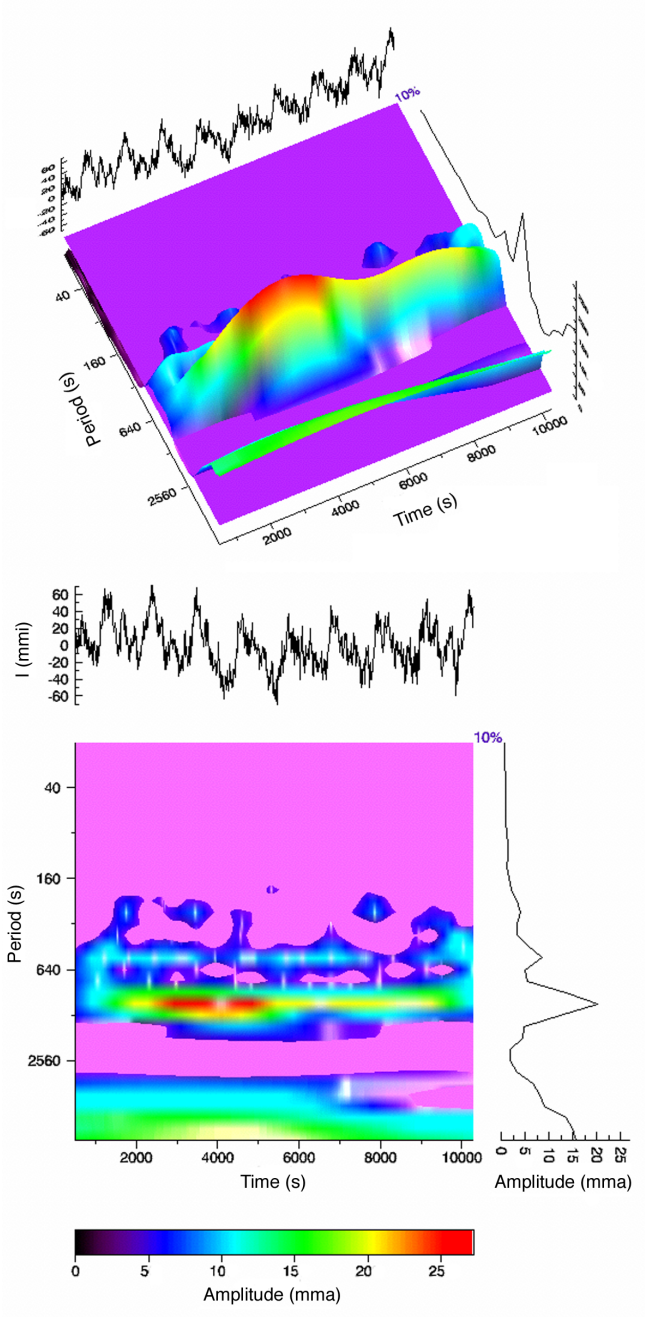

Fig. 91. .

HP Lib wavelet analysis of the run 3. The upper part of the figure shows the wavelet result in 3D and the lower panel in 2D. The light curve of the run is presented on the top of both panels.

harmonic period but with low amplitude and confined in short time intervals (∼500 s). The first is found around the second 3900 and the second around the second 6800. This feature is more clear in run 3.

The wavelet analysis of the run 3 presents a more stable amplitude for both the main period and first harmonic. The amplitude of the main peak is relatively constant during the whole run. The first section of the night shows an amplitude ∼24 mma, and the second ∼20 mma. The value found in the temporal spectrum for this run was 22 mma. The first harmonic also shows constant amplitude during the whole run ∼12 mma. However we found two small intervals in time where the amplitude decreases a little: around the seconds 4000 and 5500.

An interesting feature in the wavelet analysis of the run 3 is the presence of amplitude (∼10 mma) for the second harmonic during three short intervals of time (∼ 500 s). These are found around 1800, 3300 and 4800 s after the beginning of the run. There is a relation between the places where this amplitude for the second harmonic is found and the pulse form of the main modulation in the light curve. This is clearly seen comparing the wavelet analysis in the 2D representation and the light curve which is presented above it. The pulse shape has a triple humped structure around the time this amplitude is found. The pulse shape in the other regions presents a double humped structure which is slightly less pronounced than during the run 1 (see figure 90).

4.4. Accretion Discs in AM CVn systems.

Simpson and Wood (1998) explain the light curves of dwarf novae superhumpers in general and the AM CVn high state systems in particular by simulating energy production time series in smoothed particle hydrodynamics (SPH) accretion discs. The authors present simulations for 4 mass ratio: 0.025, 0.05, 0.075 and 0.1. The three larger mass ratio models develop progradely precessing discs (viewed in the orbital plane), whereas the model q=0.025 does not. For the three larger mass ratios the periodic flux variations are mainly the results of changes in the viscous energy production as the discs experience tidal stress and oscillate between nearly circular and highly distorted shapes over a superhump period. Thus, for these models, it is the changes in the disc shapes over a superhump period that causes the superhump modulation. In addition, for mass ratios close to AM CVn and HP Lib values, spiral waves rotate about 1.5 time per binary orbit, in agreement with Lubow (1991). The authors suggest that the rotation of these spiral waves could lead to an observed frequency of about 3 times the superhump frequency, as well as some additional harmonics if viewed from a nonzero inclination. The double-armed spiral density waves extend deeply into the interiors when the discs are nearly circular, while being located

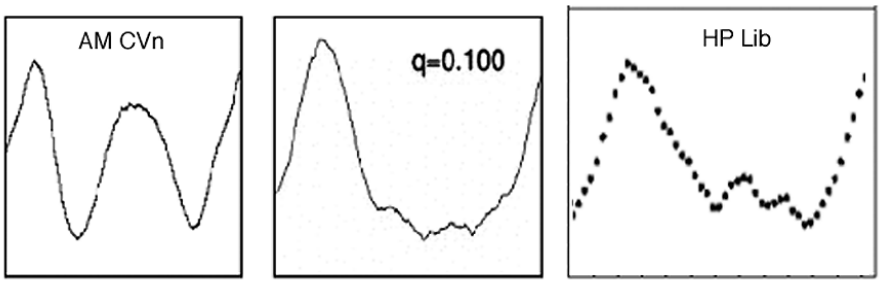

Fig. 92. Double humped average pulse shape of AM CVn superhump period (left) and HP Lib (right) compared with output from SPH (middle).

only around the disc edges when the discs are eccentric. Based on these simulations, synthetic pulse shapes were produced to analyse the corresponding FT and compare with observations.

The results obtained by Simpson and Wood (1998) fit well the average pulse shape of HP Lib but present differences with the temporal spectra and pulse shape of AM CVn (see Fig 91). The main characteristics present in SPH simulations are: the main period (superhump) is always present, and the first harmonic amplitude is ∼15% of the main period amplitude for inclination ∼ 30°. However, from observations: the main period is not present in AM CVn temporal spectra (Solheim et al. 1998). In HP Lib, the first harmonic amplitude is ∼60% the main period amplitude (estimated inclination 30°), therefore 4 times higher than the SPH prediction. In addition, we have reported in the previous section rapid changes in the amplitudes of the first harmonic of HP Lib reaching one night the superhump amplitude. The pulse shape obtained from the simulations does not reproduce the pronounced double humped structure observed for the superhump pulse shape in AM CVn (see figure 91).

4.4.1. Active density wave model

To explain these photometric properties, we propose to consider the existence of an active density wave in the disc related to the m=2 spiral wave and how it interacts with the matter of the disc. The domain of the existence of the spiral density wave is confined between the inner and outer Linblad resonances, which covers a large fraction of the disc for extreme mass ratio objects. From AM CVn, SPH results show that the external resonance of the spiral waves is quite close to the end of the accretion disc and stable, while the inner

resonance vary during one superhump period, reaching a deeper inner radius when the viscosity energy level is small.

The distribution of velocities of the matter in the disc and the spiral density wave itself is different and may develop big areas in the disc where supersonic shocks are possible. This event could modulate the light curve. We have considered a keplerian distribution of velocities for the matter of the disc and compare it with the wave velocity which rotate as a rigid body around 1.5 times per superhump period.

The supersonic shocks happens when the difference of velocity between the density wave and the matter of the disc is higher than the local sound velocity. This difference is especially noticeable in the inner part of the accretion disc. The velocity of the matter in the inner part of the disc is V_{in}=2340 km/s and in the outer part V_{out}=860 km/s (Patterson et al. 1993). The disc in AM CVn extends from 1.4 times the radius of the central white dwarf (R_{in}=1.5 $R_\star$) to R_{out}=17.5 $R_\star$ (Nasser 2001). The density wave rotates as a rigid body 1.5 times per superhump period (1051 s) which gives a velocity for the wave at the inner radius: $V_{w\ in} \sim 57$ km/s.

The local sound velocity for an helium disc is:

$$V_{sound} = 5\sqrt{\frac{T}{10^4}}\ km/s, \tag{14}$$

where T is the local temperature. The distribution of temperatures in the disc varies from ∼100000 K in the inner part to ∼20000 K in the outer (Nasser 2001). We used T=100000 K to calculate, using the equation 14, the sound velocity in the inner area of the disc:

$$V_{sound\ in} = 15.8\ km/s \tag{15}$$

Therefore, $V_{in} - V_{w\ in} \gg V_{sound\ in}$, so supersonic shocks may happen in this area. We have repeated the calculations for the outer disc radius and have also obtained a difference of velocities higher than the local sound velocity. Therefore, these supersonic shocks are happening in the whole disc. However, the difference in velocities is higher in the inner areas.

To explain the first harmonic, we propose the combination of the tidal stress results of the SPH simulations plus the action of the active density wave. Then, in one superhump period, the system reaches two maxima levels of energy. From SPH simulations, the disc tidal stressing reaches one maximum in the viscous energy production when the oscillation goes over a highly distorted shape, and one minimum when it is nearly circular. But when

the disc is nearly circular, the domain of existence of the density wave grows significantly covering more area of the disc. This is especially noticeable at the Linblad inner resonance. Therefore, the area of possible supersonic shocks also grows and the system can go into a secondary maximum, and develop a double humped light curve as observed for AM CVn (see figure 92). The active density wave may help to explain the high amplitude of the first harmonic in AM CVn. To get rid of the fundamental period, the two peaks have to be equal.

To explain the second harmonic notice that the effect of the active density wave in the light curve may be more important at higher angles since the relative contribution of the spiral arms facing the observer is higher than the more obscured opposite spiral arm. This may modulate three times per superhump frequency the light curve, since the observer sees three times a spiral arm in one superhump period. The amplitude values for the second harmonic in AM CVn and HP Lib are consistent with this description since the average value for the first object is 2.9 mma (Solheim et al. 1998) (estimated angle around 45°) while for the second it is lower: 1.8 mma (30°).

4.5. Discussion

In this chapter we have analysed light curves of the two AM CVn objects which are in permanent high state: AM CVn and HP Lib. We have used some statistical methods searching for properties of the different pulsation frequencies. This may help to understand the nature of the physical process which is modulating the light curve at a particular frequency. Our first approach was done by using the statistical method Intrinsic Noise Scatter (KL95) over the main period (superhump) of HP Lib, and the first harmonic of the superhump period in AM CVn. We have found that both periods have intrinsic noise ('phase jitter'), having the first harmonic of AM CVn more than the main period in HP Lib.

We have also presented temporal spectra on three consecutive runs for HP Lib presenting changes in the amplitude of the main period and harmonics from run to run. This is especially noticeable in the first harmonic, which has the same amplitude as the main period during the first run, but decrease ∼7 mma in the temporal spectrum of the next run. The wavelet analysis indicates that the presence of amplitude in the first and second harmonic depends of the pulse shape of the main period. Each superhump pulse shape is slightly different to the previous one. In average, it presents a double humped structure

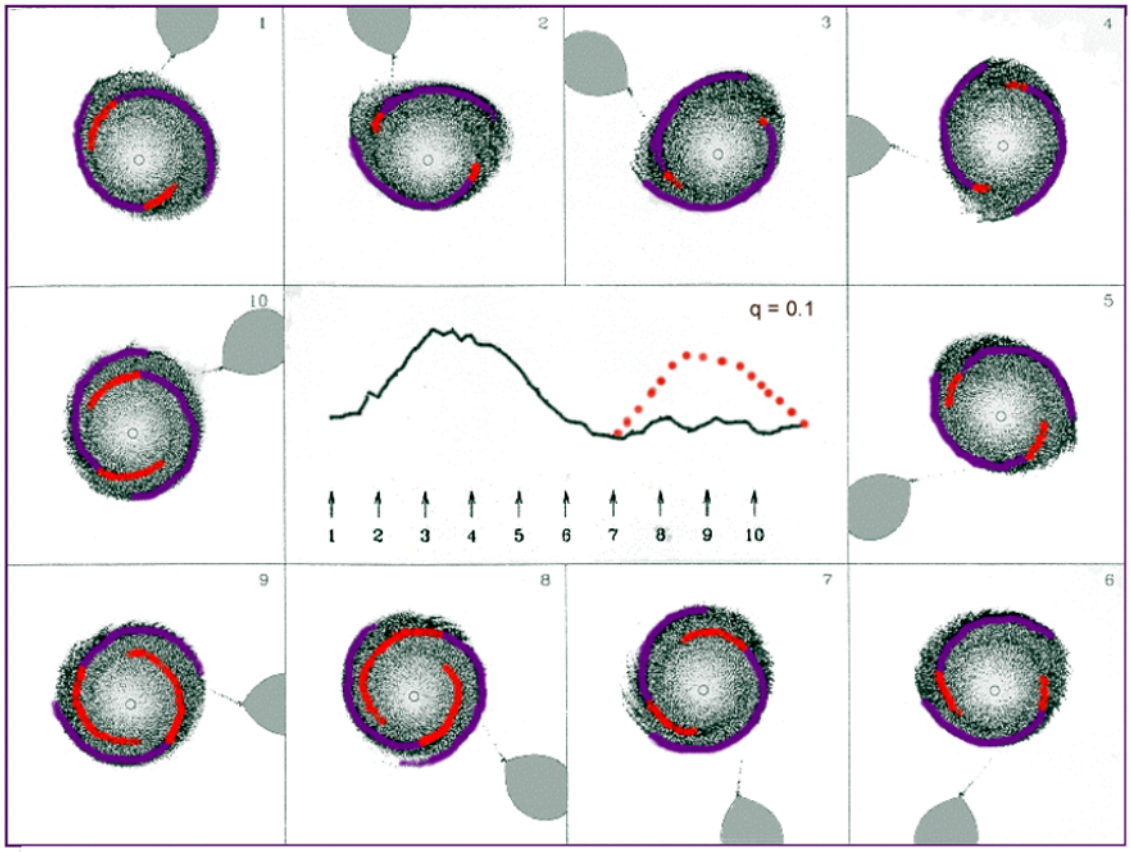

Fig. 93. Active density wave in AM CVn. The red part shows how the inner Linblad resonance of the spiral density wave varies dramatically over one superhumps period. This may modulate the light curve since the area where supersonic shocks are produced also change substantially. This mechanism will generate more energy exactly when the viscosity energy from SPH models goes into a minimum. The combination of both mechanisms could develop a strong 1st harmonic and a double humped pulse shape over a superhump period (see red points). This graphs have been based in the figure 10 of Simpson & Wood (1998).

which can be more or less pronounced from pulse to pulse. At some occasions the pulse form presents a triple humped structure with the presence of three peaks during the pulse shape. The second harmonic is only present when this triple humped pulse form appears. The temporal spectrum displays an average over several pulses and, therefore, the average of the relative amplitudes of the different pulses for the harmonics. However, we have showed with the wavelet analysis that the power, especially for the second harmonic, is confined to short intervals of time.

The average pulse shape presented for NGC 246 for the 4350 s period (see chapter 3), showed different average shapes for the different runs. Some of them have a clear double humped structure and others a triple humped, which resemble the different pulse shapes

found for HP Lib during runs 1 and 3 for the superhump modulation frequency. This may indicate that an accretion disc may be responsible for the 4350 s period harmonic structure found for NGC 246, and this period may be the orbital or superhump period. However, in the NGC 246 case, several pulses have a triple humped shape and, for these runs, the temporal spectra show the presence of power in the main peak and second harmonic but lack the first.

This may indicate that there is a competition between the physical process producing structures in the accretion disc which modulate the light curve one, two and three times per superhump period. In AM CVn this modulation twice per superhump period is dominating, and this object present clear double humped pulse form. For HP Lib, the process originating at the superhump period is dominating. The modulation twice per superhump has also high amplitude which may change in time scale of hours. For this object we have found at some occasions, that is, during some concrete superhump periods, that the process modulating the light curve three times per superhump period is also strong. For NGC 246 case, the latest process seems to be dominating.

In the last section we have presented the active density wave model as an attempt to try to add to the SPH simulations (Simpson and Wood 1998) to explain the photometric behaviour of the accretion disks in AM CVn systems in high state. This model is based on the extra energy generated when the inner Linblad resonance varies during one superhump period, reaching a deeper inner radius when the viscosity energy level is small. This changes the area in the accretion disk where supersonic shocks are produced, increasing it when the disc has a more circular shape. From SPH simulations, the disc tidal stress reaches one maximum in the viscous energy production when the disc has a highly distorted shape, and one minimum when it is nearly circular. Therefore, two maxima may be reached when considering the action of an active density wave and the SPH simulations. These may produce a clear double humped structure and higher amplitude for the first harmonic in the temporal spectrum.

The average pulse shapes presented for NGC 246 (see section 3.3.6), have in many runs a triple humped structure. The temporal spectra presents in several cases power in the second harmonic but not in the first harmonic. This may indicate a no precessing disk and a mass ratio $q \lesssim 0.025$. Simpson and Wood (1998) SPH models for q=0.025 showed only random energy production (noise). The relative positions of the secondary star, the double armed spiral density wave, and the disc were stationary. No disk precession was observed

in this model. However, the authors indicate that, if an observer viewed this system at a high inclination angle, the orbital period should be evident from geometrical effects and, in addition, the observer may also see the second harmonic because the spiral arms wave points to the observer three times per orbital period. Another option, which may allow a higher mass ratio for NGC 246, is the presence of an unstable disc. In some occasions the disc may be large enough to reach the 2:1 resonance but no the 3:1 resonance. In this case a clear double armed spiral density wave appear but a lack of precession is observed (Simson & Wood 1998, Lubow 1991).

Acknowledgment: I wish to thanks Ramin Aminzade for his help with the Intrinsic Period Scatter method and Jan-Erik for the fruitful and constructive discussions, and patient revision of the earlier versions of the chapter.

References

Aminzade, R. 1998, Cand. Scient. Thesis, University of Tromsø

Iben, I. Jr., Tutukov, A. V. 1991, ApJ, 370, 615

Kellogg, E. M., González Pérez J. M. & Solheim, J.-E. 2000, http://www.astro.keele.ac.uk/workshop/xray/main.htm

Kepler, S.O. 1993, Baltic Atronomy, 2, 515

Koen, C., & Lombard, F. 1995, MNRAS, 274, 821 (KL95)

Lubow, S. L. 1991, ApJ, 381, 259 & 368

Nasser R. M. 2001, PhD thesis, University of Tromsø

Nather, R. E., Winget, D. E., Clemens, J. C., Hansen, C. J., Hine, B. P., 1990, ApJ, 361, 309

Nelemans, G., Steeghs, D., & Groot, P. J. 2001, MNRAS, 336, 621

Patterson, J. 2001, PASP, 113, 736

Patterson, J., Fried, R. A., Rea, R. et al. 2002, PASP, 114, 65

Patterson, J., Halpern, J., & Shambrook, A. 1993, ApJ, 419, 803

Provencal, J. L., Winget, D. E., Nather, R. E. et al. 1997, ApJ, 480, 383

Savonije, G. J., Papaloizou, J. C. B., & Lin, D. N. C. 1994, MNRAS, 168, 13

Simpson, J. C., & Wood, M. A. 1998, ApJ, 506, 360

Skillman, D. R., Patterson, J., Kemp, J. et al. 1999, PASP, 111, 1281

Solheim, J.-E., et al. 1998, A&A, 332, 939

Teseling, A., Verbunt, F. 1994, A&A, 292, 519

Ulla, A. 1995, A&A, 301, 469

Warner, B., & Robinson, E. L. 1972, MNRAS, 159, 101

Warner, B. 1995, Ap&SS, 225, 249

Chapter 5

Testing the evolution of the DB white dwarf GD 358: First results of a new approach using asteroseismology

Abstract.

This chapter will present a method which analyses the possible evolutionary history of the DB white dwarfs GD 358 using asteroseismology. This is done by computing the relation between pulsation periods and the internal C/O profiles, which describe the relative abundances of carbon and oxygen from the core of the star to its surface. Different evolutionary channels lead to the generation of different C/O profiles. We have tested and compared profiles associated with binary evolution where the object experienced one or two episodes of mass lost during one or two common envelope phases, and have also analyzed a profile related with single star evolution. We compute the different profiles and use a genetic algorithm GA (Metcalfe et al. 2000) to optimize the search in the parameters space: mass and temperature of the star, and helium mass of the external layer, to find the best fit to the pulsations periods for a given profile. This is done for different profiles. Our first results suggest that binary evolution describes better the pulsations periods of GD 358. The best fit to the observations uses a profile related to an evolutionary history where two episodes of mass loss happen during two common envelopes phases, the first one during the RGB stage. The values obtained are T_{eff}=22 700 K , $M_{\star}$=0.662 $M_{\odot}$, $log(M_{He}/M_{\star})$=-2.79, which are close to previous fits using GA (Metcalfe et al. 2000, 2001). The best fit model has a mass and temperature marginally consistent with those inferred from spectroscopy, and a thick outer layer of helium.

'From Close Binary White Dwarfs to White Dwarfs': J. M. González Pérez, e-mail: jose@phys.uit.no

5.1. Pulsating DB white dwarf stars

Pulsating stars are found among white dwarfs. Almost every star in our Galaxy will eventually become a white dwarf. Since they are relatively simple compared to main sequence stars, white dwarfs provide one of the best opportunities for learning about stellar structure and evolution. Their interior structure contains a record of the physical processes that operate during the later stages in the lives of most stars, so there is a potential wealth of information encoded in their pulsation frequencies. The observational requirements of white dwarfs asteroseismology have been addressed by the development of the Whole Earth Telescope (Nather et al. 1990).

There are presently three known classes of pulsating white dwarfs. The hottest class is the planetary nebula nucleus variables (PNNVs), which have atmospheres of ionized helium and are also called DOVs. These objects require detailed calculations that evolve a main sequence stellar model to the pre-white dwarf phase to yield accurate pulsation periods. The two cooler classes are the helium-atmosphere variable (DBV) and hydrogen-atmosphere variable (DAV) white dwarfs. The pulsation periods for these objects can be calculated accurately by evolving simpler, less detailed models. The DAV stars are generally modeled with a core of carbon and oxygen with an overlying blanket of helium covered by a thin layer of hydrogen on the surface. The DBV stars are the simplest of all, with no detectable hydrogen and only a helium layer surrounding the carbon/oxygen core. Robinson et al. (1982) and Kepler (1984) demostrated that the variable white dwarf stars pulsate in non-radial gravity modes. The study of their pulsations has allowed us to measure the stellar mass and composition layers, to probe the physics at high densities, including crystallization, and has provided a chronometer to measure the age of the oldest stars and consequently, the age of the Galaxy.

The helium-atmosphere DB white dwarf stars are very interesting from the standpoint of stellar structure and evolution. The chemical evolution of their atmospheres cannot be satisfactorily explained to date (see Shipman 1997 for a review). In particular, the presence of the so-called DB gap, which is the absence of DB white dwarfs between temperatures of ∼30 000 - 45 000 K (Liebert 1986), is poorly understood. It is also not clear whether DBs are mostly produced by single-star evolution or whether a significant fraction of them originates from binary progenitors. The examination of these problems can be aided by asteroseismology. Compared with other classes of pulsating stars, the DBVs are promising

Table 15. GD 358 identified frequencies for l=1, from 1990 WET campaign (Winget et al. 1994).

k	**Frequency** (μHz)	**Power** (μmp)	**Period** (s)
8	2362.56	24.8	423.27
9	2154.10	20.5	464.23
10	1993.68	1.2	501.59
11	1845.88	1.8	541.75
12	1733.88	1.8	576.76
13	1617.38	33.4	618.28
14	1518.95	69.7	648.35
15	1427.27	362.1	700.64
16	1361.85	12.0	734.30
17	1297.58	210.7	770.67

candidates for asteroseismology: their mode spectra are shown or believed to be rich, and a pulsation theory for these stars is quite advanced and well tested.

GD 358, also called V777 Herculis, is the prototype of the DBVs and is one of the classical examples of the application of asteroseismological methods (Winget et al. 1994; Vuille et al. 2000). GD 358 was the first pulsating star detected based on a theoretical prediction (Winget et al. 1985), and is the pulsating star with the largest number of periodicities detected after the Sun. Detecting as many modes as possible is important, as each periodicity detected yields an independent constraint on the star's structure. When the Whole Earth Telescope observed GD 358 in 1990, 181 periodicities were detected, but only modes from radial order $k = 8$ to 18 were identified, most of them showing triplets, consistent with the degree $l = 1$ identification. Table 15 shows the identified frequencies for l=1 in the interval 1000-2400 μHz, from 1990 WET data (Winget et al. 1994). Asteroseismological analysis on GD 358 has been a successful tool to test the pulsation theory. For instance, the central oxygen abundance of the models has been shown to have a measurable effect on the pulsations frequencies (Metcalfe, Winget & Charbonneau 2001), and the possible presence of a ^{3}He/^{4}He transition zone caused by chemical diffusion has also been shown to produce a measurable effect (Montgomery, Metcalfe & Winget 2001), although recent observations have ruled out this latest possibility (Wolff et al. 2002).

Metcalfe et al. (2001), hereafter M1, and Metcalfe et al. (2002), hereafter M2, used GD 358 observed periods from Winget et al. (1994) to search for the optimum theoretical

model with static diffusion envelopes. This search was based in the application of a genetic-algorithm-based optimization (GA) to white dwarf pulsation models, which perform global searches and provide objective global best-fit models for the observed pulsation frequencies (Metcalfe et al. 2000), here after M0. The best fit obtained has a thick helium layer which may help to understand the evolutionary connection between PG 1159 stars and the DBVs. The helium layer mass for PG 1159-035 from the asteroseismological investigation of Winget et al. (1991) was also relatively thick, at $\sim 3 \times 10^{-3} M_{\odot}$. The original best-fit model for GD 358 by Bradley & Winget (1994) had a relatively thin helium layer, at $\sim 1.2 \times 10^{-6} M_{\odot}$ which posed a problem to associate this star with PG 1159 progenitors in the cooling sequence. The thick envelope solution may also relate GD 358 to an end result of close binary evolution. Some interacting close binary systems are thought to be a CO degenerate core accreting helium from a close companion. These system are called helium cataclysmic-variables or He CVs (Iben & Tutukov 1991). The process of accreting helium may generate a peculiar white dwarf with a thick outer layer of this element.

5.1.1. $^{12}C(\alpha,\gamma)^{16}O$ *versus triple-*α

The interior structure of the white dwarfs contains a record of the physical processes that operate during the later stages in the lives of most stars. The distribution of the ratio C/O depends on the evolution of the star. Stellar evolution theory predicts that a big number of WDs are post Asymptotic Giant Brach (AGB) stars, therefore they should consist of the primary ashes of He-burning, i.e. carbon and oxygen. The central ratio C/O depends on the interplay between the 3-α and the $^{12}C(\alpha,\gamma)^{16}O$ reactions during the core helium burning phase. In the first part of the burning the most efficient process is the triple-α, which produces ^{12}C. When the central abundance of helium decreases below about 0.15 $M_{\star}$, the production of ^{16}O via the $^{12}C(\alpha,\gamma)^{16}O$ becomes the dominant process.

While they are still embedded in the cores of red giant models, the internal chemical profiles of white dwarfs models show a relatively constant C/O ratio near the center, with a size determined by the extent of the helium-burning convective region. The degree of mixing at the edge of this region is unknown, so a convective overshooting parameter is used to investigate the effect of different assumptions about mixing. With no convective overshooting, the final C/O ratio is constant out to the 50% mass point, while with the convective overshooting the central oxygen mass fraction is unchanged a the level of a few percent, but the region with C/O ratio extends out to the 65% mass point. Further

out in both cases the oxygen mass fraction decreases as a result of the helium-burning shell moving towards the surface of the red giant model while gravitational contraction causes the temperature and density to rise. This increases the efficiency of the triple-α reaction, producing more carbon relative to oxygen. The central oxygen mass fraction is lower in higher mass white dwarfs models. The rate of the triple-α reaction increases faster at higher densities than does the $^{12}C(\alpha,\gamma)^{16}O$ reaction. As a consequence, more helium is used up in the production of carbon, and relatively less is available to produce oxygen in higher mass models.

Therefore, the ratio carbon/oxygen is different from the center of the WD to its surface. This distribution of C/O creates C/O profiles that contains information about the physical processes that took place at different internal radii of the star, and record the evolutionary stages it has gone through during its previous evolution. Different evolutionary histories will create different C/O profiles (e.g. see Iben & Tutukov 1985 -hereafter IT85-)

5.1.2. C/O profiles.

Metcalfe et al. (2001) demonstrated that the pulsations periods in their white dwarfs models are sensitive to the shape of the C/O profiles. This opens a possibility that may help to investigate intrinsic characteristics of pulsating white dwarfs. The tests of different C/O profiles in white dwarfs models can be used as a tool to study physical processes relevant to white dwarfs model interiors, such as convective overshooting and crystallization, and also as a method to investigate the evolutionary model that fits better the observational data.

M0 used a three-parameter model including the total mass ($M_\star$), the effective temperature (T_{eff}), and the mass of the atmospheric helium layer (M_{He}) to search for, using a genetic-algorithm-based optimization (GA), the best-fit model. They obtained fits for six different combinations of core composition and transition profiles: pure C, pure O, and both "steep" and "shallow" transition profiles for 50:50 and 20:80 C/O cores (see Bradley et al. 1993; Bradley & Winget 1994). Mixed C/O shallow profiles produced better fits, and, among them, the 20:80 mix produced the best. The results showed that both the initial central oxygen abundance and the shape of the profile affect the pulsation pattern. Table 16 presents the results obtained by M0 for these different profiles. The quality of the fit is indicated by the period residual (r.m.s.) which is obtained by comparing the models with the observed periods.

Table 16. M0 three-parameter best models for different profiles. The best-fit is indicated with bold letters.

Profile	T_{eff} **(K)**	$M/M_{\odot}$	$log(M_{He}/M_{\star})$	r.m.s. (s)
pure C	20 300	0.795	-5.66	2.17
	23 100	0.655	-2.74	2.30
50:50 C/O "shallow"	22 800	0.665	-2.00	1.76
	23 100	0.610	-5.92	2.46
50:50 C/O "steep"	20 700	0.630	-5.97	2.42
	24 300	0.625	-2.79	2.71
20:80 C/O "shallow"	20 600	0.650	-2.74	**1.50**
	23 100	0.605	-5.97	2.48
20:80 C/O "steep"	22 900	0.630	-5.97	2.69
	27 300	0.545	-2.16	2.87
pure O	20 500	0.805	-5.76	2.14
	23 400	0.655	-2.79	2.31

M1 modified the code to include as free parameters any central oxygen mass fraction (X_0) between 0 and 1 with resolution 1% and a fractional mass parameter (q). The GA fitting process explored different chemical profiles built in the following way: the value X_0 was fixed to its central value out to q that varied between 0.1 and 0.85 with resolution 0.75%. From this point X_0 decreased linearly in mass to zero oxygen at the 95% mass point. This simple parameterization generalized the M0 "steep" and "shallow" profiles. The results of this extension of the GA approach showed that the initial three parameters ($M_{\star}$, T_{eff}, M_{He}) remains identical in the five-parameter fit ($M_{\star}$, T_{eff}, M_{He}, X_0, q) so they are the most important parameters for matching the gross period structure. However, significant improvement to the fit was possible by including X_0 and q as free parameters, confirming that the observed pulsations really contain information about the hidden interiors of the stars. The best fit obtained was: $T_{eff} = 22.600K$; $M_{\star} = 0.650M_{\odot}$; $log(M_{He}/M_{\star}) = -2.74$; $X_0 = 0.84$; $q = 0.49$. The fit quality is better than in the previous case with a period residual (r.m.s.) of 1.11 s. M1 used the value obtained for X_0 to constrained the $^{12}C(\alpha,\gamma)^{16}O$ cross section, a crucial parameter for many fields in astrophysics and difficult to constrain in terrestrial laboratories. This profile obtained for the best fit has helped to investigate the determination of such important parameters, but it does not reproduce completely the profiles obtained from evolutionary codes, which are in general more complex. This may indicate that a more redefined profile may improve

the fit, and/or that the models are lacking or using wrong some physics. Metcalfe (2003) used this five-parameter approach to investigate how to improve the physics contained in the models. The author obtained a better fit by using the $ML\ 2/\alpha = 1.25$ prescription for convection adopted for spectroscopic fits by Beauchamp et al. (1999) rather than the "ML 3" prescription used before.

The information about the hidden interiors of the star can also be used to explore the previous history of the star. The C/O profiles are different depending on the evolution followed for the star. C/O profiles obtained from single evolutionary models present differences respect to profiles obtained from models of evolutions of close binary systems (e.g. see IT85; Iben 1986 -hereafter I86). Changes in the structure of the C/O profiles are due to the different times scales associated with evolutionary stages like the red giant branch (RGB) and asymptotic giant branch (AGB) if common envelopes in these stages are produced during close binary evolution. The inclusion in the code of these different profiles may tell us which evolutionary history determines the best-fit model.

5.1.3. Close binary evolution possibilities.

Different possibilities lead to the creation of peculiar white dwarf stars through binary evolutionary channels. IT85 and I86 analyzed many different options. We have concentrated on the evolutionary channels which produce white dwarfs without hydrogen. Hydrogen may be completely removed from the system due to previous common envelopes stages. The resulting white dwarfs have a surface rich in helium and may contribute to the DB population.

IT85 analyzed the possibility to obtain such white dwarf evolving components of close binary systems of intermediate mass (component masses in the range 3-12 $M_{\odot}$). They assumed models where the more massive component fill its Roche lobe during the red giant brach phase (RGB), after the central hydrogen exhaustion, but before or near the onset of core helium burning (case B). The binary components experience one or two mass loss processes due to common envelope stages depending upon the initial main-sequence mass. Several of these cases lead to the formation of DB white dwarfs where all hydrogen has been removed of the system. Examples are components which have masses in the range 2.3 to 4.8 $M_{\odot}$. These stars experience just one episode of mass loss and become degenerate dwarfs of mass in the range 0.32 to about 0.7 $M_{\odot}$. The remnants experience several small hydrogen shell flashes and one large final flash which, for the more massive degenerates

dwarfs, remove almost all the hydrogen-rich layer. In these cases the total mass in the hydrogen layer is reduced to about $10^{-5}M_{\odot}$. This evolutionary channel may produce remnants with masses as small as 0.4 $M_{\odot}$ and can convert 70% of its initial helium into carbon/oxygen. This represent a substantial difference from single low-mass star, which does not ignite and burn helium until the mass of its electron-degenerate core reaches $\sim$0.5 $M_{\odot}$. More recently Han, Tout & Eggleton (2000) have carried out new close binary evolutionary calculations and found that a carbon/oxygen white dwarf with mass as low as 0.33 $M_{\odot}$ may be formed from stable Roche overflow (RLOF) if the initial mass of the primary is close to 2.5 $M_{\odot}$. IT85 found that binary components of initial mass in the range 4.8 - 10.3 $M_{\odot}$ loose the hydrogen-rich matter in two episodes of Roche-lobe overflow and become CO degenerate dwarfs of mass in the range 0.7 - 1.08 $M_{\odot}$. This channel produces also DB white dwarfs with different characteristics. For the more massive remnants (over 0.8 $M_{\odot}$), a substantial part of the helium layer is also removed from the system during the second Roche-lobe overflow, so the degenerate dwarf would have a thin helium outer layer. This layer is expected to be thicker for remnants below 0.8 $M_{\odot}$. IT85 estimated a formation rate of $\sim 10^{-2}yr^{-1}$ of non-DA degenerate dwarfs created for these binary scenarios and conclude that they may produce 15%-20% of all hot non-DA white dwarfs.

I86 analyzed the evolution of close binary components of initial mass 3 - 7 $M_{\odot}$ where only one episode of mass loss happens during the asymptotic giant brach phase (AGB). Models with components of initial mass $\sim$4 - 5 $M_{\odot}$ produced degenerate dwarfs without hydrogen if mass loss is initiated at an arbitrary point during the early AGB phase (early case C event). Comparing with IT85 results, the mass of degenerate dwarfs produced by early case C mass loss is considerably larger that that produced by case B mass loss. For instance, for the case of a initial mass $\sim$4 $M_{\odot}$, early case C mass loss produced a 0.770 $M_{\odot}$ and case B a 0.523 $M_{\odot}$ degenerate dwarf.

5.2. Computation of models.

5.2.1. DB white dwarfs models.

To find the theoretical model of a white dwarf, we start with a static model of a pre-white dwarf and allow it to evolve quasi-statically until it reaches the desired temperature. We then calculate the adiabatic non-radial oscillation frequencies for the output model. The initial models can come from detailed calculations that evolve a main sequence star all the way to its pre-white dwarf phase, but this is only important for accurate models of the hot

DO white dwarfs. For the cooler DB and DA white dwarfs, it is sufficient to start with a hot polytrope of order 2/3 (i.e. $P \alpha \rho^{5/3}$). The cooling tracks of these polytropes converge with those of the pre-white dwarfs models well above the temperatures at which DB and DA white dwarfs are observed to be pulsationally unstable (Wood 1990). A grid of 100 starter models is generated to allow fitting total masses between 0.45 and 0.95 $M_{\odot}$. The grid is originated from a 0.6 $M_{\odot}$ carbon-core polytrope by using homology transforms.

The White Dwarf Evolution Code (WDEC) is used to evolve a starter model to a specific temperature. This code is described in detail by Lamb & Van Horn (1975) and by Wood (1990). It was originally written by Martin Schwarzschild, and has subsequently been updated and modified by many others including: Kutter & Savedoff (1969), Lamb & Van Horn (1975), Winget (1981), Kawaler (1986), Wood (1990), Bradley (1993), and Montgomery (1998). The equation of state (EOS) for the cores of our models come from Lamb (1974), and from Fontaine, Graboske & Van Horn (1977) for the envelopes. We use the updated OPAL opacity tables from Iglesias & Rogers (1993), neutrino rates from Itoh et al. (1996), and the ML3 mixing-length prescription of Böhm & Cassinelli (1971). The evolution calculations for the core are fully self-consistent, but the envelope is treated separately. The core and envelope are stitched together and the envelope is adjusted to match the boundary conditions at the interface. Adjusting the helium layer mass involves stitching an envelope with the desired thickness onto the core before starting the evolution. Because this is done while the model is still very hot, there is plenty of time to reach equilibrium before the model approaches the final temperature.

The pulsations frequencies of the output models are determined using the adiabatic non-radial oscillation (ANRO) code described by Kawaler (1986). Practical modifications to these programs were done by M0, primarily to allow models to be calculated without any intervention by the user.

5.2.2. The genetic algorithm.

The global search for the optimal model parameters to fit the independent pulsations periods of GD 358 is done by using the optimization method developed by Metcalfe et al. (2000, 2001). This method improves the objective search in the parameter space over traditional procedures like iterative procedures used to improve upon a first guess in order to find the best-fit model in a multi-dimensional parameter space. This standard approach has a potential problems: the initial set of parameters is usually subjectively determined.

This, combined to a local search in the parameter space, may produce a local good fit which is not the best fit. To avoid this problem Metcalfe et al (2000, 2001) optimized a user independent global search based on the genetic algorithm (GA). Restriction by this method regarding the range of the parameters space are imposed only by observational constraints and the physics of the model. GA provides a relatively efficient way of searching globally for the best-fit model. The basic idea were inspired by Darwin's notion of biological evolution through natural selection, and proceed to solve an optimization problem by evolving to the best solution from an initial set of completely random guesses. In this scheme, the theoretical model provides the framework within which the evolution takes place, the individual parameters controlling it act as the genetic building blocks and the observations provide the selection pressure.

The first step GA do is to fill up the parameter space with trials consisting of randomly chosen values for each parameter, within a range based on the physics that the parameters are supposed to describe. The model is evaluated for each trial, and the result compared with the observational data. This comparison assigns a fitness to the trial inversely proportional to the variance. The new generation of trials is then created taking into account the previous fitness. The bests fitness survive to the next generation and the parameter space is better sampled around these values. Operators emulating reproduction and mutation are applied to produce the new generation of trials. Reproduction is simulated by the genetic operator crossover, which exchange the genes (parameters) between two chromosomes (models encoded into a long string of numbers). Another operator called mutation serves to explore new areas in the parameter space. The new generation is formed after these operators have been applied and the strings are decoded back into sets of numerical values for the parameters. The new generation replaces the old one, and the process begins again. The evolution continues for a specified number of generations, chosen to maximize the efficiency of the method. We used a population size of 128 trials and allowed the GA to run for 200 generations. We have performed a total of 10 GA runs for each core composition to reduce the chances of not finding the best answer to less than about 3 in 10 000.

5.2.3. Darwin

The GA code has been implemented in a network of 64 PCs running Linux (Metcalfe & Nather 1999a and 1999b). Figure 94 presents a picture of this network. The white dwarf

Fig. 94. Darwin is the main computer of this collection of 64 PCs connected by a network.

code runs on this metacomputer by using the Parallel Virtual Machine (PVM) software (Geist et al., 1994) which allows a collection of networked computers to cooperate on a problem as if they were a single multiprocessor parallel machine. The central computer in the network is called Darwin and runs the parallel version of the genetic algorithm (PIKAIA) which is the master program. After generating a new generation, Darwin distributes to the slave computers an array with the models to check. The slave computers perform the following actions: evolve a white dwarf model to a specify temperature, determine the pulsation periods of the model, and compare observations with the calculated pulsation periods. Then it sends this fit back to Darwin which will included it in the GA code. The slave computer will also let know that it is ready for a new trial so Darwin can send a new trial of the generation.

The implementation of GA in Darwin has produced an efficient system to search in the complete parameter space for the best fit solution to DB pulsating white dwarfs models. This analysis was done using only 32 PCs due to problems with the others 32 section of the network.

5.2.4. Parameters space and profiles.

The main objective of the present work is to investigate the possibilities to use our current understanding of the pulsating DB white dwarfs to infer, using asteroseismology, their previous history. For this purpose we have used models with three free parameters: the mass of the star ($M_\star$), the effective temperature (T_{eff}) and the mass of the helium layer (M_{he}), and fixing in the code the C/O profiles which results from evolutionary models (IT85, I86). The authors present in these papers profiles obtained from various evolutionary channels

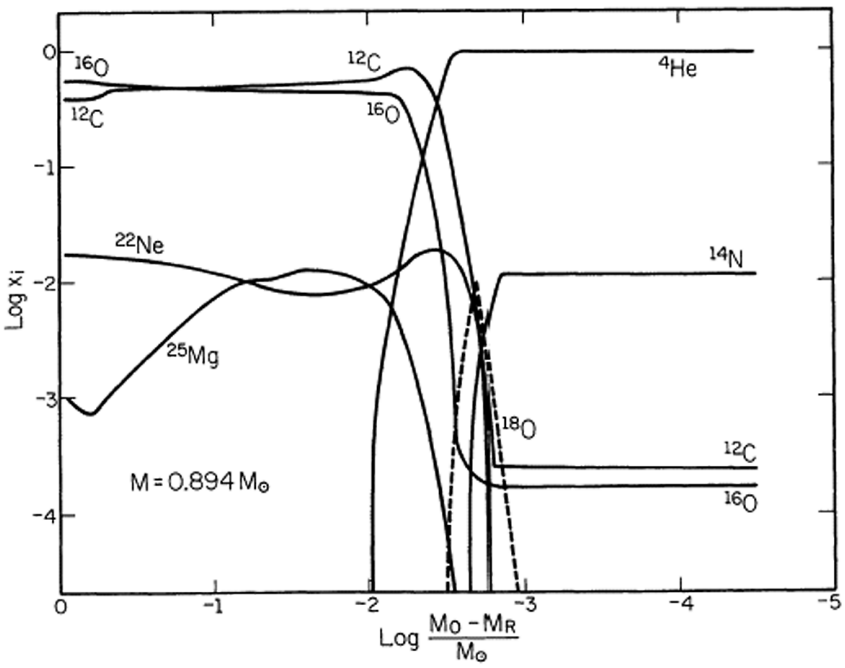

Fig. 95. IT85 profile example (their figure 13): this case corresponds to a 0.894 $M_{\odot}$ remnant model of initial mass 6.95 $M_{\odot}$. The model have experienced two process of mass lost during 2 episodes of CE, the first one happened during the RGB stage. The axis scales need to be changed in order to compute the profile.

in close binary evolution. Some profiles obtained from single evolutionary channels are also included in the same papers to compare. Figure 95 presents an example of IT85 profile. The authors present results on logarithmic scales in order to show more clearly the surface chemical abundances.

The parameters space used for the three free parameters models is based on the current parameter space ranges available for the GA global search in Darwin: the masses are confined between 0.45 $M_{\odot}$ and 0.95 $M_{\odot}$. Although some white dwarfs are known to be more massive than this upper limit, they represent a very small fraction and, for reasonable assumptions about the mass-radius relation, all known DBVs appear to have masses within this range (Beauchamp et al. 1999). The temperatures search includes temperatures between 20 000 K and 30 000 K. The most recent temperature determination for the known DB instability strip, that is, the strip in the T_{eff} versus $log(g)$ diagram where the DB white dwarfs are pulsationally unstable, was done by Beauchamp et al (1999). The authors, depending on various assumptions, place the red edge as low as 21800 K, and the blue edge as high as 27800 K. Finally, the search interval for the mass of the atmospheric helium layer has a lower limit 10^{-8} $M_{\star}$ and an upper limit 10^{-2} $M_{\star}$. Masses must not

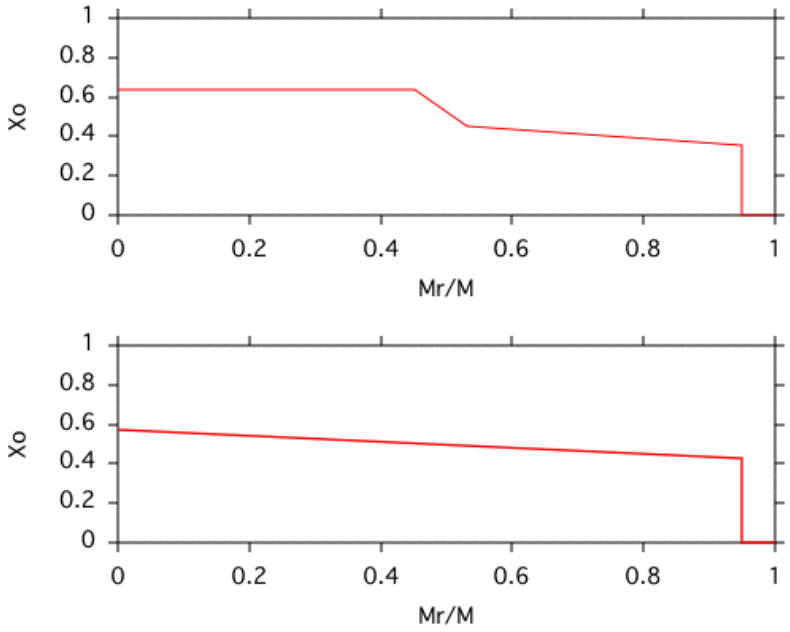

Fig. 96. Profiles for evolutionary histories affected by 2 process of mass lost during 2 episodes of CE, the first one happened during the RGB stage. The upper part shows the profile obtained for a 0.752 $M_{\odot}$ remnant and the lower for a 0.894 $M_{\odot}$ remnant .

be greater than this because the pressure on the overlying material will then theoretically initiate helium burning at the base of the envelope. At the other extreme, none models pulsate for helium masses less than 10^{-8} $M_{\star}$ over the entire temperature range we consider (Bradley & Winget 1994).

A two-digit decimal is used for encoding the different parameters. This results in a temperature resolution of 100 K, a mass resolution of 0.005 $M_{\odot}$, and a resolution for the helium layer thickness of 0.05 dex.

The profiles are fixed in the model. The different profiles tested are adaptations of IT85 and I86 evolutionary models for close binary systems. These profiles have been adapted from the original papers to to be able be compute them. We have selected the oxygen abundance from the original papers. The axis scales have been transformed to X_O (Fraction of oxygen) versus $M_r/M_{\star}$ (relative mass fraction at different radius). The C/O profiles are computed by including a series of pairs of points (X_C, $M_r/M_{\star}$), where $X_C = 1 - X_O$. These pairs define the profile shape in the model. We have used between 6 and 8 points to define the profiles. This parametrization procedure simplifies the original shape of the profiles. However, in many cases, this number of points reproduces quite well the original profile.

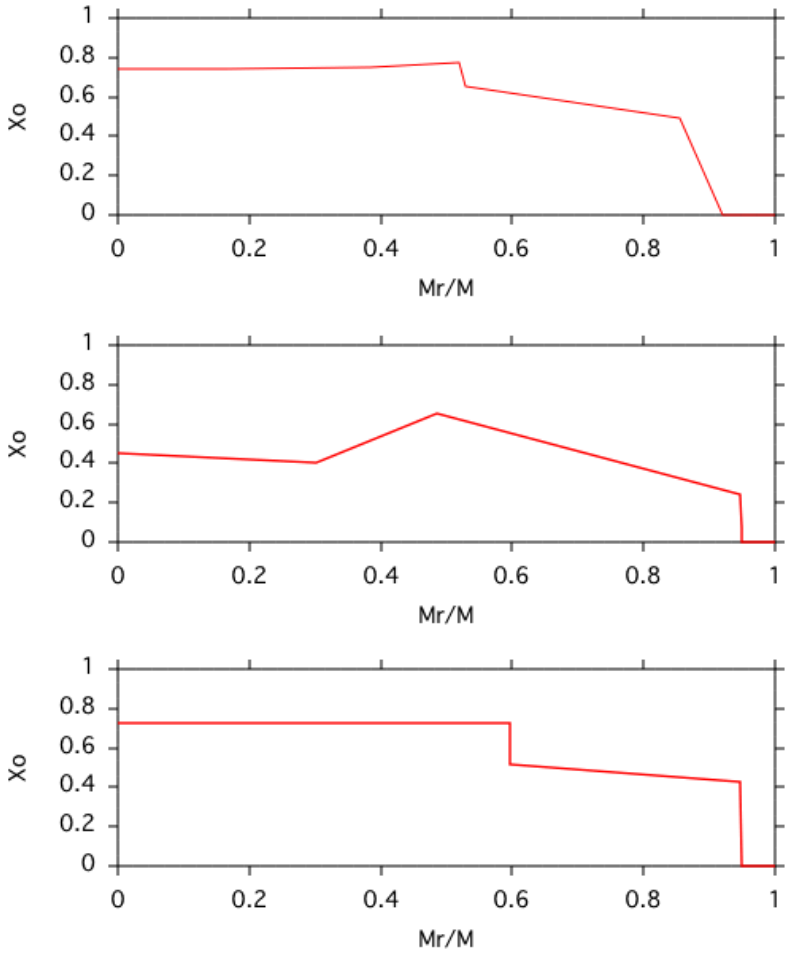

Fig. 97. The upper panel show the profile related with evolutionary history affected by 1 process of mass lost due to a CE during the RGB stage and obtained for a 0.523 $M_{\odot}$ remnant. The middle panel shows the profile obtained for a single evolutionary case: a white dwarf model of mass 0.599 $M_{\odot}$ which derives from the evolution of a horizontal-branch model of initial mass 7 $M_{\odot}$. The lower panel shows another profile related to single evolutionary history; in this case a white dwarf model of mass 0.965 $M_{\odot}$ evolved from a single AGB model star of mass 7 $M_{\odot}$

Amother simplification is that our models consider carbon and oxygen as the only nuclear species in the interiors of the white dwarfs. However IT85 and I86 evolutionary models shows the presence of a little amount of other elements like ^{22}Ne and ^{25}Mg. However, in the worst case ^{22}Ne constitute only $\sim$3% of the oxygen (in mass) and ^{25}Mg $\sim$1%. We do not consider other elements beside carbon and oxygen to compute our profiles.

The group of profiles selected are from papers of the 1980s. However, we have selected them for our study because we have not found in the litterature a more recent group of profiles including different evolutionary channels. IT85 and I86 present several profiles for

different evolutionary channels, and including for comparison single evolutionary options. We wanted also to test profiles coming from different evolutionary channels based on the same physics, to have better possibilities for a qualitative comparison. More recent profiles for single evolutionary scenarios are available (e.g., Salaris et al. 1997). However, the physics included in these evolutionary models is slightly different, e.g. how overshooting is treated, or nuclear reactions rates. Models with different physics may produce different profiles shapes for the same evolutionary channel. Therefore, the comparison of the best-fits models for different profiles may not give information about the evolutionary channels which fit better to the observations, but the differences in the physics applied. Figure 96 and 97 show the profiles tested.

The profiles have been selected according to close binary evolutionary channels where, due to evolutionary episodes of interaction with the close companion, such as common envelope stages, all the hydrogen of a white dwarf is removed. The white dwarf then becomes surface rich in helium, like the DB white dwarfs. Close binary evolutionary channels may produce a fraction of the observed DB white dwarfs. IT65 and I86 produced profiles for different possible close binary evolutionary scenarios. The models start with an initial pair of stars of certain masses and separations which are evolved and produce a white dwarf with certain mass without hydrogen on the surface. The profiles obtained for the evolutionary scenarios are therefore related to a specific mass of the resulting degenerate dwarf. The shape of the profile is related to the white dwarf mass. Table 17 present the different profiles tested, and characteristics associated. We have tested two profiles associated with a degenerate white dwarf which has experienced 2 episodes of mass lost in common envelopes episodes, the first happening during the RGB phase: one profile is related to a 0.894 $M_{\odot}$ remnant of a model of initial mass 6.95 $M_{\odot}$ (see fig. 13 of IT85) and the other to a 0.752 $M_{\odot}$ remnant of a model of initial mass 5 $M_{\odot}$ (see fig. 12 of IT85) The third profile checked corresponds to a 0.523 $M_{\odot}$ remnant of a model of initial mass 4 $M_{\odot}$ which has experienced only one episode of mass loss because of a common envelope during the RGB phase. This model conserves some hydrogen in the surface layer, $\sim 2.6 \times 10^{-4}$ $M_{\star}$ (see fig. 27 in IT85). We have completed our comparative analysis by checking the best-fit for 2 profiles coming from a single evolutionary scenario: a white dwarf model of mass 0.599 $M_{\odot}$ which comes from the evolution of a horizontal-branch model of initial mass 7 $M_{\odot}$ (Iben 1982). In this case all initial CNO abundances and the abundances of species derived from them are 20 times smaller than in the previous cases.

Table 17. Characteristics of the evolutionary channels of the profiles tested. The second colum indicates the amount of mass loss during the common envelopes (CE) phases in the previous evolution. RGB indicates that the first happen during the Red Giant Brach stage. SE indicates single evolution. HB indicates white dwarfs coming from horizontal branch model, and AGB from Asymptotic Giant Branch model.

Profile id	**Evolution**	**Mass WD ($M_\odot$)**	**Hydrogen**
1	1 CE, RGB	0.523	$\sim 2.6 \times 10^{-4}$
2	2 CE, RGB	0.894	no
3	2 CE, RGB	0.752	no
4	SE, HB	0.599	yes
5	SE, AGB	0.965	yes

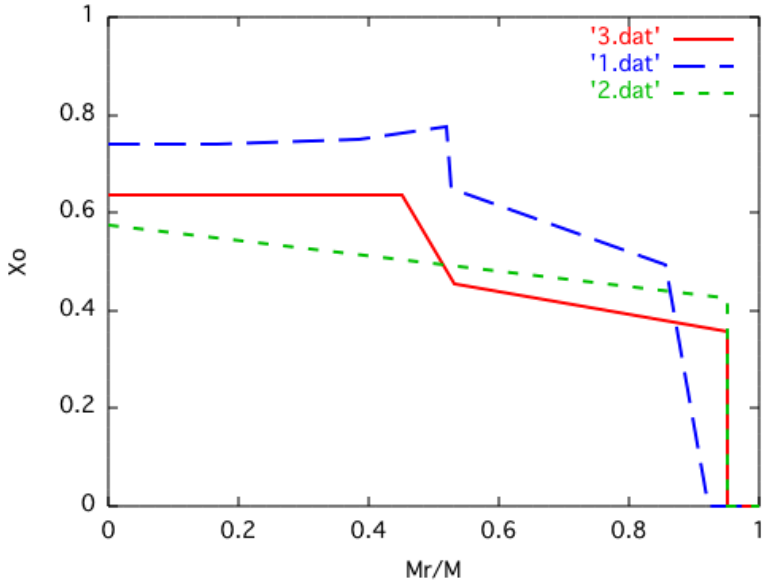

Fig. 98. Comparison of profiles. The identification number is given in the table 17

And we have also tested a remnant of 0.965 $M_\odot$ core of a single AGB model star of mass 7 $M_\odot$ (Iben 1976). This last model present a problem since our parameter space for the mass is limited to $0.95 M_\odot$.

A consistent test for a profile must produce a best-fit model associated with a mass not too far away from the value it is related to in the evolutionary models.

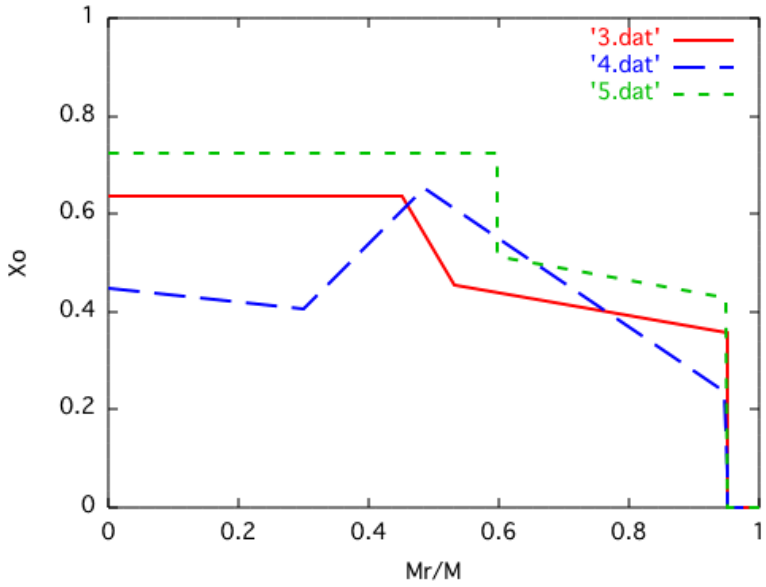

Fig. 99. Comparison of profiles. The identification number is given in the table 17

Table 18. Results: The best models obtained for the different evolutionary channels tested. The table presents the two best fits found for the different profiles. The fits labeled with 'a' are not compatible with the observed parallax of GD 358.

Profile id	T_{eff} **(K)**	$M/M_{\odot}$	$log(M_{He}/M_{\star})$	r.m.s. (s)
1	21 700	0.687	-3.27	2.45
	23 500	0.642	-2.69	2.59
2	20 500	0.772	-5.60	1.92^{a}
	23 200	0.647	-2.69	2.36
3	22 700	0.662	-2.79	1.91
	22 000	0.687	-2.90	2.10
4	28 900	0.76	-2.31	1.88^{a}
	24 600	0.835	-4.07	2.05^{a}
5	25 600	0.56	-5.50	3.16

5.3. Results.

We have used the GA optimization method to look for the optimal solution for 3 different profiles (table 17). The best fits obtained are presented in table 18. The best residuals corresponds to the profiles 2, 3 and 4 presenting a best quality fit for these 3 different evolutionary histories. The profiles 2 and 3 are results of evolutionary channels where the

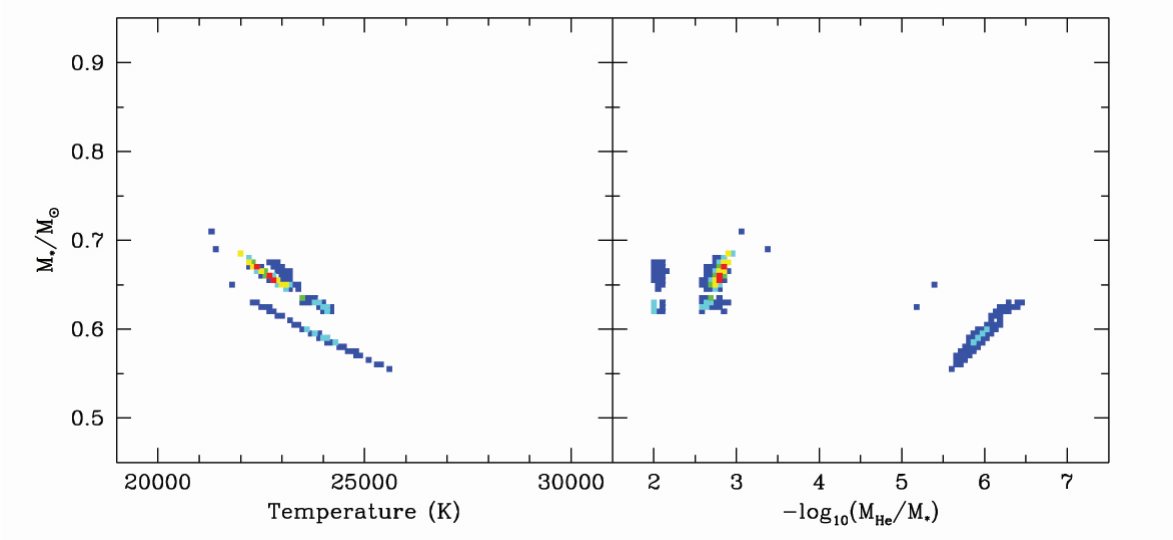

Fig. 100. Front and side views of the search space for the best model: binary evolution with two episodes of mass loss due to common envelopes (profile 3). Square points mark the location of models that yields a reasonable match to the periods observed for GD 358. The color of a point indicates the relative quality of the match (see text for details).

star experiences two common envelope phases. The profile 3 is related to an evolutionary model which creates a less massive white dwarf than the profile 2 (0.752 and 0.894 $M_{\odot}$). The masses obtained in our fits are in both cases ∼0.1 $M_{\odot}$ smaller: 0.662 and 0.772 $M_{\odot}$. In this case, our fits have produced a higher value for the white dwarf mass when we used the input profile related to a more massive remnant. Both fits have almost the same residuals (1.91 and 1.92 s) but our results show slightly different values for the 3 parameters: T_{eff}, $M_{\star}$ and $log(M_{He}/M_{\star})$. This confirms the dependence of the best models to the intrinsic shape of the profile. The best fit to the profile 2 is inconsistent with the observed parallax of GD 358 (Harrington et al. 1985). The same inconsistency is found for the two best fits obtained for the profile 4, which is related to a single star evolution channel.

Therefore, the best fit obtained consistent with the observations is for the model 3. The parameters obtained (T_{eff}=22 700 K , $M_{\star}$=0.662 $M_{\odot}$, $log(M_{He}/M_{\star})$=-2.79) are close to the best fits obtained by Metcalfe et al (2000 and 2001). The best fit model has a mass and temperature marginally consistent with those inferred from spectroscopy.

Figure 100 shows the general characteristics of the three-dimensional parameter space (M, T_{eff}, $log(M_{He}/M_{\star})$) where is presented all combinations of parameters found by the GA algorithm for our best fit model (with profile 2) with residuals smaller than 3.3 s. The two panels are orthogonal projections of the search space, so each point in

the left panel corresponds to one point in the right panel. The fit is displayed using the following colour scale: a red point if the residuals (r.m.s.) are smaller than 2 s; yellow: $2 \leq r.m.s. < 2.2$; green: $2.2 \leq r.m.s. < 2.5$; cyan: $2.5 \leq r.m.s. < 2.86$; green colour: $2.86 \leq r.m.s. < 3.3$. The figure shows the presence of more than one region that yields a good match to the observations. Two families of good fits, for thick and thin helium layers, are displayed, but the amount and quality of of the fits found for thick layers are larger. The distribution of the best models forms stripes in the search spaces panels. This is due to the parameter degeneracies in both projections. The parameter degeneracy between $M_\star$ and $log(M_{He}/M_\star)$ is described by Brassard et al. (1992), who showed that the pulsations periods of trapped modes in white dwarfs models are strongly influenced by the scaled location of the composition transition zone. They showed that these periods are directly proportional to the fractional radius of the composition interface. As the total mass of a white dwarf increases, the surface area decreases, so the mass of helium required to keep the interface at the same fractional radius also decreases. Thus, a thinner helium layer can compensate for an overestimate of the mass.

The parameter degeneracy between $M_\star$ and T_{eff} is related to the Brunt-Väisälä frequency, which reflect the difference between the actual an the adiabatic density gradients. The pulsation periods of a white dwarf model reflect the average of the Brunt-Väisälä frequency through the star. If the temperature decreases, the matter becomes more degenerate, so the Brunt-Väisälä frequency tends to be zero in much of the star, leading to lower pulsation frequencies. So an overestimate of the mass can compensate for an underestimate of the temperature.

Figure 101 present the observed and calculated periods for the different evolutionary channels plotted against the deviations from the mean period spacing (dP), which were calculated using the same set of periods in both cases. Note that the GA only fits the periods of the pulsations modes, and the agreement between the deviations from the mean period spacing is a reflection of the overall quality of the match.

5.4. Discussion.

We have presented an asteroseismological analysis of the DB GD 358 in order to investigate the evolutionary history of the star. This was done using the dependence of the pulsation modes to the internal C/O ratio distribution. Different evolutionary channels lead to the generation of different profiles describing how the C/O ratio changes from the core of the

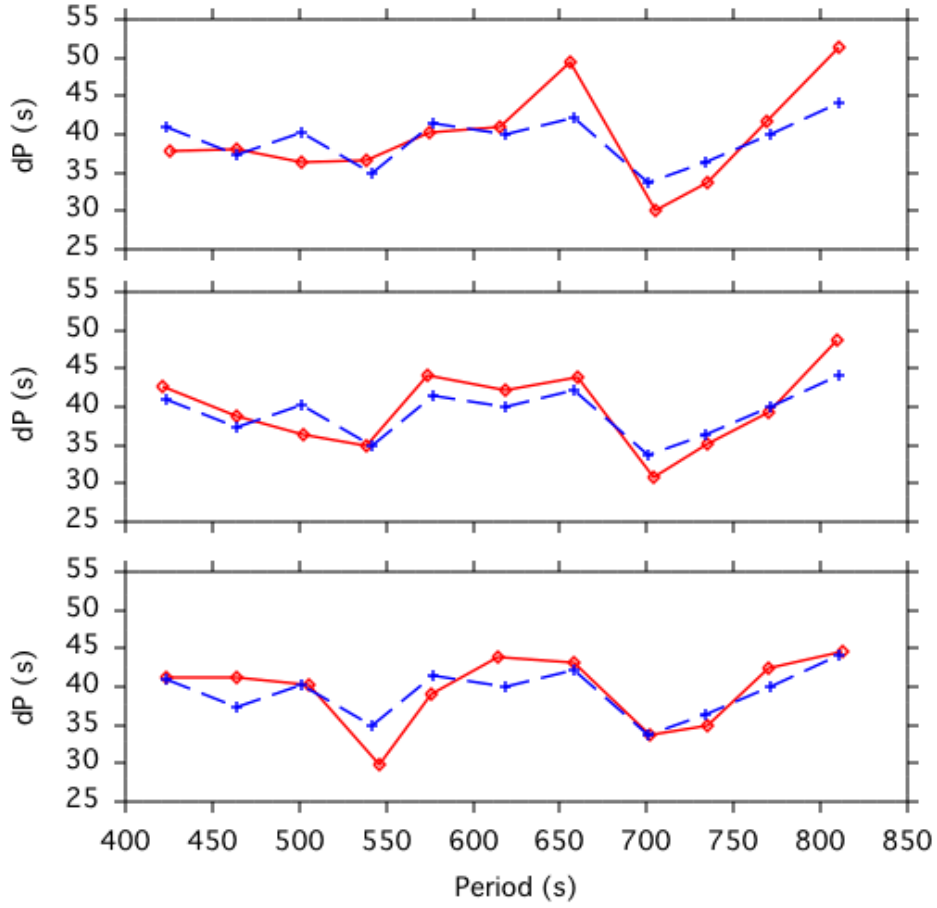

Fig. 101. The observed periods of GD 358, (dashed blue) and the optimal model periods found by the genetic algorithm (solid red) using a profile related to a remnant of 0.523 $M_{\odot}$ from binary evolution with 1 CE (upper panel), profile for remnant of 0.752 $M_{\odot}$ from binary evolution with 2 CE (middle panel), and profile for a remnant of 0.894 $M_{\odot}$ from binary evolution with 2 CE (lower panel)

star to its surface. We have tested and compared profiles associated to binary evolution where the object experienced one or two episodes of mass lost during one or two common envelope phases. In all the cases the first common envelope happens during the RGB phase. We have also analysed a profile related with single evolution. All the profiles computed are extracted from IT85. The results obtained confirm the dependence of the pulsations of the shape of the profile. The best fit obtained compatible with observations was using a profile related to an evolutionary model which produce a remnant of of 0.752 $M_{\odot}$ from binary evolution with 2 CE. The value obtained for the mass 0.662 $M_{\odot}$ is slightly lower than the mass related with the computed profile. This may indicate that the physics of the evolutionary code and/or the white dwarf model is not completely correct. However,

we have used all the profiles coming from the same evolutionary models to be able to do qualitative comparisons and to avoid difference in the fits because of the possible different physics included in the models. Our first results suggest that the binary evolution describes better the pulsations characteristics of GD 358. The values obtained: T_{eff}=22 700 K , $M_{\star}$=0.662 $M_{\odot}$, $log(M_{He}/M_{\star})$=-2.79, are close to previous fits reported by Metcalfe et al (2000, 2001). The difference between the approaches is that Metcalfe et al (2000) used profiles which are not related with evolutionary calculations but average shapes. However, this analysis was extremely important because they demonstrated the dependence of the best fit with the shape of the profile computed. Metcalfe et al (2001) left 2 parameters related with the profile shape as free parameter and extend the search of fits including these parameters space. This led them to estimate the $^{12}C(\alpha,\gamma)^{16}O$ cross section, a crucial parameter for many fields in astrophysics and difficult to constrain in terrestrial laboratories. Our approach is different since we are using profiles which are results of different evolutionary histories and comparing the best fit between them. Our best fit is related to an evolutionary history with two episodes of common envelope which has removed all the hydrogen of the surface of the star. This is an alternative way to explain this lack of hydrogen in DBs white dwarfs. IT85 estimated a formation rate of $\sim 10^{-2} yr^{-1}$ of non-DA degenerate dwarfs created from these binary scenarios, and conclude that they may produce 15%-20% of all non-DA white dwarfs. Our first results suggests that GD 358 may be one of those. The best fit model has a mass and temperature marginally consistent with those inferred from spectroscopy, and a thick outer layer of helium. However, it is necessary to do more fits in order to complete this first approach. We will implement in the near future with profiles coming from double evolutionary scenarios where the star experienced one episode of mass loss during one common envelope phase. In this case, the common envelope happens during the early AGB phase. We will check in addition more profiles related with single evolutionary channels of remnant evolved from AGB stages.

The results showed indicate that the method presented may be a good alternative to study the evolution of pulsating DB white dwarfs. This method is strongly related to observational properties of the stars since it is related to their pulsation periods. However, one of the main problem of this method is that it can only be applied to few pulsating DB white dwarfs: those which have been extensively observed in multisite campaigns like the WET (Whole Earth Telescope) in order to resolve their pulsational spectra. Currently there are only two candidates suitable for this study: GD 358 and CBS 114 (Handler

et al. 2002). We have presented the first promising results obtained for GD 358 using this approach. However, this methodology must be improved in the future because of the limitations explained in the next section.

5.5. Future.

This first approach had limitations which should be removed in order to obtain a better test. We have been limited to the published evolutionary models comparing single and binary evolutionary channels, and showing chemical profiles. At the same time, we wanted to use the same evolutionary models to avoid possible differences in the fits due to the different ways the models are computed. We have not found recently published profiles which include different evolutionary histories. Therefore, our work is based in IT85. On the other hand, these authors present profiles for different evolutionary scenarios producing different mass for the remnants. This make our qualitative study more difficult. The best option for this analysis would be to compute sets of profiles for different evolutionary histories producing the same remnant mass. This is important because the C/O profiles, specially the amount of oxygen in the center of the star, also depends on the mass of the degenerate core.

Some ranges of the parameters search for the GA have to be extended. This is important for the mass range, which actually is confined between 0.45 $M_{\odot}$ and 0.95 $M_{\odot}$. Although this range covers a large amount of the DB white dwarfs observed. Double evolutionary histories give the possibility to create C/O degenerate cores for a wider range of masses. The possibilities to compute the profiles have also limitations since actually the fraction of oxygen must be set to zero outside the following mass fraction: (M_r/M)=0.95. However, many profiles obtained in evolutionary models present substantial amount of oxygen outside this fractional mass, that is, closer to the surface. This is the case for some of the profiles computed in this study, which have been modified in order to set the oxygen fractional mass to zero at (M_r/M)=0.95. Other limitation is that the shape of the profile changes some during the cooling process of the white dwarfs. However, the basic main shape is kept in the range of temperatures where the DBVs are found.

Acknowledgment: the research presented in this chapter has been possible thanks to the help and assistance of Travis Metcalfe. I want to express my gratitude to him for his assistant preparing Darwin

and solving all sort of problems that have appeared; and also for his comments, suggestions and fruitful discussions. I want also to thanks Jan-Erik for his revision of the earlier versions of this chapter.

References

Beauchamp, A., Wesemael, F., Bergeron, P., Fontaine, G., Saffer, R. A., Liebert, J., & Brassard, P. 1999, ApJ, 516, 887

Bradley, P. A. 1993, Ph.D. thesis, University of Texas-Austin

Bradley, P. A., Winget, D. E., & Wood, M. A. 1993, ApJ, 406, 661

Bradley, P. A. & Winget, D. E. 1994, ApJ, 430, 850

Brassard, P., Fontaine, G., Wesemael, F., & Hansen, C. J. 1992, ApJS, 80, 369

Böhm, K. H. & Cassinelli, J. 1971, A&A, 12, 21

Geist, A., Beguelin, A., Dongarra, J., Jiang, W., Manchek, R., & Sunderam, V. 1994, PVM: Parallel Virtual Machine, A Users Guide and Tutorial for Networked Parallel Computing (Cambridge: MIT Press)

Fontaine, G., Graboske, H. C., Jr., & Van Horn, H. M. 1977, ApJS, 35, 293

Han, Z., Tout, C. A., Egglenton, P. P. 2000, MNRAS, 319, 215

Handler, G., Metcalfe, T. S. & Wood, M. A. 2002, MNRAS, 335, 698

Iben, I. Jr. 1976, ApJ, 208, 165

Iben, I. Jr. 1982, ApJ, 259, 244

Iben, I. Jr. 1986, AJ, 304, 201 (I86)

Iben, I. Jr., Tutukov, A. V. 1985, ApJS, 58, 661 (IT85)

Iben, I. Jr., & Tutukov, A. V. 1991, ApJ, 370, 615

Iglesias, C. A., & Rogers, F. J. 1993, ApJ, 412, 752

Itoh, N., Hayashi, H., Nishikawa, A., & Kohyama, Y. 1996, ApJS, 102, 411

Kepler, S. O. 1984, ApJ, 286, 314

Kawaler, S. 1986, Ph.D. thesis, University of Texas-Austin

Kutter, G. S. & Savedo, M. P. 1969, ApJ, 156, 1021

Lamb, D. Q. 1974, Ph.D. thesis, University of Rochester

Lamb, D. Q. & Van Horn, H. M. 1975, ApJ, 200, 306

Liebert J., 1986, Proc. IAU Coll. 87. D. Reidel Publishing Co., Dordrecht, p. 367

Metcalfe, T. S., & Nather, R. E. 1999a, Linux J., 65, 58

Metcalfe, T. S., & Nather, R. E. 1999b, Baltic Astron., 9, 479

Metcalfe, T. S., Nather, R. E., & Winget, D. E. 2000, ApJ, 545, 974 (M0)

Metcalfe, T. S., Winget, D. E., & Charbonneau, P. 2001, ApJ, 557, 1021 (M1)

Metcalfe, T.S., Salaris M., & Winget D.E. 2002, ApJ, 573, 803 (M2)

Metcalfe, T. S,, 2003, ApJ, 587, L43

Montgomery, M. H. 1998, Ph.D. thesis, University of Texas-Austin

Montgomery M.H., Metcalfe T.S. & Winget D.E. 2001, ApJ, 548, L53

Nather, R. E., Winget, D. E., Clemens, J. C., Hansen, C. J., Hine, B. P., 1990, ApJ, 361, 309

Salaris, M., Dominguez, I., Garcia-Berro, E., Hernanz, M., Isern, J., & Mochkovitch, R. 1997, ApJ, 486, 413

Shipman H., 1997, in Isern J. et al., eds, White dwarfs: Proc. 10th European Workshop on White Dwarfs. Kluwer, Dordrecht, p.165

Robinson, E. L., Kepler, S. O., & Nather, R. E. 1982, ApJ, 259, 219

Vuille F. et al., 2000, MNRAS, 314, 689

Winget, D. E. 1981, Ph.D. thesis, University of Rochester

Winget, D. E., Robinson, E. L., Nather, R. E., Kepler, S. O., & ODonoghue, D. 1985, ApJ, 292, 606

Winget, D. E., Nather, R. E., Clemens, et al. 1991, ApJ, 378, 326

Winget D.E. et al., 1994, ApJ, 430, 839

Wolff B., Koester D., Montgomery M.H., & Winget D.E. 2002, A&A, 388, 320

Wood, M. 1990, Ph.D. thesis, University of Texas-Austin

The road ahead

The observations and techniques presented in this thesis have revealed interesting facts and have opened new questions which are necessary to investigate in detail in the future. The results obtained have shown that photometric studies may be important searching for signatures in PNNs which may relate some of these objects as close binary systems. Spectroscopic and imaging studies of the shapes of planetary nebulas have revealed connexions with binary evolution. This thesis have focused the same problem but looking instead to the central star. The photometric signatures described in this thesis have opened an interesting way to probe that some of these systems may be close interacting binary stars and, in particular, may be related with evolutionary stages close to CVs.

NGC 246 and VV 47 may be objects of a new kind of family. The photometric signatures observed for these objects present common properties, such as the presence of pulsations in the high frequency domain showing short lifetimes, and pulsation periods ~4500 s with harmonics that may be related to orbital or superhump periods. Models predict that many CVs should be observed with orbital periods around 4500 s but none are observed. Our results may indicate that they do exist but, in order to find them, we should look in the nucleus of bipolar or elliptical PNs.

Further photometric monitoring of PNNs must be done to look for more candidates of this new family and to confirm this interesting hypothesis. We plan to complete the photometric analysis on VV 47 and NGC 246 by doing multicolour fast photometry. We have presented evidences that the pulsations in these objects are related to different sources: stellar pulsations or due to interaction with a close companion (orbital or superhump period). These different sources are expected to create pulsations with relatively different amplitudes in different filters. Once the photometric analysis identifies a possible orbital period, the natural way to confirm its nature is by using time resolved spectroscopy. We plan to investigate that for the PNN NGC 246 in the close future to confirm if the period at 4350 s is the orbital period.

Other intriguing question opened in this thesis is about time scales. Many of the pulsations observed seem to be related to the star (g-modes), but we have reported fast variability for many of these pulsations that can't be explained with our current understanding of the pulsating PNNs and PG 1159 stars. We have also shown for the first time evidences of observations of g-modes triggered by the κ-mechanism. Theoretical studies predicted these

modes some time ago. Therefore, our observations suppose a success of the pulsation theory. However, the same theory is not able to explain other fact reported: the short lifetime observed for these peaks. We hope these observations awake further theoretical studies and a better understanding of the physics in these systems.

Until now, in most of the cases, photometric studies have been done using the Fourier Transform, which supposes that the pulsations are stable in time. Merge light curves is a normal process in photometry, in order to achieve a better temporal resolution. This analysis provides good information, but may be loosing other. We have presented evidences of rapid changes in the temporal spectra of some PNNs and have shown that the analysis of these rapid variability may provide a lot of information intrinsic to the systems that may reveal important properties. We have extended the classical photometric analysis by using a method which also gives information of possible changes of the pulsations in time. The results obtained have been interesting, revealing facts that have opened new questions that current models cannot solve.

The use of wavelet analysis should be extended to more candidates. This analysis may create new families of objects, which may show common properties in the wavelet results. This may help to understand the nature of many of these objects and to investigate further evolutionary connexions. We plan to extend this analysis in the future to more AM CVn objects. Long light curves of AM CVn and V803 Cen are our next objectives. The first one to try to understand better the physics and structure of the accretion disks by monitoring how the power of the superhump and harmonics change with time. The case of V803 Cen is quite interesting, specially an analysis when the object change from low to high state. This may also give insights to how the structures of the accretion disk develop. Multisite campaigns will be valuable in this research in order to obtain long uninterrupted light curves. We will propose NGC 246 as secondary target for the next WET campaign.

The last research line opened in this thesis has been the test of the possible evolutionary history of GD 358 using asteroseismology. The use of Darwin principles has helped investigating the evolution of pulsating white dwarfs! This research line must be explored in detail in the future. We have discussed the next improvements to achieve in chapter 5. This method has shown the power of the asteroseismological studies. Asteroseismology have been proven to be a powerful tool giving important parameters of the pulsating white dwarfs stars. Now we have shown that it can also be used to investigate their previous evolution. The first results obtained are promising. However, the model needs to be refined and more adequate profiles should be computed. We have contacted groups working with evolutionary models in order to compute more adequate profiles.